# VERSLAGEN EN VERHANDELINGEN

REPORTS AND TRANSACTIONS

# NATIONAAL LUCHT- EN RUIMTEVAART-LABORATORIUM

NATIONAL AEROSPACE LABORATORY NLR

## THE NETHERLANDS

*

## XXXII - 1967

# PREFACE

This volume of Reports and Transactions of the National Aerospace Laboratory NLR contains a selection of reports completed in recent years.
In reports TR F.250 and TR S.613 investigations are discussed which have been performed under contract for respectively the Netherlands Aircraft Development Board (NIV), and the European Office of Aerospace Research of the U.S. Air Force and the NIV jointly. The permission for publication is herewith acknowledged.
In addition to the selected reports which are collected at more or less regular intervals in the volumes of Reports and Transactions, numerous others are published on subjects studied by the NLR. A complete list of publications issued from 1921 through 1966 is available upon request.

Amsterdam, March 1967

A. J. Marx

(Director)

## CONTENTS

C.C.L. Class. D 962: M 41

REPORT NLR-TR F. 238

# Theoretical and experimental results for the dynamic response of pressure measuring systems

by

H. Bergh and H. Tijdeman


## Summary

For a series-connection of $N$ thin tubes and $N$ volumes a general recursion formula has been derived that relates the sinusoidal pressure disturbance in volume $j$ to the pressure disturbances in the preceding volume $j-1$ and the next volume $j+1$. From this recursion formula the expressions for the complex ratio of the pressure fluctuation of each volume $j$ to the sinusoidal input pressure $p_0$ can be derived by successively putting $j = N, N-1, \ldots 2, 1$. For a single pressure measuring system ($N = 1$) and a double pressure measuring system ($N = 2$) these dynamic response formulae are given explicitely.

Theoretical results for single pressure measuring systems are presented that demonstrate the influence of the different parameters. As an illustrative example of the double pressure measuring system some calculations have been performed for a system with a discontinuity in tube radius.

Comparison of theoretical and experimental results shows that the response characteristics of the pressure measuring systems considered can be predicted theoretically to a high degree of accuracy.


## Contents



## List of symbols

| | |
|---|---|
| $a_0 = \sqrt{\dfrac{\gamma p_s}{\rho_s}}$ | — mean velocity of sound |
| $C_p$ | — specific heat at constant pressure |
| $C_v$ | — specific heat at constant volume |
| $g$ | — gravity constant |
| $\mathrm{i} = \sqrt{-1}$ | — imaginary unit |
| $J_n$ | — Bessel function of first kind of order $n$ |
| $k$ | — polytropic constant for the volumes |
| $L$ | — tube length |
| $m$ | — mass flow |
| $n$ | — kind of polytropic constant constant given in eq.(1) |
| $N$ | — number of tubes and volumes |
| $\bar{p} = p_s + p\,\mathrm{e}^{i\nu t}$ | — total pressure |
| $p_0$ | — amplitude of sinusoidal input pressure |
| $p_s$ | — mean pressure |
| $p$ | — amplitude of pressure disturbance |
| $P_r = \dfrac{\mu g C_p}{\lambda}$ | — Prandtl number |
| $r$ | — co-ordinate in radial direction (figure 1) |
| $R$ | — tube radius |
| $R_e$ | — effective tube radius |
| $R_m$ | — mean tube radius |
| $R_0$ | — gas constant |
| $t$ | — time |
| $\bar{T} = T_s + T\,\mathrm{e}^{i\nu t}$ | — total temperature |
| $T_s$ | — mean temperature |
| $T$ | — amplitude of temperature disturbance |
| $\bar{u} = u\,\mathrm{e}^{i\nu t}$ | — velocity component in axial direction |

| | |
|---|---|
| $\tilde{v} = v\,\mathrm{e}^{i\nu t}$ | — velocity component in radial direction |
| $V_v$ | — pressure transducer volume |
| $V_t = \pi R^2 L$ | — tube volume |
| $Y_n$ | — Neumann function of first kind of order $n$ |
| $\alpha = i^{\frac{3}{2}} R \sqrt{\dfrac{\rho_s \nu}{\mu}}$ | — shear wave number |
| $\gamma = \dfrac{C_p}{C_v}$ | — specific heat ratio |
| $\lambda$ | — thermal conductivity |
| $\mu$ | — absolute fluid viscosity |
| $\nu$ | — frequency |
| $\tilde{\rho} = \rho_s + \rho\,\mathrm{e}^{i\nu t}$ | — fluid density |
| $\rho_s$ | — mean density |
| $\rho$ | — amplitude of density disturbance |
| $\sigma$ | — dimensionless increase in transducer volume due to diaphragm deflection |
| $\phi = \dfrac{\nu}{a_0}\sqrt{\dfrac{J_0\langle\alpha\rangle}{J_2\langle\alpha\rangle}}\sqrt{\dfrac{\gamma}{n}}$ | |

subscripts:

| | |
|---|---|
| $j$ | refers to pressure transducer $j$ or tube $j$ |
| $v$ | pressure transducer volume |

## 1 Introduction

To support the development at the NLR of a technique for measuring pressure distributions on oscillating windtunnel models (ref. 1) a better knowledge of the pressure propagation through thin circular tubes with connected volumes was needed.

The response of pressure measuring systems to a sinusoidal input pressure has been considered by several authors. The method of Taback (ref. 2) is based on the analogy between the propagation of sinusoidal disturbances in electrical transmission lines and pressure measuring systems. To predict the response of a pressure measuring system, he uses the propagation velocity calculated from the Rayleigh formula combined with measured values of the attenuation. The fact that the attenuation constants have to be determined experimentally is one of the main disadvantages of this method.

In ref. 3 Davis presents asymptotic forms of the dynamic response formulae that can be used as basic guides for the selection of a pressure measuring system. In his work also some comparisons with experimental results are given. Iberall (ref. 4) derives the formulae for the dynamic response from the fundamental flow equations, i.e. the Navier-Stokes equations, the equation of continuity, the equation of state and the energy equation. The analytical part of his derivation has been omitted and no comparison with experimental values has been made.

Proceeding along the same lines as Iberall, the present report gives the derivation of a general recursion formula for the dynamic response of a series connection of $N$ tubes and $N$ volumes (figure 2).

From this recursion formula the expressions for the dynamic response of a single pressure measuring system ($N = 1$, figure 3) and a double pressure measuring system ($N = 2$, figure 4) are obtained and presented explicitely. The importance of the various parameters is illustrated by numerical examples representative for applications of the mentioned measuring technique.

The reliability of the theoretical predictions has been verified by comparing calculated and experimental results for single pressure measuring systems with different tube lengths and radii and for a system with one discontinuity in tube diameter (figure 5).

The authors wish to express their thanks to mr. A. C. A. Bosschaart for his valuable contribution in the earlier stage of this investigation.

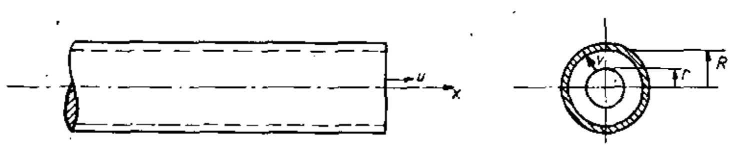


Fig. 1. Co-ordinate system.

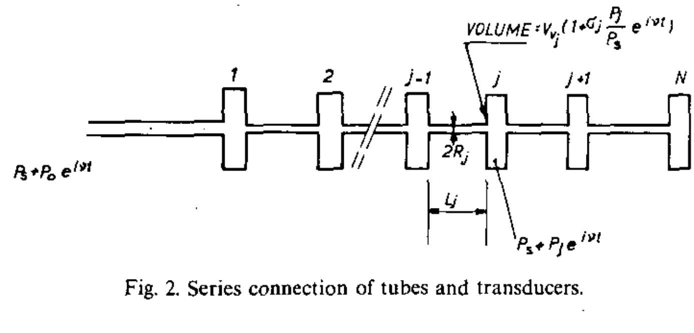


Fig. 2. Series connection of tubes and transducers.

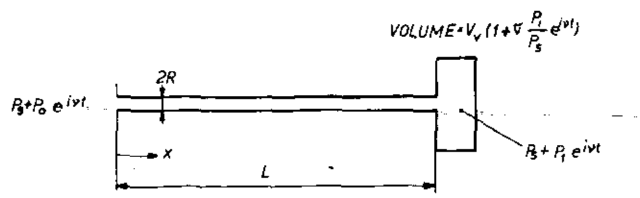


Fig. 3. Single pressure measuring system.

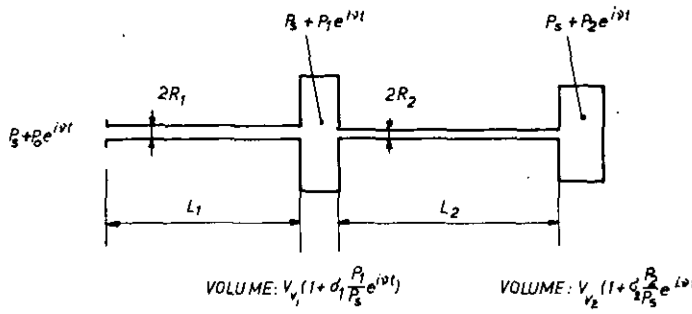


Fig. 4. Double pressure measuring system.

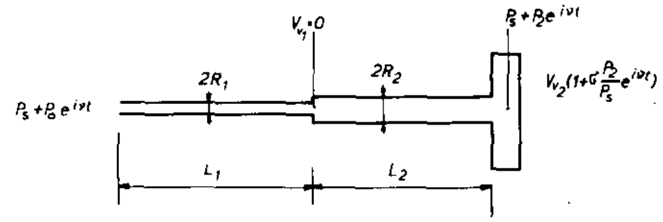


Fig. 5. Tube with discontinuity in tube radius.

## 2 Theoretical investigation

### 2.1 *General solution*

The motion of the fluid in a tube with a circular cross-section can be described by the fundamental flow equations, i.e., the Navier-Stokes equations, the equation of continuity, the equation of state and the energy equation that gives the balance between thermal and kinetic energies (see appendix).

As only the behaviour of sinusoidal oscillations in a fluid without steady velocity component are considered it can be assumed that:

$$\bar{p} = p_s + p\,e^{i\nu t}, \quad \bar{\rho} = \rho_s + \rho\,e^{i\nu t}, \quad \bar{T} = T_s + T e^{i\nu t}, \quad \bar{u} = u\,e^{i\nu t} \quad \text{and} \quad \bar{v} = v\,e^{i\nu t}$$

where $u$ and $v$ are the oscillatory axial and radial velocity components respectively.

Furthermore assuming that:

— the sinusoidal disturbances are very small
— the internal radius of the tube is small in comparison with its length
— the flow is laminar throughout the system

the mentioned equations can be simplified considerably.

To solve the unknown quantities $p$, $\rho$, $T$, $u$ and $v$ the following boundary conditions have been prescribed. At the rigid wall of the tube the velocity components $u$ and $v$ must be zero. Due to the axial-symmetry of the problem the velocity component $v$ must be also zero at the centerline of the tube. At the wall $T$ has been taken zero, supposing the heat conductivity of the wall being so large that the temperature variations at the wall disappear.

The latter condition, that gives a good representation of what happens in reality, has the advantage that it is not necessary to study in detail the heat exchange between the fluid within the tube, the tubewall and the environment.

For a tube of finite length the solution of the linearized flow equations, that satisfies the former boundary conditions has been given in the appendix.

The two remaining constants can be determined by specifying the boundary conditions at both ends of the tube. That means that at the entrance of tube $j$ the pressure variation must be equal to the given pressure disturbance $p_{j-1}\,e^{i\nu t}$, while at the end of the tube, where the volume $j$ is connected, the increase of mass of the pressure transducer must be equal to the difference in mass flow leaving tube $j$ and the mass flow entering tube $j+1$.

To describe the physical process within the transducer volume it is assumed that the pressure and density are only time dependent within this volume and that the pressure expansion takes place polytropically.

The transducer volume has been defined by $V_{v_j}[1+\sigma_j(p_j/p_s)e^{i\nu t}]$, where $\sigma_j$ is a dimensionless factor giving the increase in volume due to diaphragm deflection. This formulation is valid if the resonance frequency of the diaphragm is large in comparison with the frequency $\nu$ of the pressure fluctuation.

## 2.2 *Series connection of N circular tubes and N volumes*

For a series connection of $N$ tubes and $N$ volumes (see figure 2) a recursion formula has been derived that relates the sinusoidal pressure disturbance in volume $j$ to the sinusoidal pressure disturbances in the preceding volume $j-1$ and the next volume $j+1$.

The derivation of this formula is given in the appendix. The result is:

$$\frac{p_j}{p_{j-1}} = \Bigg[\cosh\langle\phi_j L_j\rangle + \frac{V_{v_j}}{V_{t_j}}\left(\sigma_j + \frac{1}{k_j}\right) n_j \phi_j L_j \sinh\langle\phi_j L_j\rangle + \frac{V_{t_{j+1}}\phi_{j+1}L_j J_0\langle\alpha_j\rangle J_2\langle\alpha_{j+1}\rangle}{V_{t_j}\phi_j L_{j+1} J_0\langle\alpha_{j+1}\rangle J_2\langle\alpha_j\rangle}\,\frac{\sinh\langle\phi_j L_j\rangle}{\sinh\langle\phi_{j+1}L_{j+1}\rangle}\left\{\cosh\langle\phi_{j+1}L_{j+1}\rangle - \frac{p_{j+1}}{p_j}\right\}\Bigg]^{-1} \qquad (1)$$

with $\phi_j = \dfrac{\nu}{a_{0_j}}\sqrt{\dfrac{J_0\langle\alpha_j\rangle}{J_2\langle\alpha_j\rangle}}\sqrt{\dfrac{\gamma}{n_j}}$

$\alpha_j = i\sqrt{i}\, R_j\sqrt{\dfrac{\rho_{s_j}\nu}{\mu_j}}$, the so-called shear wave number, being a measure of the wall shearing effects.

$$n_j = \left[1 + \frac{\gamma-1}{\gamma}\,\frac{J_2\langle\alpha_j\sqrt{P_r}\rangle}{J_0\langle\alpha_j\sqrt{P_r}\rangle}\right]^{-1}$$

From formula (1) the expressions for the complex ratio of the pressure fluctuation in each transducer $j$ to the sinusoidal input pressure $p_0$ can be derived by successively putting $j = N, N-1, \dots 2, 1$.

It appears that a solution identical to (1) is obtained if the equation of state and the energy equation are replaced by the polytropic relation

$$\frac{\bar{p}}{\bar{\rho}^n} = \text{constant, with } n = \left[1 + \frac{\gamma-1}{\gamma}\,\frac{J_2\langle\alpha_j\sqrt{P_r}\rangle}{J_0\langle\alpha_j\sqrt{P_r}\rangle}\right]^{-1}.$$

Evidently the pressure expansion in tube $j$ can be interpreted as a polytropic process with a polytropic factor

$$n_j = \left[1 + \frac{\gamma-1}{\gamma}\,\frac{J_2\langle\alpha_j\sqrt{P_r}\rangle}{J_0\langle\alpha_j\sqrt{P_r}\rangle}\right]^{-1}.$$

Asymptotic values are $\lim_{\alpha_j\to 0} n_j = 1$ and $\lim_{\alpha_j\to\infty} n_j = \gamma$, corresponding to isothermal and isentropic conditions respectively. In figure 6 the factor $n$ is given as a function of the parameter $\alpha\sqrt{P_r}$.

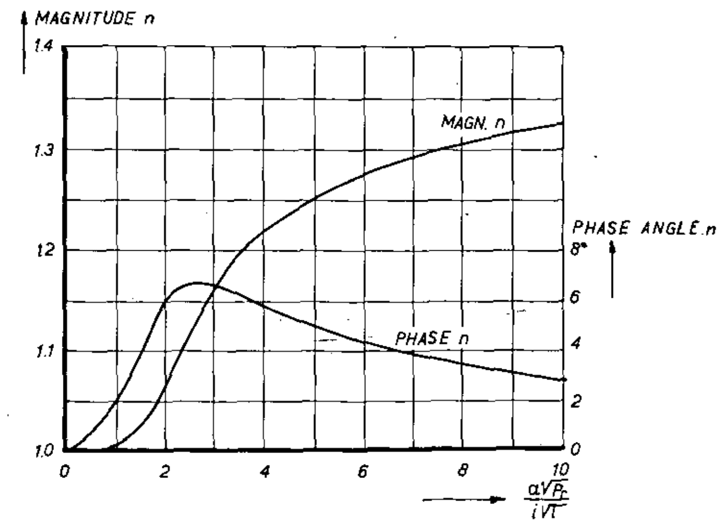


Fig. 6. "Polytropic" factor $n$ as a function of $\alpha\sqrt{P_r}/i\sqrt{i}$.

It will be remarked that by putting $V_{v_j}=0$ expression (1) offers the possibility for calculating the dynamic response for a system with a discontinuity in tube radius or in temperature.

2.3 *Single pressure measuring system* (figure 3)

The formula for the dynamic response to a sinusoidal pressure input $p_0$ of a system consisting of one tube connected at the end to the instrument volume $V_v$ can be derived immediately from the general recursion formula by putting $j=N=1$.

The result yields:

$$\frac{p_1}{p_0} = \left[\cosh\langle\phi L\rangle + \frac{V_v}{V_t}\left(\sigma + \frac{1}{k}\right) n\phi L \sinh\langle\phi L\rangle\right]^{-1} \tag{2}$$

It can be shown easily that the expression (2) is identical to that derived by Iberall (ref. 4) for the complex attenuation of the fundamental.

In the case of an inviscid isentropically expanding fluid in the tube ($\mu=0$; $n=\gamma$)

$\sqrt{\dfrac{J_0\langle\alpha\rangle}{J_2\langle\alpha\rangle}} \to \mathrm{i}$ and the formula for the pressure ratio becomes

$$\frac{p_1}{p_0} = \left[\cos\left\langle\frac{\nu L}{a_0}\right\rangle - \gamma\frac{V_v}{V_t}\left(\sigma + \frac{1}{k}\right)\frac{\nu L}{a_0}\sin\left\langle\frac{\nu L}{a_0}\right\rangle\right]^{-1}. \tag{3}$$

From eq.(3) it follows that resonance will occur if

$$\operatorname{cotg}\left\langle\frac{\nu L}{a_0}\right\rangle = \gamma\frac{V_v}{V_t}\left(\sigma + \frac{1}{k}\right)\frac{\nu L}{a_0}. \tag{4}$$

In the limiting cases $V_v=0$ and $V_v=\infty$ eq.(4) yields the well known organ pipe resonance formulae for a closed and open organ pipe.

$$\left.\begin{aligned} V_v=0:&\quad \operatorname{cotg}\left\langle\frac{\nu L}{a_0}\right\rangle = 0,\ \text{that means}\ \frac{\nu}{2\pi} = \frac{2s+1}{4}\frac{a_0}{L}\quad (s=0,1,2,\ldots)\\ V_v=\infty:&\quad \operatorname{cotg}\left\langle\frac{\nu L}{a_0}\right\rangle = \infty,\ \text{that means}\ \frac{\nu}{2\pi} = \frac{s}{2}\frac{a_0}{L}\quad (s=1,2,\ldots)\end{aligned}\right\} \tag{5}$$

2.4 *Double pressure measuring system* (figure 4)

Using the recursion formula (1) for the system formed by a series connection of two systems as treated above the following formulae for the dynamic response of this system are obtained:

$$j=2:\quad \frac{p_2}{p_1} = \left[\cosh\langle\phi_2 L_2\rangle + n_2\frac{V_{v_2}}{V_{t_2}}\left(\sigma_2 + \frac{1}{k_2}\right)\phi_2 L_2\sinh\langle\phi_2 L_2\rangle\right]^{-1} \tag{6}$$

$$\begin{aligned} j=1:\quad \frac{p_1}{p_0} = \Bigg[&\cosh\langle\phi_1 L_1\rangle + n_1\frac{V_{v_1}}{V_{t_1}}\left(\sigma_1 + \frac{1}{k_1}\right)\phi_1 L_1\sinh\langle\phi_1 L_1\rangle + \\ &+ \frac{V_{t_2}\phi_2 L_1 J_0\langle\alpha_1\rangle J_2\langle\alpha_2\rangle}{V_{t_1}\phi_1 L_2 J_0\langle\alpha_2\rangle J_2\langle\alpha_1\rangle}\,\frac{\sinh\langle\phi_1 L_1\rangle}{\sinh\langle\phi_2 L_2\rangle}\left\{\cosh\langle\phi_2 L_2\rangle - \frac{p_2}{p_1}\right\}\Bigg]^{-1}\end{aligned} \tag{7}$$

The complex pressure ratio $\dfrac{p_2}{p_0} = \dfrac{p_2}{p_1}\cdot\dfrac{p_1}{p_0}$ can be found from eqs.(6) and (7).

## 3 Theoretical results

### 3.1 *Calculations*

Besides calculations for comparison with experimental results (see section 5) a number of specific cases has been calculated to show the influence of different parameters on the dynamic response of a pressure measuring system.

From the theoretical expressions it can be seen that the dynamic response depends on the following parameters:

geometric parameters: $R$ = tube radius
$L$ = tube length
$V_v$ = pressure transducer volume
$\sigma$ = dimensionless increase in transducer volume due to diaphragm deflection

physical parameters:
$k$ = polytropic constant for the pressure expansion in the transducer volume
$T_s$ = mean temperature
$p_s$ = mean pressure

It must be noted that the quantities $V_v$, $\sigma$ and $k$ only appear in the combination $V_v\left(\sigma + \frac{1}{k}\right)$; a variation in one of these parameters separately can be expressed as an equivalent variation in one of the others.

The cases given in table 1 have been calculated to demonstrate the influence of the mentioned parameters on the dynamic response of the single pressure measuring system of figure 3.

As an example of a double pressure measuring system, the dynamic response has been calculated for a system with a discontinuity in tube radius (figure 5). The different cases that have been considered for this system are summarized in table 2.

### 3.2 *Discussion of theoretical results*

*a. Influence of the different parameters*

The results of figures 9, 10 and 11 show that in most cases, just like in organ pipes, resonance peaks occur. As could be expected it appears that for a given length a wider tube produces higher resonance peaks than a smaller one. Lengthening a tube of a given diameter results in lower resonance peaks at smaller values of the frequency. Furthermore for certain combinations of $L$ and $R$ no resonances occur as is demonstrated in figure 11 for $R =$ 0.50 mm. From figure 12 it can be seen that the product $V_v\left(\sigma + \frac{1}{k}\right)$ must be changed considerably to have much effect on the dynamic response characteristic. Mostly the increase in pressure transducer volume due to the deflection of the diaphragm is only a very small part of the total volume. The influence of the factor $\sigma$ itself therefore will be very small. The extreme values of the factor $k$ are 1 and 1.4, corresponding respectively to isothermal and isentropic pressure expansion in the instrument volume. Figure 13 shows that this factor only has a small influence on the response characteristic.

The variations of the mean pressure $p_s$ that have been considered appear to have a strong influence on the dynamic response of a pressure measuring system (figure 14). A variation in mean temperature between 0° and 30°C does not have much effect (see figure 15).

*b. System with discontinuity in tube radius*

The results for the given systems with a discontinuity in tube radius show some remarkable facts. From figures 16, 17 and 18 it can be seen that a wider second tube does not always have a favourable effect on the dynamic response. A smaller second tube on the contrary does not always act unfavourable.

This can be explained as follows: For a system consisting of a smaller tube followed by a wider one, the latter tube is more easy to overcome for a pressure disturbance due to relatively smaller effect of wall friction. On the other hand the wider tube acts like a kind of additional volume, thus reducing the output of the first tube. This two opposite effects are responsible for the final behaviour of the total system. The same effects, but working in opposite sense, are responsible for the behaviour of a system of a wider tube followed by a smaller one.

It will be clear that by changing the lengths of the two connected tubes also the ratio of the mentioned effects will be changed, thus giving other response characteristics.

From figures 19 and 20 it follows that a restriction at the entrance of a tube generally results in lower values of the amplitude ratio than in the case of a restriction at the end of the tube. Also in these figures it can be seen that changing the lengths of the restrictions gives other response characteristics. By proper selection of the ratio of tube lengths and of the ratio of tube diameters, a response characteristic can be obtained which is most suitable for a given purpose. In practice however one must be careful, because the discontinuities in the tube offer the possibility of non-linearities.

## 4 Experimental investigation

### 4.1 *Test program*

To get an insight into the reliability of the theoretical formulae an experimental investigation has been performed for a series of tubes of various dimensions (see tables 3 and 4). Except the two longer tubes, which are of plastic, all the tubes are made of stainless steel. With the aid of the equipment described in section 4.3 the dynamic responses have been measured in the frequency range $10 \leqslant \nu \leqslant 200$ c.p.s. At the entrance of the systems a sinusoidal pressure disturbance of about 65 kg/m$^2$ has been applied. To investigate the linearity of the systems with a discontinuity in tube radius two values of the input pressure $p_0$ have been used.

### 4.2 *Determination of tube radius and pressure transducer volume*

The dynamic response of a pressure measuring system is very sensitive to small variations in tube radius. This implies that it is necessary to have an accurate method for determining that internal radius of the thin tubes. In the present investigation the mean tube radius $R_m$ is determined as follows:

1) by weighing the tube empty and measuring the mean external diameter. From the tube weight, the specific weight of the tube material and the external diameter the mean wall-thickness can be calculated.
2) by weighing the tube empty and filled with water. The mean radius $R_m$ than can be calculated from the increase in weight.

Results:

| tube length | $R_m$(method 1) | $R_m$(method 2) | $R_m$(used in calculations) |
|---|---|---|---|
| 500 mm | 0.519 mm | 0.529 mm | 0.525 mm |
| 1000 | 0.490 | 0.492 | 0.49 |
| 1000 | 0.792 | 0.799 | 0.795 |
| 1000 | 1.092 | 1.092 | 1.09 |
| 3000 | — | 0.70 | 0.70 |
| 3910 | — | 0.965 | 0.965 |

To determine the volumes of the pressure transducers the test set up of figure 7 has been used. A variation of $p_1$ results in a variation of $p_2$ and thus in a variation of the volume of the instrument plus connecting glass tube of

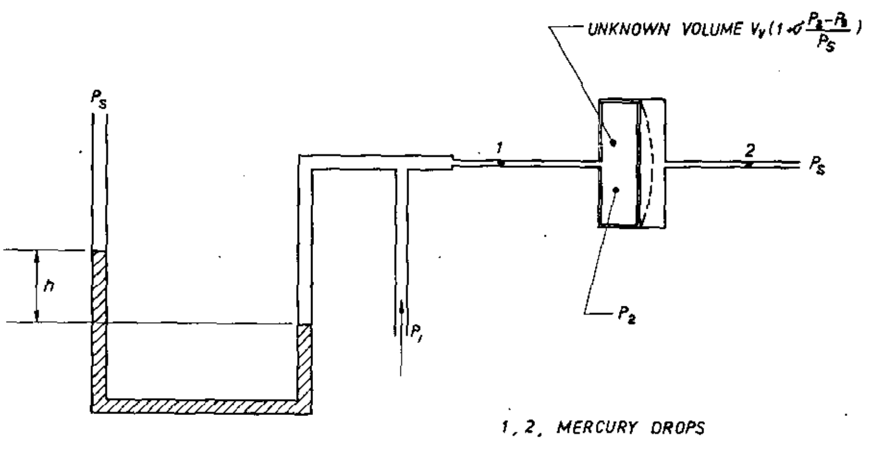


Fig. 7. Test set up for the determination of $V_v$ and $\sigma$.

known diameter. From the displacement of mercury drop 2 the value of $\sigma$ can be determined. From the displacement of drop 1 the value of $V_v$ can be calculated with the aid of Boyle's law.

### 4.3 *Measuring technique*

The semi-automatic measuring system, which has been developed at the NLR to enable a quick determination of a large number of pressures on oscillating windtunnel models (ref. 1) has been used to perform the present experiments. A block-diagram of the equipment is drawn in figure 8. In the electro-dynamically driven pressure generator a harmonically varying pressure with amplitude $p_0$ and frequency $\nu$ is generated. The signals of the pressure transducers 1 and 2 are amplified one after the other and fed into the vector component resolver, that decomposes them into one component in phase with the 0-degree oscillator signal and one in quadrature to it. The resolver rejects all signals, except those, having a frequency equal to that of the oscillator. The two components of each signal are measured by a digital voltmeter.

The results $p_2/p_1$ have been corrected for the attenuation of the small tube, that connects transducer 1 to the internal volume of the pressure generator. In the frequency range considered this correction is only of the order of a few percent.

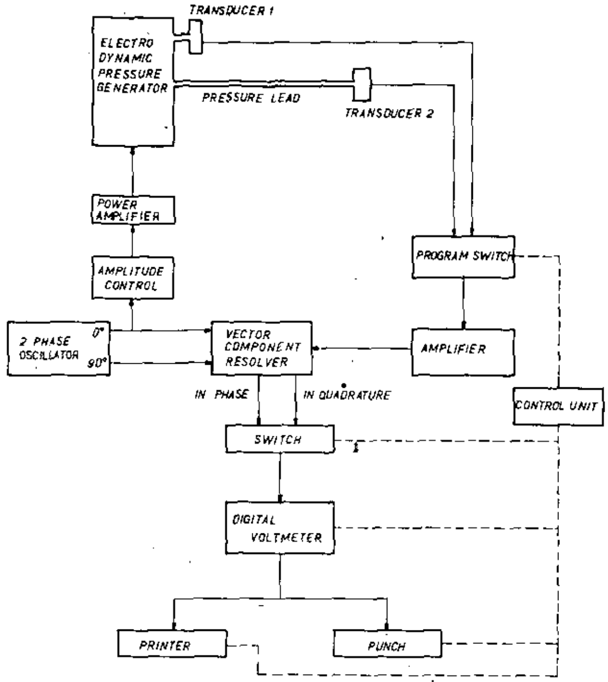


Fig. 8. Block diagram of equipment.

## 5 Experimental results and comparison with theory

The experimental and theoretical results for a single pressure measuring system with different tube lengths and tube radii have been plotted in the figures 21–26. In figure 27 and 28 the results for the system with a discontinuity in tube radius are presented.

The theoretical results have been calculated assuming an ideal tube with circular cross section and constant internal radius. In reality an exact measurement of the tube radius is not possible and furthermore local deviations may occur. A comparison of the experimental results with theoretical results calculated with the experimentally determined mean tube radius $R_m$ shows that in most cases small deviations exist. It appears that these differences can be completely cancelled by performing the calculations with an effective tube radius $R_e$ which is only slightly (2–5%) smaller than the mean radius $R_m$. The fact that the largest correction must be applied to the smallest tube seems to indicate that the determination of the mean tube radius was not accurate enough. This is supported by the two experiments with the discontinuous system (figures 27 and 28).

In the first case the pressure disturbance has been applied at the entrance of the wider part of the tube and the pressure transducer was connected to the end of the smaller one. In the second case the same tube has been used, but now in opposite direction. In both cases the same effective radii for the two parts must be taken to obtain theoretical results that are in perfect agreement with experiment. Furthermore it is striking that these values agree with the effective radii of the tubes of the single systems of figures 21 and 23, that are coming from the same original tubes as the two parts of the discontinuous system. The results with different values of the pressure input $p_0$ show that in the range considered non linear effects are hardly present.

Finally, since both steel tubes and plastic tubes give a good agreement between theory and experiment, the tube material appears to have no noticeable influence.

## 6 Conclusions

From the investigation, the following conclusions can be drawn:

1) The response characteristics of the pressure measuring systems considered can be predicted theoretically to a high degree of accuracy.
2) In the range of applied sinusoidal input pressures the non-linearities are negligible.
3) The tube material does not have any noticeable influence on the dynamic response.
4) The present theory enables the optimal design of pressure measuring systems adapted to the NLR technique for measuring pressure distributions on oscillating windtunnelmodels.

## 7 References

[1] Bergh, H., A new method for measuring the pressure distribution on harmonically oscillating wings. Proceedings of the 4th ICAS-congress, Paris 1964 (also NLR-MP. 224).

[2] Taback, I., The response of pressure measuring systems to oscillating pressures. NACA TN 1819; 1949.

[3] Davis jr., E. L., The measurement of unsteady pressures in windtunnels. AGARD rep. 169; 1958.

[4] Iberall, A. S., Attenuation of oscillatory pressures in instrument lines. Journal of research of the national bureau of standards. Vol. 45, July 1950.

# APPENDIX

## Derivation of the formulae

The equations governing the motion of a fluid in a circular tube (figure 1) are:

(a) The Navier-Stokes equations (for constant value of the absolute fluid viscosity $\mu$):

$$\bar{\rho}\frac{\partial\bar{u}}{\partial t}+\bar{v}\frac{\partial\bar{u}}{\partial r}+\bar{u}\frac{\partial\bar{u}}{\partial x}=-\frac{\partial\bar{p}}{\partial x}+\mu\left\{\left[\frac{\partial^2\bar{u}}{\partial x^2}+\frac{\partial^2\bar{u}}{\partial r^2}+\frac{1}{r}\frac{\partial\bar{u}}{\partial r}\right]+\frac{1}{3}\frac{\partial}{\partial x}\left[\frac{\partial\bar{u}}{\partial x}+\frac{\partial\bar{v}}{\partial r}+\frac{\bar{v}}{r}\right]\right\} \tag{1}$$

$$\bar{\rho}\frac{\partial\bar{v}}{\partial t}+\bar{v}\frac{\partial\bar{v}}{\partial r}+\bar{u}\frac{\partial v}{\partial x}=-\frac{\partial\bar{p}}{\partial r}+\mu\left\{\left[\frac{\partial^2\bar{v}}{\partial r^2}+\frac{1}{r}\frac{\partial\bar{v}}{\partial r}-\frac{\bar{v}}{r^2}+\frac{\partial^2\bar{v}}{\partial x^2}\right]+\frac{1}{3}\frac{\partial}{\partial r}\left[\frac{\partial\bar{u}}{\partial x}+\frac{\partial\bar{v}}{\partial r}+\frac{\bar{v}}{r}\right]\right\} \tag{2}$$

(b) The equation of continuity:

$$\frac{\partial\bar{\rho}}{\partial t}+\bar{u}\frac{\partial\bar{\rho}}{\partial x}+\bar{v}\frac{\partial\bar{\rho}}{\partial r}+\bar{\rho}\left[\frac{\partial\bar{u}}{\partial x}+\frac{\partial\bar{v}}{\partial r}+\frac{\bar{v}}{r}\right]=0 \tag{3}$$

(c) The equation of state for an ideal gas:

$$\bar{p}=\bar{\rho}R_0\bar{T} \tag{4}$$

(d) The energy equation:

$$\bar{\rho}gC_p\left[\frac{\partial\bar{T}}{\partial t}+\bar{u}\frac{\partial\bar{T}}{\partial x}+\bar{v}\frac{\partial\bar{T}}{\partial r}\right]=\lambda\left[\frac{\partial^2\bar{T}}{\partial r^2}+\frac{1}{r}\frac{\partial\bar{T}}{\partial r}+\frac{\partial^2\bar{T}}{\partial x^2}\right]+\frac{\partial\bar{p}}{\partial t}+\bar{u}\frac{\partial\bar{p}}{\partial x}+\bar{v}\frac{\partial\bar{p}}{\partial r}+\mu\phi \tag{5}$$

where $\phi$ is the dissipation function that represents the heat transfer due to internal friction:

$$\phi=2\left[\left(\frac{\partial\bar{u}}{\partial x}\right)^2+\left(\frac{\partial\bar{v}}{\partial r}\right)^2+\left(\frac{\bar{v}}{r}\right)^2\right]+\left[\frac{\partial\bar{v}}{\partial x}+\frac{\partial\bar{u}}{\partial r}\right]^2-\frac{2}{3}\left[\frac{\partial\bar{u}}{\partial x}+\frac{\partial\bar{v}}{\partial r}+\frac{\bar{v}}{r}\right]^2.$$

Putting
$$\left.\begin{aligned}\bar{p}&=p_s+p\,e^{i\nu t}\\ \bar{\rho}&=\rho_s+\rho\,e^{i\nu t}\\ \bar{T}&=T_s+T e^{i\nu t}\\ \bar{u}&=u\,e^{i\nu t}\\ \bar{v}&=v\,e^{i\nu t}\end{aligned}\right\} \tag{6}$$

and assuming that:

— the sinusoidal disturbances are very small
— the internal radius of the tube is small in comparison with its length
— the flow is laminar throughout the system

the eqs. (1) to (5) can be simplified to:

$$i\nu u=-\frac{1}{\rho_s}\frac{\partial p}{\partial x}+\frac{\mu}{\rho_s}\left[\frac{\partial^2u}{\partial r^2}+\frac{1}{r}\frac{\partial u}{\partial r}\right] \tag{6}$$

$$0=-\frac{\partial p}{\partial r} \tag{7}$$

$$i\nu\rho=-\rho_s\left[\frac{\partial u}{\partial x}+\frac{\partial v}{\partial r}+\frac{v}{r}\right] \tag{8}$$

$$\rho=\frac{\gamma}{a_0^2}\left(1+\frac{\rho_s}{T_s}\frac{T}{\rho}\right)\quad\text{or}\quad\rho=\frac{\gamma}{a_0^2}(p-\rho_sR_0T) \tag{9}$$

$$i\nu\rho_sgC_pT=\lambda\left[\frac{\partial^2T}{\partial r^2}+\frac{1}{r}\frac{\partial T}{\partial r}\right]+i\nu p\,. \tag{10}$$

The unknown quantities $p$, $\rho$, $T$, $u$ and $v$ must satisfy the following boundary conditions:

At the wall of the tube ($r=R$):

zero radial and axial velocity, i.e.: $u=0$; $v=0$ (11)

The conductivity of the wall is supposed to be so large that the variation in temperature at the wall will be zero: $T=0$ (12)

At the center of the tube ($r=0$):

Due to the axial-symmetry of the problem: $v=0$ (13)

A further requirement is that the values of $u$, $T$, $p$ and $\rho$ remain finite.

## General solution

—From eq. (7) it follows that the amplitude of the pressure disturbance $p$ is a function of the $x$-co-ordinate only. Eq. (10) can be written as:

$$T-\frac{\lambda}{\mathrm{i}\nu\rho_s g C_p}\left[\frac{\partial^2 T}{\partial r^2}+\frac{1}{r}\frac{\partial T}{\partial r}\right]=\frac{p}{\rho_s g C_p} \tag{14}$$

Introducing the notation $\alpha=\mathrm{i}^{\frac{3}{2}}R\sqrt{\frac{\rho_s\nu}{\mu}}$ and $P_r=\frac{\mu g C_p}{\lambda}$ (the so-called Prandtl-number) and putting $T=f\langle x\rangle\, h\langle z\rangle$, where $z=\frac{\alpha r}{R}\sqrt{P_r}$, equation (14) reads:

$$\frac{\mathrm{d}^2 h\langle z\rangle}{\mathrm{d}z^2}+\frac{1}{z}\frac{\mathrm{d}h\langle z\rangle}{\mathrm{d}z}+h\langle z\rangle=\frac{p}{\rho_s g C_p}\frac{1}{f\langle x\rangle} \tag{15}$$

with the solution:

$$h\langle z\rangle=C_1 J_0\langle z\rangle+C_2 Y_0\langle z\rangle+\frac{p}{\rho_s g C_p}\frac{1}{f\langle x\rangle}. \tag{16}$$

From the condition that $T$ must remain finite for $r=0$, it follows $C_2\equiv 0$. For $r=R$ $T$ must be zero, so:

$$f\langle x\rangle=-\frac{1}{C_1 J_0\langle\alpha\sqrt{P_r}\rangle}\frac{p}{\rho_s g C_p} \tag{17}$$

From (16) and (17)

$$T=f\langle x\rangle\, h\langle z\rangle=\left[1-\frac{J_0\left\langle\frac{\alpha r}{R}\sqrt{P_r}\right\rangle}{J_0\langle\alpha\sqrt{P_r}\rangle}\right]\frac{p}{\rho_s g C_p} \tag{18}$$

and substituting this result in eq. (9):

$$\rho=\frac{\gamma}{a_0^2}p\left[1-\frac{\gamma-1}{\gamma}\left\{1-\frac{J_0\left\langle\frac{\alpha r}{R}\sqrt{P_r}\right\rangle}{J_0\langle\alpha\sqrt{P_r}\rangle}\right\}\right]. \tag{19}$$

Eq. (6) can be rewritten as:

$$u-\frac{\mu}{\mathrm{i}\nu\rho_s}\left[\frac{\partial^2 u}{\partial r^2}+\frac{1}{r}\frac{\partial u}{\partial r}\right]=-\frac{1}{\mathrm{i}\nu\rho_s}\frac{\mathrm{d}p}{\mathrm{d}x}. \tag{20}$$

This equation can be solved in a similar way as eq. (14). The solution that fulfils the requirements that $u$ remains finite for $r=0$ and is zero for $r=R$ yields:

$$u=\left[\frac{J_0\left\langle\frac{\alpha r}{R}\right\rangle}{J_0\langle\alpha\rangle}-1\right]\frac{1}{\mathrm{i}\nu\rho_s}\frac{\mathrm{d}p}{\mathrm{d}x}. \tag{21}$$

Finally the equation of continuity, eq. (8), has to be satisfied, thus

$$\frac{1}{r}\frac{\partial(v\cdot r)}{\partial r}=\mathrm{i}\nu\frac{\rho}{\rho_s}-\frac{\partial u}{\partial x} \tag{22}$$

or with the aid of the expressions (19) and (21):

$$\frac{1}{r}\frac{\partial(v\cdot r)}{\partial r}=\frac{1}{\mathrm{i}\nu\rho_s}\left[\frac{\nu^2}{a_0^2}\gamma p\left\{1-\frac{\gamma-1}{\gamma}\left(1-\frac{J_0\left\langle\frac{\alpha r}{R}\sqrt{P_r}\right\rangle}{J_0\langle\alpha\sqrt{P_r}\rangle}\right)\right\}-\frac{\mathrm{d}^2 p}{\mathrm{d}x^2}\left\{\frac{J_0\left\langle\frac{\alpha r}{R}\right\rangle}{J_0\langle\alpha\rangle}-1\right\}\right] \tag{23}$$

After integration with respect to $r$:

$$v \cdot r = \frac{1}{i\nu\rho_s}\left[\frac{\nu^2}{a_0^2}\gamma p\left\{\tfrac{1}{2}r^2 - \frac{\gamma-1}{\gamma}\left(\tfrac{1}{2}r^2 - \frac{rR}{\alpha\sqrt{P_r}}\,\frac{J_1\left\langle\frac{\alpha r}{R}\sqrt{P_r}\right\rangle}{J_0\langle\alpha\sqrt{P_r}\rangle}\right)\right\} - \frac{d^2p}{dx^2}\left\{\frac{rR}{\alpha}\,\frac{J_1\left\langle\frac{\alpha r}{R}\right\rangle}{J_0\langle\alpha\rangle} - \tfrac{1}{2}r^2\right\} + F\langle x\rangle\right] \tag{24}$$

From the boundary condition $v=0$ for $r=R$ it follows:

$$-F\langle x\rangle = \frac{\nu^2}{a_0^2}\gamma\frac{R^2}{2}p\left\{1+\frac{\gamma-1}{\gamma}\,\frac{J_2\langle\alpha\sqrt{P_r}\rangle}{J_0\langle\alpha\sqrt{P_r}\rangle}\right\} - \frac{R^2}{2}\,\frac{d^2p}{dx^2}\,\frac{J_2\langle\alpha\rangle}{J_0\langle\alpha\rangle}. \tag{25}$$

Due to the axial symmetry; it must hold that $\lim_{r\to 0} v=0$. (26)

This requirement is fulfilled if $F\langle x\rangle=0$, or

$$\frac{\nu^2}{a_0^2}\gamma p\left\{1+\frac{\gamma-1}{\gamma}\,\frac{J_2\langle\alpha\sqrt{P_r}\rangle}{J_0\langle\alpha\sqrt{P_r}\rangle}\right\} - \frac{J_2\langle\alpha\rangle}{J_0\langle\alpha\rangle}\,\frac{d^2p}{dx^2} = 0. \tag{27}$$

From this differential equation $p$ can be solved as:

$$p = A\exp\left[\frac{\nu x}{a_0}\sqrt{\frac{J_0\langle\alpha\rangle}{J_2\langle\alpha\rangle}}\left\{\gamma+(\gamma-1)\frac{J_2\langle\alpha\sqrt{P_r}\rangle}{J_0\langle\alpha\sqrt{P_r}\rangle}\right\}^{\frac{1}{2}}\right] + B\exp\left[-\frac{\nu x}{a_0}\sqrt{\frac{J_0\langle\alpha\rangle}{J_2\langle\alpha\rangle}}\left\{\gamma+(\gamma-1)\frac{J_2\langle\alpha\sqrt{P_r}\rangle}{J_0\langle\alpha\sqrt{P_r}\rangle}\right\}^{\frac{1}{2}}\right] \tag{28}$$

introducing the notation

$$n = \frac{1}{1+\dfrac{\gamma-1}{\gamma}\,\dfrac{J_2\langle\alpha\sqrt{P_r}\rangle}{J_0\langle\alpha\sqrt{P_r}\rangle}} \tag{29}$$

the general solution for the fluid motion in a tube yields:

$$p = A\exp\left[\frac{\nu x}{a_0}\sqrt{\frac{J_0\langle\alpha\rangle}{J_2\langle\alpha\rangle}}\sqrt{\frac{\gamma}{n}}\right] + B\exp\left[-\frac{\nu x}{a_0}\sqrt{\frac{J_0\langle\alpha\rangle}{J_2\langle\alpha\rangle}}\sqrt{\frac{\gamma}{n}}\right] \tag{30}$$

$$u = \frac{i}{a_0\rho_s}\sqrt{\frac{J_0\langle\alpha\rangle}{J_2\langle\alpha\rangle}}\sqrt{\frac{\gamma}{n}}\left\{\frac{J_0\left\langle\frac{\alpha r}{R}\right\rangle}{J_0\langle\alpha\rangle} - 1\right\}\left\{A\exp\left[\frac{\nu x}{a_0}\sqrt{\frac{J_0\langle\alpha\rangle}{J_2\langle\alpha\rangle}}\sqrt{\frac{\gamma}{n}}\right] - B\exp\left[-\frac{\nu x}{a_0}\sqrt{\frac{J_0\langle\alpha\rangle}{J_2\langle\alpha\rangle}}\sqrt{\frac{\gamma}{n}}\right]\right\} \tag{31}$$

$$v = -\frac{i\nu}{a_0^2\rho_s}\left[\tfrac{1}{2}r\left\{1+\frac{J_0\langle\alpha\rangle}{J_2\langle\alpha\rangle}\,\frac{\gamma}{n}\right\} + \frac{(\gamma-1)R}{\alpha\sqrt{P_r}}\,\frac{J_1\left\langle\frac{\alpha r}{R}\sqrt{P_r}\right\rangle}{J_0\langle\alpha\sqrt{P_r}\rangle} - \frac{R\gamma}{n\alpha}\,\frac{J_1\left\langle\frac{\alpha r}{R}\right\rangle}{J_2\langle\alpha\rangle}\right]p \tag{32}$$

$$\rho = \frac{\gamma}{a_0^2}\left[1-\frac{\gamma-1}{\gamma}\left\{1-\frac{J_0\left\langle\frac{\alpha r}{R}\sqrt{P_r}\right\rangle}{J_0\langle\alpha\sqrt{P_r}\rangle}\right\}\right]p \tag{33}$$

$$T = \frac{1}{\rho_s g C_p}\left[1-\frac{J_0\left\langle\frac{\alpha r}{R}\sqrt{P_r}\right\rangle}{J_0\langle\alpha\sqrt{P_r}\rangle}\right]p. \tag{34}$$

The constants $A$ and $B$ can be determined after the boundary conditions at both ends of the tube have been prescribed.

## Application

With the aid of the solutions (30)–(34) a system consisting of a series connection of $N$ tubes and $N$ volumes (figure 2) can be treated. To solve this problem some additional assumptions are made:

— the pressure and the density in the instrument volumes are only time dependent.

— the pressure expansion in the instrument volume is a polytropic process, described by

$$\frac{\bar{p}_v}{(\bar{\rho}_v)}k_j = \text{constant}. \tag{35}$$

For the flow through tube $j$ the following expressions are valid:

$$p = A_j \exp(\phi_j X_j) - B_j \exp(-\phi_j X_j) \tag{36}$$

and

$$u = \frac{\mathrm{i}}{\nu \rho_{s_j}} \phi_j \left\{ \frac{J_0 \left\langle \frac{\alpha_j R_j}{r} \right\rangle}{J_0 \langle \alpha_j \rangle} - 1 \right\} \{A_j \exp(\phi_j X_j) - B_j \exp(-\phi_j X_j)\} \tag{37}$$

where $\phi_j = \dfrac{\nu}{a_{0_j}} \sqrt{\dfrac{J_0 \langle \alpha_j \rangle}{J_2 \langle \alpha_j \rangle}} \sqrt{\dfrac{\gamma}{n_j}}$ and $j = 1, 2, 3, \ldots N$ (38)

For tube $j$ it holds:

at the entrance: $X_j = 0$: $p_{j-1} = A_j + B_j$ (39)

at the exit: $X_j = L_j$: $p_j = A_j \exp(\phi_j L_j) + B_j \exp(-\phi_j L_j)$ (40)

$$u_{ji} = \frac{\mathrm{i}}{\nu \rho_{s_j}} \phi_j \left\{ \frac{J_0 \left\langle \frac{\alpha_j R_j}{r} \right\rangle}{J_0 \langle \alpha_j \rangle} - 1 \right\} \{A_j \exp(\phi_j L_j) - B_j \exp(-\phi_j L_j)\} \tag{41}$$

and the mass leaving tube $j$:

$$m_{j_i} = \int_0^{R_j} \rho_{s_j} u_{j_i} 2\pi r \,\mathrm{d}r = \frac{\pi R_j^2 \phi_j}{\mathrm{i}\nu} \frac{J_2 \langle \alpha_j \rangle}{J_0 \langle \alpha_j \rangle} \{A_j \exp(\phi_j L_j) - B_j \exp(-\phi_j L_j)\} \tag{42}$$

For tube $j+1$ it holds:

at the entrance: $X_{j+1} = 0$:

$$p_j = A_{j+1} + B_{j+1} \tag{43}$$

$$u_{j_0} = \frac{\mathrm{i}}{\nu \rho_{s_{j+1}}} \phi_{j+1} \left\{ \frac{J_0 \left\langle \frac{\alpha_{j+1} R_{j+1}}{r} \right\rangle}{J_0 \langle \alpha_{j+1} \rangle} - 1 \right\} + \{A_{j+1} - B_{j+1}\} \tag{44}$$

the mass entering tube $j+1$:

$$m_{j_0} = \int_0^{R_{j+1}} \rho_{s_{j+1}} u_{j_0} 2\pi r \,\mathrm{d}r = \frac{\pi R_{j+1}^2 \phi_{j+1}}{\mathrm{i}\nu} \frac{J_2 \langle \alpha_{j+1} \rangle}{J_0 \langle \alpha_{j+1} \rangle} \{A_{j+1} - B_{j+1}\} \tag{45}$$

at the exit: $X_{j+1} = L_{j+1}$:

$$p_{j+1} = A_{j+1} \exp(\phi_{j+1} L_{j+1}) + B_{j+1} \exp(-\phi_{j+1} L_{j+1}) \tag{46}$$

From eqs. (39) and (40) it can easily be found that:

$$A_j = \frac{p_j - p_{j-1} \exp(-\phi_j L_j)}{\exp(\phi_j L_j) - \exp(-\phi_j L_j)} \quad \text{and} \quad B_j = \frac{p_{j-1} \exp(\phi_j L_j) - p_j}{\exp(\phi_j L_j) - \exp(-\phi_j L_j)} \tag{47}$$

and from eqs. (43) and (46) it follows:

$$A_{j+1} = \frac{p_{j+1} - p_j \exp(-\phi_{j+1} L_{j+1})}{\exp(\phi_{j+1} L_{j+1}) - \exp(-\phi_{j+1} L_{j+1})} \quad \text{and} \quad B_{j+1} = \frac{p_j \exp(\phi_{j+1} L_{j+1}) - p_{j+1}}{\exp(\phi_{j+1} L_{j+1}) - \exp(-\phi_{j+1} L_{j+1})} \tag{48}$$

For the instrument volume it is assumed that

$$\frac{\bar{p}_v}{(\bar{\rho}_v)} k_j = \frac{p_s + p_v e^{\mathrm{i}\nu t}}{(\rho_s + \rho_v e^{\mathrm{i}\nu t})} k_j = \frac{p_s}{(\rho_{s_j})} k_j . \tag{49}$$

Considering small values of $p_v (= p_j)$ and $\rho_v$ eq. (49) can be simplified to

$$p_j = a_{0_j}^2 \frac{k_j}{\gamma} \rho_v . \tag{50}$$

The instrument volume, corrected for diaphragm deflection is defined as:

$$V_{v_j}\left(1+\sigma_j \frac{p_j}{p_s} e^{i\nu t}\right) \tag{51}$$

The mass of air within this volume is than:

$$m_v = V_{v_j}\left(1+\sigma_j \frac{p_j}{p_s} e^{i\nu t}\right)(\rho_{s_j}+\rho_v e^{i\nu t}) \approx V_{v_j}\left(\rho_{s_j} + \frac{\sigma_j \rho_{s_j}}{p_s} p_j e^{i\nu t} + \frac{\gamma}{a_0^2 k_j} p_j e^{i\nu t}\right). \tag{52}$$

The variation of mass within the instrument volume is:

$$\frac{dm_v}{dt} = \frac{i\nu\gamma}{a_{0_j}^2} V_{v_j}\left(\sigma_j + \frac{1}{k_j}\right) p_j e^{i\nu t}. \tag{53}$$

The mass increase of the instrument volume must be equal to the difference in mass leaving tube $j$ and the mass entering tube $j+1$, thus:

$$\frac{dm_v}{dt} = (m_{j_i} - m_{j_o})\, e^{i\nu t}. \tag{54}$$

Substituting the expressions (42), (45), (47), (48) and (53) into eq. (54) the following recursion formula can be derived:

$$\frac{p_j}{p_{j-1}} = \Bigg[\cosh\langle\phi_j L_j\rangle + \frac{V_{v_j}}{V_{t_j}}\left(\sigma_j + \frac{1}{k_j}\right) n_j \phi_j L_j \sinh\langle\phi_j L_j\rangle + \\ + \frac{V_{t_{j+1}}}{V_{t_j}} \frac{\phi_{j+1}}{\phi_j} \frac{L_j}{L_{j+1}} \frac{J_0\langle\alpha_j\rangle}{J_0\langle\alpha_{j+1}\rangle} \frac{J_2\langle\alpha_{j+1}\rangle}{J_2\langle\alpha_j\rangle} \frac{\sinh\langle\phi_j L_j\rangle}{\sinh\langle\phi_{j+1} L_{j+1}\rangle} \times \\ \left\{\cosh\langle\phi_{j+1} L_{j+1}\rangle - \frac{p_{j+1}}{p_j}\right\}\Bigg]^{-1} \tag{55}$$

with $V_{t_j} = \pi R_j^2 L_j$, the volume of tube $j$.

From the recursion formule (55) the expressions for the complex ratio of the pressure fluctuation of each transducer $j$ to the sinusoidal input pressure $p_0$ can be derived by successively putting $j = N, N-1, \ldots 2, 1$.

It will be noted that for $j = N$ the last two terms of expression (55) disappear.

TABLE 1. SINGLE PRESSURE MEASURING SYSTEMS

(calculations)

| $R$ | $L$ | $V_v$ | $\sigma$ | $k$ | $T_s$ | $p_s$ | fig. | Remarks |
|---|---|---|---|---|---|---|---|---|
| 0.50 mm | 500 mm | 300 mm$^3$ | 0 | 1.4 | 15°C | 1 ata | 9 | Influence of $R$ and $L$ |
| 0.75 | 500 | 300 | 0 | 1.4 | 15 | 1 | | |
| 1.25 | 500 | 300 | 0 | 1.4 | 15 | 1 | | |
| 0.50 | 1000 | 300 | 0 | 1.4 | 15 | 1 | 10 | |
| 0.75 | 1000 | 300 | 0 | 1.4 | 15 | 1 | | |
| 1.25 | 1000 | 300 | 0 | 1.4 | 15 | 1 | | |
| 0.50 | 3000 | 300 | 0 | 1.4 | 15 | 1 | 11 | |
| 0.75 | 3000 | 300 | 0 | 1.4 | 15 | 1 | | |
| 1.25 | 3000 | 300 | 0 | 1.4 | 15 | 1 | | |
| 0.75 | 1000 | 100 | 0 | 1.4 | 15 | 1 | 12 | Influence of $V_v$ |
| 0.75 | 1000 | 300 | 0 | 1.4 | 15 | 1 | | |
| 0.75 | 1000 | 1000 | 0 | 1.4 | 15 | 1 | | |
| 0.75 | 1000 | 300 | 0 | 1.4 | 15 | 1 | 13 | Influence of $k$ |
| 0.75 | 1000 | 300 | 0 | 1.0 | 15 | 1 | | |
| 0.75 | 1000 | 300 | 0 | 1.4 | 15 | 2 | 14 | Influence of $p_s$ |
| 0.75 | 1000 | 300 | 0 | 1.4 | 15 | 1 | | |
| 0.75 | 1000 | 300 | 0 | 1.4 | 15 | 0.5 | | |
| 0.75 | 1000 | 300 | 0 | 1.4 | 0 | 1 | 15 | Influence of $T_s$ |
| 0.75 | 1000 | 300 | 0 | 1.4 | 30 | 1 | | |

TABLE 2. SYSTEMS WITH DISCONTINUITY IN TUBE RADIUS

(calculations)

| $L_1$ mm | $L_2$ mm | $R_1$ mm | $R_2$ mm | | | |
|---|---|---|---|---|---|---|
| 250 | 750 | 0.75 | 0.50 | 0.75 | 1.25 | $V_{v_1} = 0$ |
| 250 | 750 | 0.50 | 0.50 | 0.75 | — | $V_{v_2} = 300$ mm$^3$ |
| 500 | 500 | 0.75 | 0.50 | 0.75 | 1.25 | $\sigma_2 = 0$ |
| 500 | 500 | 0.50 | 0.50 | 0.75 | — | $k_2 = 1.4$ |
| 750 | 250 | 0.75 | 0.50 | 0.75 | 1.25 | standard sea level conditions |

TABLE 3. SINGLE PRESSURE MEASURING SYSTEMS

(calculations and experiments)

| $L$ mm | $R_m$ mm | |
|---|---|---|
| 500 | 0.525 | |
| 1000 | 0.49 | $V_v = 285$ mm$^3$ |
| 1000 | 0.795 | $\sigma = 0.02$ |
| 1000 | 1.09 | |
| 3000 | 0.70 | |
| 3910 | 0.965 | |

TABLE 4. SYSTEMS WITH DISCONTINUITY IN TUBE RADIUS

(calculations and experiments)

| $L_1$ mm | $L_2$ mm | $R_{1m}$ mm | $R_{2m}$ mm | |
|---|---|---|---|---|
| 500 | 500 | 0.525 | 0.79 | $V_v = 285$ mm$^3$ |
| 500 | 500 | 0.79 | 0.525 | $\sigma = 0.02$ |

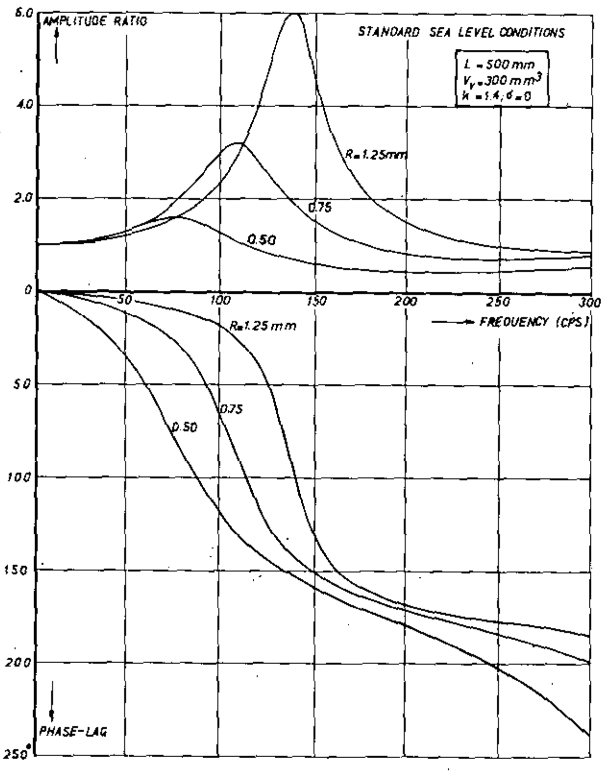


Fig. 9. Influence of tube radius $R$ on the dynamic response.

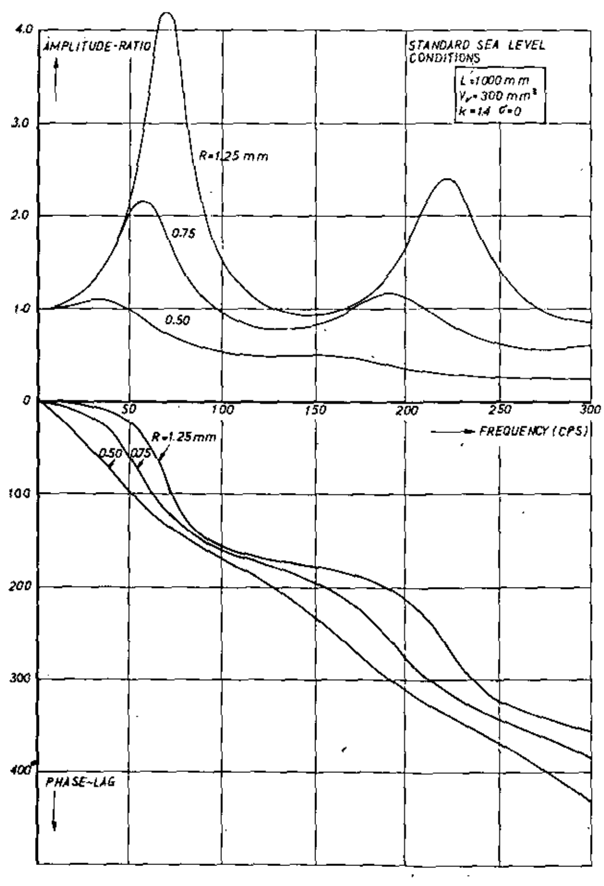


Fig. 10. Influence of tube radius $R$ on the dynamic response.

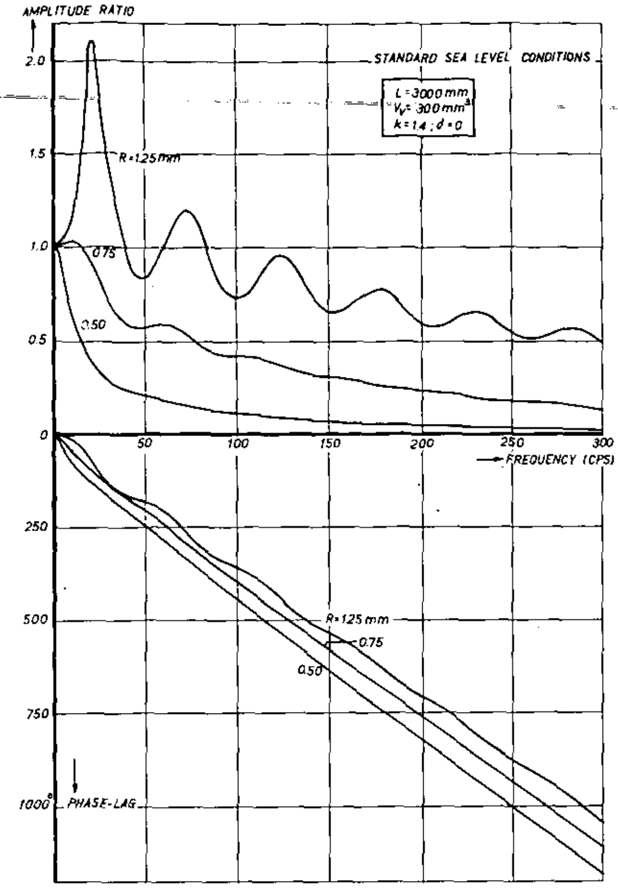


Fig. 11. Influence of tube radius $R$ on the dynamic response.

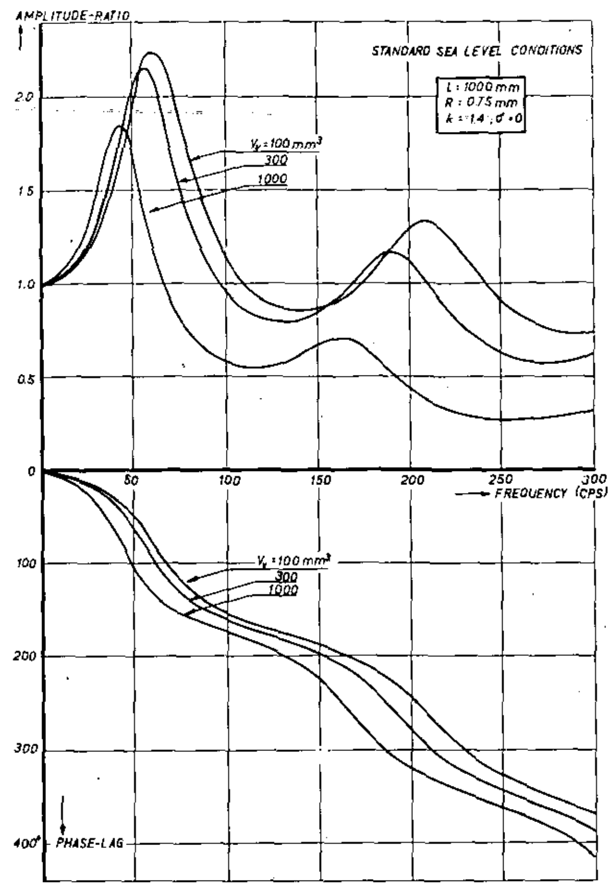


Fig. 12. Influence of pressure transducer volume $V_v$ on the dynamic response.

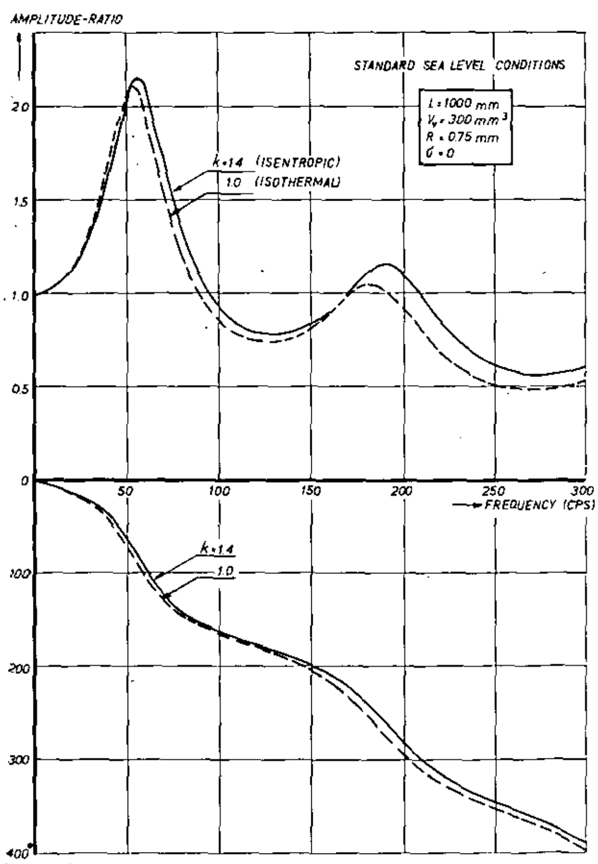


Fig. 13. Influence of polytropic constant $k$ on the dynamic response.

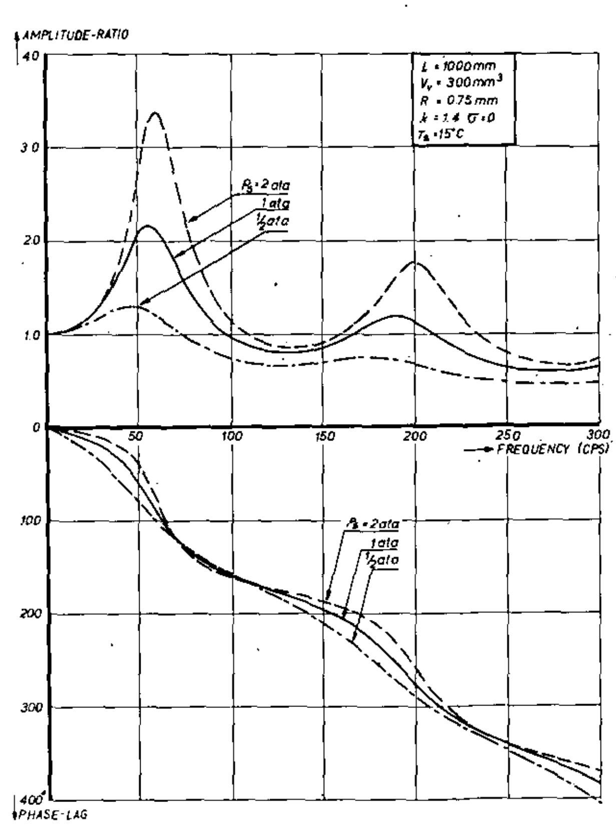


Fig. 14. Influence of mean pressure on the dynamic response.

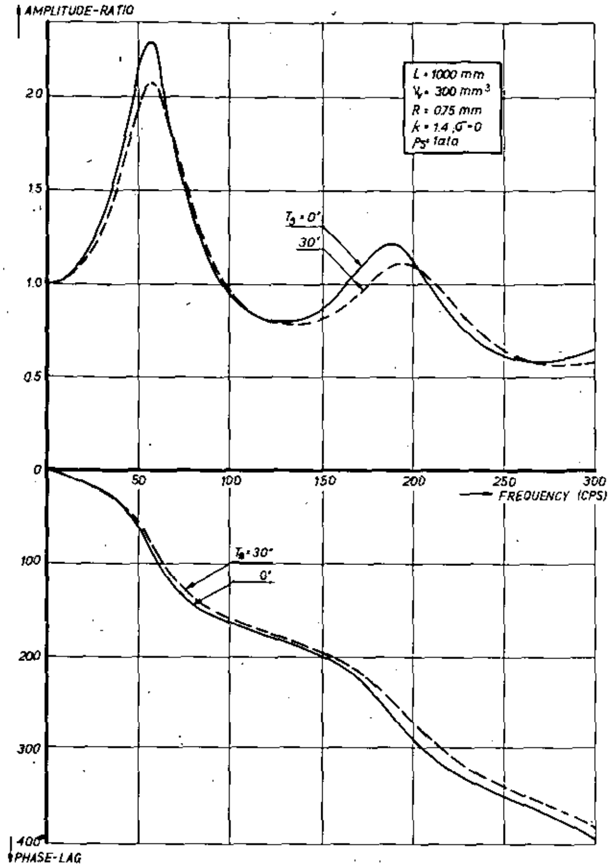


Fig. 15. Influence of mean temperature on the dynamic response.

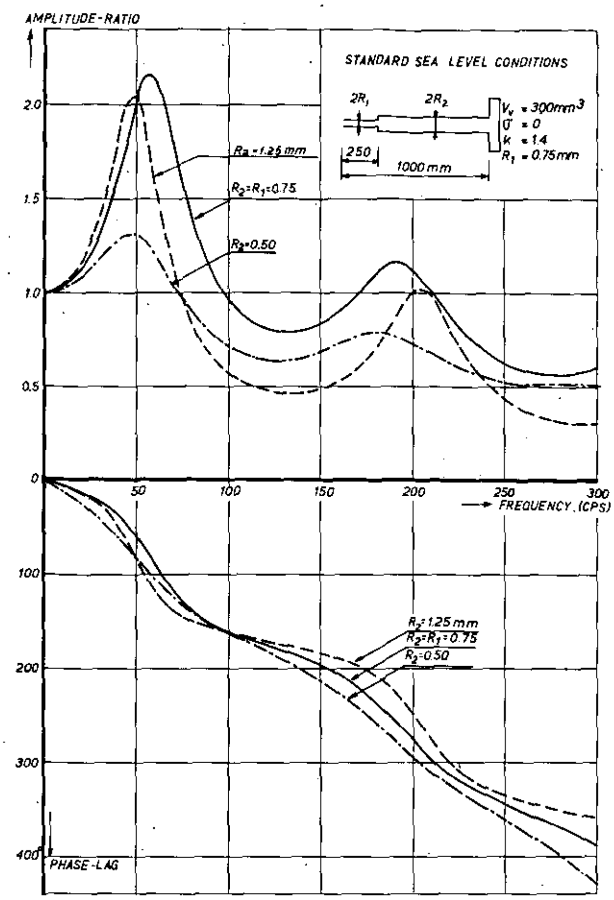


Fig.16. Influence of $R_2$ on the dynamic response of a double pressure measuring system.

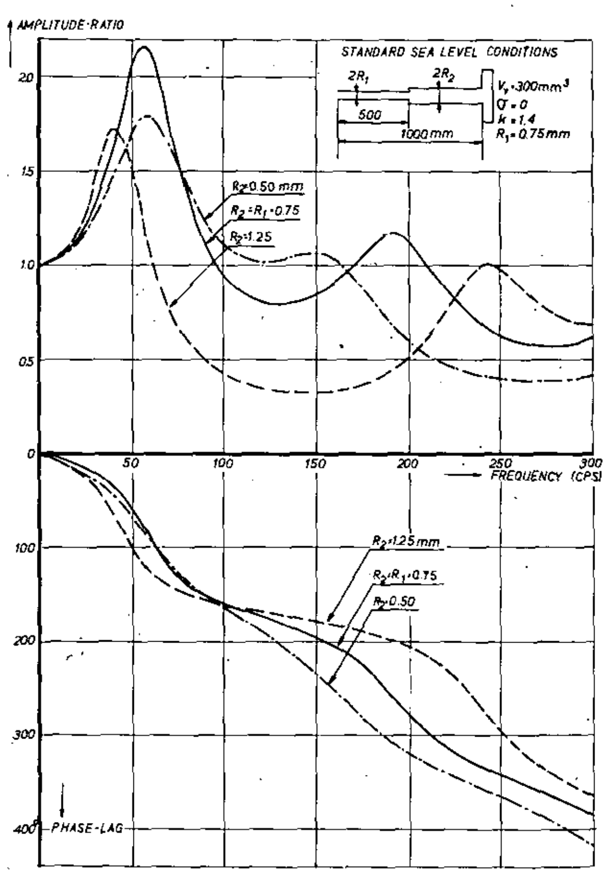


Fig. 17. Influence of $R_2$ on the dynamic response of a double pressure measuring system.

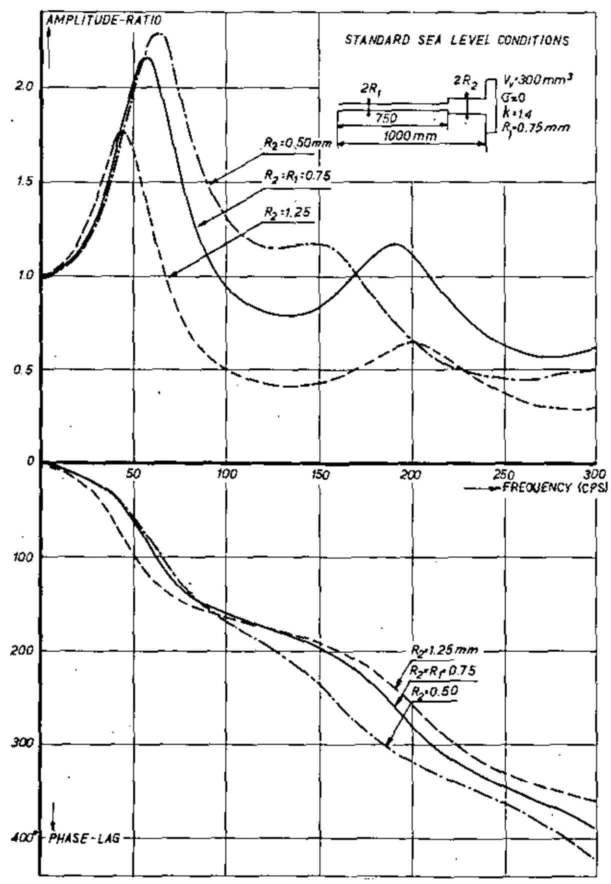


Fig. 18. Influence of $R_2$ on the dynamic response of a double pressure measuring system.

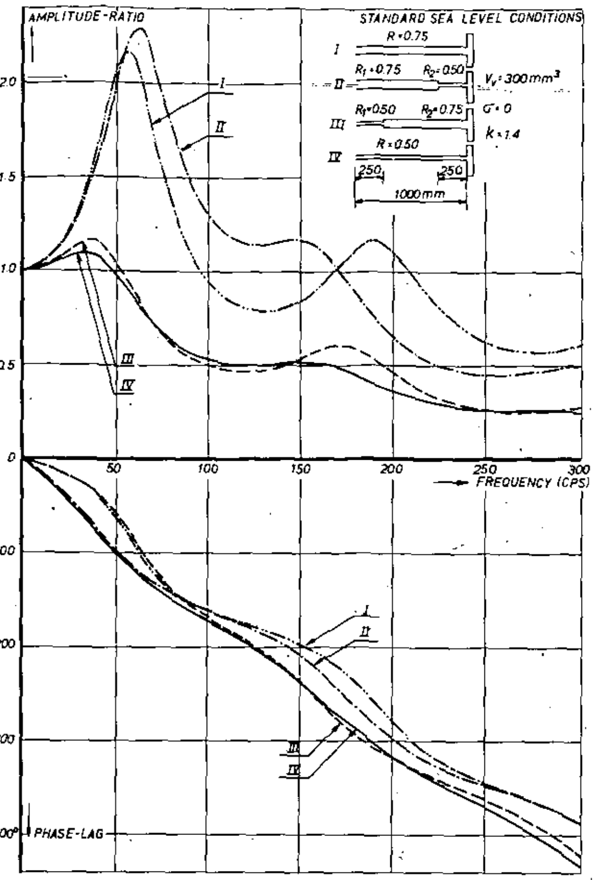


Fig. 19. Influence of restrictions at the entrance and at the end of the tube.

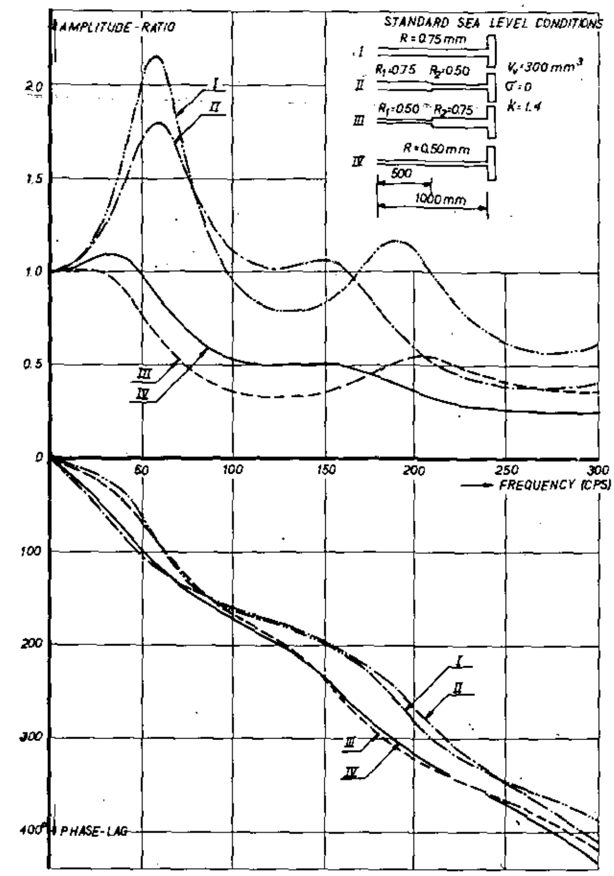


Fig. 20. Influence of restrictions at the entrance and at the end of the tube.

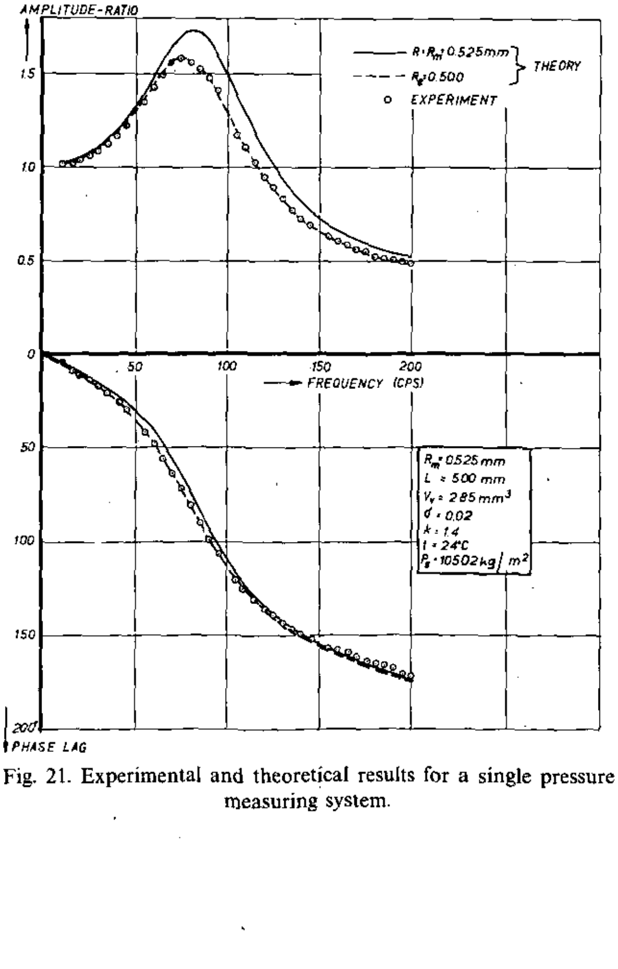


Fig. 21. Experimental and theoretical results for a single pressure measuring system.

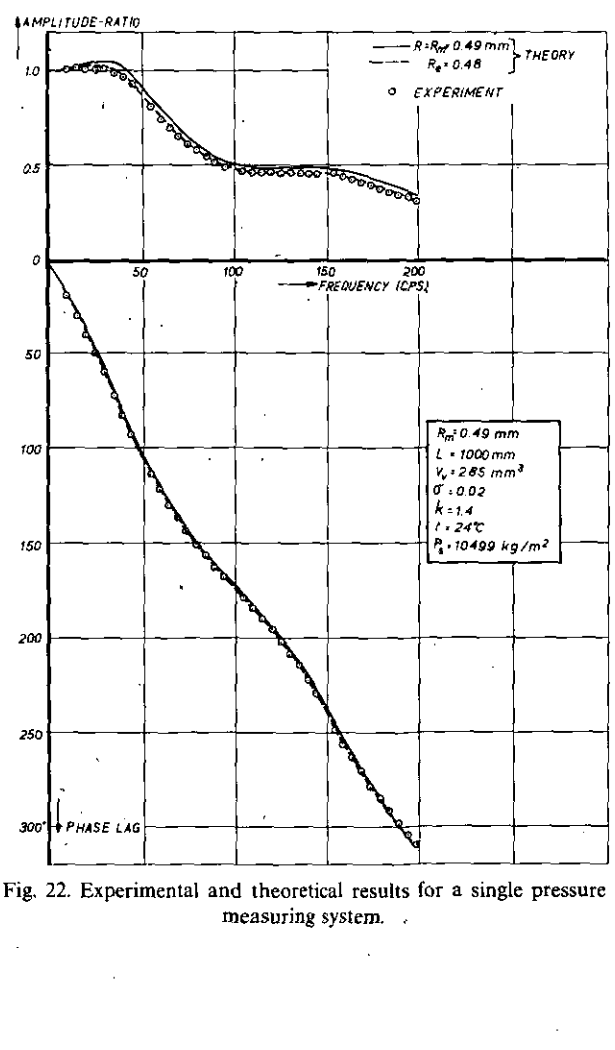


Fig. 22. Experimental and theoretical results for a single pressure measuring system.

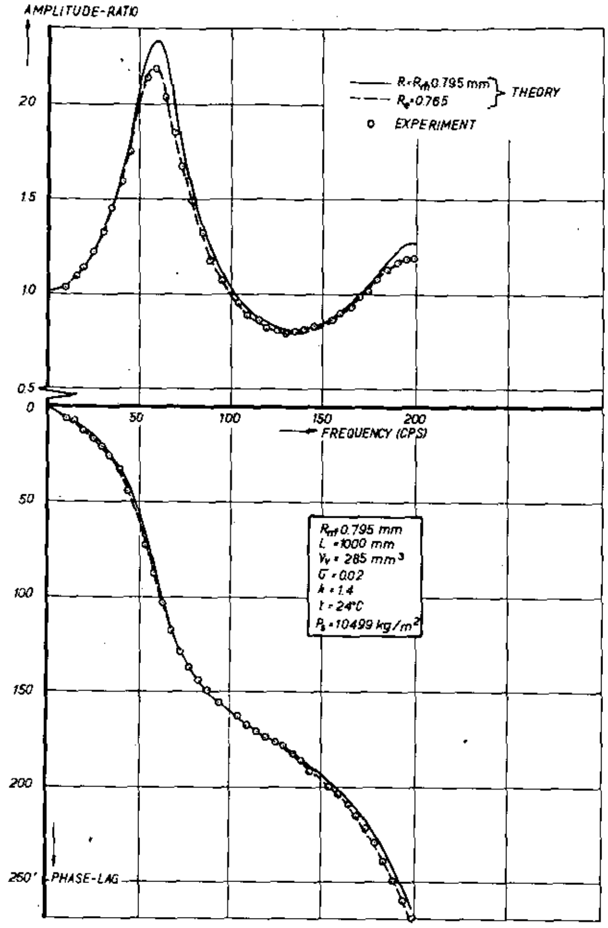


Fig. 23. Experimental and theoretical results for a single pressure measuring system.

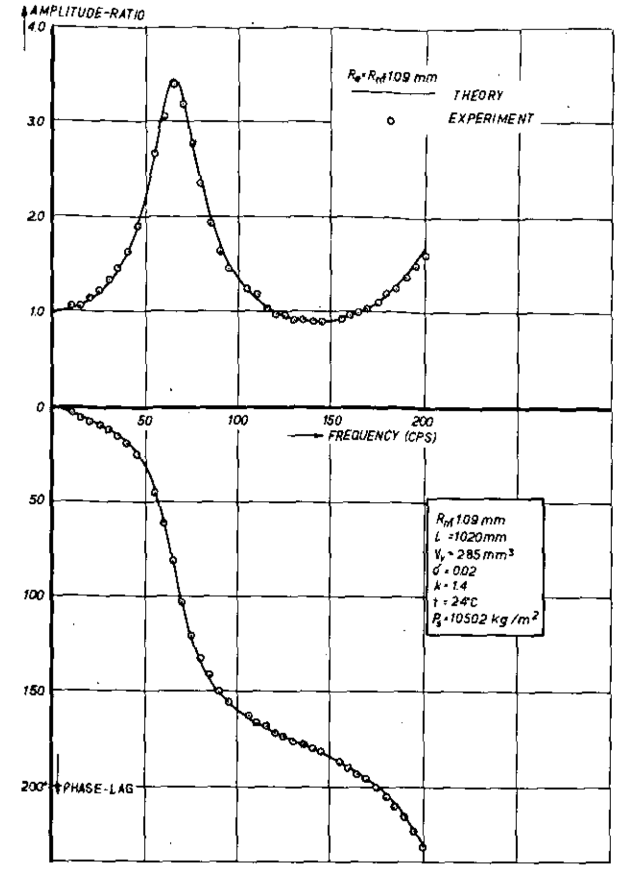


Fig. 24. Experimental and theoretical results for a single pressure measuring system.

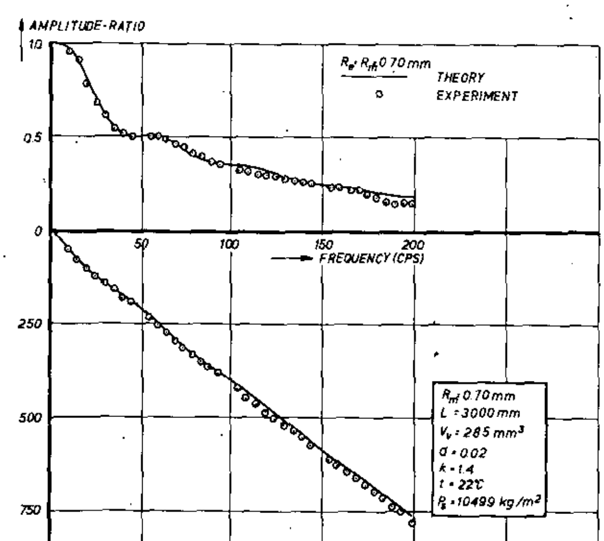


Fig. 25. Experimental and theoretical results for a single pressure measuring system.

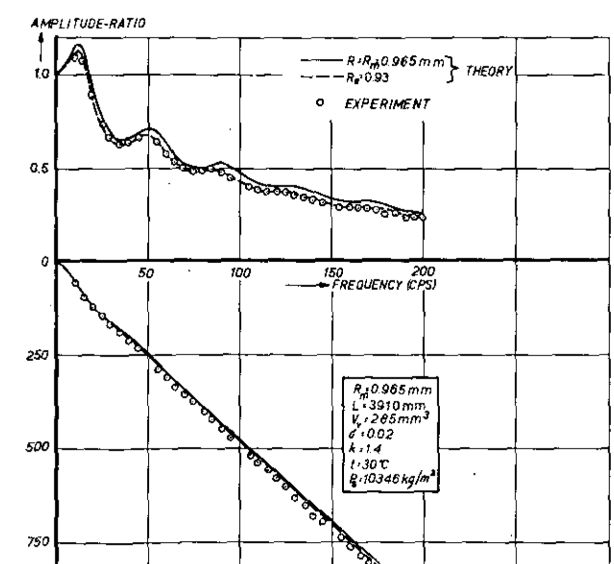


Fig. 26. Experimental and theoretical results for a single pressure measuring system.

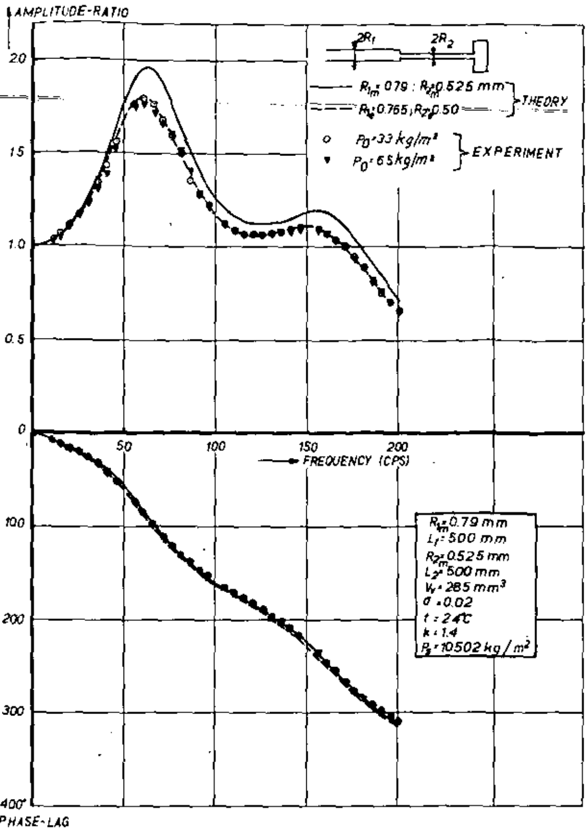

Fig. 27. Experimental and theoretical results for a double pressure measuring system.

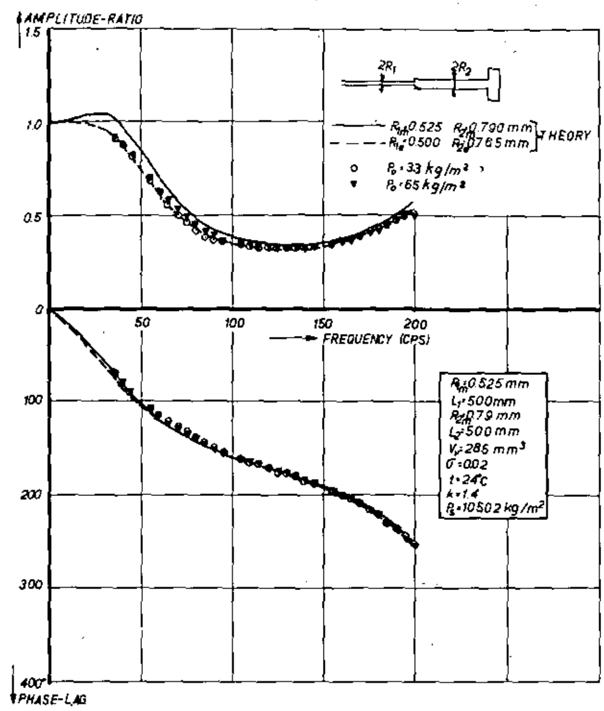

Fig. 28. Experimental and theoretical results for a double pressure measuring system.

C.C.L. Class. F 400

REPORT NLR-TR F.250

# A method for estimating unsteady pressure distributions for arbitrary vibration modes from theory and from measured distributions for one single mode

by

H. BERGH and R. J. ZWAAN

**Summary**

A method is proposed to estimate for a lifting surface pressure distributions to be measured for arbitrary vibration modes by the aid of theory and measured distributions for one single mode. Its usefulness is demonstrated on hand of two swept wings of small aspect ratio oscillating in incompressible flow.

Due to insensitivity to reduced frequency variations of the correction procedure it appears to be possible to predict experimental pressure distributions for reduced frequencies, more or less different from the values used in the measurements.

**Contents** *Page*



**List of symbols**

$a$ — coefficient in series for approximating the pressure distribution.
$C$ — aerodynamic influence coefficient.
$\Delta C_p$ — differential pressure.
$F$ — aerodynamic force.
$h$ — linear deflection.
$W$ — element of correction as well as weighting matrix.
$\alpha$ — downwash
$\beta$ — angular deflection
$\omega$ — reduced frequency

[ ] — matrix
⌈ ⌋ — diagonal matrix
{ } — column matrix

This report has been prepared under contract with the Netherlands Aircraft Development Board (N.I.V.).

## 1 Introduction

In recent years considerable progress has been made in developing measuring techniques for the determination of unsteady aerodynamic forces. At the moment it is possible to obtain rapidly accurate experimental data for a multitude of mach numbers and reduced frequencies. For instance, in ref. 1 Bergh describes a method for the measurement of unsteady pressures on harmonically oscillating wings.

However, the flutter engineer is still faced with severe problems if he wants to employ these measured aerodynamic data in order to improve his flutter calculations. The reason is that the measurements are often performed on relatively simple models, oscillating in modes being different from those needed in the flutter calculations. In this situation he is forced to transfer his experimental data in one way or another to make them suitable for the modes required. The apparent solution to measure the data directly for all the modes he wants is hardly possible in practice as it requires pressure measurements on dynamically similar models.

In this report a method is presented enabling the estimation of pressure distributions to be measured for arbitrary modes proceeding from experimental *and* corresponding theoretical distributions for one single mode. In this way pressure distributions have been predicted for two swept wings oscillating in incompressible flow. A satisfactory agreement is shown to exist between estimated and measured distributions.

## 2 Some previously suggested methods

The method in question has been based on the work of Rodden and Revell (ref. 2), and Bergh (ref. 1). For clearness their ideas will be summarized to begin with. The first two authors represent the theoretical aerodynamic forces in their flutter calculations by "control point forces" $\{F\}$, related by a matrix of aerodynamic influence coefficients $[C]$ to the "control point deflections" $\{h\}$ of the lifting surface:

$$\{F\}_{\text{th}} = [C]_{\text{th}}\,\{h\}\,. \tag{1}$$

They assume only results of static measurements to be available and therefore provide an agreement between theory and experiment in this limiting case by introducing a diagonal matrix $\lceil W \rfloor_{\text{stat}}$ to weight matrix $[C]$, defined by

$$\{F_{\text{stat}}\}_{\text{exp}} = \lceil W_{\text{stat}} \rfloor\,[C_{\text{stat}}]_{\text{th}}\,\{h\}\,. \tag{2}$$

In this equation $\{h\}$ is connected actually to a wing with prescribed angle of attack. Once the $\lceil W_{\text{stat}} \rfloor$-matrix has been determined, Rodden and Revell suppose $\lceil W_{\text{stat}} \rfloor$ to be also applicable in unsteady cases, so that for an arbitrary vibration mode $\{h\}$ the experimental unsteady forces may be predicted by the equation:

$$\{F\}_{\text{exp}} = \lceil W_{\text{stat}} \rfloor\,[C]_{\text{th}}\,\{h\}\,. \tag{3}$$

It is reasonable to expect that the application of the $\lceil W_{\text{stat}} \rfloor$-matrix will be justified for small values of the reduced frequency. At higher values however the validity of this method may be questionable.

A generalisation has been suggested by Bergh. He proceeds from the following theoretical formulation of the unsteady pressure distribution:

$$\{\alpha\} = [C]_{\text{th}}\,\{a\}_{\text{th}}\,, \tag{4}$$

where $\{\alpha\}$ represents values of the downwash in a number of collocation points, $[C]_{\text{th}}$ a matrix of aerodynamic influence coefficients, and $\{a\}_{\text{th}}$ coefficients in the series used to approximate the pressure distribution in a number of streamwise sections. Bergh assumes a matrix of experimental aerodynamic influence coefficients to exist in such a way that analogous to theory the relation holds:

$$\{\alpha\} = [C]_{\text{exp}}\,\{a\}_{\text{exp}}\,, \tag{5}$$

where the pressure distribution $\{a\}_{\text{exp}}$ has been approximated by the same kind of series as in theory. Analogous to Rodden and Revell he introduces a diagonal matrix $\lceil W \rfloor$ to weight matrix $[C]_{\text{th}}$

$$[C]_{\text{exp}} = \lceil W \rfloor\,[C]_{\text{th}}\,, \tag{6}$$

so that substitution of (6) in (5) yields:

$$\{\alpha\} = \lceil W \rfloor\,[C]_{\text{th}}\,\{a\}_{\text{exp}}\,. \tag{7}$$

If for a specified combination of vibration mode and reduced frequency the corresponding experimental pressure distribution in the form of $\{a\}_{\text{exp}}$ is known, the matrix $\lceil W \rfloor$ can be determined and used consequently to estimate experimental distributions for other modes at that frequency.

Thus the main difference with the method of Rodden and Revell is, that here the $\lceil W \rfloor$-matrix is dependent on the reduced frequency: to each reduced frequency an other matrix belongs.

A disadvantage of Bergh's method is that it needs a prescribed series approximation for the measured pressure distributions in stead of the measured distributions itselves. That means the results will depend on the accuracy of this approximation. In practice this has shown to be a serious limitation. For instance, while testing the effectiveness of Bergh's method it appeared that the experimental pressure distributions could not be approximated with sufficient accuracy by three terms, using the method of least squares. This is demonstrated in fig. 1 (for simplicity only real values are given), where the errors caused by approximation are shown to be of the same order of magnitude as the discrepancies between theory and experiment. It is clear that such errors will disturb the possible improvements in the estimated pressure distributions. The other way of increasing terms in the series approximation leads to impractical large computational work to obtain the corresponding theoretical distributions. Besides, Bergh's formulation has the limitation to be exclusively coupled to the so-called kernel function method, as used for this report. If the theoretical distributions should be obtained from an other theory, it is questionable if this formulation could be maintained.

## 3 The present method

To avoid the disadvantages of the before-mentioned methods an other generalisation of Rodden and Revells method has been developed, that uses the measured pressure distribution without any approximation.

Starting point has been the following relation between the experimental and theoretical "control point forces" for any vibration mode, that must exist according to eqs. (1) and (3):

$$\{F\}_{\text{exp}} = \lceil W_{\text{stat}} \rfloor\,\{F\}_{\text{th}} \tag{8}$$

to be applied again to both steady and unsteady cases.

As the "control point forces" are related directly to specific integrated pressure values, a logical extension is to assume a similar relation as eq. (8) for the pressures itselves. The following step is to take this ratio between experimental and theoretical pressures dependent on the reduced frequency analogous to the method of ref. 1.

In this way the following expression is obtained:

$$\{\Delta C_p\}_{\text{exp}} = \lceil W \rfloor \cdot \{\Delta C_p\}_{\text{th}}, \qquad (9)$$

with $\lceil W \rfloor$ being independent on the mode of vibration.

In this formulation the correction matrix $\lceil W \rfloor$ for a given reduced frequency can be calculated from corresponding theoretical and experimental pressure distributions for one single mode. Then results for other modes at the same value of the reduced frequency can be estimated with eq. (9) by applying the same matrix $\lceil W \rfloor$ to correct the corresponding theoretical distributions.

Which kind of calculation scheme has been used to obtain the theoretical distributions is of minor importance.

In the following sections the usefulness of this method will be demonstrated on hand of two swept wings oscillating in incompressible flow. Furthermore the correction matrix itself will be shown to have certain properties that can be used to enlarge the flexibility of the proposed method.

## 4 Data for examples used to demonstrate the method

Two lifting surfaces will be considered, called:

1 stabiliser with detachable tip (for planform see fig. 2);

2 fin (for planform see fig. 3).

The maximum profile thicknesses are about 10%. After removal of the tip the stabiliser is sharply cut off.

For each surface theoretical and experimental pressure distributions have been determined in five streamwise sections. The flow is considered to be incompressible. The theoretical distributions have been obtained using a method developed by Laschka (ref. 3, 4) for an infinite thin lifting surface oscillating in an ideal fluid.

During the measurements each surface could perform two motions, namely a pure flapping motion (no. 1) about axis 1, and a pure pitching motion (no. 2) about axis 2. In chapter 5.2 two new motions will be introduced (nos. 3 and 4); they are linear combinations of motions 1 and 2 so that the rotation axes are lying in positions 3 and 4.

The results are available for the following reduced frequencies:

stabiliser: $\omega = 0$; 0.15; 0.20; 0.25; 0.35; 0.45; 0.55;
fin : $\omega = 0$; 0.20; 0.35; 0.55;
where $\omega$ for both surfaces is related to the half mean geometric chord of the fin, $\bar{c}/2 = 0.475$ m.

In the discussion the results for sections 1 will be left out of consideration, as the measured pressures for these sections are not representative due to disturbing influences of the tunnel wall.

## 5 Discussion of the results

### 5.1 *The correction matrix.*

An obvious question is: Are the $\lceil W \rfloor$-matrices, when derived from different modes at the same reduced frequency, sufficiently equal?

In fig. 4 the matrices following from modes 1 and 2 have been depicted for the stabiliser with tip at $\omega = 0.55$ by plotting the values of the matrix elements for various spanwise sections in chordwise direction. If complete agreement should exist between theory and experiment, all elements should take the (real) value 1; thus one has to note the deviations from this value.

In all spanwise sections the matrices show the same features. Over the front parts the real values lie slightly above 1, as the imaginary values are about zero. Over the rear parts the real values decrease and the imaginary ones just grow out. These peculiarities become more pronounced towards the tip. They will be discussed below.

Comparing the matrices derived from modes 1 and 2 the distributions of the element values appear to agree very good; only a small difference in level can be observed. One has to consider that the underlying modes are quite different: the downwash in mode 2 originates from both instantaneous incidence and dynamic profile curvature, as in mode 1 the instantaneous incidence is zero; in this view the downwash in mode 2 may be called more complete than in mode 1.

The features shown by the matrix elements are probably governed by two important effects, occurring in physical reality but not taken into account in theory, namely finite thickness of the stabiliser and fluid viscosity. To demonstrate the influence of thickness $\lceil W \rfloor$-matrices have been derived by comparing theoretical results for a 14.4% thick and for an infinitely thin profile in two-dimensional flow. The modes considered are heaving and pitching. The pressure distributions for the thick aerofoil are taken from the work of Van de Vel (ref. 5). The elements of the $\lceil W \rfloor$-matrices have been plotted in fig. 5 for both modes at a reduced frequency of 0.24, this value being related to the half wing chord. Over the front parts the matrices show large resemblance with the matrices of the stabiliser; over the rear parts a clear correspondence does not arise. The latter is partly due to the fact that in the theory of Van de Vel the Kutta-condition could not be applied in a satisfactory way, leading to the existence of non-zero pressures at the trailing edge. The main reason however, is the influence of viscosity in the experimental distribution of the stabiliser that becomes more pronounced towards the trailing edge.

5.2 *Estimation of pressure distributions.*

With the aid of theoretical pressure distributions for mode 1 and the $\lceil W \rfloor$-matrix from mode 2, experimental distributions for mode 1 have been estimated; likewise has been done for the experimental distributions for mode 2 using the theoretical distributions of mode 2 and the $\lceil W \rfloor$-matrix from mode 1. As an example in fig. 6 the theoretical, measured and estimated experimental pressure distributions for the stabiliser with tip at $\omega = 0.55$ have been plotted for both modes, the one per unit flapping angle $\beta_1$ and the other per unit pitching angle $\beta_2$. Between measured and estimated distributions a reasonable agreement appears to exist, demonstrating anyhow that all typical differences between theoretical and experimental distributions could be caught by applying the $\lceil W \rfloor$-matrix.

So far, the effectiveness of the present method has been tested for two rather extreme modes. For a clear judgement it is better to apply the method to more common modes for this type of swept wings with small aspect ratio, but then a comparison with measured results is hampered by lack of experimental data for such modes. As a compromise modes 3 and 4 have been created with swept forward and backward node lines resp., both modes being linear combinations of modes 1 and 2. Supposing linearity of the measured pressure distributions as well, the experimental data for modes 3 and 4 can be derived from those of modes 1 and 2 by superposition. In this way experimental pressure distributions for mode 3 and 4 have been obtained for both stabiliser with tip and fin. They have been compared with estimated pressure distributions by using the $\lceil W \rfloor$-matrix from mode 2.

In fig. 7 the comparison is shown for the stabiliser with tip at $\omega = 0.55$. The estimation appears to be very good for both modes, even at the tip sections. This statement is not surprising as the greater part of the predicted distributions comes from mode 2.

An analogous comparison is shown for the fin in fig. 8, again at $\omega = 0.55$. Also for this surface, having a somewhat different planform, the agreement between experimental and estimated pressure distributions is very good.

For the stabiliser without tip only the direct comparison between measured and estimated pressure distributions for modes 1 and 2 is presented as it is doubtful whether linear superposition of the measured pressure values in the tip region is allowed or not. Fig. 9 shows that even in this case application of the $\lceil W \rfloor$-matrices leads to reasonable agreement, although the differences in level are larger than in the previous examples.

In this chapter only results for $\omega = 0.55$ have been presented. Calculations for lower values of $\omega$ however have shown similar results.

## 6 A possibility to enlarge the applicability

An interesting point of study is the dependence of the $\lceil W \rfloor$-matrix on the reduced frequency. To show this in an example, in fig. 10 values of the matrix elements at various values of $\omega$ have been plotted for the stabiliser with tip, sections 3 and 5. It is striking that the matrix elements have nearly the same trend along each chord and only diverge slightly over the rear part towards the tip. It is worth investigating if the feature of small $\omega$-dependence can be used to enlarge the applicability of the method in question.

a A first possibility is to choose a $\lceil W \rfloor$-matrix from the middle of the range of reduced frequencies considered and to employ this matrix in case of other frequencies. For demonstration experimental pressure distributions have been predicted in fig. 11 for the stabiliser with tip, sections 3 and 5, and mode 4 at $\omega = 0$, 0.20 and 0.55, making use of the $\lceil W \rfloor$-matrix from mode 2 for $\omega = 0.35$. In case of $\omega = 0$ complex pressure values are found, but then only the real parts are taken to be significant. The agreement between measured and estimated distributions appears to be fairly good through the whole range of reduced frequencies. As the correction matrix was shown to be rather independent of $\omega$, this agreement is not surprising.

b Another possibility is, according to Rodden and Revell, to take the $\lceil W \rfloor$-matrix for $\omega = 0$ (necessarily derived from mode 2) and to employ this matrix in case of reduced frequencies unequal to zero. This procedure has been demonstrated in fig. 12 by estimating pressure distributions in the same sections and for the same mode as under *a*, now at $\omega = 0.20$, 0.35 and 0.55. The agreement is good for the forward part of the chords, but the prediction over the rear part is less accurate, especially towards the tip.

These two procedures have been applied also to the fin, for which the experimental pressure distributions could be estimated with about the same accuracy as for the stabiliser with tip.

So far only surfaces with a smooth thickness distribution have been considered. However the possibility exists to check the two procedures for a less smooth distribution, viz. the stabiliser with the sharply cut off tip. In fig. 13 $\lceil W \rfloor$-matrices are given for this stabiliser, section 5, at $\omega = 0$, 0.35 and 0.55. Here the matrices show a clear dependence on reduced frequency. Application of the matrix for $\omega = 0$ to estimate experimental pressure distributions for mode 1 and 2 at $\omega = 0.55$ consequently leads to extravagant pressure values, see fig. 14, as the matrix for $\omega = 0.35$ yields only just reasonable distributions. But it must be noted that in this special case the correction matrices have exceptional large magnitudes, indicating that the theory completely fails to approximate the actual pressure distribution.

As for more regular cases with correction matrices of the order 1 the influence of reduced frequency seems to be of minor importance, this property can be used to limit the number of reduced frequencies in the programme of pressure measurements to a few, widely spaced values. For intermediate values of the reduced frequency pressure distributions can be estimated by using matrices, calculated from measurements at neighbouring reduced frequencies.

As the present investigation is of a too limited scope to derive general conclusions, the authors suggest the following procedure in applying the proposed method.

1 To measure pressure distributions for at least two different modes.
2 To measure these distributions at not too widely spaced values of the reduced frequency.
3 To compare in both cases the derived correction matrices mutually in order to check the assumptions.

## 7 Conclusions

The following conclusions can be drawn from the present investigation:

1 The proposed method appears to be a convenient means to estimate pressure distributions to be measured for arbitrary modes of vibration from the measured distribution for one single mode.
2 The influence of the reduced frequency on the correction matrix seems to be of minor importance in case the experimental distribution is described reasonably by theory.
3 This insensitivity to reduced frequency can be used to derive from pressure measurements at a few, rather widely spaced values of the reduced frequency experimental pressure distributions for intermediate values of this parameter.
4 The proposed method offers the flutter engineer a means to improve his flutter calculations with experimental aerodynamic data, derived from a limited programme of unsteady pressure measurements.

## 8 Final remark

In this report the usefulness of the proposed method is demonstrated only for swept wings in incompressible flow. Its general formulation however enables a much wider application and the authors believe it will give acceptable results in those cases where theory already gives rather good results. To check this they suggest to investigate the applicability on the following aspects:

1 compressibility,
2 interference effects (e.g. a T-tail configuration),
3 non-planar bodies (e.g. fuselages, nacelles, pylons).

## 9 References


[1] Bergh, H., Some aspects of unsteady pressure measurements. AGARD Report 498 Part II (1965). NLR Report MP.227 (1964).

[2] Rodden, W. P. and Revell, J. D., The status of unsteady aerodynamic influence coefficients. I.A.S./S.M.F. Fund Paper No. FF-33 (1962).

[3] Laschka, B., Zur Theorie der harmonisch schwingenden Fläche bei Unterschallanströmung. Zeitschrift für Flugwissenschaften 11, Heft 7 (1963).

[4] van Gennip, M. J. M. G. and Wouters, J. G., An ALGOL 60 programme for the calculation of aerodynamic forces on wings oscillating harmonically in subsonic, compressible flow using Laschka's method. NLR Report W.28 (1964).

[5] van de Vel, H., Unsteady profile theory in incompressible flow. Doctor Thesis, Rijksuniversiteit Groningen (1965).

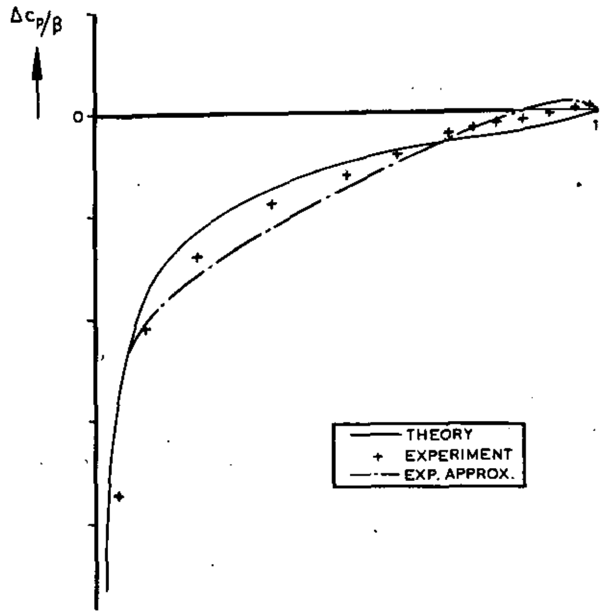


Fig. 1 Example of approximating experimental pressure distributions with method after ref. 1.

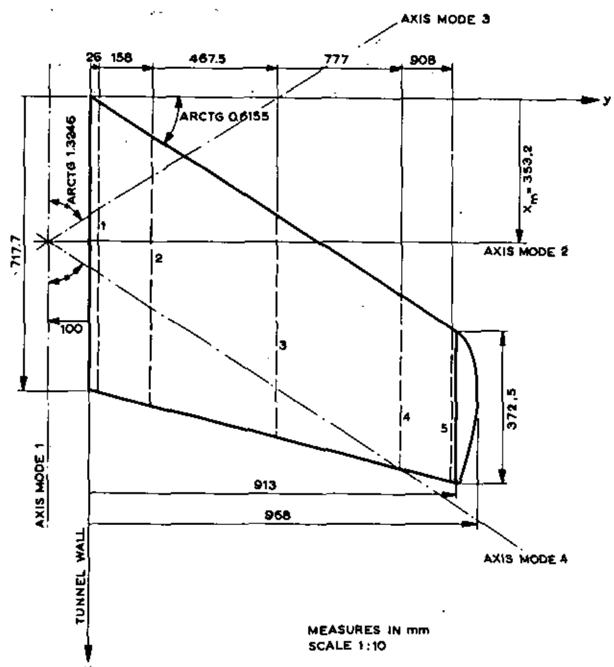


Fig. 2 Stabiliser planform.

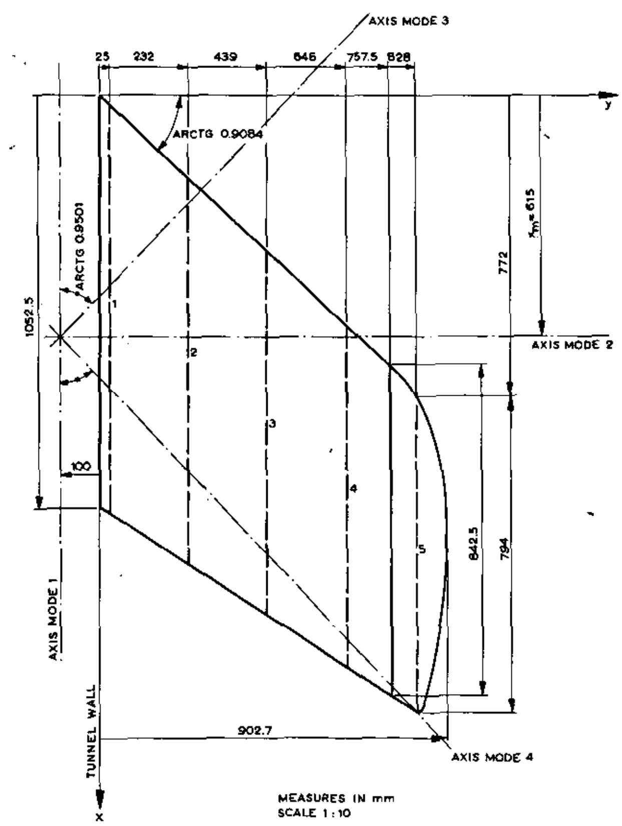


Fig. 3 Fin planform.

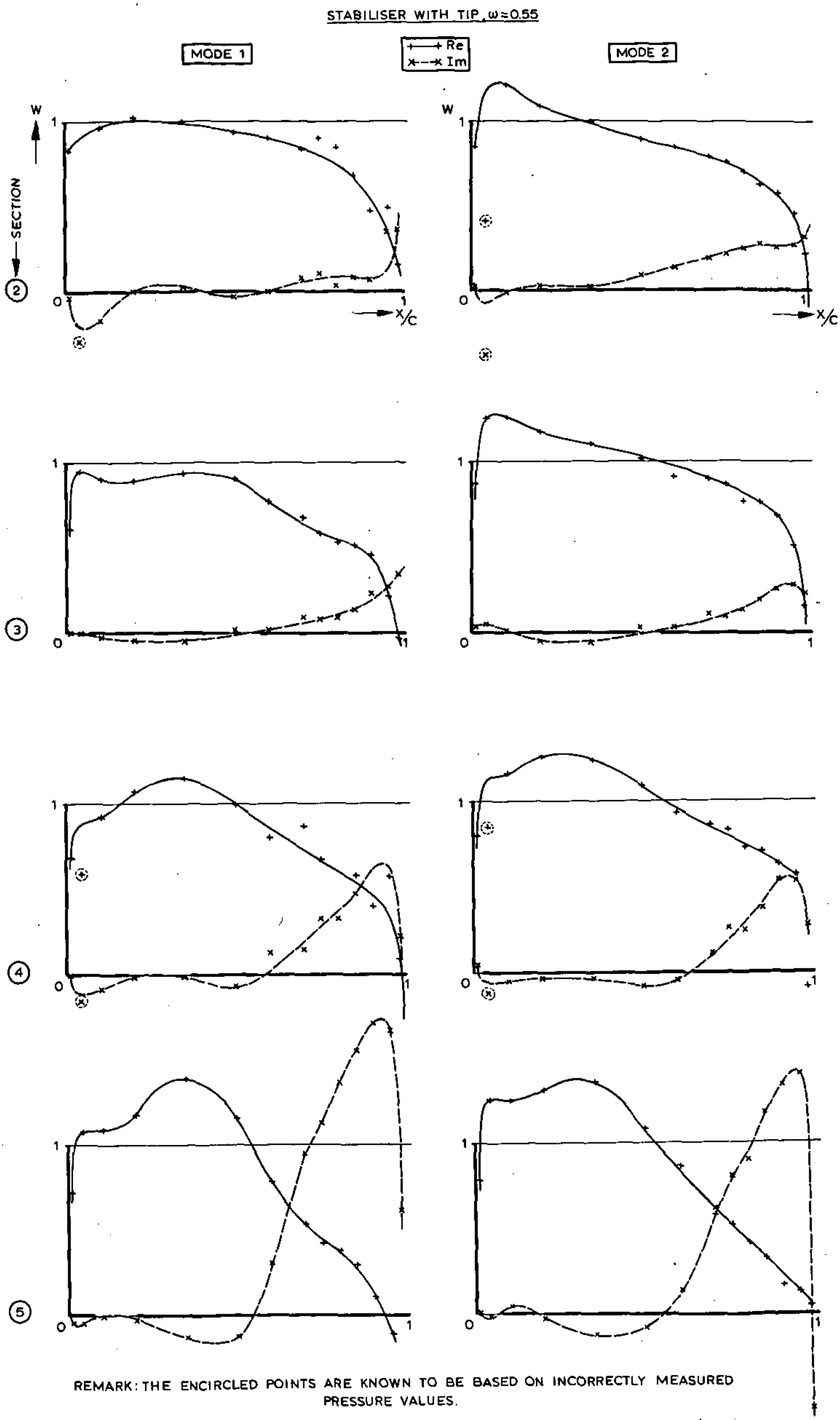


REMARK: THE ENCIRCLED POINTS ARE KNOWN TO BE BASED ON INCORRECTLY MEASURED PRESSURE VALUES.

Fig. 4 [$\ulcorner W \lrcorner$]-matrices for stabiliser with tip calculated from modes 1 and 2 at $\omega = 0.55$.

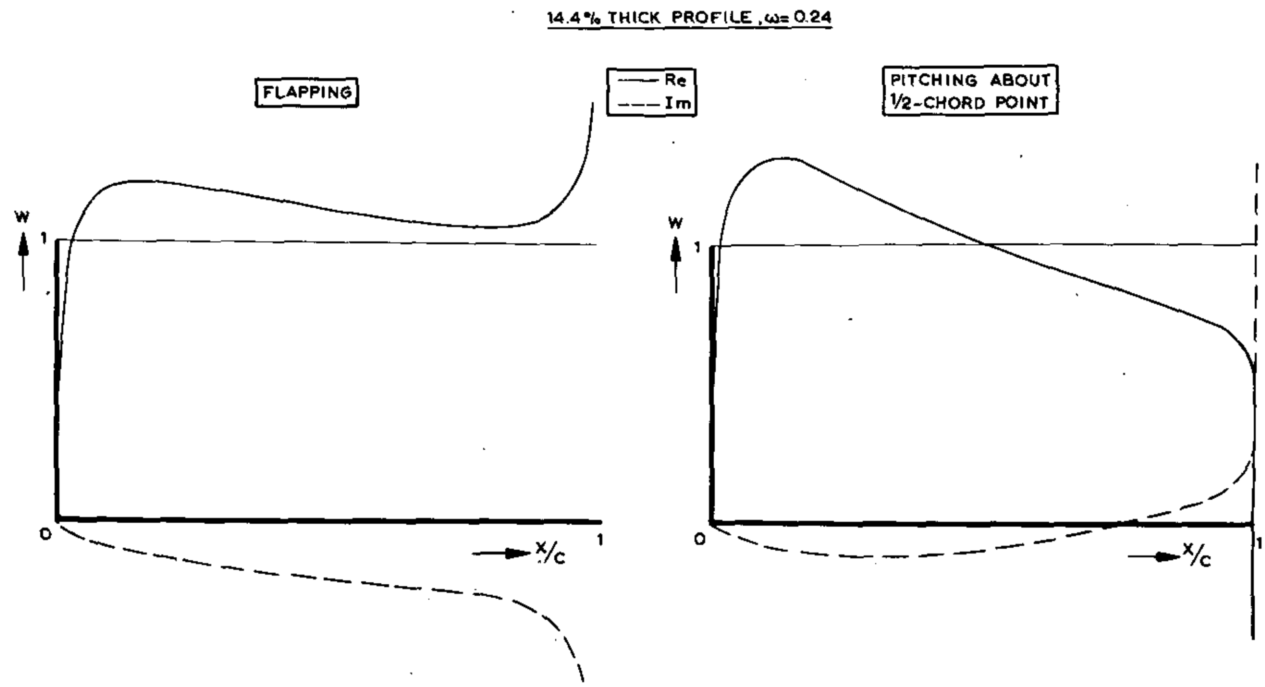


Fig. 5 [$W$]-matrices for 14.4% thick profile calculated from unsteady pressure distributions in ref. 5.

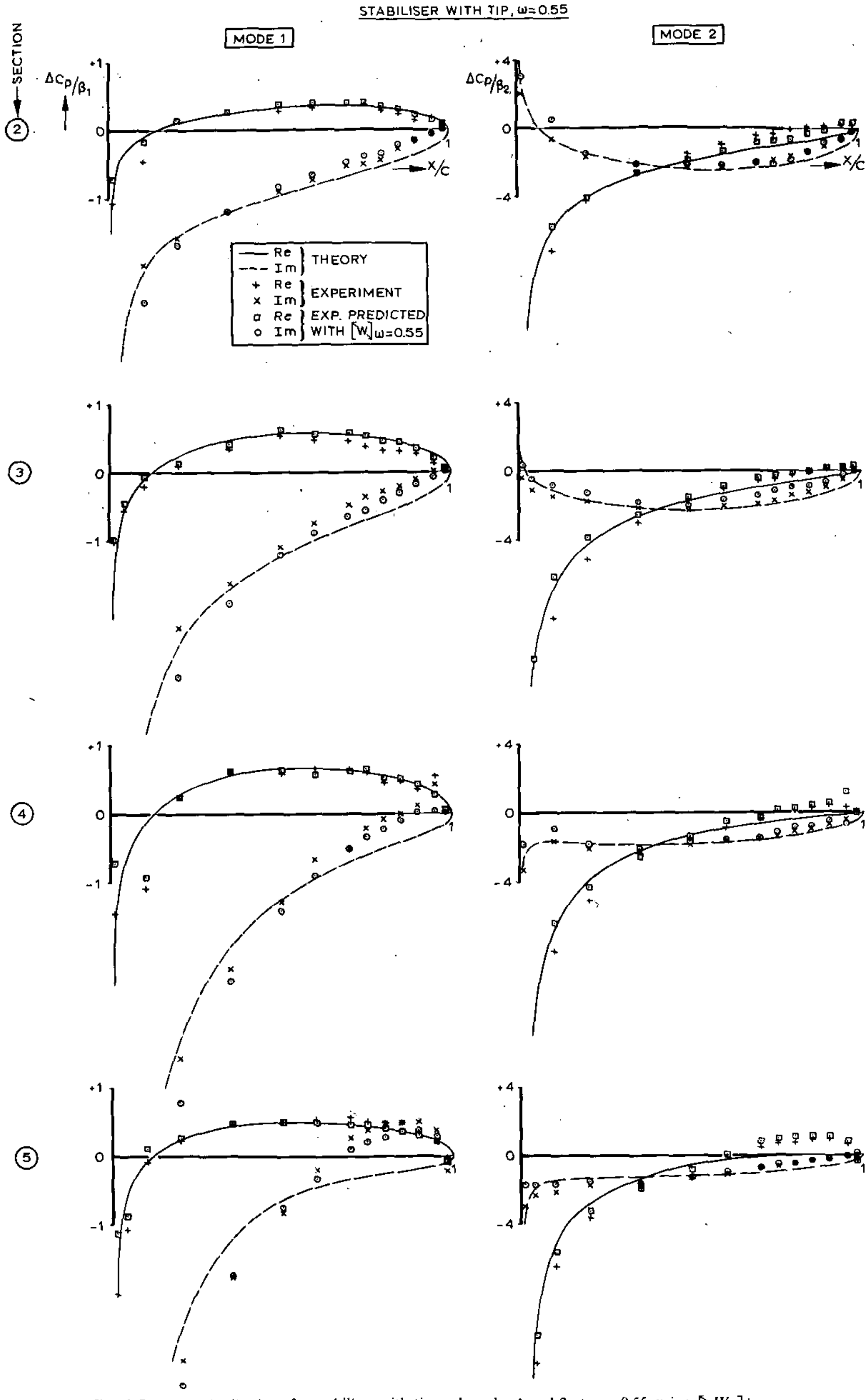


Fig. 6 Pressure distributions for stabiliser with tip and modes 1 and 2 at $\omega = 0.55$, using $[\ulcorner W \lrcorner]_{\omega=0.55}$.

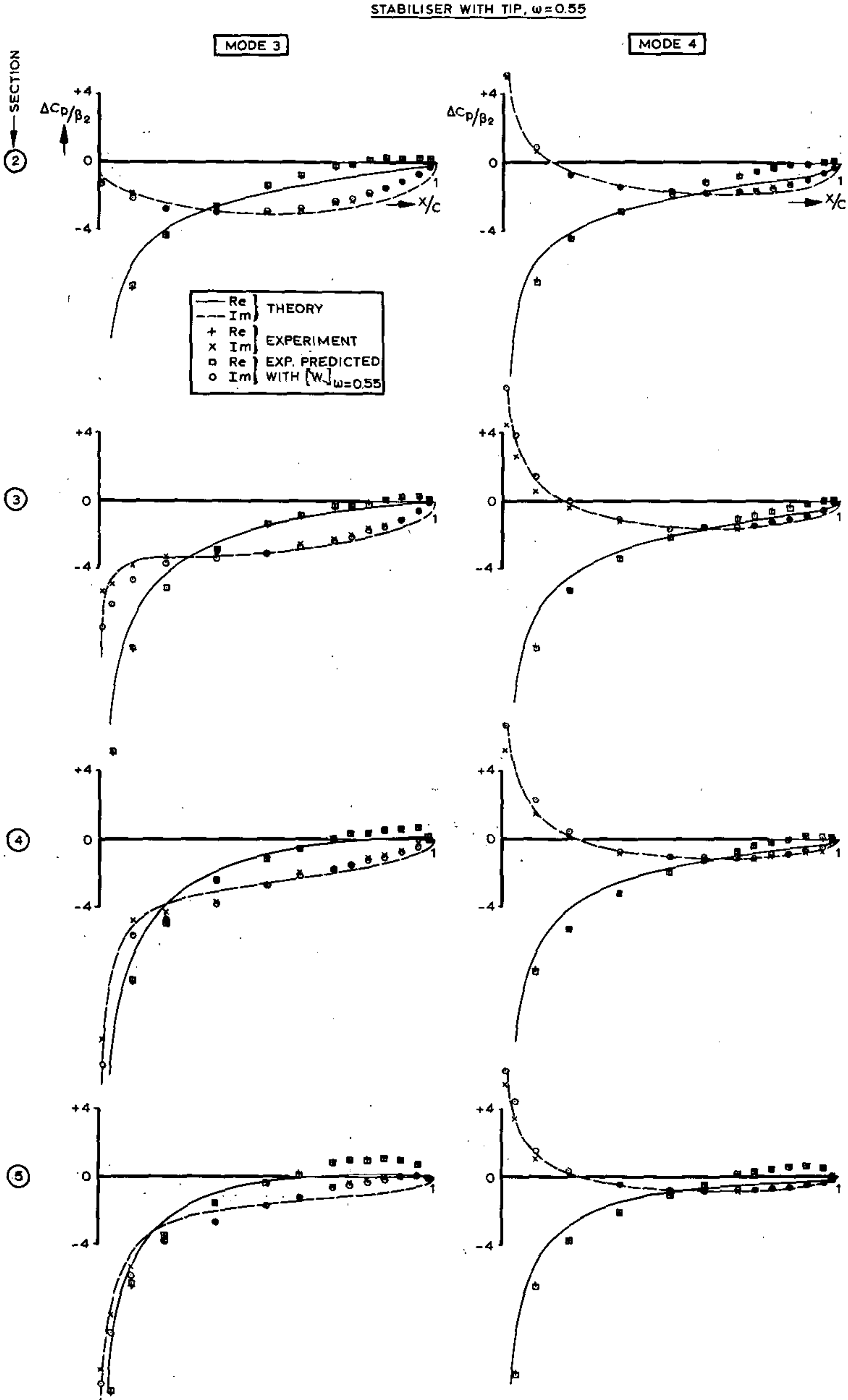


Fig. 7 Pressure distributions for stabiliser with tip and modes 3 and 4 at $\omega = 0.55$, using $[\ulcorner W \lrcorner]_{\omega=0.55}$ from mode 2.

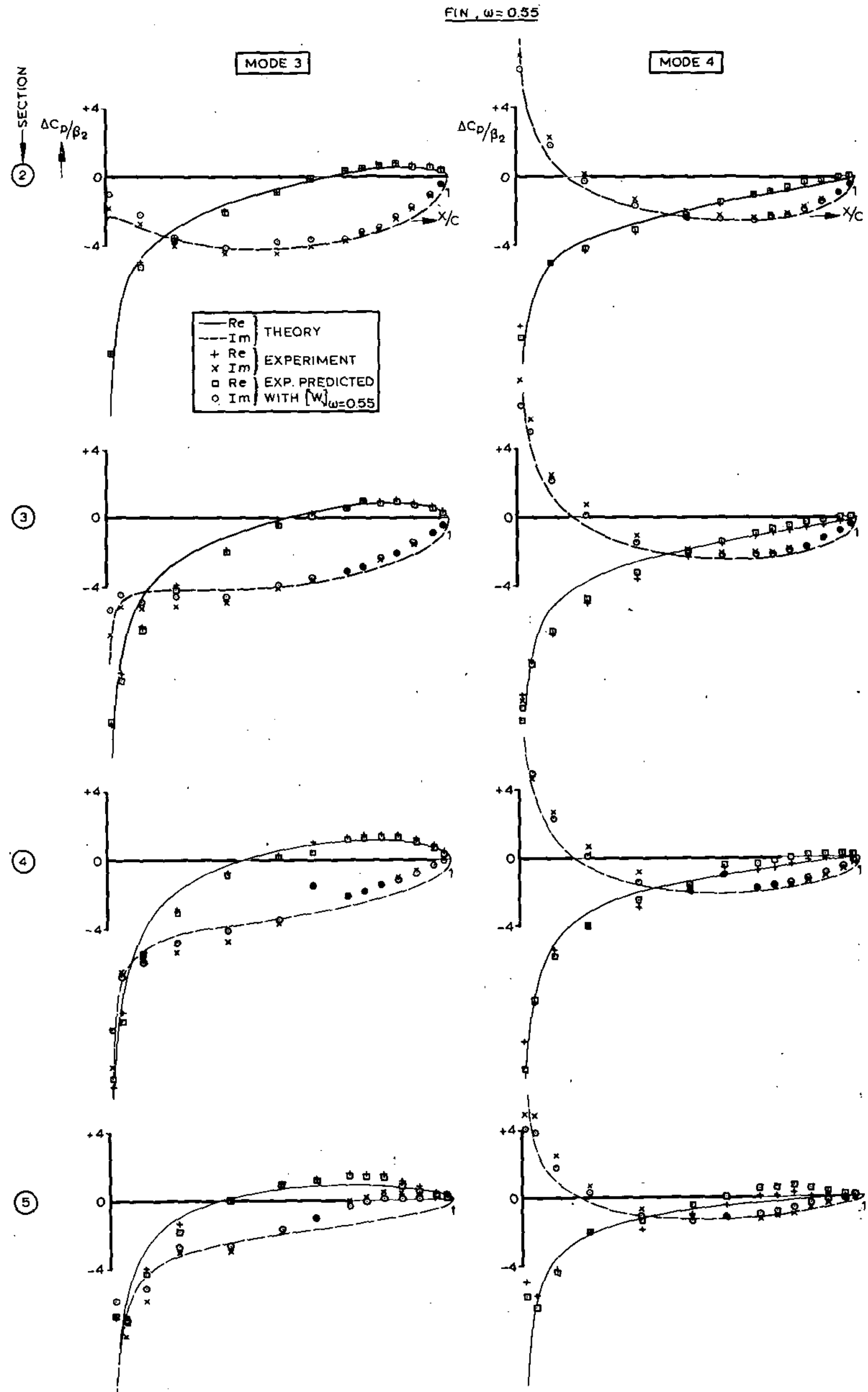


Fig. 8 Pressure distributions for fin and modes 3 and 4 at $\omega = 0.55$, using $[\backslash W \lrcorner]_{\omega=0.55}$ from mode 2.

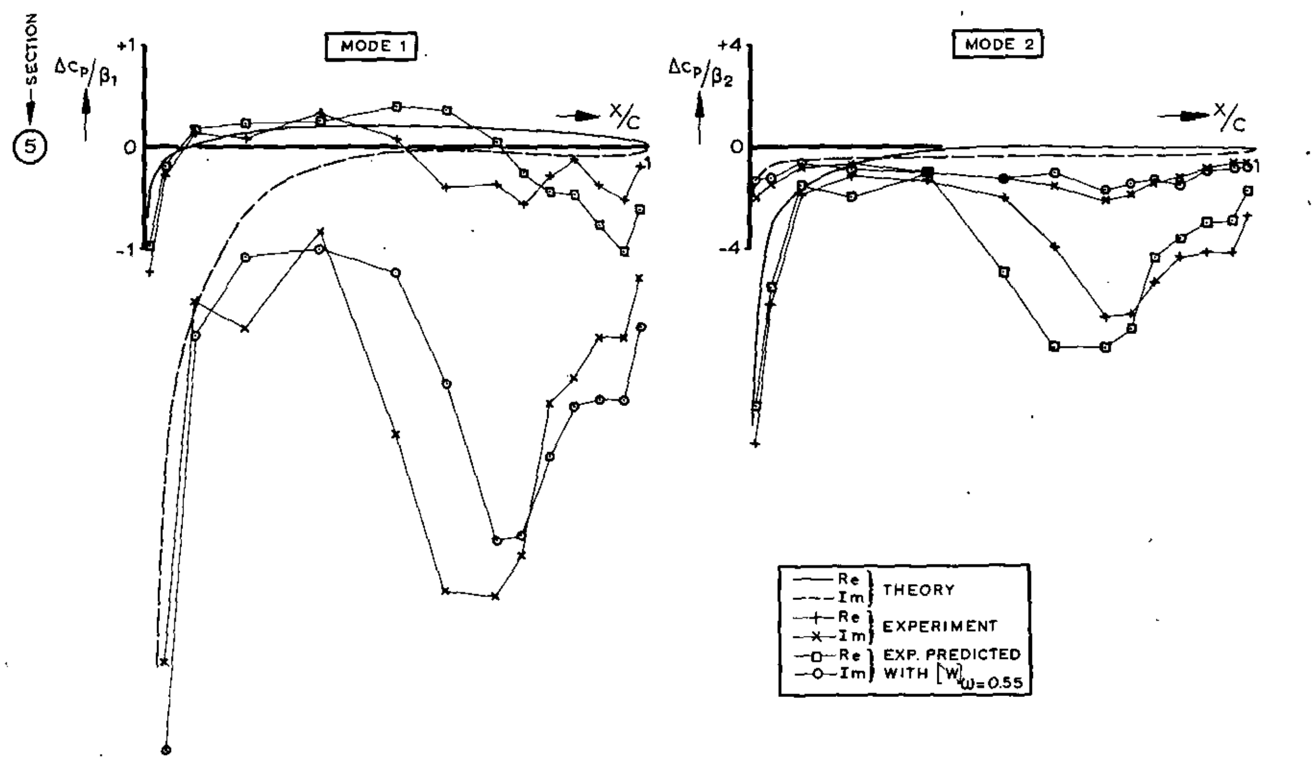


Fig. 9 Pressure distributions for stabiliser without tip, section 5, and modes 1 and 2 at $\omega = 0.55$, using $[W]_{\omega=0.55}$.

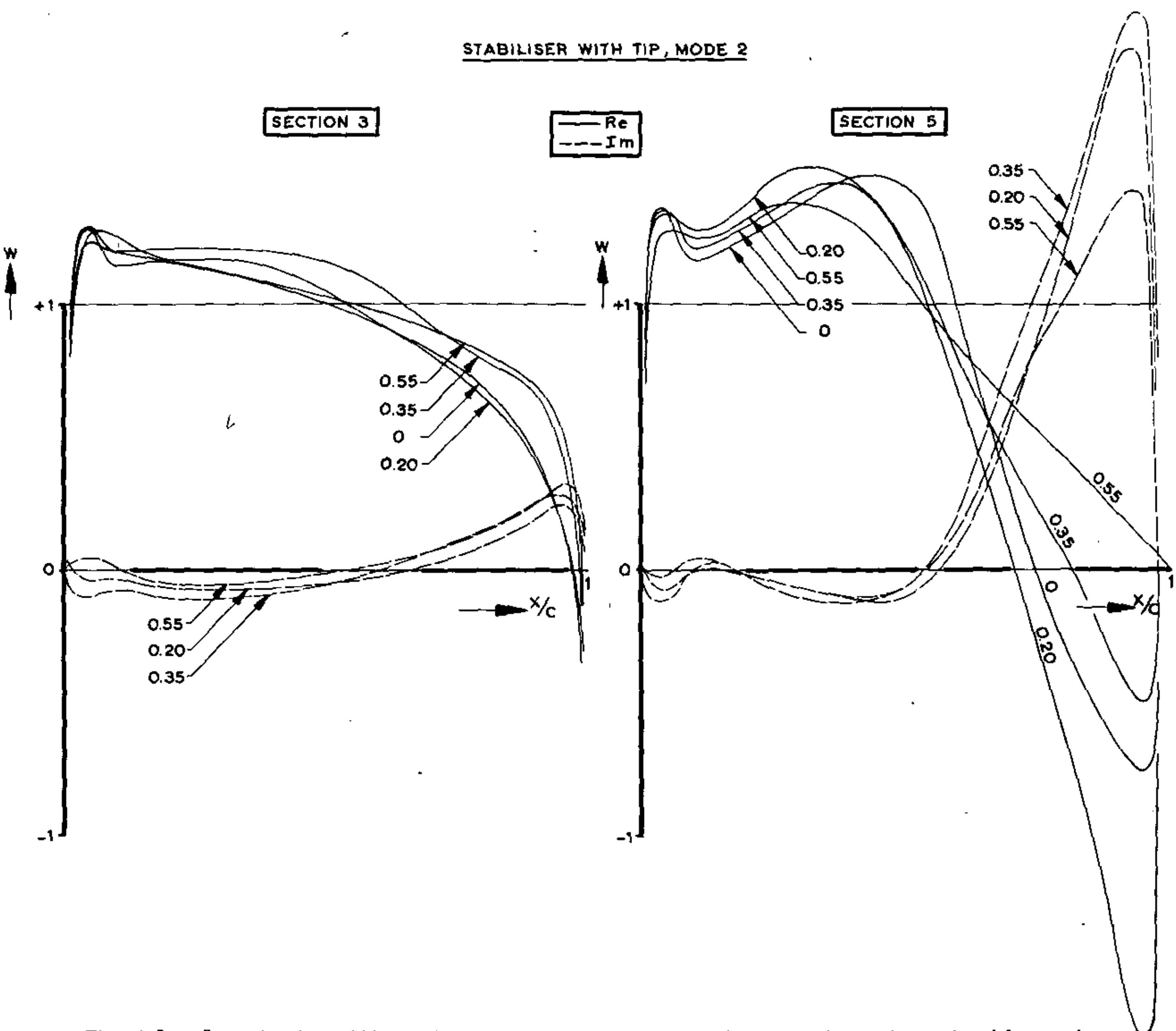


Fig. 10 $[W]$-matrices for stabiliser with tip, sections 3 and 5, calculated from mode 2 at various reduced frequencies.

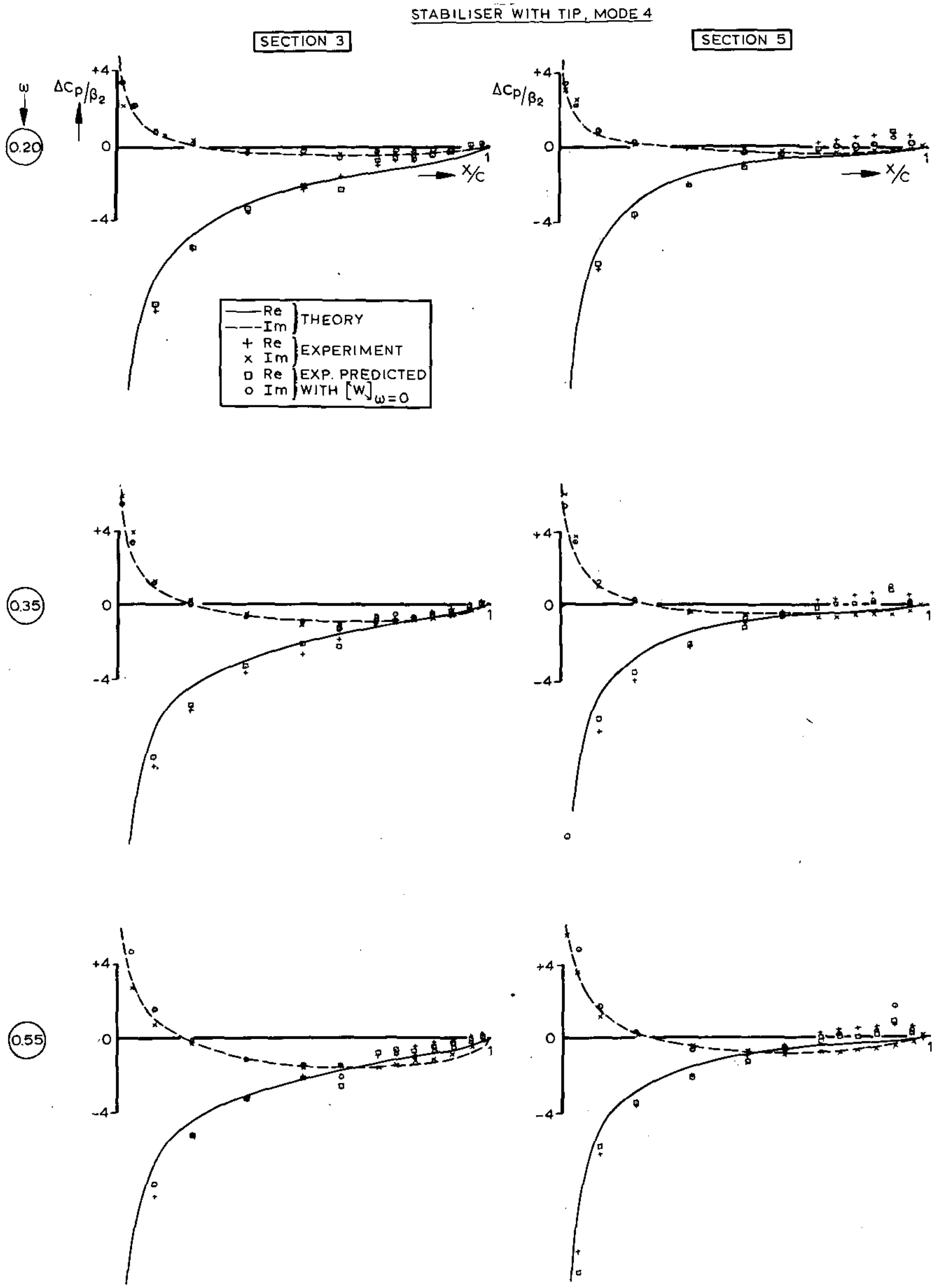


Fig. 11 Pressure distributions for stabiliser with tip, sections 3 and 5, and mode 4 at various frequencies, using $[\bar{W}]_{\omega=0.35}$ from mode 2.

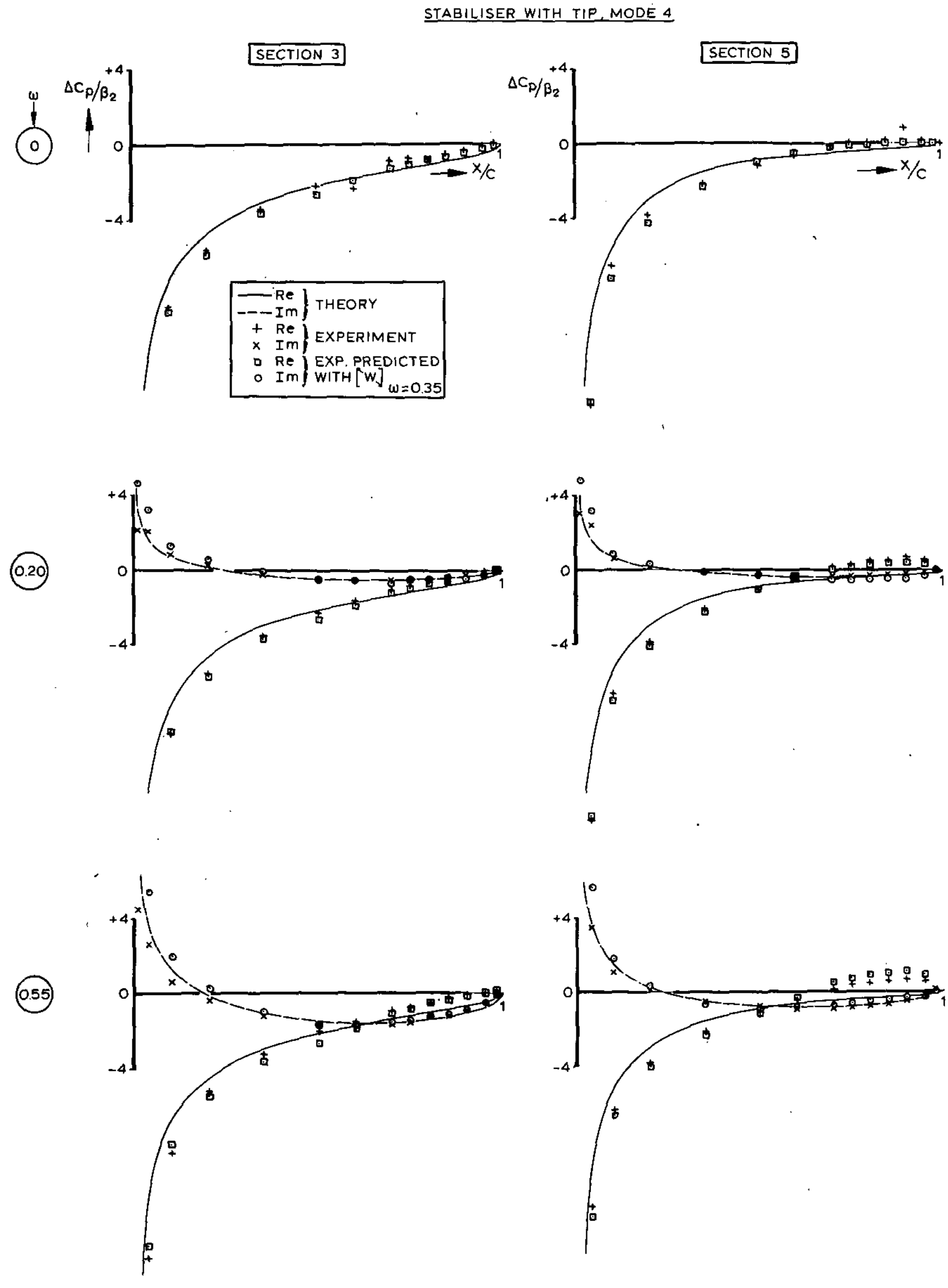


Fig. 12 Pressure distributions for stabiliser with tip, sections 3 and 5, and mode 4 at various reduced frequencies, using $\lceil W \rfloor_{\omega=0}$.

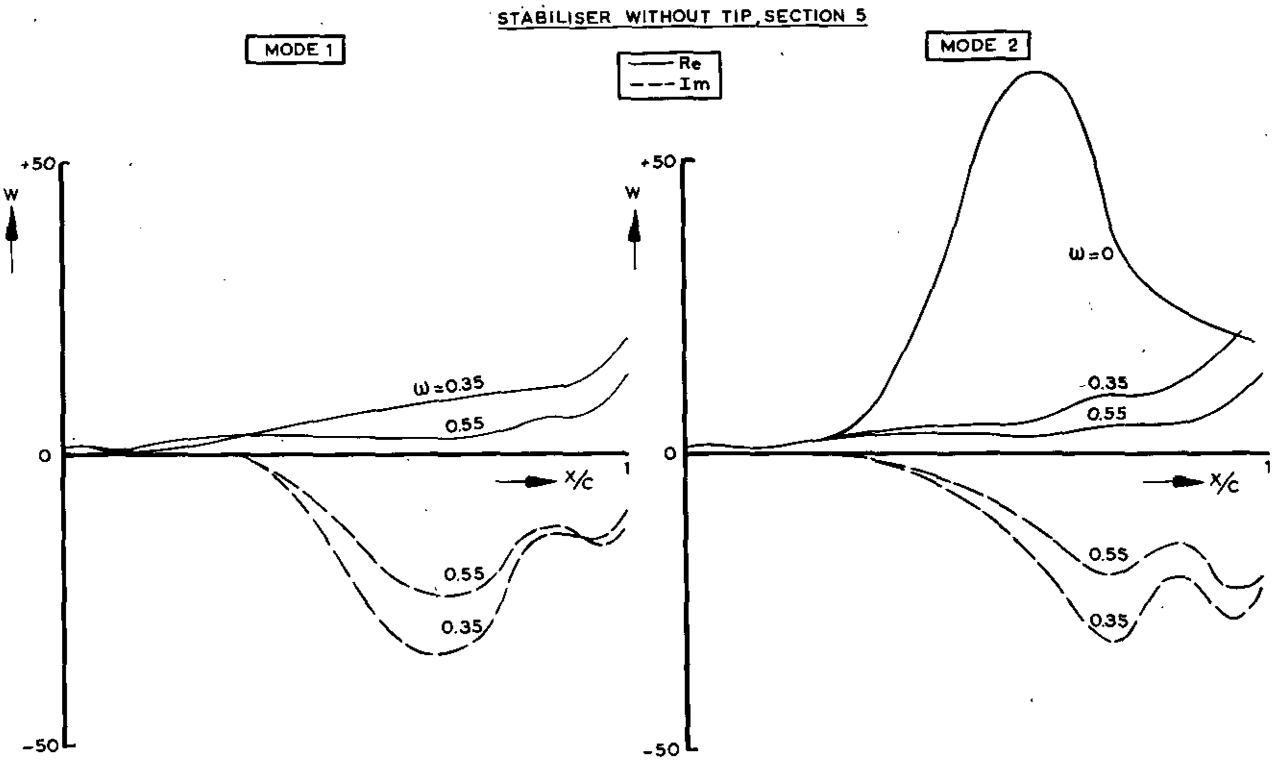


Fig. 13 [$\lceil W \rfloor$]-matrices for stabiliser without tip, section 5, calculated from modes 1 and 2 at various reduced frequencies.

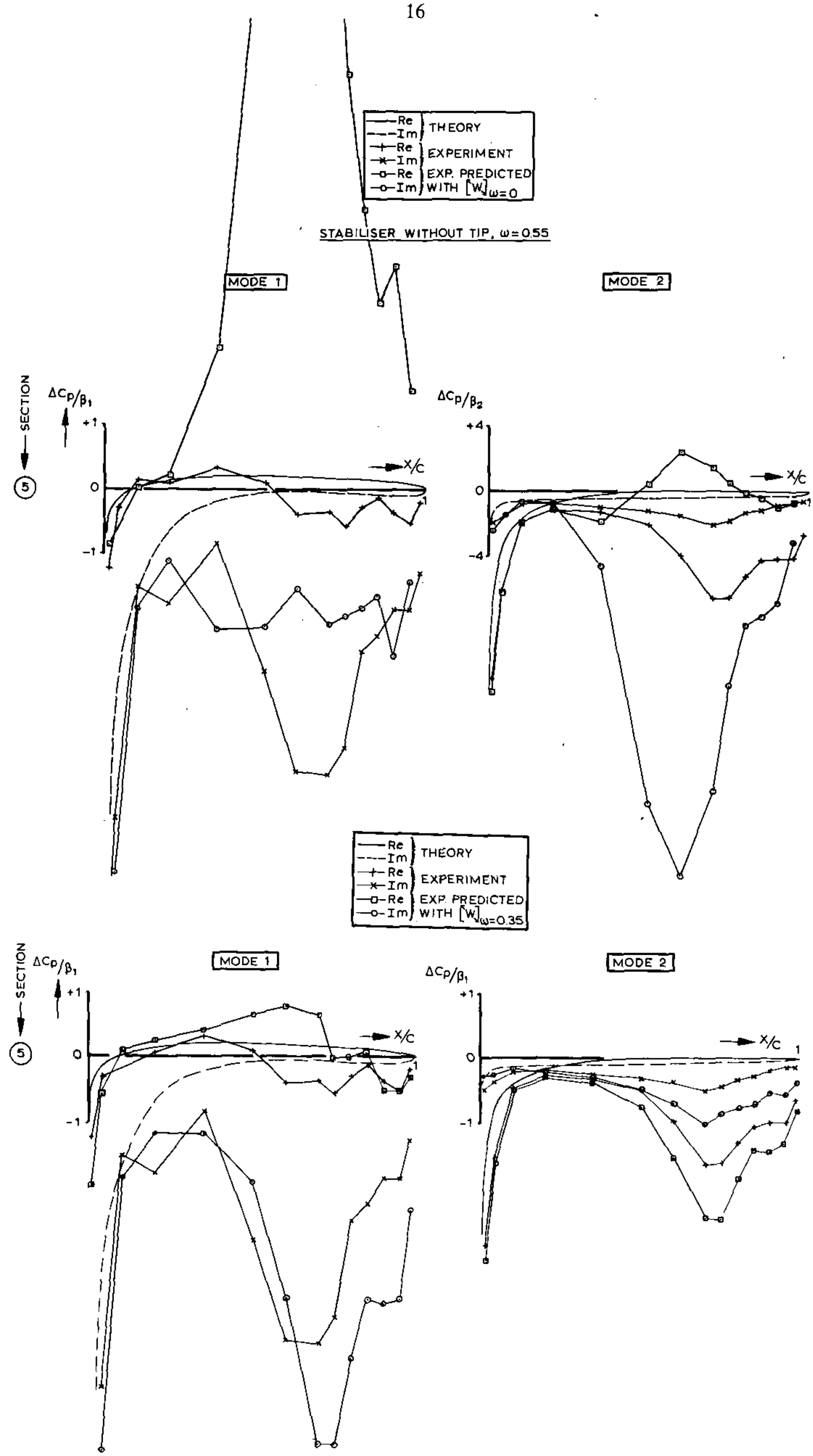


Fig. 14 Pressure distributions for stabiliser without tip, section 5, and modes 1 and 2 at $\omega = 0.55$, using $\lceil W \rfloor_{\omega=0}$ and $\lceil W \rfloor_{\omega=0.35}$.

C.C.L. Class. D 911 :D 078

REPORT NLR-TR T.124

# Numerical methods for the design of variable Mach number Laval nozzles

by

G. Y. Nieuwland

**Summary**

This report presents applications of a number of computational methods connected with the design of a variable Laval nozzle. First, Laval nozzle flows are defined as a Cauchy problem with the axial velocity distribution as initial conditions. Then, an initial value perturbation problem is considered; this case is of some more general interest as an example of a perturbation solution involving a sonic line and uses the PLK-technique. Alternatively, a boundary perturbation problem for supersonic flow is presented. Finally, the application of the methods developed to the central problem of the design of a Laval nozzle with a partially prescribed contour is discussed, and a practical example given. Some numerical aspects are discussed in an Appendix.

**Contents**



**List of symbols**

| | |
|---|---|
| $f(m)$ | — def. (A 1.6) |
| $M$ | — Mach number |
| $P$ | — def. (A 1.6) |
| $Q$ | — def. (A 1.6) |
| $q, q_{max}$ | — velocity magnitude; maximum velocity |
| $u$ | — arbitrary 2 component vector |
| $x, y$ | — physical plane coordinates |
| $z$ | — $x+iy$ |
| $\beta$ | — Mach angle |
| $\gamma$ | — specific heat ratio |
| $\delta^{(1)}$ | — boundary displacement rate function, eq (2.3.2) |
| $\theta$ | — flow angle |
| $\zeta$ | — $\int \tau_{(\psi=0)}^{-\frac{1}{2}} d\phi$ |
| $\rho$ | — flow density |
| $\tau$ | — $(q/q_{max})^2$ |
| $\phi$ | — potential function |
| $\psi$ | — stream function |
| $\xi, \eta$ | — arc length parameter along characteristic curves. |

## 1 Introduction

This is a report on a number of computational methods that originally were developed for the practical problem of designing a set of contours for a variable Mach number wind tunnel nozzle operating in the transonic speed range ($0.5 < M < 1.3$). The central problem is the numerical computation of Laval nozzle flows having part of the flow boundary prescribed, however, also a number of independent applications of the methods developed will be presented.

For these low supersonic Mach number nozzles the subsonic part of the throat region should be given consideration. This decided the choice on an indirect approach to the design as the basic procedure, where a suitable velocity distribution on the axis is prescribed throughout the nozzle including the subsonic region, and the corresponding flow field found as the solution of an initial value (Cauchy)problem. From this solution, an arbitrary pair of streamlines can be chosen as the flow boundary, and when this contour can be realized in practice, the design procedure is finished. A different situation exists, however, when constraints are to be imposed on the nozzle contour. To begin with, a solution of a Cauchy problem is defined in a limited and usually a priori unknown neighbourhood of the axis only, consequently it is impossible for a given axial velocity distribution to specify, say, an arbitrary test section height.

In practice, much more severe constraints are often to be imposed on the nozzle contour, in order to obtain a simple variable nozzle mechanism. Consider the construction sketched in fig. 1. Part of the nozzle generating an accelerating supersonic flow, consists of a contoured block, rotating around a sliding center to give the test section Mach number variations. The remaining part of the nozzle contour, converting the accelerating flow into a homogeneous parallel supersonic jet, is realised as a flexible plate, controlled by the block positions and a (number of) variable jack(s). This poses the problem to construct a sequence of Laval nozzle flows generating a uniform jet and admitting a given one parameter family of curves as part of the flow boundary. However, it is impossible to give to this problem a direct mathematical formulation and solution. In the first place, it is unknown what conditions must be imposed on the shape and smoothness of a curve to be acceptable as part of the contour of a Laval nozzle (existence problem, cf. ref. 5). On the other hand, when a solution following a given flow boundary can be found, it can usually be continued to give uniform conditions further downstream in many different ways (uniqueness problem). These difficulties can be circumvented, however, when it is sufficient to attain a solution in an "engineering approximation". The procedure, then, is first to estimate axial velocity distributions for a number of "pivotal" throat positions, to yield (via the solution of a Cauchy problem) a set of boundary contours near the prescribed ones. It is natural then to correct for the remaining contour differences by a perturbation scheme. In fact, two such procedures have been developed to serve different purposes, although in the practical context the use of only one was found necessary.

First, an initial value perturbation scheme yields a family of contour perturbations for a prescribed set of perturbations of the initially given velocity distributions on the axis. Within this family the necessary boundary corrections can be constructed, say in a least square approximation. This perturbation procedure works in the entire domain of definition of the original approximating solution, and provides an analytic perturbation solution for analytical initial value perturbations. Secondly, a boundary perturbation procedure operates in the opposite direction: for a given perturbation of the boundary in a supersonic part of the given flow field the corresponding variations of the velocity distribution on the axis can be found. Being a characteristics method, this procedure is necessarily confined to supersonic regions of the flow field, but not to analytic perturbations, which is of course a rather unnatural restriction in a supersonic flow.

Thus, by combination of the basic initial value problem with one or both of these perturbation schemes, an "iterative" procedure consisting entirely of tractable mathematical operations has been found, which will solve the engineering problem in a practical sense. It is not known, however, under what conditions such a procedure could be expected to converge in a precise mathematical sense.

In this report, a number of explicit examples of the procedures mentioned are given. As an example of the inverse approach in Laval nozzle design, two Laval nozzle flows are defined as the solution of a Cauchy problem with given axial velocity distributions as initial conditions. One is a complete Laval nozzle flow such as can be used for design purposes; the second represents the flow at the throat for a linearly increasing velocity distribution, and can immediately be compared with Sauer's well known approximate solution (ref. 16). The formulation and numerical procedures of these problems are patterned along the lines of a method developed at RAE and reported by Barritt (ref. 1).

Next, two simple examples of the initial value perturbation problem are given. It was found unnecessary to use this method in the practical design problem, however, the method is of considerable intrinsic interest as a perturbation of a solution involving a singular ("sonic") line. The key here is in the use of the PLK-method (ref. 17), which has been suggested in the mathematically related blunt body problem by Vaglio-Laurin (ref. 18). The examples have been selected such that the solution of the perturbation problem can immediately be compared with a non-linearised numerical solution of the initial value problem.

The boundary perturbation problem for the characteristics method has several useful applications. In an example it is used to assess the aerodynamical consequences of realizing the theoretical flow contour as a flexible plate which in practice gives only an approximation of the ideal shape. For the numerical treatment of the resulting hyperbolic problems we have drawn upon the experience built up by Zandbergen and his group at NLR.

Finally an example is given of the practical solution of the originating design problem for a Laval nozzle with partially prescribed contour. The boundary perturbation procedure is used to find a correction to an estimated axial velocity distribution. This corrected velocity distribution then defines a flow boundary giving a sufficiently accurate approximation to the prescribed one.

The relevant differential and perturbation equations are derived in Appendix A. The second Appendix presents a brief discussion of the numerical integration of the Cauchy problem by a finite difference method. Some tests are discussed for assessing the numerical accuracy for this inherently unstable numerical method.

The collaboration of T. J. Burgerhout, who has written the computer programmes and took the burden of all matters numerical, is gratefully acknowledged. The programme for the characteristics perturbation problem has been written by H. I. Baurdoux and Th. E. Labrujère.

## 2 Laval nozzle flow problems and results

2.1 *The initial value problem*

2.1.1 In the indirect approach to Laval nozzle computation, the equations for plane compressible potential flow of an ideal gas (cf. par. A 1.1) written on streamfunction/potential function coordinates are used, together with a prescribed analytical axial velocity distribution as initial conditions:

$$\begin{aligned} P\tau_\phi &= \theta_\psi \\ Q\theta_\phi &= \tau_\psi \end{aligned} \tag{2.1.1a}$$

$$P = \frac{\dfrac{\gamma+1}{\gamma-1}\tau - 1}{2\tau(1-\tau)^{\gamma/(\gamma-1)}}$$

$$Q = \frac{2\tau}{(1-\tau)^{1/(\gamma-1)}}$$

$$\begin{aligned} \bar{\tau}(\phi) &= \tau(\phi, 0) \\ \bar{\theta}(\phi) &= \theta(\phi, 0) \equiv 0 \end{aligned} \tag{2.1.1b}$$

In this formulation, the velocity parameter $\tau = (q/q_{\max})^2$ is chosen as a dependent variable to obtain the simplest possible form of the differential equations.

In the domain of definition of the solution of this Cauchy problem a pair of streamlines is chosen, defining the nozzle boundary. Note that the analyticity condition on the initial values means that uniform conditions can only be reached asymptotically.

It is convenient to transform to a new independent variable $\zeta$ instead of $\phi$, defined by:

$$\zeta = \int \bar{\tau}^{-\frac{1}{2}} \mathrm{d}\phi \tag{2.1.2}$$

then on the axis ($\psi = 0$), $\zeta$ coincides with the physical plane $x$-coordinate. Eq. (2.1.1) can now be written:

$$\begin{aligned} \bar{P}\tau_\zeta &= \theta_\psi \\ \bar{Q}\theta_\zeta &= \tau_\psi \end{aligned} \tag{2.1.3}$$

where

$$\begin{aligned} \bar{P}(\tau, \zeta) &= \bar{\tau}^{-\frac{1}{2}}(\zeta) P(\tau) \\ \bar{Q}(\tau, \zeta) &= \bar{\tau}^{-\frac{1}{2}}(\zeta) Q(\tau) \end{aligned}$$

and the transformation back to the physical plane reads (cf. eq. A 1.7)

$$x + \mathrm{i}y = \zeta + \mathrm{i}\int \mathrm{e}^{\mathrm{i}\theta} \frac{\mathrm{d}\psi}{\tau^{\frac{1}{2}}(1-\tau)^{1/(\gamma-1)}} \tag{2.1.4}$$

The initial conditions can then be given in the form:

$$\begin{aligned} \bar{\tau} &= \tau(\zeta, 0) \equiv \bar{\tau}(x) \\ \bar{\theta} &= \theta(\zeta, 0) \equiv 0 \end{aligned} \tag{2.1.5}$$

where $\bar{\tau}(\zeta)$ is an analytic function.

In the next two paragraphs, examples of Laval nozzle flows for different initial conditions (2.1.5) will be described, which have been constructed using the numerical scheme of Appendix B.

2.1.2 In fig. 2 a Laval nozzle flow such as can be used for practical design purposes is represented as a hodograph mapping. The prescribed axial velocity distribution is given by:

$$\frac{\tau - \tau_{-\infty}}{\tau_\infty - \tau_{-\infty}} = \tfrac{1}{2}[1 + \tanh\{a_1(\zeta - c) + a_3^3(\zeta - c)^3\}] \tag{2.1.6}$$

where in the case presented

$$\begin{aligned} \tau_\infty &= 0.2499 \quad (M_\infty = 1.2907) \\ \tau_{-\infty} &= 0 \\ a_3/a_1 &= 0.7570 \end{aligned}$$

have been chosen.

The parameter $\tau_\infty$ defines the velocity far downstream in the nozzle, while $\tau_{-\infty}$ represents conditions at the other extreme. Roughly, the constant $a_1$ controls the velocity gradient at the throat region, and $a_3$ the rate of convergence to uniform conditions*. Of course, $a_1$ and $a_3$ contain a scale factor and also the location of the origin as controlled by $c$ is physically irrelevant.

In the hodograph representation of fig. 2 the flow quantities $M$ and $\theta$ are for clarity plotted as cartesian coordinates. This hodograph illustrates clearly the geometry of a Laval nozzle flow as discussed in Appendix C of ref. 14. In particular the occurrence of a triply covered region in the hodograph near the branch line characteristic (through the point $M=1$, $\theta=0$) and the location of the image of the region downstream of the throat in between the branch line and the limiting characteristic (through $M=M_\infty$, $\theta=0$) is shown. As discussed in ref. 14, this means geometrically that the jacobian $J=\det(u_{i,j})>0$ for this region, which in turn expresses physically that in a well designed Laval nozzle only expansion waves occur downstream of the throat region.

2.1.3 In fig. 3 a flow in the throat region of a Laval nozzle corresponding to a linearly increasing velocity distribution on the symmetry axis is shown. This case has been chosen as the basis field for the perturbation problems to be studied in section 2.2.

The axial distribution can be written

$$\bar{\tau}=(a+b\zeta)^2 \tag{2.1.7}$$

where $a=\left(\frac{\gamma-1}{\gamma+1}\right)^{\frac{1}{2}}$ (the sonic speed) so that $M=1$ for $\zeta=0$, and $b$ determines the linear scale of the flow field.

The solution is graphically presented in term of isogonals and isochores drawn in the physical plane; this representation can be compared with the hodograph image of the throat region of fig. 2.

The present solution can be compared with Sauer's approximation (ref. 16) for the conditions at the throat of a Laval nozzle. In fig. 4a a comparison is made between the locations of isochores and isogonals as predicted by Sauer's solution and the present numerical results, which may be considered to represent the exact solution within the numerical accuracy attainable. For sonic curve and throat position ($\theta=0$) the agreement is rather good in the range shown, the maximum deviation for these curves being in the order of 2%. In fig. 4b a comparison is given for the streamline curvature at the throat ($\theta=0$). In Sauer's approximation this is given by the expression

$$\frac{1}{R}=(\gamma+1)\alpha^2 y$$

where $y$ denotes throat height and $\alpha=2\frac{\gamma-1}{\gamma+1}(\tau_x)_{\tau=\tau^*}$ is the velocity gradient on the axis. For the present case, the value of the throat curvature as predicted by Sauer's expression is already 8% off. Fig. 4c presents a comparison for the value of the streamfunction $\psi$ on the line $\theta=0$, which in Sauer's approximation again is proportional to $y$.

2.2 *The initial value perturbation problem*

2.2.1 In this paragraph, perturbations of the previous initial value problem will be considered. In this case, difficulties are encountered at the sonic line, which can be formally resolved by application of the PLK-technique (ref. 17), of which details are given in Appendix A 2. Briefly, this involves the interposition of a coordinate perturbation, mapping the perturbed field onto the basis field, which in the present case is most simply specified by mapping corresponding streamlines on streamlines and isobars on isobars, and thus sonic line on sonic line.

This leaves a system of everywhere regular linear differential equations (A 2.10) for the displacement function $\phi^{(1)}$ (or equivalently $\zeta^{(1)}$) and the angular perturbation function $\theta^{(1)}$ (see Appendix A 2), both functions being defined on the coordinate system of the basis field. The relations of these functions with quantities in the perturbed field are given by eqs (A 2.13), or equivalently eq. (2.2.6).

2.2.2. As before, transforming $\phi$ by eq. (2.1.2), the perturbation equations (A 2.10) become:

$$\begin{aligned}-\theta_\zeta\cdot\zeta_\psi^{(1)}+\theta_\psi\cdot\zeta_\zeta^{(1)}+\theta_\psi^{(1)}&=0\\-\tau_\zeta\cdot\zeta_\psi^{(1)}+\tau_\psi\cdot\zeta_\zeta^{(1)}-\bar{Q}\cdot\theta_\zeta^{(1)}&=0\end{aligned} \tag{2.2.1}$$

Consider initial conditions with a perturbation term:

$$\begin{aligned}\tau'(\zeta,0)&=\bar{\tau}(\zeta)+\varepsilon\bar{\tau}^{(1)}(\zeta)\\\theta'(\zeta,0)&\equiv 0\end{aligned} \tag{2.2.2}$$

Then, in the perturbed coordinate system, the initial data by (A 2.7), (A 2.9), (A 2.11) read to the first order in $\varepsilon$:

$$\tau^{(1)}(\zeta',0)=\bar{\tau}^{(1)}(\zeta)+\zeta^{(1)}\cdot\bar{\tau}_\zeta(\zeta)\equiv 0 \tag{2.2.3}$$

where

$$\zeta'=\zeta+\varepsilon\zeta^{(1)}$$

* Compare tanh $x+\frac{x^3}{3}+\frac{x^5}{5}+\ldots=x$ for $-1<x<1$.

In accordance with the general specification (eq. A 2.9) of the coordinate perturbation, eq. (2.2.3) expresses that at the point $(\zeta',\psi')$ of the perturbed field (where $\zeta'=\zeta+\varepsilon\zeta^{(1)}$, $\psi'=\psi$) the velocity magnitude has the same value to the first order in $\varepsilon$ as at the point $(\zeta,\psi)$ of the undisturbed field.

The initial conditions for the equations (2.2.1) then follow:

$$\zeta^{(1)}(\zeta,0) = -\frac{\bar{\tau}^{(1)}(\zeta)}{\bar{\tau}_\zeta} \qquad \theta^{(1)}(\zeta,0)\equiv 0 \tag{2.2.4}$$

Solving the system (2.2.1) for these initial values by the numerical schema of Appendix B, the functions $\zeta^{(1)}$, $\theta^{(1)}$ are found.

In the perturbed field it follows then at a point $(\zeta,\psi)$ to the first order in $\varepsilon$:

$$\begin{aligned} \tau'(\zeta,\psi) &= \tau(\zeta,\psi)-\varepsilon\tau_\zeta\cdot\zeta^{(1)} \\ \theta'(\zeta,\psi) &= \theta(\zeta,\psi)+\varepsilon\{\theta^{(1)}-\theta_\zeta\cdot\zeta^{(1)}\} \end{aligned} \tag{2.2.5}$$

In the physical plane the corresponding point is displaced by $\varepsilon z^{(1)}$ where

$$\begin{aligned} z^{(1)} &= -\textstyle\int_0^\psi e^{i\theta}\{R\cdot\hat{\theta}-iR_\tau\cdot\hat{\tau}\}\,d\psi \\ \hat{\theta} &= \theta^{(1)}-\theta_\zeta\cdot\zeta^{(1)} \\ \hat{\tau} &= -\tau_\zeta\cdot\zeta^{(1)} \\ R &= \tau^{\frac{1}{2}}(1-\tau)^{-1/(\gamma-1)} \end{aligned} \tag{2.2.6}$$

2.2.3 The first perturbation problem is obtained by perturbation of the constant term in (2.1.7):

$$\bar{\tau}' = \{(1+\varepsilon)a+b\zeta\}^2 \tag{2.1.7a}$$

the linear perturbation term reads

$$\bar{\tau}^{(1)} = 2a(a+b\zeta)$$

Then, however,

$$\zeta^{(1)}(\zeta,0) = -\frac{a}{b} \qquad \theta^{(1)}(\zeta,0)=0$$

and it is immediately seen that

$$\zeta^{(1)} \equiv -\frac{a}{b} \qquad \theta^{(1)}\equiv 0 \tag{2.2.7}$$

trivially satisfies eqs (2.2.1). This property is, of course, independent of the particular basis field, and provides an immediate numerical check on the stability of the integration scheme (cf. fig. 7 and Appendix B).

The second perturbation problem is defined by perturbation of the linear term in (2.1.7):

$$\bar{\tau}' = \{a+(1+\varepsilon)b\zeta\}^2 \tag{2.1.7b}$$

then

$$\bar{\tau}^{(1)} = 2b\zeta(a+b\zeta)$$

and

$$\zeta^{(1)}(\zeta,0) = -\zeta \qquad \theta^{(1)}(\zeta,0)=0 \tag{2.2.8}$$

Results for this problem are shown in fig. 5, where the displacements of the streamline-equipotentialline grid and of the isogonals and isochores are presented for a particular value of the parameter $\varepsilon$.

2.2.4 As already has been mentioned, the choice of the above linear perturbation problems has the advantage that the solutions can be easily checked against the non-linear numerical solution for the perturbed initial conditions. The latter solutions are trivially obtained by a shift or scale transformation respectively, and the corresponding numerical values can be obtained by interpolation in the original solution. In the present case, a direct comparison has been made, as (2.1.7a) has been evaluated for three slightly different values of $\varepsilon$ to obtain a numerical accuracy test.

Writing for convenience $u$ for the vector $\binom{\zeta}{\theta}$, the quantity $u(\zeta,\psi;\varepsilon_1)-u(\zeta,\psi;0)$ can be compared with $\varepsilon_1\hat{u}$ where $\hat{u}$ is defined in eq. (2.2.6)). However, the difference $u(\zeta,\psi,\varepsilon_1)-u(\zeta,\psi,0)$ includes also the effect of the higher order terms in the expansion in $\varepsilon$, while only the first order term is represented by $\varepsilon_1\hat{u}$. These non-linear effects can be estimated when a third exact solution for a value $\varepsilon_2$ is available by a well known argument, the use of which in the present context was suggested by T. J. Burgerhout. In fact, as the solutions depend analytically on $\varepsilon$ one can write:

$$u(\zeta,\psi;\varepsilon_1) = u(\zeta,\psi;0) + \varepsilon_1 \left.\frac{d}{d\varepsilon}\right|_{\varepsilon=0} u(\zeta,\psi;\varepsilon) + \frac{\varepsilon_1^2}{2!}\left.\frac{d^2}{d\varepsilon^2}\right|_{\varepsilon=0} u(\zeta,\psi;\varepsilon) + 0(\varepsilon_1^3)$$

and the analogous expression for $u(\zeta,\psi;\varepsilon_2)$.

Then solving for $\frac{d}{d\varepsilon}u$ it follows:

$$\hat{u} \equiv \left.\frac{d}{d\varepsilon}\right|_{\varepsilon=0} u = \frac{\varepsilon_2^2 u(\zeta,\psi;\varepsilon_1) - \varepsilon_1^2 u(\zeta,\psi;\varepsilon_2) - (\varepsilon_2^2-\varepsilon_1^2)u(\zeta,\psi;0)}{\varepsilon_1\varepsilon_2(\varepsilon_2-\varepsilon_1)} + 0(\varepsilon^3) \tag{2.2.9}$$

and the expression in the righthand side can be evaluated from the known solutions and compared with $\hat{u}$. The initial value problem (2.1.7a) has been numerically solved for $\varepsilon_0 = 0$, $\varepsilon_1 = +0{,}01$, $\varepsilon_2 = -0{,}01$.

In this case, application of eq. (2.2.9) reduces to taking the arithmetic mean between the absolute values of the differences in $\tau$ or $\theta$ for $\varepsilon = 0{,}01$ and $\varepsilon = -0{,}01$. A comparison of the values $\tau_{\varepsilon=-0{,}01} - \tau_{\varepsilon=0}$, $\tau_{\varepsilon=0{,}01} - \tau_{\varepsilon=0}$ and the arithmetic mean of their absolute values with $|\varepsilon\hat{\tau}|$, taken along an equipotentialline is made in Table 1. It is seen that near the axis, taking the arithmetic mean (giving a value to $0(\varepsilon^3)$) effectively improves numerical accuracy. Further off the axis, however, higher order effects dominate.

TABLE 1
Comparison of perturbation velocity with differences of non-linearised computations

| | (1) | (2) | (3) | (4) | (5) |
|---|---|---|---|---|---|
| $\zeta = C$ | $\tau_{\varepsilon=0}$ | $(\tau_{\varepsilon=-.01} - \tau_{\varepsilon=0})10^3$ | $(\tau_{\varepsilon=.01} - \tau_{\varepsilon=0})10^3$ | $\frac{\lvert(2)\rvert+\lvert(3)\rvert}{2}$ | perturb. value $\lvert\varepsilon\hat{\tau}\cdot 10^3\rvert$ |
| $\psi =$ 0 | .1958427 | −.3034 | +.3036 | .3035 | .3035 |
| 1 | .1959144 | −.3050 | +.3053 | .3051 | .3051 |
| 2 | .1961299 | −.3098 | +.3101 | .3099 | .3099 |
| 3 | .1964905 | −.3178 | +.3183 | .3180 | .3180 |
| 4 | .1969986 | −.3292 | +.3299 | .3295 | .3295 |
| 5 | .1976574 | −.3442 | +.3450 | .3446 | .3445 |
| 6 | .1984713 | −.3629 | .3639 | .3634 | .3632 |
| 7 | .1994459 | −.3856 | .3870 | .3663 | .3858 |
| 8 | .2005880 | −.4126 | .4145 | .4136 | .4128 |
| 9 | .2019065 | −.4444 | .4470 | .4457 | .4444 |
| 10 | .2034118 | −.4816 | .4849 | .4834 | .4812 |
| 11 | | | | | |
| 12 | .2070372 | −.5753 | .5806 | .5780 | .5734 |
| 13 | | | | | |
| 14 | .2116078 | −.7025 | .7112 | .7069 | .6974 |
| 15 | | | | | |
| 16 | .2173490 | −.8791 | .8935 | .8863 | .8681 |

2.3 *A boundary perturbation problem for supersonic flow*

2.3.1 In this paragraph a plane supersonic potential flow is assumed given, and a perturbation of a boundary streamline considered.

The relevant definitions of the perturbation functions $M^{(1)}$, $\theta^{(1)}$ defined in the characteristic coordinate system of the basis field and the governing system of differential equations for these quantities are written down in Appendix A 3, so that only the appropriate boundary conditions need be given here.

Consider a variation $C'$ of a boundary streamline $C$ of the given flow field, described by

$$C' : y' = y + \Delta y \qquad x' = x + \Delta x \tag{2.3.1}$$

The basis flow field is assumed imbedded in a one-parameter family analytically dependent on a parameter $\varepsilon$ and the perturbation of the boundary contour is identified with the representation of the contour by the first order term in the expansion in $\varepsilon$. This is written:

$$\Delta y = \varepsilon\delta^{(1)}\cos\theta \qquad \Delta x = \varepsilon\delta^{(1)}\sin\theta \tag{2.3.2}$$

where $\delta^{(1)}$ is the displacement rate function measured along a normal to $C$. Define:

$$\Delta M = M(x'y') - M(x,y)$$
$$\Delta\theta = \theta(x',y') - \theta(x,y)$$

To formulate the boundary condition for $M^{(1)}$, $\theta^{(1)}$ on the unperturbed boundary $C$, the first order correction for the gradient in the basis field has to be considered as before, and it follows:

$$\varepsilon\theta^{(1)} = \Delta\theta + \frac{\varepsilon\delta^{(1)}}{2\sin\beta}(\theta_\eta - \theta_\xi) + 0(\varepsilon^2) = \Delta\theta - \varepsilon\delta^{(1)} \cdot \frac{M^2-1}{M\left(1+\frac{\gamma-1}{2}M^2\right)} \cdot M_s + 0(\varepsilon^2) \tag{2.3.4}$$

where $\frac{\delta}{\delta s}$ denotes differentiation along the unperturbed contour.

Then, when $M^{(1)}$ is found from the solution of eqs (A 3.6) the velocity along the perturbed contour can be found from:

$$\Delta M = \varepsilon M^{(1)} - \frac{\varepsilon\delta^{(1)}}{2\sin\beta}(M_\eta - M_\xi) + 0(\varepsilon^2) = \varepsilon M^{(1)} + \varepsilon\delta^{(1)} \cdot M\left(1+\frac{\gamma-1}{2}M^2\right) \cdot \theta_s + 0(\varepsilon^2) \tag{2.3.5}$$

here $\theta_s$ is the streamline curvature.

This implies that the velocity perturbation $\Delta M$ can only be computed on a contour where the displacement function $\varepsilon\delta^{(1)}$ is given (say, on the axis of a Laval nozzle for a symmetric perturbation, $\delta^{(1)} = 0$). In the field however, the velocity and angular perturbations $\Delta M$ and $\Delta\theta$, as distinguished from $M^{(1)}$ and $\theta^{(1)}$, are unknown.

2.3.2 A practical example is presented in fig. 6. A theoretical flow contour has been computed, which must in practice be realised as a flexible wall, supported by a number of jacks and clamped at the ends. Obviously, this can only approximate the ideal contour, and an assessment of the aerodynamical consequences is required. This is all the more of practical importance, as one is of course interested in the simplest possible nozzle variation scheme (least number of jacks) compatible with an allowable level of departure from flow uniformity in the test section.

The Laval nozzle solution in fig. 2 is taken as the basis field, the difference between part of this contour and an approximation by two smoothly faired third degree curves imposed as a boundary perturbation in the supersonic region. The associated characteristics field of the undisturbed solution can be found by interpolation, or can be constructed anew by using the known velocity distribution along part of the contour as initial conditions for the characteristics integration method, further using the known geometry as a boundary condition. This procedure has been found to work well, and gives an independent check on the accuracy of both numerical methods.

The contour perturbation is shown in fig. 6, here $d$ is the distance of the perturbed contour from the original boundary to be identified with the displacement function $\varepsilon\delta^{(1)}$ (cf. eq. (2.3.2.)), and $\varepsilon\theta$ is the difference in flow angle. Then, along the unperturbed contour $\theta^{(1)}$ can be found by eq. (2.3.4), along the axis $\theta^{(1)} = 0$ and also on the right running characteristics through the upstream end of the perturbed contour, $\theta^{(1)} = 0$ and $M^{(1)} = 0$. From these initial and boundary values, the equations (A 3.6) can be solved numerically, yielding along the axis the perturbation Mach number $\Delta M = \varepsilon M^{(1)}$.

The numerical scheme is basically the standard first order implicit characteristic difference scheme, involving local iteration to obtain (roughly) second order accuracy in the discretization error. This scheme is modified to enable a convenient evaluation to the same order of accuracy of the "cross terms" in the perturbation equations.

2.4 *Application to a practical design case*

In this sub-section, the application of the numerical methods developed in this report to the originating problem: the design of a Laval nozzle with partially given contour, will be indicated. This problem resulted from the aerodynamical design for a nozzle variation mechanism as sketched in fig. 1.

The basic nozzle shape fixed by choosing a velocity distribution of the form (2.1.6) for the maximum design Mach number in the test section ($M_\infty = 1.29$). The other extreme of the position of the rotating block is given by the condition, that for subsonic test section Mach numbers, the nozzle must be in line with the test section walls. (We dispense with a discussion of the correction for boundary layer effects.) Choosing the centre of rotation for one of these positions, the intermediate positions of the block are then known from the kinematics of the mechanism, and a number of "pivotal" throat positions can be selected. The problem is then to design a number of Laval nozzle flows admitting this family of block contours as a flow boundary. The remainder of the ideal flow boundary is to be matched with sufficient accuracy by the flexible part of the contour, controlled by a number of jacks. This can be verified by the method described in sub-section 2.3.

The inclination $\theta$ of the block contour in one intermediate position is given in fig. 8.

Now, first, a velocity distribution on the axis is estimated from the given geometry, by choosing suitable values of the parameters in the expression (2.1.6). At least three conditions must be imposed:

1) the test section Mach number $M_\infty$ (or $\tau_\infty$) can be obtained from the tunnel height/throat height ratio by one dimensional considerations (in this case $M_\infty = 1,20$);

2) the location of the sonic point at the axis and the velocity gradient at this point can be estimated using, say, Sauer's approximation, from the throat curvature;
3) the rate of convergence of the velocity distribution to the asymptotic value downstream must be sufficiently fast to obtain a negligible deviation from flow uniformity at the entrance of the test section. This can be ensured by prescribing that at a distance $H/\tan\beta_\infty$ (where $H$ is the test section half-height and $\beta_\infty$ denotes the Mach angle for $M_\infty$) upstream of the test section the velocity differs from its asymptotic value by less than a definite small fraction.

The expression (2.1.6) contains a sufficient number of parameters to accommodate these conditions. The estimate can further be improved by exploiting the corrections to Sauer's approximation which can be obtained from fig. 4.

The resulting velocity distribution can now be used as an initial condition in the Cauchy problem eq. (2.1.1) to obtain a flow boundary which serves as a first approximation to the given block contour. The result of this first approximation is given in fig. 8.

Now, the comparison of the first approximation and the prescribed boundary condition implies a criterion on the accuracy with which the given contour should be matched. In the practical design work, an envelope tolerance of $\pm$ .001 radians on the nozzle contour inclination with respect to an ideal flow boundary was taken to be admissable, the acceptable level of approximation to the boundary conditions was therefore taken to be 10% of this value. On this basis, it was found that the first approximation gave a satisfactory approximation to the boundary condition in the immediate neighbourhood of the throat for the design case under discussion. This made it possible to effect the necessary boundary correction by the use of the perturbation scheme described in sub-section 2.3 only. In more difficult situations, however, it might be necessary to use the much more laborious scheme developed in sub-section 2.2.

The differences in inclination and the distance between the contour of the first approximation and the prescribed block contour in the supersonic region are now used as initial conditions for the boundary perturbation problem as described in paragraph 2.3.2. This yields the velocity correction on the axis given in fig. 8. This function is then continued back to a zero correction further downstream, numerically smoothed and interpolated.

Finally, this velocity correction is added to the first estimate for the axial velocity distribution, and the result again used as an initial condition for the Cauchy problem eq. (2.1.1). This results in a corrected flow boundary given in fig. 8, which matches the block contour within a sufficient accuracy. At the same time, this corrected solution provides the continuation of the flow boundary to the test section, which must be approximated by the flexible part of the contour.

Making the usual assumptions for the boundary layer development (based on a two-dimensional calculation) and correcting for the weight of and aerodynamic loading on the flexible plate, it appears then technically feasible for the construction of the type sketched in fig. 1 to maintain the above mentioned envelope tolerance between the ideal ("corrected") flow boundary and the real plate contour. Roughly, in the Mach number interval $1 < M_\infty < 1{,}3$ a flow uniformity in the order of $\Delta M = \pm.005$ can then be expected.

## 3 References


[1] Barritt, M. M., Calculation of flexible wall shapes and preparation of control tapes for the Bedford 8 ft × 8 ft wind tunnel. RAE rep. MS 54 (1959).

[2] Busemann, A., Gasdynamik; in: Wien-Harms, Handbuch der Experimental Physik, vol 4 (1931).

[3] Cherry, T. M., Exact solutions for flow of a perfect gas in a two dimensional Laval nozzle. Proc. Roy. Soc. A 203 pp 551–571 (1950). cf. art. F 9 in: W. R. Sears (ed.) General theory of high speed aerodynamics Princeton, (1954).

[4] van Dyke, M. D., The blunt body problem: review and extensions, J.A.S. vol 25 no. 8 p. 485 (1958).

[5] Frankl, F. I. Untersuchungen auf dem Gebiete der schnallnahe Strömungen. ZAMM vol 41, nr. 9 (1961).

[6] Friedrichs K. O., et al., Theoretical studies on the flow through nozzles and related problems. AMG-NYU rep. no. 43 (1944).

[7] Garabedian, P. R., Stability of Cauchy's problem in space for analytic systems of arbitrary type. Journ. Math. Mech., vol. 9 no. 6 (1960).

[8] Hall, I. M. and Sutton, E. P., Transonic flow in ducts and nozzles, a survey, in: Oswatitsch, K. (ed.), Symposium Transsonicum, Springer (1964).

[9] Hamming, R. W., Stable predictor-corrector methods for ordinary differential equations. Journ. ACM vol. 6 nr. 1 pp 37–47 (1959).

[10] Harker, K. J. and Llacer, L., Conditions for the solubility of an elliptic difference equation as an initial value problem. Quart. Appl. Math. vol. 21 no. 3 pp. 223–234 (1963).

[11] Holt, M., The design of plane and axisymmetric nozzles by the method of integral relations; in: Oswatitsch, K. (ed.), Symposium Transsonicum, Springer (1964).

[12] John, F., Continuous dependence on data for solutions of partial differential equations with a prescribed bound. Comm. Pure and Appl. Math., vol. 13 pp. 551–585 (1960).

[13] Lighthill, M. J., The hodograph transformation in transonic flow, I. Symmetric channels. Proc. Roy. Soc. A 191, pp. 323–341 (1947).

[14] Nieuwland, G. Y., The computation by Lighthill's method of transonic potential flow around a family of quasi-elliptical aerofoils. NLR TR T. 83 (1964).

[15] Richtmyer, R. D., Power series solutions, by machine, of a non-linear problem in two-dimensional fluid flow. Annals New York Ac. Sci., vol. 86, pp. 828–843 (1960).

[16] Sauer, R., General characteristics of the flow through nozzles at near critical speeds. NACA TM 1147 (1947).

[17] Tsien, H. S., The Poincaré-Lighthill-Kuo method. Advances in Appl. Mech., vol. IV New York (1956).

[18] Vaglio-Laurin, R., On the PLK-method and the supersonic blunt body problem. J.A.S. vol. 29 no. 2 p. 185 (1962.)

# APPENDIX A

## The equations for plane compressible potential flow and associated perturbation equations

A 1 *The equations for plane potential flow*

A 1.1 In this report the equations for plane irrotational flow of an ideal gas obeying the isentropic pressure/density relation will be used. These will be written on a equi-potentialline/streamline coordinate system in the form:

$$\begin{aligned} P\tau &= \theta_\psi \\ Q\theta_\phi &= \tau_\psi \end{aligned} \qquad \text{(A 1.1)}$$

$$P = \frac{\frac{\gamma+1}{\gamma-1}\tau - 1}{2\tau(1-\tau)^{\gamma/(\gamma-1)}}$$

$$Q = \frac{2\tau}{(1-\tau)^{1/(\gamma-1)}}$$

Here the velocity parameter

$$\tau = (q/q_{\max})^2 \qquad \text{(A1.2)}$$

is used. The density speed relation reads

$$\rho = (1-\tau)^{1/(\gamma-1)}$$

and

$$M^2 = \frac{2}{\gamma-1}\,\frac{\tau}{1-\tau} \qquad \text{(A 1.3)}$$

A slightly modified form of (A 1.1) has been used for the computations in par. 2.2. The transformation back to the physical plane is obtained from the definitions of velocity potential and streamfunction:

$$x+iy = \int e^{i\theta}\left\{\frac{d\phi}{\tau^{\frac{1}{2}}} + \frac{i d\psi}{\tau^{\frac{1}{2}}(1-\tau)^{1/(\gamma-1)}}\right\} \qquad \text{(A 1.4)}$$

A 1.2 Alternatively, these equations will for supersonic flow be written on a characteristics coordinate system. The two families of characteristic curves $(\xi, \eta)$ will be oriented such that the positive directions enclose angles $\pm\beta$ with the velocity vector, where

$$\mathrm{tg}^2\beta = \frac{1}{M^2-1} \qquad \text{(A 1.5)}$$

Then the equations (A 1.1) reduce to a system of two ordinary differential equations, which using now $M$ and $\theta$ as dependent variables read:

$$\begin{aligned} M_\xi &= f(M)\theta_\xi \\ M_\eta &= -f(M)\theta_\eta \end{aligned} \qquad \text{(A 1.6)}$$

$$f(M) = \frac{M\left(1+\frac{\gamma-1}{2}M^2\right)}{(M^2-1)^{\frac{1}{2}}}$$

A 2 *Perturbation problem for plane compressible potential flow*

A 2.1 Consider a one parameter family of solutions of eq (A 1.1):

$$\begin{aligned} \tau &= \tau(\phi, \psi; \alpha) \\ \theta &= \theta(\phi, \psi; \alpha) \end{aligned} \qquad \text{(A 2.1)}$$

depending analytically on a parameter $\alpha$.

Taking two solutions for values $\alpha$ and $\alpha'$ of the parameter and expanding the difference in powers of $\alpha' - \alpha = \varepsilon$, it follows

$$\begin{aligned} \tau' &= \tau + \varepsilon\tau^{(1)} + 0(\varepsilon^2) \\ \theta' &= \theta + \varepsilon\theta^{(1)} + 0(\varepsilon^2) \end{aligned} \qquad \text{(A 2.2)}$$

Substituting in (A 1.1), the equations for the first order perturbation quantities read:

$$\begin{aligned} \tau_\phi^{(1)} &= \frac{1}{P}\,\theta_\psi^{(1)} + \left(\frac{1}{P}\right)_\tau \cdot \theta_\psi \cdot \tau^{(1)} \\ \tau_\psi^{(1)} &= Q\theta_\phi^{(1)} + Q_\tau \cdot \theta_\phi \cdot \tau^{(1)} \end{aligned} \qquad \text{(A 2.3)}$$

and analogous equations for the higher order systems can be found.

Now note, that $\frac{1}{P}$ is singular on the sonic line $\tau = \frac{\gamma-1}{\gamma+1}$, correspondingly for a regular solution of eq (A 1.1), $\theta_\psi = 0$ on this curve. However, it is clear that in general, a solution of the perturbation equations (A 2.3) will not approximate to the first order the values of $\tau'-\tau$, $\theta'-\theta$ in the neighbourhood of the singular curve, nor can the higher order terms in the expansion in $\varepsilon$ be expected to converge in this region.

The PLK technique (ref. 17) presents a method to regularize these singular perturbation problems and to construct a uniformly valid approximation. The application in the present mathematical context (perturbation of a Cauchy problem involving a transition line) has been suggested by Vaglio-Laurin (ref. 18) in the blunt-body problem.

A 2.2 In this paragraph, uniformly valid first order perturbation equations will be derived, using the PLK-technique.

Again, consider two solutions for different values of the parameter $\alpha$, where the variables (including the coordinates) of the second solution are indicated by primes:

$$\begin{aligned} \tau &= \tau(\phi, \psi; \alpha) \qquad & \tau' &= \tau'(\phi', \psi'; \alpha') \\ \theta &= \theta(\phi, \psi; \alpha) \qquad & \theta' &= \theta'(\phi', \psi'; \alpha') \end{aligned} \tag{A 2.4}$$

In the PLK-technique a mapping is interposed between the $(\phi, \psi)$ – into the $(\phi', \psi')$ – coordinates, which is one to one, differentiable and analytically dependent on the parameter $\alpha$:

$$\begin{aligned} \phi' &= \phi'(\phi, \psi; \alpha) \\ \psi' &= \psi'(\phi, \psi; \alpha) \end{aligned} \tag{A 2.5}$$

Differentiation in the two coordinate systems is then connected by the relations:

$$\begin{aligned} \frac{\delta}{\delta\phi'} &= \frac{1}{J}\left(\psi'_\psi \frac{\delta}{\delta\phi} - \psi'_\phi \frac{\delta}{\delta\psi}\right) \\ \frac{\delta}{\delta\psi'} &= \frac{1}{J}\left(-\phi'_\psi \frac{\delta}{\delta\phi} + \phi'_\phi \frac{\delta}{\delta\psi}\right) \\ J &= \phi'_\phi \psi'_\psi - \phi'_\psi \psi'_\phi \end{aligned} \tag{A 2.6}$$

$J$ must be finite and non-zero.

Now the difference between the solutions (A 2.4) can be expanded in powers of $\varepsilon = \alpha' - \alpha$:

$$\begin{aligned} \tau'(\phi', \psi') &= \tau(\phi, \psi) + \varepsilon\tau^{(1)}(\phi, \psi) + 0(\varepsilon^2) \\ \theta'(\phi', \psi') &= \theta(\phi, \psi) + \varepsilon\theta^{(1)}(\phi, \psi) + 0(\varepsilon^2) \\ \phi' &= \phi \qquad + \varepsilon\phi^{(1)}(\phi, \psi) + 0(\varepsilon^2) \\ \psi' &= \psi \qquad + \varepsilon\psi^{(1)}(\phi, \psi) + 0(\varepsilon^2) \end{aligned} \tag{A 2.7}$$

Substituting in (A 1.1) and using (A 2.6), the equations for the first order quantities read:

$$\begin{aligned} \tau^{(1)}_\phi + \tau_\phi \psi^{(1)}_\psi - \tau_\psi \psi^{(1)}_\phi &= \frac{1}{P}\left[-\theta_\phi \phi^{(1)}_\psi + \theta_\psi \phi^{(1)}_\phi + \theta^{(1)}_\psi\right] + \left(\frac{1}{P}\right)_\tau \cdot \theta_\psi \tau^{(1)} \\ -\tau_\phi \phi^{(1)}_\psi + \tau_\psi \phi^{(1)}_\phi + \tau^{(1)}_\psi &= Q\left[\theta_\phi \psi^{(1)}_\psi - \theta_\psi \psi^{(1)}_\phi + \theta^{(1)}_\phi\right] + Q_\tau \cdot \theta_\phi \tau^{(1)} \end{aligned} \tag{A 2.8}$$

At this point the transformation (A 2.5) still has to be specified. It will be used to regularize the perturbation problem, a necessary condition for this is that the coefficient of $\frac{1}{P(\tau)}$ be zero on the sonic line $\tau = \frac{\gamma-1}{\gamma+1}$, where $P = 0$.

The simplest way to do this is to let this coefficient vanish identically, which can be accomplished by specifying the mapping (A 2.5) such that the other terms in the first of (A 2.8) are identically zero. Then this mapping is to be determined implicitly to the first order in $\varepsilon$ by the conditions:

$$\begin{aligned} \psi^{(1)} &\equiv 0 \\ \tau^{(1)} &\equiv 0 \end{aligned} \tag{A 2.9}$$

i.e. by mapping corresponding streamlines and isobars in the two fields onto each other.

It follows then from (A 2.8):

$$\begin{aligned} -\theta_\phi \cdot \phi^{(1)}_\psi + \theta_\psi \phi^{(1)}_\phi + \theta^{(1)}_\psi &= 0 \\ -\tau_\phi \cdot \phi^{(1)}_\psi + \tau_\psi \phi^{(1)}_\phi - Q\theta^{(1)}_\phi &= 0 \end{aligned} \tag{A 2.10}$$

For a known analytical solution $\tau(\phi, \psi)$, $\theta(\phi, \psi)$, (A 2.10) is a system of linear differential equations for the perturbation quantities $\theta^{(1)}$, $\phi^{(1)}$, with analytic, everywhere regular coefficients.

It remains to consider the connection of the displacement function $\phi^{(1)}$ and the angular perturbation function $\theta^{(1)}$, *which are defined in the* $(\phi, \psi)$ *system of the unperturbed (basis) field, with the physical quantities in the* perturbed field.

By (A 2.7) and (A 2.9), it follows that in the perturbed field at the point $\phi' = \phi + \varepsilon\phi^{(1)}$, $\psi' = \psi$ the flow quantities are to the first order in $\varepsilon$ given by $\tau' = \tau$, $\theta' = \theta + \varepsilon\theta^{(1)}$. Then, for the perturbation field quantities at the point $(\phi, \psi)$ it follows:

$$\begin{aligned} \tau' &= \tau - \varepsilon\tau_\phi \phi^{(1)} + 0(\varepsilon^2) \\ \theta' &= \theta + \varepsilon(\theta^{(1)} - \theta_\phi \cdot \phi^{(1)}) + 0(\varepsilon^2) \end{aligned} \tag{A 2.11}$$

Mapping back into the physical plane it follows:

$$z'(\phi, \psi) = z(\phi, \psi) + \varepsilon z^{(1)}(\phi, \psi) + 0(\varepsilon^2) \tag{A 2.12}$$

where the displacement in the physical plane

$$z^{(1)} = \int i\hat{\theta} \cdot e^{i\theta} \left\{ \frac{d\phi}{\tau^{\frac{1}{2}}} + \frac{i\, d\psi}{\tau^{\frac{1}{2}}(1-\tau)^{1/(\gamma-1)}} \right\} + \int \hat{\tau} \cdot e^{i\theta} \left\{ -\frac{d\phi}{2\tau^{\frac{3}{2}}} + i \frac{\frac{\gamma+1}{\gamma-1}\tau - 1}{2\tau^{\frac{3}{2}}(1-\tau)^{2/(\gamma-1)}}\, d\psi \right\} \tag{A 2.13}$$

and

$$\begin{aligned} \hat{\theta} &= \theta^{(1)} - \theta_\phi \cdot \phi^{(1)} \\ \hat{\tau} &= \quad -\tau_\phi \cdot \phi^{(1)} \end{aligned}$$

A slightly modified form of these equations is used in sub-section 2 to formulate an initial value perturbation problem.

A 3 *Characteristic perturbation problem for a plane supersonic potential flow*

In this section, the Mach number will be used to represent velocity magnitude in a plane, supersonic potential flow.

Consider a family of solutions of eqs (A 1.6) analytically dependent on a parameter $\alpha$

$$\begin{aligned} M &= M(\bar{x}; \alpha) \\ \theta &= \theta(\bar{x}; \alpha) \end{aligned} \tag{A 3.1}$$

where $\bar{x}$ is the position vector in the physical plane. The difference between two solutions from the family is expanded in powers of $\varepsilon = \alpha' - \alpha$:

$$\begin{aligned} M' &= M + \varepsilon M^{(1)} + 0(\varepsilon^2) \\ \theta' &= \theta + \varepsilon\theta^{(1)} + 0(\varepsilon^2) \end{aligned} \tag{A 3.2}$$

In the derivation of perturbation equations from (A 1.6) the dependence of the characteristic coordinates on the solution must be allowed for.

Writing

$$\beta' = \beta + \varepsilon\beta^{(1)} + 0(\varepsilon^2) \tag{A 3.3}$$

where $\beta$ is given by (A 1.5) and thus

$$\beta^{(1)} = -\frac{1}{\cos\beta} \frac{M^{(1)}}{M^2} \tag{A 3.4}$$

it follows to the first order in $\varepsilon$:

$$\begin{aligned} \frac{\delta}{\delta\xi'} &= \{1 + \varepsilon(\theta^{(1)} + \beta^{(1)}) \operatorname{cotg} 2\beta\} \frac{\delta}{\delta\xi} - \varepsilon \frac{\theta^{(1)} + \beta^{(1)}}{\sin 2\beta} \frac{\delta}{\delta\eta} \\ \frac{\delta}{\delta\eta'} &= \varepsilon \frac{\theta^{(1)} - \beta^{(1)}}{\sin 2\beta} \frac{\delta}{\delta\xi} + \{1 - \varepsilon(\theta^{(1)} - \beta^{(1)}) \operatorname{cotg} 2\beta)\} \frac{\delta}{\delta\eta} \end{aligned} \tag{A 3.5}$$

Then, substituting in (A 1.6) it follows to the first order:

$$\begin{aligned} \frac{\delta M^{(1)}}{\delta\xi} &= f(M) \frac{\delta\theta^{(1)}}{\delta\xi} + \frac{df}{dM} \cdot \frac{\delta\theta}{\delta\xi} M^{(1)} + (\theta^{(1)} + \beta^{(1)}) \frac{2}{\sin 2\beta} \frac{\delta M}{\delta\eta} \\ \frac{\delta M^{(1)}}{\delta\eta} &= -f(M) \frac{\delta\theta^{(1)}}{\delta\eta} - \frac{df}{dM} \frac{\delta\theta}{\delta\eta} M^{(1)} - (\theta^{(1)} - \beta^{(1)}) \frac{2}{\sin 2\beta} \frac{\delta M}{\delta\xi} \end{aligned} \tag{A 3.6}$$

*A mixed initial value-boundary value problem for this system is considered in par. 2.3.*

# APPENDIX B

## Numerical treatment of a Cauchy problem

B 1 *Introduction*

The necessity of an accurate design of a Laval nozzle for wind tunnel purposes has always been clear, and it was for this problem that one of the first approximate solutions of the non-linear equations for a supersonic potential flow was constructed by a characteristics method (Prandtl-Busemann (1927), cf. ref. 2). Since then, a large number of methods has come available; a survey with many interesting historical details has been given by Hall and Sutton (ref. 8).

Restricting attention to formulation of the design problem as an initial value problem, the work of Friedrichs et al. (ref. 6), Lighthill (ref. 13), Cherry (ref. 8), Barritt (ref. 1) and Holt (ref. 11) may be referred to. This formulation is largely equivalent to that of the well known "blunt body" problem, so that also the methods of van Dyke (ref. 4), Garabedian (ref. 7) and Richtmyer (ref. 15) could be used in this context. In fact, the numerical method used in this report, which was suggested by similar work at RAE by Barritt c.s. (ref. 1), is comparable to the approach of van Dyke (ref. 4).

The main difficulty in this method is its inherent numerical instability at least in the subsonic region of the flow field. For the present rather complicated high order numerical method there is no alternative to just living with this problem and judging the numerical results on their physical plausibility (cf. B 3). For a fundamental discussion of this problem refer to ref. 12 and for a complete numerical analysis of a linear model problem to the interesting work of Harker and Llacer, ref. 10.

B 2 *Some details of the numerical integration-scheme*

B 2.1 To simplify notations, the partial differential equation will be written:

$$Au = b \tag{B 2.1}$$

Here $A$ is a $2 \times 2$ matrix differential operator involving differentiation in $x$- and $y$-directions, and $u$ and $b$ formal vectors. The equations (2.1.1) and (2.2.1) can be written in this form, with $u \equiv \binom{\tau}{\theta}$ and $u \equiv \binom{\zeta(1)}{\theta(1)}$. The initial data $\bar{u}$ is given as an analytic function on $x = 0$. The scheme uses a rectangular domain of integration, which for a Laval nozzle flow is easily obtained by transforming to streamfunction/potential function coordinates. Then first the $x$-direction is discretised to permit numerical differentiation along lines $y = \text{const}$.

Using the differential equation (B 2.1), the $\frac{\delta}{\delta y}$-derivatives are found from the numerical values of the $\frac{\delta}{\delta x}$-derivatives obtained, and these in turn are integrated along lines $x = \text{const}$, using high order numerical integration formulas. No error analysis for the scheme is given, or would appear feasible. However, from general considerations it can be expected to be essentially unstable.

Typically, for the examples given in fig. 2 and 3, the steplength $\Delta x$ is $\frac{1}{40}$ of the interval. The number of steps in $y$-direction can be chosen at will, for the examples given this is also in the order of 40.

B 2.2 The differentiation formulas are the usual 7-point set, where the non-central formulae are employed towards the end of the interval. For the discretization used and the class of initial values typified by eq. (2.1.6), 7-point differentiation was experimentally found to be numerically optimal in comparison with the values of the analytical expression for the derivative.

The integration formulas are the predictor/corrector set given by Hamming (ref. 9):

predictor:

$$u_{n+1} = -9(u_n - u_{n-1}) + u_{n-2} + 6\Delta y(u'_n + u'_{n-1}) + \tfrac{1}{10}(\Delta y)^5 u^{(V)}$$

corrector: (B 2.2)

$$u_{n+1} = \tfrac{1}{8}\{9u_n - u_{n-2} + 3\Delta y(u'_{n+1} + 2u'_n - u'_{n-1})\} - \tfrac{1}{40}(\Delta y)^5 u^{(V)}$$

B 2.3 An integration step at the level $y_n = \text{const}$ to give $u_{n+1}$ then comprises the following cycle, when the quantities $u_{n-2}$, $u_{n-1}$, $u'_{n-1}$, $u_n$, $u'_n$ are stored (here the prime denotes $\frac{\delta}{\delta y}$, this operator indicating numerical differentiation):

1) predict $u_{n+1}^{(0)}$ by (B 2.2 a)
2) differentiate to give $\frac{\delta}{\delta x} u_{n+1}^{(0)}$
3) from the differential equation, estimate $u'^{(0)}_{n+1}$ from $\frac{\delta}{\delta x} u_{n+1}^{(0)}$
4) integrate to find $u_{n+1}^{(1)}$ by (B 2.2 b)

5) iteration: return $k$ times to 2) using $u_{n+1}^{(i+1)}$ instead of $u_{n+1}^{(i)}$
6) predict $u_{n+2}^{(0)}$ by (B 2.2 a)
etc.

The optimal number of iterations is best found experimentally, up to 5 times has been used. This procedure is in practice more convenient than to test for pre-fixed accuracy, because of the allowance that must be made for the increase of error with $y$.

B 2.4 The starting routine uses the symmetry of the solution with respect to the line $y=0$. First $u_{-1}, u'_{-1}, u_{-2}$ are estimated by linear extrapolation from the initial conditions. Then, using these values, $u_1$ and $u_2$ are found by the procedure described in B 2.3. At this point, the procedure is reversed to give improved values for $u_{-1}, u_{-2}$; this cycle can be run either for a fixed number of times or until $(u_2)$ and $(u_{-2})$ coincide up to some required accuracy.

B 2.5 For the Laval nozzle problem, the results found are again to be integrated to transform back to the physical plane (eqs. (2.1.4) and (2.26)). This has been done by Simpson's rule.

B 3 *Testing for numerical accuracy*

In the present approach, numerical accuracy can only be estimated in terms of the plausibility of the results obtained, this assessment requiring some amount of experimentation. The following series of tests can be devised to enable one to judge the validity of the results to some extent.

1) Smoothness of solution. The exact solution of the initial value problem is analytic for analytic initial conditions, then numerical results can only have any meaning as far as they are smooth. Smoothness of the results can be easily assessed by differencing along streamlines, and from this the maximum number of digits that can possibly be significant can be estimated on the basis of a statistical hypothesis. Tentatively, this can be regarded as the accuracy of the solution of the difference equations.
2) Decreasing step length. Instability of the integration scheme means that $\left(\text{for fixed ratio } \frac{\Delta y}{\Delta x}\right)$ the departure from the correct solution increases exponentially with $\frac{1}{\Delta y}$ when $\Delta y \to 0$. This does not mean that for given $\Delta y$, the solution of the difference equation might not yield a for practical purposes sufficiently accurate approximation. In fact, for a model problem (ref. 10) it has been shown that in part of the domain numerical accuracy may improve when decreasing step length, although it is expected to deteriorate asymptotically. Experience with the present scheme is in qualitative accord with this observation. Here $\Delta x$ was kept constant, but numerical accuracy was found consistently to improve (as far as could be judged) when decreasing $\Delta y$. The accuracy of the solution of the differential equation can be considered as indicated by the agreement of a numerical solution with a second one computed for say halved step lengths.
3) Some idea of the dependence of the results on the rounding of the initial data is obtained by changing the last significant digit in one or more of the discretized initial values. Variations on this theme were obtained by changing the number of times the starting cycles B 2.4 were run.

To give an indication of the accuracy actually attained in the computation, the accuracy of the computation of the Laval nozzle illustrated in fig. 1 was estimated to be in the order of 5 significant figures, perhaps slightly less near the top corners. The throat region depicted in fig. 2 was computed to at least 7 significant figures.

The most difficult regions to obtain numerical accuracy are encountered near the ends of the interval, where the non-central differentiation formulas must be used. This might be somewhat improved by deleting one ore more points at the end at every step, this could, however, not be tried out for reasons of storage limitations.

A direct indication of the error propagation through the process is obtained by numerically solving the first perturbation problem of par. 2.2.2, where the solution is known to be $\zeta^{(1)} \equiv C$, $\theta^{(1)} \equiv 0$. The results obtained are illustrated in fig. 7.

In this work, a computer using 13 digit arithmatic was used. The performance of the scheme may be expected to improve considerably in a practical sense, when double length arithmetic can be used.

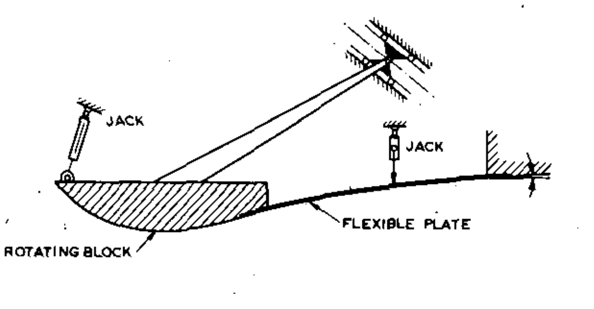


Fig. 1 Variable nozzle mechanism.

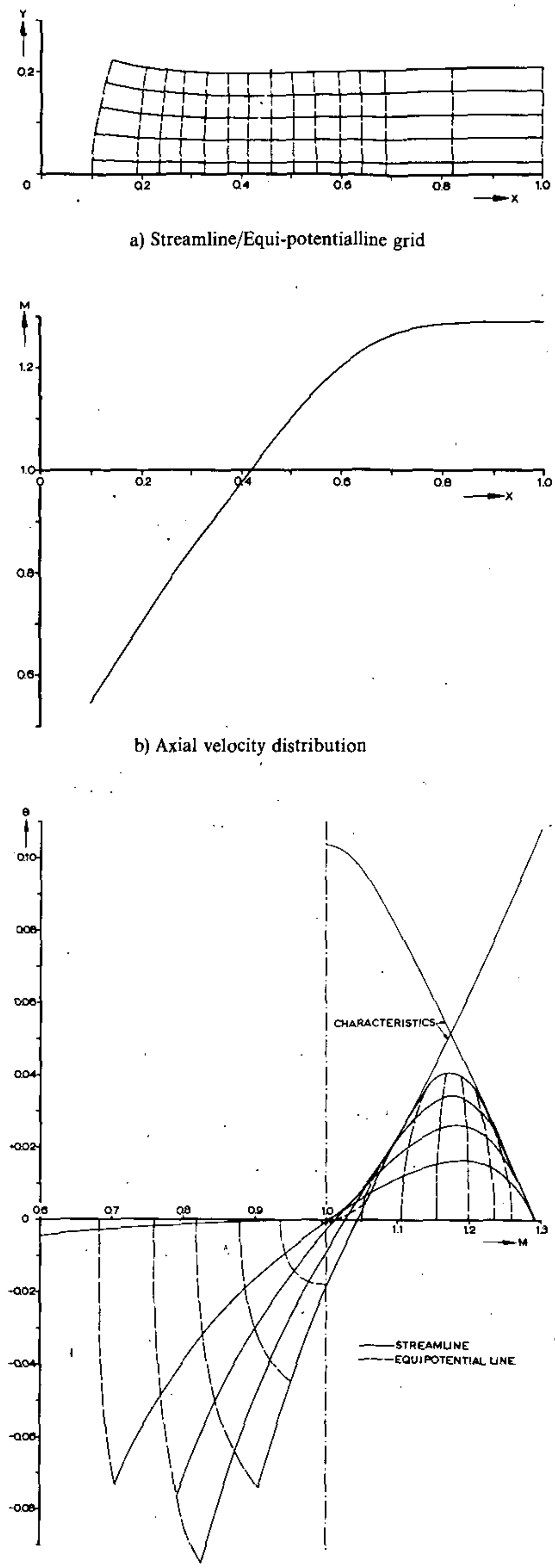


a) Streamline/Equi-potentialline grid



b) Axial velocity distribution



c) Hodograph

Fig. 2 Laval nozzle $M_{\infty} = 1.29$

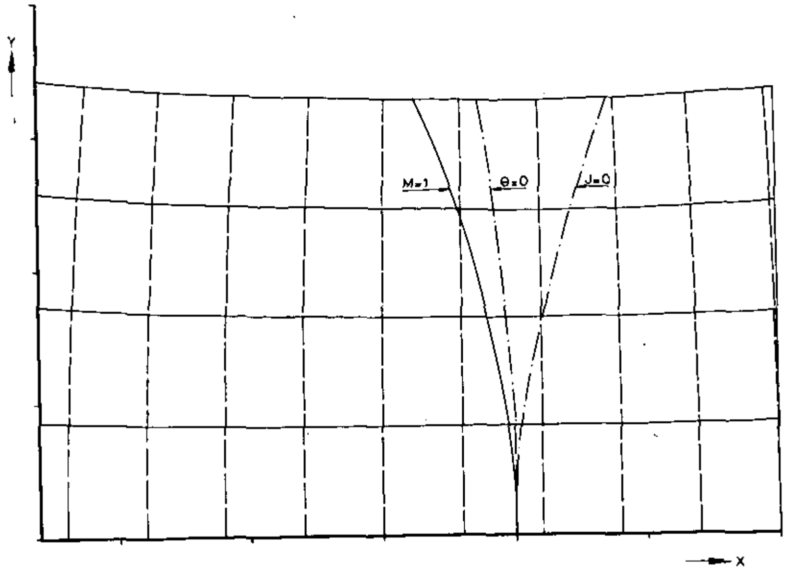


a) Streamline/equi-potentialline grid.

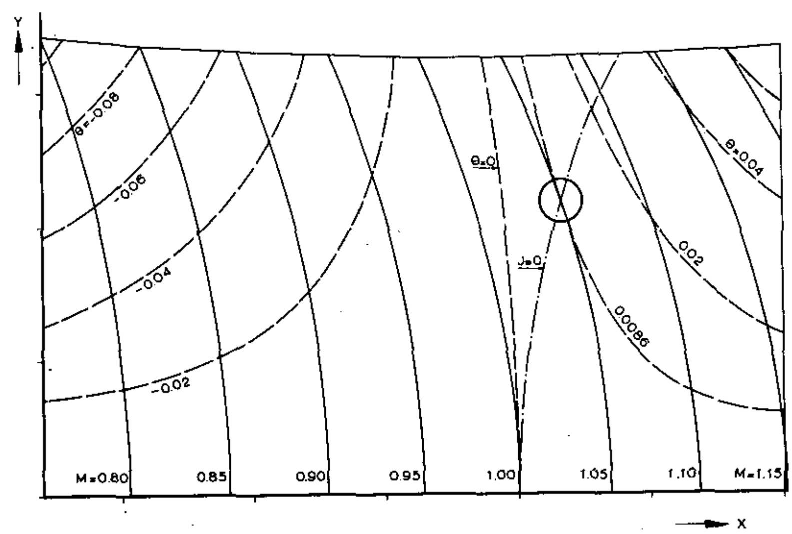


b) Isochores/isogonals

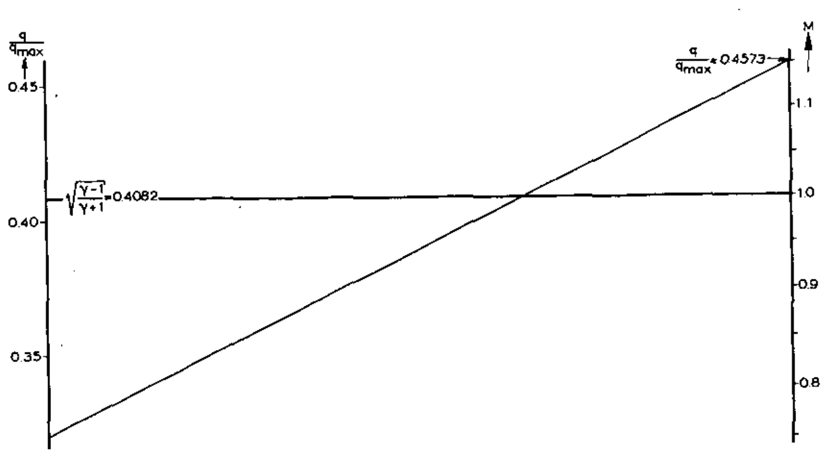


c) Axial velocity distribution

*Fig. 3 Laval nozzle, throat region.*

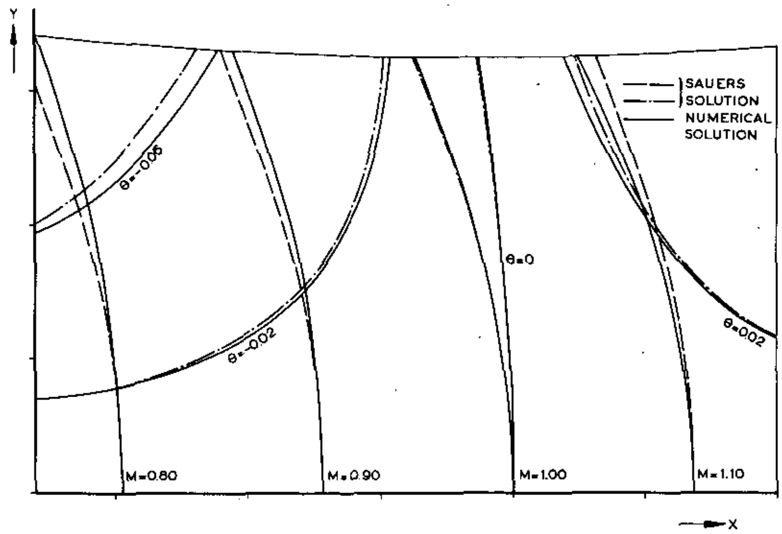


a) Comparison of isochores and isogonals

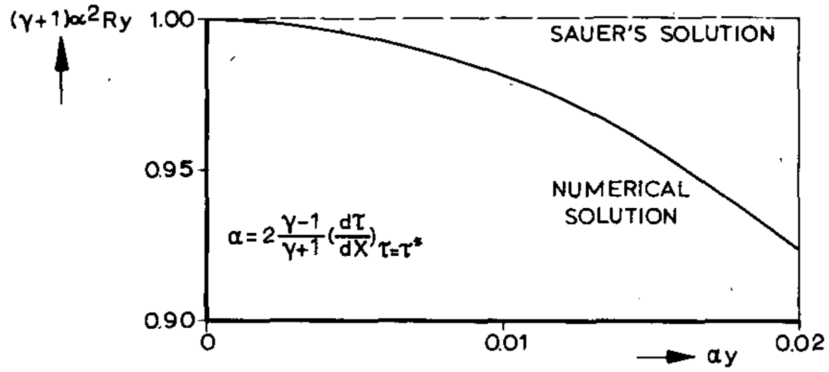


b) Comparison of throat curvature on $\theta = 0$

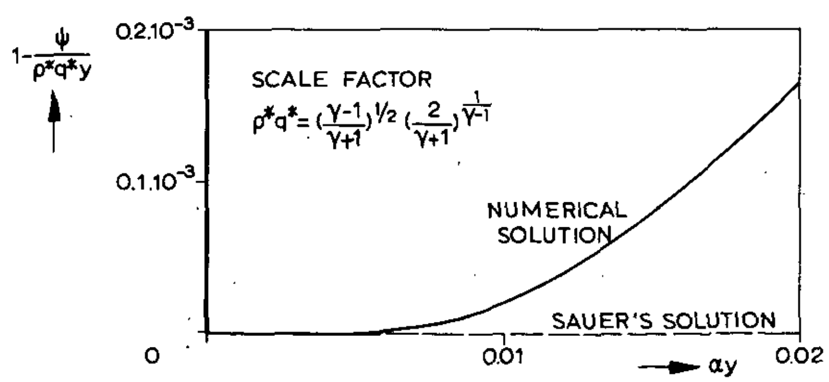


c) Comparison of streamfunction on $\theta = 0$

Fig. 4 Comparison of numerical solution with Sauer's approximation (ref. 16).

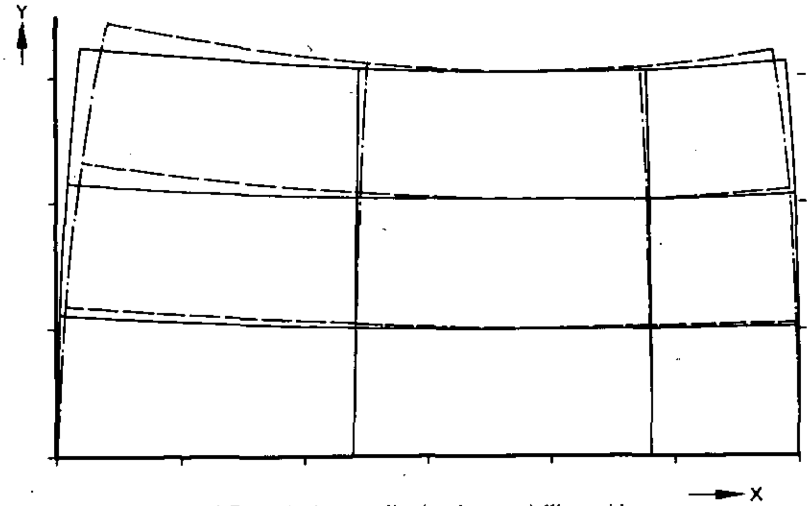


a) Perturbed streamline/equi-potentialline grid

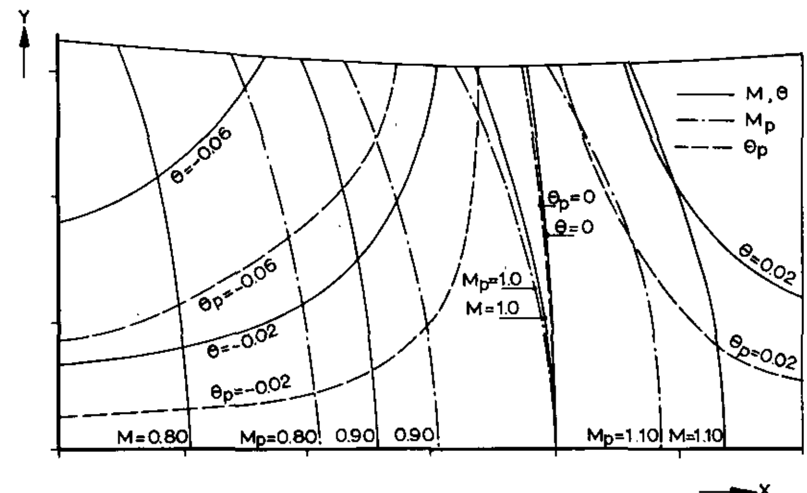


b) Perturbed isochores and isogonals

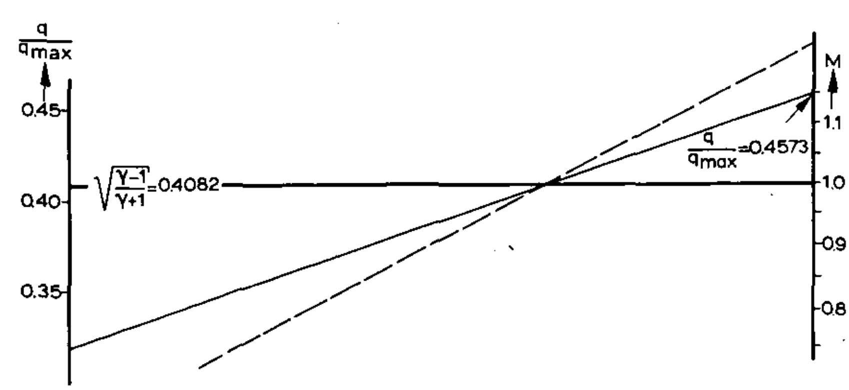


c) Perturbed velocity distribution.

Fig. 5 Initial value perturbation problem.

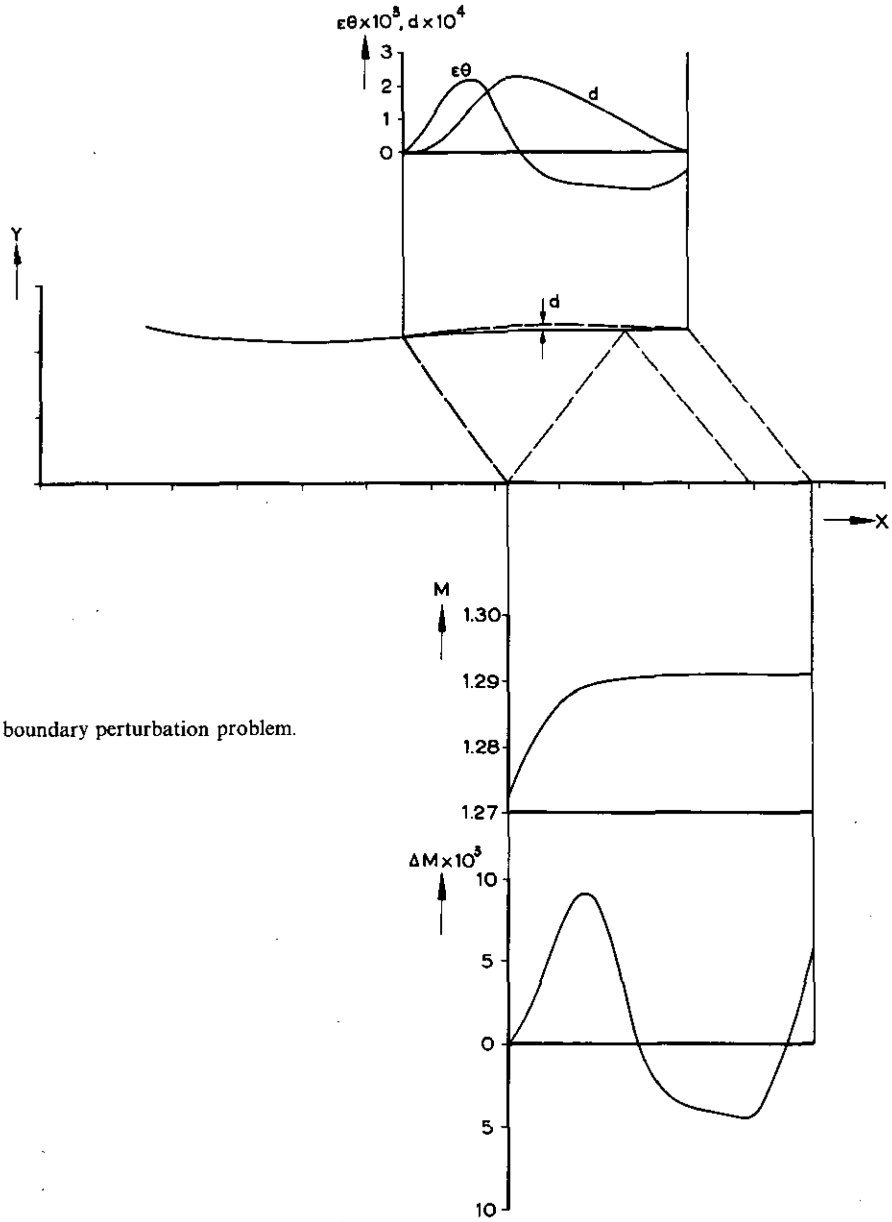


Fig. 6 Characteristic boundary perturbation problem.

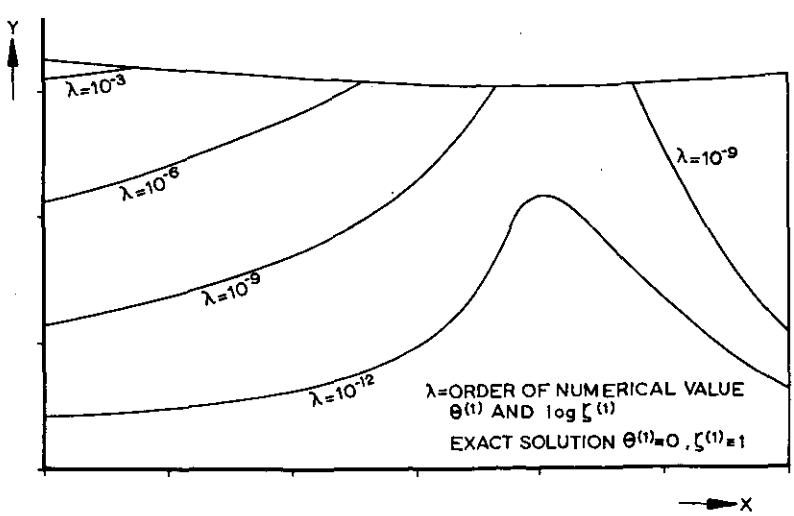


Fig. 7 Accuracy of numerical solution of initial value perturbation problem.

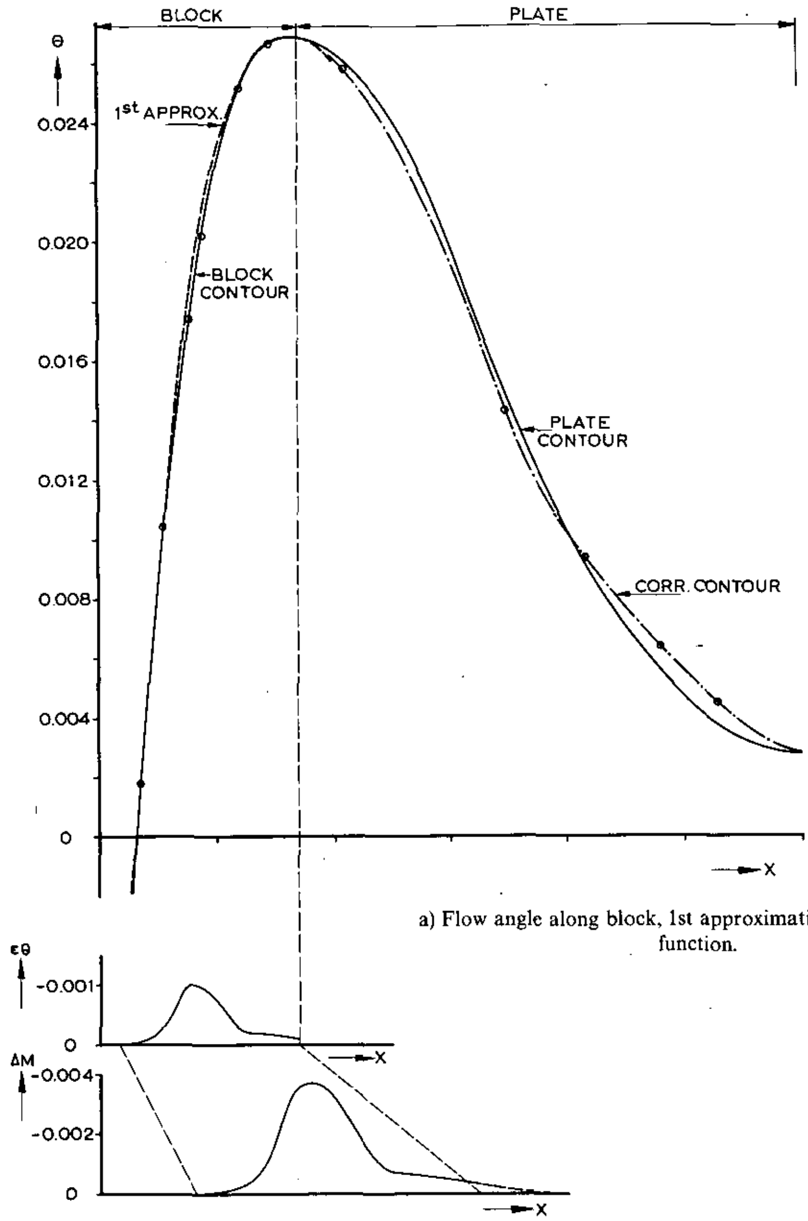


a) Flow angle along block, 1st approximation and corrected solution. function.

b) Boundary perturbation problem and velocity correction

Fig. 8 Boundary correction procedure.

C. C. L. Class. C 600–4

REPORT TR S. 613

# Fatigue tests with random and programmed load sequences, with and without ground-to-air cycles. A comparative study on full-scale wing center sections.

by

J. SCHIJVE, D. BROEK, P. DE RIJK, A. NEDERVEEN and P. J. SEVENHUYSEN

**Summary**

Fatigue tests were carried out on full-scale tension skins of a wing center section of 7075-T6 material. Variable-amplitude tests were carried out with the following load sequences: (a) random load, (b) program load, (c) random load with GTAC (ground-to-air cycles) and (d) program load with GTAC. Constant-amplitude tests were carried out with GTAC and gust amplitudes. The main objectives were to investigate (1) the equivalence of random and program loading, (2) the damaging effect of GTAC and (3) recommendations for full-scale testing. Results obtained are related to the indication of fatigue-critical components, fatigue lives, crack propagation, residual strength, $\Sigma n/N$-values, scatter and inspection methods. Relevant information of the literature is summarized. Recommendations for full-scale testing are concerned with the indication of the loads to be incorporated into the test, the assessment of load spectra, the highest loads to be applied, the smallest load fluctuations to be included, the load sequence to be adopted, the duration of the test, and experimental conditions.

**Contents** Page



This investigation has been performed partly under contract with the European Office of Aerospace Research of the United States Air Force and partly under contract with the Netherlands Aircraft Development Board (NIV).

**Nomenclature, symbols and units**

| | |
|---|---|
| Constant-amplitude test: | Fatigue test with a constant load amplitude and a constant mean load. |
| Program test (block test): | Fatigue test with a periodic variation of the load amplitude, which usually occurs in discrete steps. |
| Period: | In a program test: the period of the variable amplitude. The period is also used as a unit for the fatigue life in both the program tests and the random-load tests (see chapter 7). |
| Random-load test: | Fatigue test with an irregularly varying load. |
| Randomized-step test: | Program test with a randomized sequence of the load steps (cycles with the same load amplitude). |
| Variable-amplitude test: | Fatigue test with a varying load amplitude. Includes program tests and random-load tests. |

Random-load flight simulation }
Program-load flight simulation } see fig. 20
Simplified flight simulation }

| | |
|---|---|
| GTAC | — ground-to-air cycle(s) |
| $k$ | — rank number of load level |
| $K_t$ | — elastic stress concentration factor |
| $n$ | — number of applied cycles |
| $N$ | — fatigue life |
| $N_3$ | — fatigue life until a crack has grown to 3 mm length |
| NLR | — Nationaal Lucht- en Ruimtevaartlaboratorium (National Aeronautical and Astronautical Research Institute, Amsterdam) |
| Pr | — program loading |
| $P$ | — load |
| $P_a$ | — load amplitude |
| $P_m$ | — mean load |
| $P_u$ | — ultimate design load |
| R | — random load |
| $S$ | — stress |
| $S_a$ | — stress amplitude |
| $S_m$ | — mean stress |
| $S_u$ | — stress at $P_u$ |
| $t$ | — sheet thickness |
| $\sigma$ | — standard deviation |
| 1 mm | $= 10^{-3}$ meter $=0.04$ inch; 1 inch $=25.4$ mm |
| 1 kg/mm$^2$ | = 1,422 psi; 1000 psi = 0.703 kg/mm$^2$ |
| cpm | = cycles per minute |
| 1 kc | = 1 kilocycle = 1000 cycles. |

## 1 Introduction

At the present time it is generally recognized that full-scale testing is indispensable for the quantitative assessment of the fatigue properties of a new aircraft design. These properties include the indication of the fatigue critical components, the corresponding fatigue lives, crack propagation data, suitable inspection methods, residual strength, etc. Since full-scale testing of a prototype structure is an expensive method for acquiring such data, due consideration has to be given to the selection of the fatigue loads to be applied and the sequence of the loads in the test in order to arrive at accurate and reliable results.

One obvious approach is to adopt a complete simulation of the service loads regarding both the load magnitudes and sequences. Several problems have to be solved then and one should also consider the possibility of applying simplified loading programs. The present test series was primarily initiated to investigate the replacement of random service loadings by a simpler programmed load sequence. As a second objective the damaging effect of the ground-to-air cycle was studied; constant-amplitude tests allowed damage calculations to be made. The final aim was to arrive at recommendations concerning load sequences to be preferably adopted in full-scale tests on structures of new types of aircraft. The scope of the investigation is further explained in chapter 2. Descriptions of the experimental procedures and the test results are presented in chapters 3–8. Relevant information from the literature is discussed in chapters 9 and 10; the latter chapter also gives an analysis of the various aspects concerning the load sequences applied in full-scale tests. Chapter 11 summarizes the results and conclusions obtained. Special topics are dealt with in a number of Appendices.

Random load tests, program tests and constant-amplitude tests were performed on 13 full-scale tension skins of a wing center section of 7075-T6 material. Testing was started in January 1962 and completed in June 1965. The amount of detailed information on testing procedures and results is fairly large. The present report gives a summary of this information. The details are presented in a series of reports (refs 1–7) which, however, do not contain a thorough discussion of the test results.

*Acknowledgements:*

Ten tension skins were tested under contract with the European Office of Aerospace Research and three skins under contract with the Netherlands Aircraft Development Board (NIV).

During the investigation the authors were assisted by Messrs R. Dekker, H. H. Ruiter, H. Hultink and A. M. Otter, who were mainly in charge of inspections, repairs, strain measurements and maintenance of the equipment. The electronic part of the fatigue machine CARLA was designed by Messrs D. Bosman and A. Nauta of the Electronic Department of the NLR. The steel dummy structure was designed at the Fokker Factories, which also carried out the structural adaptation of the tension skins to the test set up. X-ray pictures were taken by the Röntgen Technische Dienst. The able assistance and the collaboration of all participants are gratefully acknowledged.

## 2 Scope of the investigation

The tension skin is sufficiently large (length 8.3 meters ~ 27 ft) to represent a structure with a number of different discontinuities from which fatigue cracks may start. The skin was loaded in tension as a part of a bent beam. The load sequences applied are shown in table 1.

TABLE 1

Survey of the load sequences

| *Test series* | *Load sequence* | *Number of tests* |
|---|---|---|
| a | Random (gust) | 2 |
| b | Programmed sequence | 2 |
| c | Random, GTAC added | 2 |
| d | Programmed sequence, GTAC added | 2 |
| e | Constant-amplitude, GTAC loading | 2 |
| f | Constant-amplitude, gust loading | 3 |

GTAC = ground-to-air cycle(s)

The load sequence in test series (a) and (c) was a simulation of a gust record obtained in flight. The gust load spectrum was the same in test series (a)–(d). The addition of the GTAC to the random gust sequence in test series (c) implied a flight by flight simulation in this test series. In test series (f) the mean load was the same as for the gust loads in test series (a)–(d). The three specimens of this test series were each loaded with a different load amplitude, allowing a part of the S–N curve to be determined.

The objectives of the investigation can be summarized as follows:

(1) To study the equivalence of random and programmed load sequences. Comparison of series (a) with (b) and (c) with (d).

(2) To study the damaging effect of the GTAC. Comparison of series (a) with (c) and (b) with (d).

(3) To compare the damaging effect of the GTAC in test series (c) and (d) with the calculated damage based on test series (e).

(4) To compare the results obtained in series (a)–(d) with the calculated ones based on test series (e) and (f).

The first objective was the prime reason for initiating the present program. The aim was to see whether the same components are fatigue critical and to compare the fatigue lives and crack propagation rates.

The ground-to-air cycle (GTAC) is generally suspected to be more damaging than predicted by the Palmgren-Miner rule. An inherent difficulty is the definition of the maximum load and the minimum load of the GTAC. The GTAC was a second object of main interest in the present test program.

In addition to the above objectives the following ones should also be mentioned:

(5) To acquire some information on several aspects related to full-scale tests, such as scatter, residual strength, inspection methods, structural features prone to fatigue.

(6) To analyze methods for full-scale testing and to arrive at recommendations for performing such tests.

## 3 The specimen

### 3.1 *General description of the specimen*

The tension skin of the center section of the F-27 aircraft was originally designed with 7075-T6 as a structural material. After a fatigue test on a prototype aircraft it was decided to replace this material by 2024-T3 and to increase the cross sectional area of the tension skin accordingly (ref. 8). This made available a number of tension skins of the former material already constructed.

The specimen essentially consists of the tension skin, the stringers and the lower spar caps of the wing center section. In the tests the remaining parts of the wing, i.e. the outer wings, the upper skin of the center section (compression skin), the ribs, and a part of the spars, were replaced by a steel dummy structure; see ref. 1 and fig. 1 of the present report.

The plan view of the structure is shown in fig. 3 and a photograph of a part of the structure is given in fig. 2. The stiffening of the skin consists of two relatively light spar caps and 11 stringers; see the cross section in fig. 3. Stringers 2 to 10 are extruded hat sections with a thickness of 1.6 mm. Stringers 1 and 11 are built up from an angle section and a Z-section, both with a thickness of 1.6 mm. The spar caps are angle sections with a thickness of 3.2 mm. The thickness of the skin is 2 mm. The cross sectional area of stringers 1 and 11 and the spar caps is slightly less than for the stringers 2 to 10. There is approximately 50% of the total cross section of the specimen in the stiffeners, including the spar caps, and 50% in the skin.

At rib 1040 there is a skin joint for manufacturing purposes, the stringers being continuous over this joint. At the joint the skin is reinforced with three thin doublers, see fig. 3, which are bonded to the skin. The stringers and the spar caps are riveted to the skin.

In both halves of the center sections there are two cut-outs with covers for access purposes. One cover is in the nacelle and the other one is situated between the fuselage and the nacelle. The skin around the cut-outs is considerably reinforced by bonding doubler plates around them. The reinforcement carries the load from the stringers 5, 6 and 7, which terminate at rib 2040. The covers also transmit part of the load.

In the fuselage and the nacelle area the skin of the specimen is protruding ahead of the front spar and behind the rear spar, where some open holes occur for structural elements, such as brackets for the joints to the fuselage and the undercarriage or for auxiliary equipment.

### 3.2 *Locations of cracks*

During the tests cracks were detected at various locations all over the specimen as indicated in fig. 3. They can be grouped into three categories:

*a* Cracks at the ends of adhesive-bonded doublers (4 types of cracks)

*b* Rivet holes and bolt holes (10 types of cracks)

*c* Open holes and sheet edges (16 types of cracks)

The cracks are indicated by a letter (a, b or c) and a number. The letter refers to the above categories and the number is used for a further subdivision. Some additional information on the structure at the locations of the cracks has been summarized in Appendix A.

Two pictures of cracks are shown in figs. 4 and 5.

## 4 Test set up

The tension skin is mounted on a welded steel dummy structure, which represents the remainder of the center section of the wing and both outer wings; see figs. 1 and 6. At the ends of the specimen (station 4155) the connection with the dummy structure occurs via two aluminum alloy coupling plates, thickness 5 mm, in view of a smooth transmission of the load into the skin. Further connections between the specimen and the dummy structure occur at the ribs by bolts. The rib spacing is approximately 500 mm (20″).

The specimen and the dummy structure are loaded in four point bending, giving a distribution of the bending moment in reasonable agreement with the distribution for the aircraft. Also the stress distribution in the skin compares favorably with that measured on the F-27 prototypes; see ref. 3.

A schematic picture of the loading system is shown in fig. 6. The load is applied by a single hydraulic jack. A strain gage dynamometer between the jack and the test rig is used for recording the loading history and for providing a feedback signal for load monitoring. The apparatus can simulate any prescribed load sequence by means of 32 load levels, preset by 32 potentiometers. Each load level has a code number. The load history is punched in a paper tape as a sequence of code numbers in binary digits. The output from a selected potentiometer is compared with the feedback signal of the dynamometer. As soon as a zero difference between the two is obtained, the zero detector gives a signal to the pump for reversing the oil flow and another signal to the tape reader for selecting the following load level punched in the tape. This procedure is continuously repeated. The loading rate is constant for both loading and unloading, leading to a triangular wave form. Although there have been some teething troubles with the fatigue machine (ref. 1) its operation during the test program was fully satisfactory. The accuracy of reproducing load levels is considered to be excellent. Some information on the measurement of the fatigue loads and the accuracy is given in Appendix B.

An electronic compensation partly eliminated the overshoot. The maximum stroke of the hydraulic jack in the tests was 26 cm. Negative loads were applied by the weight of the steel dummy structure and by two small constant-load jacks (0.8 ton each). The maximum load exerted by the hydraulic jack was about 34 tons, corresponding to an oil pressure of 160 kg/cm$^2$. The delivery of the pump was the same throughout the investigation (60 liters per minute), involving frequencies in the program tests ranging from 6 to 45 cycles per minute, depending on the load amplitude.

A more elaborate description of the test set up including the hydraulic system was given in ref. 1 and the electronic part of the fatigue machine was described in ref. 10.

## 5 Testing procedures

*In each test the following phases were carried out:* calibration of the dynamometer, bonding of the strain gages to the specimen, mounting of the specimen on the test rig, static strain measurements, fatigue testing with inspections for cracks and repairs if necessary, dismounting of the specimen at the end of the test. During the tests the load was recorded continuously. For most specimens the test was stopped when repairing of cracks was no longer feasible. One crack was then allowed to grow until final failure of the complete specimen. In some tests final failure did not occur and in some other tests final failure came unexpectedly, see table 2.

The tests were carried out in the day-time only. The specimens were continuously inspected for cracks by two inspectors during the time that the test was running. Due to the "breathing" of the cracks they are much more easily detected. A low-power magnifying glass and a light source were used. Many cracks were detected at a length of 2 to 6mm (0.08 to 0.24 inch). The outside of the specimen was examined while the inspector was standing on a gallery, partly removed in fig. 1. For the inspection of the inside of the specimen two platforms, one being visible in fig. 1, were attached to the lower side of the test rig and the inspectors standing on the platforms were moving up and down with the test rig. (This was not considered to be an inconvenience; no airsickness observed in the random tests).

Some types of cracks, which were inaccessible to visual inspections, were found by taking X-ray pictures. The sensitivity of this method appeared to be much higher if a tensile stress was present in the structure. Through-cracks were better indicated than part-through cracks. Moreover, the possible locations of the crack had to be accurately known for a correct positioning of the X-ray tube. Some more details of the X-ray experience are given in Appendix C. Finding of the important crack al in the skin at the tips of the finger plates fully relied on the X-ray inspections.

Several cracks were allowed to grow to a certain length before a repair was made. This was done to obtain some data on crack propagation rates. On the other hand, extensive repairs had to be avoided in view of the possible influence on the stress distribution. Therefore many uninteresting cracks were repaired immediately after detection. The simplest repair, which was frequently applied, consisted of drilling stop holes at the ends of the crack and filling the holes with hard driven rivets. If the latter was impossible the hole was expanded 3 to 5% by special means to introduce favourable residual stresses.

For the somewhat larger cracks it was necessary to rivet strap plates over the cracks. If possible, the repairs were made symmetrically to avoid eccentricities. The strap plates were relatively thin and the ends were staggered in order to avoid as much as possible an increase of the local stiffness and to relieve the end rivets. If repairs had to be made early in a fatigue test cracks emanating from the end rivets occurred in several cases. The repairs were made by the same people who inspected the structure for cracks.

## 6 Strain measurements

Strain measurements were made for two purposes, namely, (1) to determine the stress distribution in the structure and (2) to verify whether the same stresses were present in the 13 tension skins tested. The results of the strain measurements were given in full detail in refs. 3 and 7. A brief summary has been presented in Appendix D.

The stresses extrapolated to ultimate design load ($P_u$) were in the order of 40 kg/mm$^2$ (57 ksi) near the finger plates and in the order of 25 to 35 kg/mm$^2$ (35 to 50 ksi) for various other locations at which cracks had been found.

The scatter of the strains as measured on the 13 tension skins was small, which allowed the conclusion that the loading of the skins was well reproduced in all tests.

Dynamic strain measurements indicated 3% higher stresses than the corresponding static values. This was due to a small overshoot induced by the test rig. In view of the comparative use that is made of the fatigue loads and the fatigue lives, no corrections will be made for this overshoot.

## 7 The load sequences in the random and the program tests

The load sequences are based on a strain-gage record of the bending moment at the root of a wing of a large aircraft flying in turbulent air. The record covered 96 minutes of flying and showed the typical features of random gust loads, as well as the first wing bending frequency, see fig. 7. Although the record, indicated as tape A1, contained a large number of gust loads, it is clear that 96 minutes of flying cannot be representative of a complete gust spectrum. Other tapes B1, C1, D1 and E1 were obtained from tape A1 by increasing the maximum peak loads by different amounts (highly non-linear amplification). Subsequently five tapes A2 to E2 were produced by reducing all load peaks of the tapes A1 to E1 to a ratio of 75 per cent (linear amplification). From the ten tapes a sequence was composed consisting of $49 \times A1$, $14 \times B1$, $4 \times C1$, $2 \times D1$, $1 \times E1$ and the same numbers of tapes A2 to E2, making a total of 140 tapes. The procedure was the same as adopted by Lockheed in a test program on small sheet specimens (ref. 11)

In the random-load tests the load sequence of the gust record is exactly simulated. Since the number of load levels is limited to 32, all peaks, maxima and minima had to shift a little bit to coincide with the nearest level of the 32 available ones. For practical reasons 31 load levels were used, which are indicated by the rank numbers $k = 1, 2, 3 \ldots 30, 31$ in increasing order of magnitude. For the mean load ($P_m \sim 25\%\, P_u$) $k = 16$, whereas the 30 other load levels are grouped symmetrically around this mean load. The 15 corresponding load amplitudes have been plotted in the load spectrum in fig. 9. Numerical data on the numbers of occurrences of the load levels for each tape and the tape sequence are given in Appendix E. In this Appendix a statistical analysis of the random load is also presented. For deriving the gust load spectrum in fig. 9, the mean-crossing peak count method was used, where between two successive mean crossings only one peak, the most extreme peak, is counted. The method and four other counting methods are further explained in Appendix E, which also gives a comparison of the counting results. A sample of the load recording during a random test is shown in fig. 8.

In accordance with the contract for the tests a severe gust spectrum had to be used, so that the slope of the spectrum in fig. 9 is fairly high. For the present purpose it was considered unrealistic to include very high and infrequent loads. Therefore a truncation was made to the spectrum, see fig. 9. The maximum load amplitude, $P_a$, is $39.5\%\, P_u$, leading to a highest load of $65.2\%\, P_u$ and a lowest load of $-13.8\%\, P_u$.

In the program tests the load amplitudes were applied in an increasing-decreasing order of succession in each period. For each load cycle the maximum load was applied first which was then followed by the minimum load. A sample of a load record is shown in fig. 10. The number of cycles in one period was the same as the average number for the random tapes as counted by the mean-crossing-peak-count method, viz. 3865 cycles. Consequently, the frequency of the highest amplitudes was lower than once per period. Three different tapes P1, P2 and P3 were made, which differed for the highest amplitudes only and which were combined such that fig. 9 applies to both the random and the program tests. Moreover, if it was assumed that the mean-crossing-peak-count method is the correct counting method, one program tape (containing one program period) represents one random tape. So the fatigue life in all types of testing can be compared on the basis of numbers of tapes or test periods. Numerical data on the numbers of occurrences of the load amplitudes for the three different tapes and the tape sequence are given in Appendix E.

The mean-crossing peak count method ignores a number of peak loads of the random loads. From all peak loads applied in the random tests only 69.2% were counted with this method and were applied in the program tests.

For the random tests with ground-to-air cycles (GTAC) the minimum load of these cycles was $-7\%\, P_u$ ($k = 4$). Some touch-down load variations were added. Further it was assumed that one of two flights was a smooth flight without gusts. In other words GTAC were applied in pairs, as indicated in fig. 11. Such pairs were inserted in the random-load tapes at regular intervals. The average number of gust cycles (according to the mean-crossing-peak-count method) was 24 per interval. Apart from the GTAC the load sequence remained exactly the same.

In the program tests with GTAC the latter cycles were inserted as six batches of 56 cycles each (see fig. 12). The minimum load is the same as in the random tests with GTAC, but the touch-down loads are omitted. The maximum load is the load that on the average was exceeded once per flight in the random tests with GTAC. A more refined method of inserting GTAC could have been used, but it was the aim to compare a random test with a "simple" program test rather than comparing a complicated random test with a complicated program test.

## 8 Test results

The results were compiled in all details in refs. 4, 6 and 7. Results from the first 6 of the 13 tests were already summarized in ref. 13. In this chapter a summary of the main results is given concerning fatigue lives, crack propagation and residual strenght. A discussion of the results is presented in chapters 9–11, apart from a few special aspects which are briefly commented upon in this chapter (sections 8.5 and 8.6). This concerns structual design features sensitive to fatigue and scatter.

### 8.1 *The fatigue lives at the finger tips*

The crack which appeared to be critical in most tests occured in the skin at the tips of the finger plates bonded to the skin (crack type al, fig. 4). The notch effect of the finger plate is not considered as being severe (local increase of skin thickness from 2 mm to 2.6 mm and secondary bending due to the increase of thickness). However, the stress level at the finger plates was relatively high. The crack was detected by taking X-ray pictures and its growth was subsequently recorded on X-ray pictures. The number of finger tips in one specimen is 80 (see fig. 3). A statistical evaluation of the fatigue life data is possible for 8 out of the 13 specimens.

This is done in Appendix F, whereas some brief comments on the results are given in section 8.6.

Sufficient data on the propagation of crack al were available to assess the fatigue life the structure would have had if no repairs at the finger tips had been made. The results and some other data are compiled in table 2. These fatigue lives were used for comparative purposes and damage calculations.

A comparison between the fatigue lives under random and programmed load sequences is made in table 3, which shows that the fatigue life under program loading was 10 to 30 % larger than under random loading.

The effect of the addition of GTAC is illustrated by table 4, which shows that the fatigue life is reduced to 40–50 %. The reduction is only slightly larger than the prediction based on the linear cumulative damage rule.

The fatigue lives for the constant-amplitude tests have been plotted in fig. 13. A curve was drawn through the data points for the three gust amplitudes. The two fatigue lives for the GTAC tests are slightly above this curve, which should be attributed to the lower mean load. Damage calculations for the variable-amplitude tests were made making use of the fatigue curve of fig. 13 (ref. 7). The damage increments for the 15 load amplitudes of the program tests in 140 test periods have also been plotted in fig. 13. The figure shows that the major part of the damage (according to the linear damage rule) is done by amplitudes for which the fatigue curve needs no extrapolation. Since the load spectrum for the random tests is the same as for the program tests (according to the mean-crossing peak count method) the right-hand graph of fig. 13 also applies to the random loading. The results of the calculations of $\Sigma\, n/N$ are given in table 6, which shows values from 1.3 to 1.8 (crack al).

8.2 *The fatigue lives for the other types of cracks*

A survey of the frequency of occurrence of almost all cracks is given in table 5. The table also gives the number of possible cracks in one specimen. For the majority of cracks this number is 2 or 4 (Port and Starboard wing, fore and aft). The fatigue lives of all these cracks were given in refs. 4, 6 and 7. The presentation here will be largely restricted to a summary of the conclusions.

With respect to the comparison of the random and the program loading the results are less systematic than for the cracks at the finger tips. This was thought to be due to the lower possible number of similar cracks in one specimen and probably a somewhat larger scatter. Nevertheless, the average trend appeared to be the same, viz. a slightly larger life under program loading than for random loading, both for tests without and with GTAC. Also with respect to the effect of the GTAC a reduction of about 50 % of the fatigue life was obtained by adding the GTAC.

A remarkable result of table 5 is that there are several cracks which occur in most if not all constant-amplitude tests, whereas they do not occur in the variable-amplitude tests. This concerns cracks starting from rivet or bolt holes and open holes or sheet edges (category b, cracks b9-b12 and category c, cracks c10-c15 and c19). This results is commented upon in chapter 10.

Another noteworthy result of table 5 is that some technically important cracks in the skin (cracks a2, b2, b3, b5, b6 and b10) were found in the variable-amplitude tests, but in a minority of these tests only.

Crack b8, growing invisibly under the strap plates of the skin joint at Sta 1040, was found for the first time in specimen 11 near the end of the test at a length of 30 cm. X-ray inspections on specimens 12 and 13 indicated numerous cracks of this type, originating earlier than the cracks at the finger tips but growing much slower (ref. 7). It may certainly be expected that this crack occurred in the variable-amplitude tests as well, but due to its slow growth it did not become catastrophic and was therefore never found.

Cracks b2 and b3 occurring in the skin at the end rivets of stringers 1 and 11, were found almost to the maximum possible number in the constant-amplitude tests. In the variable-amplitude tests these cracks were rarely found. Nevertheless local dissectioning of the skin of specimen 3 after the test indicated crack nuclei at all possible locations.

There is only one crack which turned up more or less regularly in the variable-amplitude tests and almost not in the constant-amplitude tests, viz. crack type a3.

Calculations of $\Sigma\, n/N$-values could be made only for those cracks for which sufficient data in both the variable-amplitude and the constant-amplitude tests were available. The results for seven different tapes of cracks have been presented in table 6. For the $N$-values minimum lives were taken and due to the somewhat larger scatter the fatigue curves were less accurate than for the finger tip cracks (al). Consequently, also the $\Sigma\, n/N$-values will have a lower accuracy. Nevertheless, it seems justified to accept the following trends of the results: (1) The $\Sigma\, n/N$-values are clearly beyond one. (2) The values for the random and program tests with GTAC are only slightly smaller than for the same tests without GTAC. (3) The $\Sigma\, n/N$ values are higher than for crack type al.

For those cracks that occured in the constant-amplitude tests and not or almost not in the variable-amplitude tests it may be said that the $\Sigma\, n/N$-values would generally have been larger than about 2.5, the average of table 6. The $N$-values were of the same order of magnitude as for the cracks in table 6 and the fatigue lives in the variable-amplitude tests were larger. For crack a3, occurring in the variable-amplitude tests only, a smaller value may be expected.

## 8.3 *Crack propagation*

Systematic measurements of the crack propagation were available for crack type a1, except for the two random tests and one program test. For other crack locations propagation data were obtained (ref. 5), but these results were too scanty to allow comparisons to be made between different load sequences.

At the finger tips the crack propagation data were mainly obtained from the X-ray pictures. The propagation at the individual finger tips was sometimes fairly irregular due to several causes, viz: (1) It was generally experienced that crack growth predominantly occurred at the higher loads, the more so if the crack was larger. In the variable-amplitude tests the highest loads could be different from test period to test period, which caused a dependence of the crack propagation on the type of loading tape. (2) Sometimes more than one crack nucleus was initiated at the same finger tip, which accelerated the crack growth. (3) The tips of a crack indication are not always sharply defined on the X-ray pictures and cannot be accurately measured then. Nevertheless the crack growth data were sufficiently abundant for allowing the median results to be considered as representative for the tests concerned. Crack propagation curves are presented in fig. 14.

Fig. 14a shows that the propagation rates under random and program loading (both with GTAC) were hardly different. Excluding the GTAC from the program loading led to a slightly slower propagation.

Starting from the curves in fig. 14 damage calculations were made for a crack extension from 3 mm to 20 mm in the same way as for the fatigue lives. Some curves had to be extrapolated for this purpose. The accuracy of the $\Sigma\, n/N$-values, which are given in table 7, will not be high. It is still thought justified to conclude that the $\Sigma\, n/N$-values were on the average slightly above one.

When the crack exceeded a length of 20 mm there was a potential risk of unstable crack extension (explosive failure) in the random and program tests due to the high loads in these tests. This is further discussed in the following section.

The fracture surfaces were examined macroscopically and microscopically. The program load sequences produced the well-known growth bands on the fractures. An example is shown in fig. 15. Under the microscope growth lines were observed in these bands (see fig. 16), which could be correlated with the individual cycles of the programmed load sequence. That means that one such line was produced by a single cycle and indicates the successive stages of the crack front. The observations of the growth lines confirmed that crack propagation is mainly caused by the higher loads.

Fig. 15 also shows a dull area around the brighter crack nuclei. Similar dull-coloured bands with a tongue-shaped crack front were also observed on the fractures produced by the random load. The bands are generally believed to be brittle crack extensions, which are typical for 7075-T6 material. The bands emphasize the significance of high loads for crack growth in this material.

## 8.4 *Residual strength*

In 11 tests unstable growth of a crack occured, which for 6 specimens resulted in final failure of the complete specimen. An example of such a failure is shown in fig. 17. The load at which unstable crack growth occurred was derived from the load records and the crack length at which this occurred was deduced from the fracture surface. At the moment that the crack extension becomes unstable the fracture changes over from a fatigue crack to a rapidly extending static fracture. This point is marked by macro-plastic deformation at the two surfaces of the sheet. There are also colour differences on the fracture surface between the fatigue part and the static part. The absence of growth lines (see previous section) was another indication that the fatigue part had ceased. In general it was not difficult to assess the crack length at which the crack became unstable. Only in a few cases was there some doubt about the accurate length (ref. 5).

The gross stress at which unstable crack growth started was deduced from the load by using the results of the strain measurements. The stress has been plotted in fig. 18 as a function of the crack length. The figure shows that for the smaller cracks complete failure of the specimen occurred at stress levels above 25 kg/mm$^2$. For the larger cracks unstable crack growth started at a lower stress, but the crack growth was stopped. A final failure did not occur and would have required a further increase of the stress.

In all cases the stringers were uncracked at the moment that unstable failure started and they remained intact if the crack growth was stopped. Comparison of the results of the present tests with two curves for unstiffened sheet of 7075 material shows that for small cracks, say not larger than 50 mm, there is a reasonable agreement between the present results and the lower curve. For larger cracks instability of the crack occurs in the tension skin at a higher stress than in the unstiffened sheet, but contrary to the unstiffened sheet the crack growth can be stopped. The higher stress required for unstable crack extension has apparently to be attributed to the presence of the stringers, which reduce the crack opening and thus relieve the intensity of the stress at the tip of the crack.

Stopping of the unstable crack growth is effectuated by two factors:
(1) the increasing part in the load transmission taken by the stringers and (2) the running of the crack into rivet holes or under bonded finger tips. Although the

crack stopping action of a rivet hole may be considerable it cannot be relied upon. In several cases the unstable crack sticked to a path along the finger tips because small crack nuclei were already present there, see fig. 17. If such nuclei were not present, the crack in most cases but not in all ran into a rivet hole. In some of the latter cases the crack growth was then stopped, depending on crack length and load level.

From the above experience it appears that the onset of unstable crack growth was not affected by neighbouring cracks, but they were important with regard to the question whether the growth could be stopped.

8.5 *Structural design features*

In section 3.2 and Appendix A the various types of cracks were grouped in three categories: (a) cracks at the ends of adhesive-bonded doublers, (b) cracks at rivet holes and bolt holes and (c) cracks at open holes and sheet edges. Many cracks are not technically significant for various reasons and can be regarded as nuisance cracks. Nevertheless, it may be concluded from table 5 that the large number of cracks in category (c) shows that open holes and sheet edges are prone to fatigue crack nucleation. This view was further confirmed by cracks occurring at open rivet holes. Several rivets of the original structure had to be replaced in order to adapt it to the present test rig. In some cases the replacement was not carried out, either because it was difficult or because it was simply forgotten. Cracks frequently emanated from such empty holes. This experience concerns holes of rivets that are supposed to carry no shear load.

As said in section 8.1 the notch effect of an adhesive-bonded doubler is considered to be small. Crack al frequently occurred because it was located at a high stress level. Crack a2 occurred in 3 of the 13 tests only (table 5), although a doubler of 1.5 mm thickness was bonded to the skin of 2 mm thickness, i.e. the increase of thickness was relatively large.

An interesting observation was made regarding crack b8, occurring in skin and doublers under the strap plate of the skin joint at rib 1040. The crack growth started in the doublers and at a later stage penetrated into the skin. Crack propagation was about 10–15 times slower than at the neighbouring finger tip (crack type al). It was thought (ref. 7) that the crack rate had to be about 3 times slower in view of the lower stress level (increased area) and that the remaining 3–5 times slower rate had to be attributed to the bonded layers which prevent a rapid penetration in the thickness direction. In other words, if the reinforcement of the skin had been an integral part of it a faster crack rate would have occurred.

8.6 *Scatter*

Sufficient data to evaluate the scatter became available for the cracks at the finger tips (al). The standard deviation of log life was determined for the $N_3$-values obtained on the same specimen, $N_3$ being the fatigue life until a crack length of 3 mm. This could be done for 8 of the 13 tension skins. The average of the 8 standard deviations was $\sigma_{\log N} = 0.085$. Life distribution graphs and further data are given in Appendix F. It is noted in the Appendix that two life distribution functions for two similarly tested tension skins show small but probably significant differences. Hence, apart from the scatter within a single structure, there may be other sources of scatter giving differences between structures. As such, one might think of variations in production techniques and structural materials. It has been observed recently that the speed of crack propagation in 2024 sheet material from different manufacturers varied as much as 1:2, although the static properties were approximately the same (to be published). Smaller, but still systematic differences were found between sheets from different batches from the same manufacturer.

It is thought that the mean value $\sigma_{\log N} = 0.085$ is too small to be a realistic average value. A few data reported in the literature may be mentioned, although it is not the intention to discuss the values and the possibilities for practical application. In program tests of the NLR on simple riveted joints (ref. 20) the mean standard deviation of 22 test series of 7 tests each was $\sigma_{\log N} = 0.11$. Ford, Graff and Payne (ref. 21) arrived at a value $\sigma_{\log N} = 0.15$ as a mean result for various wing structures. For program tests on 40 trainer wings Parish (ref. 22) found a value $\sigma_{\log N} = 0.087$.

## 9 Comparison between fatigue lives under random and program loading

In this chapter empirical investigations are summarized, which were concerned with the possible equivalence of random and programmed load sequences. A comparison with the results of the present investigation will be made. The desirability of replacing a random load by a program loading is discussed in the following chapter.

Before reviewing the investigations on the equivalence of the two types of loading it has to be said that there are various methods for replacing a random load sequence by a programmed one. The problem thus could also be stated as: Which is the best method for reducing a random load to a program load, so that both induce the same fatigue damage?

*Mustang wings*. Random and program tests were carried out on Mustang wings (ref. 23). The results did not allow to draw firm quantitative conclusions, although the fatigue behavior was more or less similar under the two types of loading. The number of load amplitudes in the random tests was 11, whereas in the program tests this number was only 3. The latter number is considered to be very small for a correct representation of a gust spectrum.

*Kowalewski.* A second study was conducted by Kowalewski (ref. 24). Small light alloy specimens were loaded in plane bending. The random load was obtained as random noise of a limited frequency band (about 10 to 35 cps). Kowalewski studied four types of random loading with different power spectra. He derived the program loading from the random load sequence in two ways. In the first program the distribution of peak loads was the same as for the random load. In the second program the distribution of ranges (the differences between successive maxima and minima) was the same as for the random load. For the first type of program loading the life was about half the life under random loading for all four types of random loading. For the second type of program loading no systematic correlation was found. In reference 15 it was stated that a representation of a random load by its ranges cannot be expected to be a good representation (see also Appendix E). The limitations of Kowalewski's results are that the loading was plane bending with $S_m = 0$ and that the specimen was only mildly notched ($K_t = 1.77$).

*Lockheed investigation.* An extensive test program was conducted by Lockheed (refs. 11 and 25) on 7075-T6 sheet material. The axially loaded specimens were notched by a central elliptical hole, $K_t$-values being 4.0 and 7.0. The random load sequences included gust loads (constant mean load, $S_m$-values 8.5 and 4.2 kg/mm$^2$), maneuver loads (constant minimum load = 1-g load, $S = 3.8$ kg/mm$^2$), taxiing loads (random vibrations superimposed on ground loads), ground-to-air cycles (cycles between 1-g load and mean ground load), and combinations of these loads. The same types of loads were also applied in programmed sequences, the load spectra being derived from the random trace by employing the mean-crossing peak count method. The load cycles within each period were applied in a sequence of increasing amplitudes. The most salient results concerning the comparison between random and program loading are summarized below.

For a severe gust spectrum the fatigue lives for random and program loading were hardly different for both $K_t = 4$ and $K_t = 7$. This also applied for a less severe gust spectrum and $K_t = 7$. However, for the latter spectrum and $K_t = 4$ the fatigue lives under program loading were 2-4 times as long as under random loading. Discrepancies of the same order of magnitude were also found between random and program loading including GTAC and taxiing loads, the number of gust load cycles being 13 per flight. A better agreement was found if 110 gust load cycles per flight were applied. It should be noted that the GTAC in the program tests were applied in batches and that the minimum and the maximum loads of the GTAC were the mean loads of the taxiing loading and the gust loading, respectively. Finally the tests with maneuver loads, taxiing loads and GTAC (30 maneuver loads per flight) yielded program test lives 1.5–3 times shorter than the random test lives.

The authors of refs. 11 and 25 indicated that the larger fatigue lives under program loading in several of their test series could partly be explained by the definition of the GTAC as adopted for the program loading. The definition, given above, was considered as being insufficiently severe. It is further thought that a somewhat unfortunate choice was made for the load amplitude sequence in the program tests. The increasing amplitude sequence implies that the largest amplitudes at the end of each period are always followed by the smallest amplitudes of the subsequent periods. This may lead to favorable interaction effects (ref. 20), which lengthen the life under program loading.

*NASA investigation.* An investigation on edge-notched sheet specimens ($K_t = 4.0$) of 2024-T3 material was carried out by Naumann (ref. 17). The specimens were axially loaded, $S_m = 12.2$ kg/mm$^2$. Four different random load-time histories were used. Naumann first showed that omitting the smaller load fluctuations from the random load sequences had a negligible effect on the fatigue life. Omitting the peak loads that were disregarded by the mean-crossing peak count method also had a small effect, viz. an increase of 1–10% of the fatigues lives. Program tests were then carried out employing 8 stress amplitudes ($S_{a\,max} = 17$ kg/mm$^2$, $S_{a,min} = 1.7$ kg/mm$^2$). In each period all cycles with the same amplitude were applied in one batch, the sequence of the batches being randomized.

The program loadings were deduced from the random loadings by several counting methods, namely the mean-crossing peak count method, the peak count method, two level-crossing count methods and a range count method (methods defined in Appendix E). The fatigue lives for the former four methods did not show much difference and were slightly larger than for the random tests. For the mean-crossing peak count method the lives were about 30% higher and for the peak count and the two level-crossing count methods about 10%. For the range count method the fatigue lives were 1.4–3.2 times larger, which confirms the unrealistic nature of this method (see Appendix E).

It should be noted that the load spectra applied by Naumann were fairly severe, leading to fatigue lives in the order of 100,000 cycles.

*Gassner and Jacoby.* These investigators (ref. 26) performed comparative tests on axially loaded specimens with a central elliptical notch ($K_t = 3.1$), of bare 2024-T3 sheet material. In one test series gust load cycles and GTAC were selected in a random sequence from a load spectrum (5 gust amplitudes). The mean life was 2500 flights, which indicates a fairly severe spectrum. Flight simulation tests were then carried out with a programmed sequence of the gust load cycles, two different sequences being used. The mean lives were 2800 and 5800 flights, respectively, i.e. 1.1 and 2.3 times as long as under the random sequence.

*NLR crack propagation tests (ref. 27)*. An investigation was carried out on the influence of atmospheric exposure during the propagation of (macro) fatigue cracks in sheet specimens of 2024-T3 Alclad and 7075-T6 Clad material. Tests were conducted in two test rigs, one located indoors and the other one outdoors. The tests were run concurrently with the present test series on the tension skins. Since the same oil pressure was used for both test programs, exactly the same random and programmed load sequences, both with and without GTAC were applied. The mean stress in the sheet specimens was relatively high ($12.1 \text{ kg/mm}^2 = 17.2$ ksi), but the stress spectrum was not severe. Consequently, the crack rates were not fast and much slower than in the tension skins. A summary of the results is presented in fig. 19 which shows that the crack rate under program loading is somewhat faster than under random loading for the 2024 alloy and slightly slower for the 7075 alloy. Fortunately the differences are small, especially for the tests with GTAC.

It cannot be said that the above résumé and the results of the present test series have given a clear picture on the general equivalence of random and program loading. In view of the large number of variables a clear picture could not be expected. If it is tried to summarize some trends of the experimental results it first has to be said that an exact and generally applicable 1:1 relation between the fatigue lives under random and program loading is apparently illusive. Nevertheless fatigue lives of similar magnitudes may be obtained under certain conditions.

The fatigue life under program loading was equal or slightly larger than the life under random loading in the present test series, in the tests of Naumann, in part of the tests of Lockheed and in the NLR crack propagation tests. This similarity of fatigue lives was obtained despite the different ways of programming. It may be that for severe load spectra (and, consequently, relatively short fatigue lives) the load sequence in the program test is less important. In this respect, however, the tests of Gassner and Jacoby involve another warning that the load sequence in a program test can be important even for short fatigue lives.

The Lockheed tests have also shown that large discrepancies between random and program fatigue lives are possible. As said before it is thought that the selected load sequence in the program tests (increasing amplitudes) has significantly contributed to the discrepancies.

## 10 Full-scale fatigue testing of prototype aircraft structures

The questions to be discussed in this chapter are (1) why should full-scale tests be carried out (section 10.1) and (2) how should these tests be conducted (section 10.2)? The first question is partly a matter of design philosophy and will be touched upon only briefly. The second question raises such aspects as: the indication of the types of loads to be simulated, the establishment of the load spectra, the selection of a load sequence and the assessment of the highest and the lowest loads to be applied. Relevant data from the literature concerning some special aspects are summarized in 3 Appendices, dealing with the importance of the ground-to-air cycle (GTAC) (Appendix G), the significance of the Palmgren-Miner rule (Appendix H) and the effect of the loading program on the indication of fatigue-critical elements (Appendix J).

This chapter is primarily concerned with full-scale testing of new types of aircraft structures. The arguments partly have some bearing on component testing as well. Brief comments on the latter topic emerging from the present discussion are given in Appendix K. The chapter is concluded with some general reflections on full-scale testing (section 10.3).

Since the above problems are rather complex it has been tried to avoid a cumbersome discussion by dealing with the various aspects in separate sections. Secondly, the discussion has been largely restricted to a wing structure. Even then it will be recognized that each case in practice has its own specific aspects which have to be taken into account. Obviously this could not be done in the present discussion. Recommendations made should therefore be considered as guide lines needing modifications if circumstances so require. On the other hand the basic reasoning could certainly have a wider applicability.

### 10.1 *Why should full-scale tests be carried out?*

Several aspects can be mentioned that make full-scale testing of a prototype aircraft structure desirable. It is thought that the most important ones have been listed below:

(1) Indication of fatigue critical elements and design deficiencies.
(2) Determination of fatigue lives until visible cracking occurs.
(3) Study of crack propagation, inspection and repair methods.
(4) Measurements on residual strength.
(5) Requirements laid down by airworthiness authorities or other bodies.

(6) Commercial aspects.

In principle, the following methods are available for solving problems connected with the above aspects:

(a) Full-scale testing.

(b) Component testing.

(c) Calculations.

(d) Relying on past experience.

It is needless to say that combinations of these methods are possible. When considering the above alternatives the following aspects are important:

(I) The desired quantitative accuracy of the results to be obtained.

(II) The costs involved.

(III) The experience of the aircraft firm.

In view of the present state of knowledge on the calculation of fatigue properties, testing is imperative if data with a quantitative meaning for direct practical application are required. On the basis of the same argument, full-scale testing has to be highly preferred to component testing. The importance of load eccentricities for local stress levels is very great. It is generally difficult to simulate the load transmission into a component in exactly the same way as it occurs in a structure, the more so since most structures are curved in at least one direction. Harpur and Troughton (ref. 28), who analyzed the results of several full-scale tests, observed that about half the numbers of defects would not have been found by component testing. These authors also evaluated the costs of full-scale testing and arrived at the conclusion that full-scale testing can be justified on economic grounds alone, even in the case of a fail-safe structure.

It has to be admitted that a full-scale test to be really meaningful requires a conscientious assessment of the load spectrum and the load sequence. This was frequently advocated by Branger (ref. 29) and was recently stressed once more by Lowndes and Miller (ref. 30). Some of the problems involved are discussed in the following section.

## 10.2 *How should full-scale testing be carried out?*

### 10.2.1 *Introduction*

When dealing with the above question a number of aspects can be listed such as:

(1) Indication of fatigue loads to be applied.

(2) Assessment of load spectra.

(3) The highest loads to be incorporated in the test.

(4) The smallest load variations to be included in the test.

(5) The load sequence to be adopted.

(6) The duration of the test.

(7) Experimental conditions.

A quantitative analysis of the above aspects would require a quantitative fatigue criterion, which is nonexistent. Therefore qualitative ideas about the fatigue process and experimental evidence have to be the guiding elements.

For the fatigue phenomenon the model outlined in ref. 31 is adopted. The phases of the fatigue process are crack nucleation, propagation of micro- and macrocracks and final failure. The duration of the nucleation period is in general so short that it can be neglected. The amount of cracking is therefore the prime parameter for indicating the fatigue damage. It is, however, not the only one. Two additional parameters are the residual stress field and the (cycle) strain hardening around the tip of the crack. Fatigue was then considered to be crack extension due to cyclic slip, the extension being dependent on the amount of cyclic slip (depending on external load variation, crack length, strain hardening) and the efficiency to convert the cyclic slip into crack extension (depending on the opening of the crack by the tensile stress, including the residual stress present). In ref. 31 it was argued that for aluminium alloys the strain hardening might be less important than the other two damage parameters. The implications for planning the loading for a full-scale test should then be:

(1) The stress variations should have the same character as those induced by the (random) service loadings.

(2) The residual stress on the average should also have similar magnitudes.

Since these criteria cannot be evaluated quantitatively they have to be used more or less intuitively, guided by experimental evidence. This is tried in the following sections, dealing with the seven aspects mentioned at the start of the present section. It is not the intention to cover all the aspects in full detail. The discussion will be mainly restricted to wing structures loaded by gusts, maneuvers, ground-to-air cycles (GTAC) and taxiing loads. Several recommendations discussed will have a wider applicability.

### 10.2.2 *Indication of fatigue loads to be applied in a full-scale test*

It may be questioned whether it is necessary to apply to a wing structure gust loads, maneuver loads, GTAC and taxiing loads and wether some of these loads can be omitted. Several years ago it was generally thought that gust loads were the predominant fatigue loads for commercial transport aircraft and maneuver loads were the predominant ones for most military aircraft.

For commercial aircraft it is accepted by now that the GTAC can have such a large influence on the fatigue life that it cannot be omitted in a full-scale test. Numerical data on the fatigue life reduction due to the GTAC, as reported in the literature, are summarized in Appendix G. In this Appendix, as well as in Appendix H on the significance of the Palmgren-Miner rule for full-scale testing, it is pointed out that the rule is unreliable for deciding whether a fatigue load will substantially contribute to the fatigue damage. It greatly underestimates the damage done by the GTAC. The life reductions caused by the GTAC (from 50–90%; see Appendix G), in most tests leave no doubt that this type of loading has to be applied in a full-scale test.

Since the Palmgren-Miner rule is apparently uncapable of indicating fatigue critical loads, decisions have to be based, as said before, on our qualitative understanding of the fatigue phenomenon, guided by experimental evidence of variable-amplitude tests. In this respect it was concluded in Appendix G that taxiing loads per se are probably not importantly contributing to the fatigue damage since they occur at a low mean load*. However, the taxiing loads cause indirect damage since they increase the load range of the GTAC. The minimum load of this load cycle is shifted further downwards and this may significantly reduce the fatigue life. The minimum load of the GTAC has, therefore, to be *corrected for the occurrence of taxiing loads.*

The significance of maneuver loads is different for a transport aircraft and for a fighter or a trainer. It is more or less common practice to neglect maneuver loads for transport aircraft because they are partly comprised in the gust load statistics used and because their severity (for a certain frequency of occurrence) is much smaller. Nevertheless it seems advisable for any new design to check whether this is true.

For several military types of aircraft it might be assumed that gusts are of minor importance as compared with the positive maneuver loads. Even negative maneuver loads are frequently thought to be unimportant in view of the much lower intensity as compared with the positive maneuvers. However, if negative maneuver loads or negative gust loads occur in between positive maneuver loads, a significant damaging effect has to be expected because of the increase of the load ranges of the positive maneuvers. Application of these downward loads (relative to the 1-g level) in addition to upward maneuver loads is considered to be imperative if accurate fatigue lives are aimed at.

For the same reason it is also objectionable to aply GTAC in batches because this would presuppose that there are numerous successive flights without any gust or maneuver loads. Since such loads do occur in most flights and then increase the load range of the GTAC, a real simulation of flight by flight has to be strongly advocated.

10.2.3 *Assessment of load spectra*

When it has been decided which types of fatigue loads will be applied in a full-scale test the load spectra have to be determined. Procedures for this purpose are outside the scope of the present report. However, a few comments related to aspects discussed elsewhere in this report may be appropriate.

In Appendix G and section 10.2.1 it is strongly advocated that full-scale tests be carried out as flight simulation tests (see fig. 20). Obviously the load-time history cannot be the same for all flights, since there are loads with a frequency lower than once per flight. These loads could be uniformly distributed over the flights to be simulated, but this procedure assumes that the fatigue loads have a statistically stationary character. The assumption is certainly incorrect for gust loads. Gust load spectra are different for poor and good weather conditions. Generally speaking something has to be known about the distribution of the weather conditions and this information has to be fed into the planning of the various types of flights to be simulated. Relevant data were recently published by Bullen (ref. 54) who discussed the chance of a rough flight. Also for wings mainly loaded by maneuver loads one has to consider the necessity of adapting the loads in the simulated flights to the usage which will be made of the aircraft. A further discussion of this aspect is beyond the scope of the report.

It is hardly necessary to say that load measurements in flight are to be strongly recommended in order to verify the calculations of the loads. Whenever possible such measurements should be made before the full-scale test is started.

When establishing load spectra for a fail-safe structure considerable conservatism should be avoided since this implies deviating from the actual spectra and thus requires reinterpretation of the results of the full-scale test. The Palmgren-Miner rule is unsuitable for the latter purpose (see Appendix H). For a safe-life part for which a long fatigue life is required it may be advisable to have a safety factor on the loads applied in the test. The latter advice cannot be given if the target life is relatively short. For instance, a wing structure of a fighter in the high-strength Al-Zn alloys, employing heavy gages is probably not fail-safe due to rapid crack propagation and poor residual strength properties. There is a risk of catastrophic crack propagation in the full-scale test. It is then necessary to have an accurate service load simulation to be sure that the most relevant information on the fatigue characteristics is obtained.

10.2.4 *The highest load to be applied in a full-scale test*

The problem of selecting the highest load to be applied in a full-scale test is a question of whether the load spectrum will be truncated and at which load level this will be done. The truncation applied in the present test series is illustrated by fig. 9. The highest load to be applied can be of great importance for the fatigue behavior of an aircraft structure since it may introduce

* The bottom skin is considered here. For the top skin the situation may be different.

load redistribution in the structure and stress redistribution around notches (ref. 23). In an aircraft structure of high-strength aluminum alloys load redistribution on a large scale probably occurs only at load levels near the ultimate design load and need not be considered here. It would not be surprising, however, to see some load redistribution in riveted joints at lower loads, say in the order of the limit load.

Stress redistribution on a local scale, i.e. around notches is expected to occur at load levels below the limit load. If it is assumed that the stress at the ultimate design load is in the order of the yield stress $S_{0.2}$, a stress concentration factor $K_t$ of 1.5 would be sufficient to initiate local yielding at limit load. Since higher values of $K_t$ are unavoidable, local yielding and consequently local stress redistribution will occur at lower loads. In other words, residual stresses will be introduced, which affect the fatigue life. It would be somewhat overoptimistic to expect that this effect will be the same for all notches, having different $K_t$-values, different stress gradients and different nominal stress levels. The picture of fatigue-critical elements turning up in a full-scale test may thus be dependent on the choice of the maximum load level to be applied. It is thought that this has been demonstrated by the present test series when comparing the variable-amplitude test results with the constant-amplitude test results. For the first group of tests $P_{max}$ was about 65% $P_u$ and for the second group it varied from 35 to 47% $P_u$. The picture of fatigue-critical elements was different for the two groups (see section 8.2), perhaps the most remarkable result being that cracks were found at more locations in the constant-amplitude tests.

Observations concerning the effect of the loading history were made in other test series on large structures. Data from tests on Mustang wings, Commando wings, Dakota wings and a sweptback wing are summarized in Appendix J. It was generally observed that the type of loading had an effect on the relative fatigue lives of the fatigue-critical components in a structure. This could be ascribed to differences in the load sequences, differences in the highest loads applied and scatter. It was concluded in the Appendix that the highest load applied in the test had a predominant influence.

In view of the foregoing conclusion it is clear that the selection of the highest load to be applied in a full-scale test is a delicate problem if accurate fatigue lives and a good picture of the fatigue-critical components are aimed at. It is recommended to truncate the load spectrum for the test at a load level that is expected to be equalled or exceeded approximately ten times in the anticipated target life in service. (This recommendation was made before in refs. 59 and 46). It cannot be denied that the recommendation is somewhat arbitrary. The background is that it would be unrealistic to apply a load that is expected only once in the service life. It is highly probable that many aircraft of a fleet will never experience this load. On the other hand, it is also thought unwise to go far down with the maximum load in view of the predominant influence of high loads. The above recommendation is considered as a reasonable compromise. There is a good probability that all aircraft will meet at least a few times the load level proposed for the truncation. The recommendation presupposes that the load spectrum is estimated as accurately as possible without attempting to be conservative.

If during a full-scale test a crack is found and its propagation is to be recorded, a temporary truncation at a lower level has to be advised. In analogy with the previous reasoning a load level equalled or exceeded approximately ten times during the anticipated period for crack propagation could be recommended.

10.2.5 *The lowest load to be applied in a full-scale test*

The application of loads with a small amplitude in a full-scale test can be an objection from the point of view of time economy. This applies especially to gust loads, for which the low-amplitude loads are numerous. On the other hand omitting of these loads can be objectionable for two reasons:

(1) The numerous low loads can be important for fretting corrosion and thus for crack nucleation.
(2) The low loads can also be damaging after cracks have been nucleated.

The damaging effect of low-amplitude cycles was shown in several test series, (for instance refs. 20, 32, 43, 47 and 49) employing program loading, although in general the effect was not large. It was already questioned in ref. 20 whether this experimental result is equally valid for a random load sequence and for a flight-by-flight service loading. The low-amplitude loads are then found in between higher loads and may be ineffective. Some confirmation is coming from Naumann's random load tests (ref. 17, see also chapter 9), which showed that the omission of the smaller load fluctuations hardly affected the fatigue life. Secondly, for visible cracks it has been observed in program tests (refs. 40 and 60) that the main part of the crack growth occured at the higher load amplitudes, whereas crack propagation at the lowest amplitude was probably negligible. Experimental research on the effect of low-amplitude loads in random-load flight simulation tests is highly desirable.

Returning to the contribution of low-amplitude cycles to fretting corrosion it has to be noted that most cracks in an aircraft structure start from riveted and bolted joints. In both types of joints fretting corrosion occurs, which has a large influence on the fatigue life. From this point of view it has still to be recommended that low-amplitude loads are incorporated as much as possible in a full-scale test. In the present test series the minimum amplitude was about 10% of the maximum amplitude and this percentage might be useful as a rough guide for wings mainly loaded by gusts and GTAC.

10.2.6 *The load sequence in a full-sclae test*

In section 10.2.2 and Appendix G it has been explained that a full-scale test should be carried out as a flight simulation test rather than a program test. After decisions have been made concerning the loads to be applied, the load spectra and the maximum and minimum loads to be included in the test, two remaining problems are: (1) how should the loads be distributed over the flights and (2) which load sequence will be adopted for each individual flight?

With respect to the first question it was already pointed out in section 10.2.3 that fatigue loads with a statistically non-stationary character, such as gusts, should not be uniformly distributed over the simulated flights. This feature should be accounted for when planning the distribution of the loads over the flights. From an experimental point of view this can hardly be considered as an important complication for a full-scale test carried out as a flight simulation test.

Broadly speaking, there are two alternatives for the selection of load sequences for the flights, namely, a programmed sequence and a random sequence, leading to a program-load flight simulation and a random-load flight simulation as schematically illustrated in fig. 20. Also in this case the argument of experimental simplicity appears to be no longer valid for apparatus that is already capable of applying a flight simulation loading. Consequently, a realistic sequence, i.e. a random sequence has to be recommended. If one wants to stick to a programmed sequence one has to be dissuaded from an increasing sequence (Lo-Hi sequence) and from a decreasing sequence (Hi-Lo sequence), which may both lead to systematic effects on the fatigue life. A randomized step sequence has to be preferred then.

An indication of the importance of the sequence was recently obtained by Gassner and Jacoby (ref. 26) who tested a notched bar specimen ($K_t = 3.1$) of 2024 material. Program-load flight simulation tests were carried out with a large number of gust loads per flight, viz. about 400 cycles. The fatigue lives for two different ways of programming were 2800 and 5800 flights (averages of 6 and 3 tests, respectively). Although the large difference could perhaps occur because of the large number of gust cycles per flight, it still emphasizes the recommendation that the sequence should be as realistic as possible.

Choosing a random sequence raises the problem of how the sequence should be arrived at. For maneuver loads it seems possible to perform imaginary flights. For gust loads one could employ the power spectral function representation. For instance, by simulating the dynamic response of the aircraft on an analog computer and feeding it with random noise having the required spectral shape, a sequence can be derived from the output signal of the computer. The question whether the magnitudes of the gust loads should also be determined by power spectral methods is beyond the discussion of this report. Load records obtained in flight under gust conditions, if available for the aircraft concerned, could obviously also be used for planning load sequences for the full scale test.

In service a positive gust load is not necessarily followed by a negative gust load. This partly depends on the dynamic response of the aircraft. If a positive gust load is followed by a negative one, the latter will generally have a different amplitude.

Tests bearing upon the degree of randomness were carried out by Naumann (ref. 39). He performed tests on an edge notched specimen ($K_t = 4$) of 7075 material with a random gust loading with and without GTAC. Three types of randomness were adopted, indicated by Naumann as:

(1) Random cycle: Each positive half cycle was followed by a negative half cycle of the same magnitude.
(2) Random half cycle, restrained: Each positive half cycle was followed by a negative half cycle, the magnitude of which was selected at random from the load spectrum and which therefore was generally not equal to that of the preceding positive half cycle.
(3) Random half cycle, unrestrained: Positive and negative half cycles were randomly selected with no restrictions on the sequence of positive and negative.

The results are summarized in table 8 below.

TABLE 8

Results of random load tests of Naumann (ref. 39)

| *Randomness* | *Fatigue life in flights* | | *Fatigue life ratio* | |
|---|---|---|---|---|
| | *No GTAC* | *GTAC* | *No GTAC* | *GTAC* |
| (1) Random cycle | 5815 | 1334 | 0.66 | 0.84 |
| (2) Random half cycle, restrained | 7358 | 1515 | 0.84 | 0.95 |
| (3) Random half cycle, unrestrained | 8798 | 1588 | 1 | 1 |

Each result is the average of 6 tests. A flight comprised 68 positive and 68 negative half cycles. For the GTAC $P_{min}$ was equal to $-1/2\, P_m$ of the gust loads. In the last two columns of the table the fatigue life is compared with the life under unrestrained random half-cycle loading. The table shows that the degree of randomness has an effect on the fatigue life, which fortunately is fairly small for the tests with GTAC. For a wing the randomness will not be fully "unrestrained", especially if the damping of the wing is low (see, for instance, fig. 7)

Naumann's results suggest that it can be acceptable to apply (instead of a sequence obtained by spectral methods or from load records) a sequence based on random numbers which can be easily generated on a digital computer. If it is then prescribed that positive half cycles are always followed by negative half cycles, the fatigue results would probably be insignificantly conservative If it also prescribed that the negative half cycle has the same amplitude as the preceding positive half cycle (assuming a symmetric gust spectrum) the results may be somewhat conservative.

10.2.7 *The duration of a full-scale test*

In the literature papers on full-scale tests almost invariably state that several fatigue-critical components were indicated, which were then suitably modified. Harpur and Troughton (ref. 28) feel that at the present time fatigue design has significantly improved and that structural inefficiencies may turn up late in the design target life. They propose to continue testing up to 3 times this life. The figure was based on the analysis of several full-scale tests, which showed that many cracks were found between once and three times the target life.

If fail-safe strength capacities have to be shown by tests and the same structure has to be used one might want to speed up the fatigue testing. Two possibilities are:

(1) To increase all fatigue loads with the same percentage (say 20%)

(2) To omit the load cycles with the lowest amplitude(s), which due their high frequencies of occurrence take up a large proportion of the testing time.

Since it is thought that the first method more significantly modifies the load spectrum, the second one is preferred. Naumann (ref. 39) found a small increase of life (in the order of 10%) if the lowest amplitude was omitted from random-load flight simulation tests on edge notched specimens (7075-T6). It is still advised to apply the second method only after the target life has been reached at least once.

It would be rather absurd to scrap a test structure that did not reveal fatigue critical components.

At the end of a full-scale fatigue test, if there are no other purposes for using the structure, it is recommended to cut tensile specimens out of the structure, including notches from which fatigue nuclei could have emanated that are still invisible. Destructive testing can then reveal the presence of such nuclei.

10.2.8 *Testing conditions*

In this section some brief comments will be made on aspects of the testing conditions that can affect the fatigue life, such as environment, load frequency, rest periods and condition of the structure to be tested.

An exact simulation of service conditions is either impossible or impracticable. It is not feasible to simulate such factors as the occurrence of rest periods and the rate of loading which, fortunately do not have a large effect on the fatigue life (ref. 20). With respect to the crack propagation rate, a small systematic effect of the load frequency has been found (ref. 61) and should be kept in mind if the loading rate in service and in the full-scale test are largely different.

Not very much is known about the effect of the environmental conditions. Many fatigue failures start at rivet holes or bolt holes. The environment in such holes probably is not very much different in a test hall and in service. A fatigue life reduction would be possible if sheet edges are exposed to the atmosphere. In two NASA investigations (refs. 62 and 63) such an influence was observed for bare sheet specimens of 2024-T3 and 7075-T6, whereas the effect was small or negligible if the sheets were in the clad condition.

Once cracks are growing and are accessible to the open air one may expect some effect of corrosion or water vapor. This was recently studied (ref. 27) in comparative random and program tests, which were run concurrently with the present tests on the tension skins. Reference to these tests has already been made in chapter 9, where further details are mentioned. It turned out that the differences between the crack rates in 2024-T3 Alclad sheet material tested indoors and outdoors were small if not negligible. However, for 7075-T6 Clad sheet material the crack propagation outdoors was about 1.5 to 2 times faster than indoors. Consequently, one has to admit that it would be better to carry out full-scale tests in the open air, especially if the material is 7075-T6. However, there are some obvious disadvantages. The problem will not be further discussed here.

A full-scale test is preferably carried out at an early stage of the production of the aircraft, in view of possible modifications deemed necessary as a consequence of the test. One should take the utmost care that the production methods for the structure to be tested are representative for normal shop practices from a fatigue point of view. This also applies to the materials from which the structure is built. The present test series has given an indication that differences between structures may be a source of scatter (see section 8.6).

Harpur and Troughton (ref. 28) observed that in several cases fatigue cracks occurring in service were not found in the full-scale test because the structure tested was not sufficiently representative. This was due to manufacturing differences and modifications, but also to simplifying the test article. Due consideration should therefore be given to the structural completeness of the specimen.

10.3 *Some concluding remarks*

The present investigation was primarily initiated to study by means of experiments on a full-scale structure whether random service loadings can be replaced by a programmed load sequence. One could mention various reasons why such a replacement could be worthwhile:

(1) Program testing may be considered as a less complicated procedure than a random load test from the experimental point of view.
(2) A random load test is aiming at an accurate simulation of service loads. This requires more information than distribution functions of peak loads. Information on load sequences is also needed, which presents an additional problem.
(3) Apparatus capable of applying a programmed load sequence may be available, whereas modifications or new apparatus may be necessary for applying random loads.
(4) There appears to be an aversion against complicated testing techniques, which are considered as rather sophisticated. If it could be explicitly shown that such techniques would yield results of a considerably improved quality, they certainly would be accepted more easily. However, even with a realistic load sequence in the full-scale test one is still left with other uncertainties regarding the fatigue life in service.

The results of the present test series can be roughly characterized by saying that the fatigue lives and the crack rates were hardly different under random and program loading. The pictures of fatigue critical elements was also the same. It still has to be admitted that the fatigue lives were not accurately equal under the two types of loading. With respect to the results of others on small specimens (see chapter 9) it can be said that the NASA investigation gave similar results as the present investigation, whereas in the Lockheed investigation the differences between the fatigue lives under the two types of loading were similar or larger, depending on the load spectrum. One could say that the differences are a consequence of the method of planning the program loading. However, with the present knowledge of fatigue it is not reasonable to expect that a unique method for programming will exist, which could give a generally valid 1:1 relation between the fatigue lives under random and program loading.

The answer to the question whether for a full-scale test program loading can be an acceptable representation of random service loads depends on what one expects from the test. If only an approximation of the magnitudes of fatigue lives and an indication of possibly unknown structural deficiencies are required, then program loading may be sufficient. However, if one desires more accurate data on fatigue properties and as many indications of potential locations for fatigue cracks as possible, a realistic load sequence, that is, a flight by flight loading is imperative and program loading cannot be recommended.

It may appear to be fairly trivial to conclude that a load sequence in a full-scale test should be as realistic as possible. It is, however, less trivial in view of the four arguments mentioned above, which developed historically. The situation has changed during the last decade, firstly, since experimental complications are much more easily overcome now and, secondly, because it is better known at the moment that misleading information may come from simplified loading programs. It is thus no longer a question whether a full-scale test should be a realistic flight by flight simulation, but rather how a reasonably realistic flight load simulation is obtained. This was the subject of the preceding sections.

Comparisons between the fatigue lives obtained in service and in full-scale tests were made by Raithby (ref. 64), Lowndes and Miller (ref. 30) and Harpur and Troughton (ref. 28). The results obtained were not encouraging. On the average, service lives were much shorter, say from 2 to 10 times. Harpur and Troughton refer to the large number of aircraft in a fleet, which implies that due to scatter (also mentioned by Raithby) the first cracks in service have to occur at shorter lives. These authors also mentioned various other reasons why descrepancies between test results and service experience may show up. The reasons are concerned with the non-representative character of either the loading, the specimen or the environment. The load-time histories applied in the tests reported in the above three references were not specified. Probably, simplifications with respect to the load histories were incorporated in all tests. Hence, although this would give partial improvement only, the limited agreement between the results from tests and from service can be considered as another warning that the load sequences to be applied in full-scale tests should be as realistic as possible.

In concluding this chapter some topics for further investigations are mentioned:

(1) The environmental effect.
(2) The effect of omitting small load fluctuations
(3) The effect of the maximum load applied
(4) The effect of modifying the load spectrum

$\Bigg\}$ on the fatigue life in random-load flight simulation tests

With respect to the first topic it was recommended in ref. 27 to carry out comparative tests under various possible service and full-scale testing conditions. It was also advised to perfom tests under closely controlled environments to improve the understanding of the mechanism which is a prerequisite for generalizing the results of the former tests.

Items 2, 3 and 4 mentioned above were studied in the past almost exclusively under program loading. Although the views obtained may be qualitatively correct for random service loading as well, experimental verifications are certainly desirable.

## 11 Conclusions

For the present investigations fatigue tests were carried out on full-scale tension skins of a wing center section, built up from 7075-T6 material. Variable-amplitude tests were carried out with a random load sequence and a programmed load sequence in order to study the equivalence of the two types of loading. Both types of loading were applied with and without GTAC (ground-to-air cycles). In constant-amplitude tests the loads represented GTAC and gust load cycles. The results are summarized below.

In addition to the experimental part an analysis was made regarding full-scale testing of new types of aircraft involving an extensive use of relevant data from the literaure. The analysis was mainly restricted to wing structures although the basic reasoning will have a wider applicability. Several recommendations for carrying out full-scale tests were made, which are also recapitulated below. The recommendations should not be regarded as strict rules, but rather as guides, since every particular case has its own specific features which should be taken into account.

Finally, some recommendations are made for program tests on components carried out for design development purposes.

*Test results*

1. The number of locations at which cracks were found was 20 for the variable-amplitude tests and 26 for the constant-amplitude tests (table 5). This different picture of fatigue-critical components was related to the differences between the maximum loads in the tests rather than to the differences between the load sequences. The values of $P_{max}$ were 65% $P_u$ and 35–47% $P_u$ for the two types of tests, respectively.
2. In all variable-amplitude tests cracks were generally found at the same locations. There were, however a few types of cracks that occurred in one or two of the eight variable-amplitude tests only.
3. The fatigue lives under program loading were about 10–30% larger than under random loading (table 3). The program loading was derived from the random loading by the mean-crossing peak count method. If the range-pair count method had been used the differences would have been slightly larger.
4. The fatigue lives were reduced to about 50% by adding GTAC to the random and the programmed load sequences (table 4).
5. For the fatigue lives the values of $\Sigma\, n/N$ were in the order of 1.4 for crack nucleation at the finger tips and in the order of 2.5 for several other locations (table 6). For tests with GTAC the $\Sigma\, n/N$ values were only slightly smaller than for tests without GTAC. For crack propagation $\Sigma\, n/N$ varied from 1.0 to 1.5 (table 7).
6. In the variable-amplitude tests crack propagation mainly occurred at the higher load levels. The crack rates were almost the same for random and program loading (fig. 14). The effect of the GTAC on the crack rate was small.
7. Cracks in the skin from 25 to 50 mm reduced the residual strength to about 25 kg/mm$^2$ and induced complete failure of the structure (fig. 10). With larger cracks unstable crack growth occurred at lower stresses but the growth was stopped. The onset of unstable crack growth is probably not affected by neighbouring cracks, but whether it will be stopped does depend on them.
8. For cracks nucleated near the finger tips the endurances obtained from one specimen showed a standard deviation $\sigma_{\log N} = 0.085$ as an average value (table F1). For two similarly tested tension skins the two life distribution functions for this type of crack showed small but probably significant differences, indicating an extra source of scatter.
9. Open holes, free sheet edges and empty rivet holes were locations prone to fatigue crack nucleation.
10. The sensitivity of the X-ray method for detecting part-through cracks was considerably increased by applying a tensile load to the specimen.
11. The sensitivity of visual inspections for detecting small cracks was considerably higher when the specimen was dynamically loaded, due to "breathing" of the cracks.

*Full-scale testing*

12. Experimental investigations on the equivalence of random and program loading with respect to fatigue life are not abundant. A review showed that a reasonable quantitative agreement was obtained in some cases, whereas considerable differences were found in other cases. With the present knowledge on the fatigue phenomenon it cannot be expected that a method of programming load sequences could be outlined that would garantee a reasonably accurate equivalence.
13. For obtaining accurate and complete information on the fatigue characteristics of an aircraft structure full-scale testing is indispensable and has to be preferred to component testing for various reasons.
14. The Palmgren-Miner rule is inadequate for judging whether a certain type of fatigue loading has to be applied or can be omitted in full-scale testing.

15. A literature review on the damaging effect of the GTAC indicated that this type of loading reduced the fatigue life with 50 to 90%. Application of the GTAC in a full-scale test is imperative.
16. Fatigue loads with small amplitudes can be damaging if they imply an increase of load ranges pertaining to other types of loading. Taxiing loads increase the load range of the GTAC. For a wing predominantly loaded by positive maneuvers, the much smaller negative maneuvers or gust loads occurring in between positive maneuvers increase the load ranges of the latter loads. Such loads have to be added to the larger loads in a full-scale test.
17. As a consequence of the previous conclusion GTAC should not be applied in batches because that implies a neglect of gusts and maneuver loads which occur in practically every flight and thus increase the load range of the GTAC. Consequently, a realistic load-time history should be a flight by flight simulation.
18. With respect to taxiing loads it may be sufficient to decrease the minimum load of the GTAC in accordance with the maximum taxi-load amplitude (occurring once per flight).
19. When establishing load spectra for a fail-safe structure an undue conservatism should be avoided.
20. The fatigue lives, the crack rates and the indication of the most fatigue-critical elements in a full-scale test depend on the highest load applied in the test (truncation of the load spectrum). This implies that the selection of the maximum load level is a delicate matter. It is proposed to adopt the load level that on the average is equalled or exceeded about 10 times in the target life. When crack propagation is studied a lower level should be assessed.
21. Low-amplitude cycles that do not increase the load ranges of other loads should be included in a full-scale test if an important contribution to fretting corrosion in joints has to be expected.
22. In a flight-simulation full-scale test a random sequence of the loads in each flight should be preferred to a programmed sequence. The latter may have a systematic effect on the fatigue life. Especially sequences with increasing amplitudes (Lo-Hi) or decreasing amplitudes (Hi-Lo) cannot be recommended.
23. The non-stationary character of gust loads and possibly also of other loads should be incorporated into the flight by flight planning of a full-scale test.
24. If a full-scale fatigue test has to be speeded up the omission of the frequent low-amplitude cycles is preferred to increasing all loads with a certain percentage. It is not advised to apply such methods before the target life has been reached at least once. A full-scale test should be continued until as many critical locations as possible have been found.
25. Care should be taken that the structure to be tested is representative for the production type aircraft.

*Component testing*

26. When comparative tests are carried out on components for design development purposes, a flight-simulation loading should be preferred to program loading. If the former type of loading cannot be carried out with the facilities available, program tests should be preferred to tests with a constant-amplitude loading. In the latter tests the relative merits of two designs may be different at different load levels (intersecting S-N curves).
27. The recommendations made for full-scale testing with respect to selecting the types of loads to be applied and the magnitudes of these loads are also valid for program tests.
28. For the GTAC in a program test the maximum load should be higher than the lg-load level. The load that on the average is equalled or exceeded once per flight is recommended for this purpose.

## 12 List of references


[1] Nederveen, A., de Rijk, P., Broek, D., Schijve, J., Experimental details of testing a full-scale structure with random and programmed fatigue load sequences. NLR Report S.608, Jan. 1964.

[2] Schijve, J., Fatigue loads applied on a full-scale structure in random and programmed sequences. NLR Report S. 609, April 1964.

[3] Sevenhuysen, P. J., Nederveen, A., Schijve, J., Strain measurements on eight full-scale wing center sections. NLR Report S. 610, Dec. 1963.

[4] Schijve, J., de Rijk, P., Fatigue lives obtained in random and program tests on full-scale wing center sections. NLR Report S. 611, Dec. 1963.

[5] Broek, D., Crack propagation and residual strength of full-scale wing center sections. NLR Report S. 612, April 1964.

[6] Schijve, J. and Broek, D., Fatigue test results of two full-scale wing center sections under ground-to-air cycle loading. NLR Report S. 635, April 1965.

[7] Schijve, J., de Rijk, P., Fatigue test results of three full-scale wing center sections under constant-amplitude loading. NLR Report S. 640, Nov. 1965.

[8] van Beek, E. J., Full-scale fatigue tests on the Fokker "Friendship". P. 326 of ref. 9.

[9] Plantema, F. J., Schijve, J., (Editors), Full-scale Fatigue Testing of Aircraft Structures. Proceedings of the 1st ICAF-AGARD Symposium. (Amsterdam, June, 1959), Pergamon Press, London, 1961.

[10] Nauta, A. and Bosman, D., Description of the Electronic Equipment Pertaining to the Code Actuated Random Load Apparatus (CARLA). NLR MS-62-15, Amsterdam, April, 1962.

[11] Melcon, M. A. and McCulloch, A. J., Simulation of random aircraft service loadings in fatigue tests. P. 347 of ref. 12.

[12] SCHIJVE, J., HEATH-SMITH, J. R. AND WELBOURNE, E. R. (EDITORS), Current Aeronautical Fatigue Problems. Proceedings of the 3rd ICAF-AGARD Symposium (Rome, April 1963), Pergamon Press, London, 1965.

[13] SCHIJVE, J., Fatigue life and crack propagation under random and programmed load sequences. P. 403 of ref. 12. Also NLR MP. 219, April 1963.

[14] BARROIS, W. AND RIPLEY, E. L. Fatigue of Aircraft Structures. Proceedings 2nd ICAF-AGARD Symposium (Paris, May 1961), Pergamon Press, 1963.

[15] SCHIJVE, J., The analysis of random load-time histories with relation to fatigue tests and life calculations. P. 115 of Ref. 14. Also NLR MP. 201, May 1961.

[16] LEYBOLD, H. A. AND NAUMANN, E. C., A study of fatigue life under random loading. Proceedings ASTM, Vol. 63, p. 717, 1963.

[17] NAUMANN, E. C., Fatigue under random and programmed loads. NASA TN D-2629, Febr. 1965.

[18] CRICHLOW, W. J., The ultimate strength of damaged structure. Analysis methods with correlating tests data. P. 149 of ref. 9.

[19] BROEK D., The effect of finite specimen width on the residual strength of light alloy sheet. NLR Report M. 2152, Sep. 1965.

[20] SCHIJVE, J., JACOBS, F. A., Program-fatigue tests on notched light alloy specimens of 2024 and 7075 material. National Aeronautical Research Institute, Amsterdam, Technical Report M. 2070, March 1960.

[21] FORD, D. G., GRAFF, D. G., PAYNE, A. O., Some statistical aspects of fatigue life variation. P. 179 of ref. 14.

[22] PARISH, H. E., Fatigue test results and analysis of 42 piston Provost wings. Ministry of Aviation, S & T Memo 1/65, April 1965.

[23] PAYNE, A. D., Determination of the fatigue resistance of aircraft wings by full-scale testing. P. 76 of ref. 9.

[24] KOWALEWSKI, J., On the relation between fatigue lives under random loading and under corresponding program loading. P. 60 of ref. 9.

[25] MCCULLOCH, A. J., MELCON, M. A., CRICHLOW, W. J., FOSTER, H. W. AND REBMAN, J., Investigation of the representation of aircraft service loadings in fatigue tests. ASD Technical Report 61-435, Sep. 1961.

[26] GASSNER, E. AND JACOBY, G., Experimentelle und rechnerische Lebensdauerbeurteilung von Bauteilen mit Start-Lande-Lastwechsel. Luftfahrttechnik Raumfahrttechnik, vol. 11, p. 138, 1965.

[27] SCHIJVE, J., DE RIJK, P., The crack propagation in two aluminium alloys in an indoor and an outdoor environment under random and programmed load sequences. NLR-TR M. 2156, Nov. 1965.

[28] HARPUR, N. F., TROUGHTON, A. J., The value of full-scale fatigue testing. Paper presented at the 4th ICAF-AGARD Symposium, München, June 1965.

[29] BRANGER, J., The full-scale fatigue test on the DH-112 Venom AC carried out on the fatigue history simulator by F & W, Emmen. Eidg. Flugzeugwerk Emmen, Bericht S-163, 1964.

[30] LOWNDES, H. B., MILLER, W. B., The U.S. Air Force Weapon Systems fatigue certification program. Paper presented at the 4th ICAF-AGARD Symposium, München, June 1965.

[31] SCHIJVE, J., Analysis of the fatigue phenomenon in alimunium alloys. NLR-TR M. 2122, July 1964.

[32] ROSENFELD, M. S., Aircraft structural fatigue research in the Navy. P. 216 of ref. 33.

[33] Symposium on Fatigue Tests of Aircraft Structures: Low-Cycle, Full-Scale and Helicopters. Los Angeles, Oct. 1962. ASTM, Special Technical Publication No. 338, 1963.

[34] BARROIS, W., Physical interpretation of metal fatigue. Minutes of the 5th conference of the International Committee on Aeronautical Fatigue, Brussels, Oct. 1957.

[35] WINKWORTH, W. J., Fatigue behaviour under service and ground test condition. RAE Technical Note, Structures 306, Nov. 1961.

[36] SCHIJVE, J., DE RIJK, P., The effect of ground-to-air cycles on the fatigue crack propagation in 2024-T3 Alclad sheet material. NLR Report M.2148, July 1965.

[37] MANN, J. Y., PATCHING, C. A., Fatigue tests on Mustang wings and notched aluminium alloy specimens under random gust loading with and without ground-to-air cycle of loading. Note ARL/SM.268, Melbourne, March 1961.

[38] FINNEY, J. M., MANN, J. Y., Fatigue behaviour of notched aluminium alloy specimens under simulated random gust loading with and without ground-to-air cycles of loading. P. 151 of ref. 14.

[39] NAUMANN, C. A., Evaluation of the influence of load randomization and of ground-air-ground cycles on fatigue life. NASA TN D-1584, Oct. 1964.

[40] SCHIJVE, J. AND BROEK, D., Crack propagation. The results of a test programme based on a gust spectrum with variable amplitude loading. Aircraft Engineering, vol. 34, p. 314, 1962. Also NLR MP. 208, Dec. 1961.

[41] GASSNER, E., HORSTMANN, K. F., Einfluss des Start-Lande Lastwechsels auf die Lebensdauer der böenbeanspruchten Flügel von Verkehrsflugzeugen. Advances in Aeronautical Sciences, Vol. 4, p. 763. Pergamon Press, London, 1961.

[42] CRICHLOW, W. J., MCCULLOCH, A. J., YOUNG, L. AND MELCON, M. A., An engineering evaluation of methods for the prediction of fatigue life in airframe structures. ASD Technical Report 61-434, March 1962.

[43] GASSNER, E., JACOBY, G., Betriebsfestigkeitsversuche zur Ermittlung zulässiger Entwurfsspannungen für die Flügelunterseite eines Transportflugzeuges. Luftfahrttechnik-Raumfahrttechnik, vol. 10, p. 6, 1964.

[44] SCHIJVE, J., Critical analysis of the fatigue damage concept and some consequences for fatigue testing of aircraft structures. Minutes, 4th Conference of the International Committee on Aeronautical Fatigue, Zürich, May, 1956, Appendix 2.

[45] SCHIJVE, J., JACOBS, F. A., Research on cumulative damage in fatigue of riveted aluminum alloy joints. NLR Report M. 1999, Jan. 1956.

[46] SCHIJVE, J., Estimation of fatigue performance of aircraft structures. P. 193 of ref. 33. Also NLR MP. 212, June 1962.

[47] MORDFIN, L. AND HALSEY, N., Programmed maneuver-spectrum fatigue tests of aircraft beam specimens. P. 251 of ref. 33.

[48] NAUMANN, E. C. AND SCHOTT, R. L., Axial-load fatigue tests using loading schedules based on maneuver-load statistics. NASA TN D-1253, May 1962.

[49] NAUMANN, E. C., Variable-amplitude fatigue tests with particular attention to the effects of high and low loads. NASA TN D-1522, Dec. 1962.

[50] YEOMANS, H., Programme loading fatigue tests on a bolted joint. RAE Tech. Note Structures 327, March 1963.

[51] GASSNER, E. AND SCHUTZ, W., Assessment of allowable design stresses and the corresponding fatigue life. Paper presented at the 4th ICAF-AGARD Symposium, München, June 1965.

[52] SCHIJVE, J. AND JACOBS, F. A., Programme-fatigue tests on aluminium alloy lug specimens with slotted holes and expanded holes. NLR Report M. 2139, Nov. 1964.

[53] HARTMAN, A., JACOBS, F. A., VAN DER VET, W. J., Constant load amplitude and programme fatigue tests on single lap joints in clad 2024-T3 and 7075-T6 aluminium alloy with two rows of rivets or Huckbolts. NLR Report M. 2147, July 1965.

[54] BULLEN, N. I., The chance of a rough flight. RAE Tech. Report 65039, Febr. 1965.

[55] JOST, G. S., The fatigue of 24 S-T aluminium alloy wings under asymmetric spectrum loading. Report ARL/SM. 295, Melbourne, Febr. 1964.

[56] HUSTON, W. B., Comparison of constant-level and randomized step tests of full-scale structures as indicators of fatigue-critical components. P. 133 of ref. 9.

[57] HEYWOOD, R. B., The effect of high loads on fatigue. IUTAM Colloquium on Fatigue, Stockholm, May 1955, p. 92. Ed. by W. Weibull and F. K. G. Odquist, Springer Verlag, Berlin.

[58] BOISSONAT, J., Experimental research on the effects of a static preloading on the fatigue life of structural components. P. 97 of ref. 14.

[59] SCHIJVE, J., The endurance under program-fatigue testing. P. 41 of ref. 9. Also NLR MP. 178, 1959.

[60] HUDSON, C. M. AND HARDRATH, H. F., Investigation of the effects of variable-amplitude loadings on fatigue crack propagation patterns. NASA TN D-1803, Aug. 1963.

[61] SCHIJVE, J., Fatigue crack propagation in light alloy sheet material and structures. Advances in Aeronautical Sciences, Vol. 3, p. 387. Pergamon Press, 1961. Also NLR-MP. 195, Aug. 1960.

[62] LEYBOLD, H. A., HARDRATH, H. F. AND MOORE, R. L., An investigation of the effect of atmospheric corrosion on the fatigue life of aluminum alloys. NACA Tech. Note 4331, Sep. 1958.

[63] LEYBOLD, H. A., The effects of combined prior stress and atmospheric corrosion on the fatigue life of aluminum alloy. NASA Tech. Note D-2359, Aug. 1964.

[64] RAITHBY, K. D., A comparison of predicted and achieved fatigue lives of aircraft structures. P. 249 of ref. 14.

TABLE 1

Survey of the load sequences

See text page 3

TABLE 2

Some general data on the fatigue tests

| *Type of loading* | *Specimen no.* | *X-rayed* | *Final failure* | | | *Fatigue life (test periods or cycles)* | | *Increase of life due to repairs* |
|---|---|---|---|---|---|---|---|---|
| | | | *Location* | *Wing* | *Station*[1] | $N^2$ | *at end of test* | |
| Random | 1 | no | At finger tips | P | Sta 1350 | 54 | 54 | —[3] |
| | 4 | no | At fingers tips | SB | Sta 750 | 38 | 38 | —[3] |
| Program | 2 | no | At finger tips | P | Sta 1350 | 50.5 | 50.5 | —[3] |
| | 5 | yes | Did not occur | | | 64 | 88.5 | 38% |
| Random +GTAC | 3 | yes | At finger tips | SB | Sta 750 | 24 | 28 | 17% |
| | 6 | yes | At repair | SB | Sta 1480 | 19 | 24 | 26% |
| Program +GTAC | 7 | yes | At repair | SB | Sta 520 | 29.5 | 34.5 | 17% |
| | 8 | yes | At finger tips | P | Sta 1350 | 27.5 | 41.5 | 51% |
| Const. ampl. (GTAC) | 9 | yes | At finger tips | SB | Sta 1350 | 19000 | 21500 | 13% |
| | 10 | yes | At finger tips | SB | Sta 750 | 21000 | 25000 | 19% |
| Const. ampl. (Gusts) | 11 | yes | At finger tips | SB | Sta 1350 | 32000 | 36760 | 15% |
| | 12 | yes | At finger tips | P | Sta 750 | 100000 | 185640 | 86% |
| | 13 | yes | Did not occur | | | 17000 | 20300 | 19% |

[1] Station number gives the distance to the plane of symmetry of the aircraft in mm.
[2] Fatigue life if no repairs had been made at the finger tips.
[3] In these tests no repairs at the finger tips were made.

TABLE 3

Comparison between the fatigue lives at the finger tips under random and program loading

| *Type of loading* | *Specimen nos* | *Fatigue life (test periods)* | *Life ratio (program/random)* |
|---|---|---|---|
| | | Mean $N^1$ | |
| R | 1 and 4 | 46 | 1.2 |
| Pr | 2 and 5 | 57.25 | |
| R+GTAC | 3 and 6 | 21.5 | 1.3 |
| Pr+GTAC | 7 and 8 | 28.5 | |
| | | $N_3(50\%)^2$ | |
| R+GTAC | 3 | 33.9 | 1.1 |
| Pr+GTAC | 8 | 37.1 | |

[1] $N$ is the fatigue life if no repairs had been applied at the finger tips. Data from table 2.

[2] $N_3$ (50%) is the fatigue life at 50% probability of failure, failure being defined as reaching a crack length of 3 mm. Data from table F1.

TABLE 4

Influence of the ground-to-air cycles (GTAC) on the fatigue life

| *Type of loading* | *Specimen nos* | *Fatigue life (test periods)* | *Life ratio (with GTAC/ without GTAC)* | |
|---|---|---|---|---|
| | | | *Tests* | *Predicted*[3] |
| | | Mean $N^1$ | | |
| R | 1 and 4 | 46 | | |
| R+GTAC | 3 and 6 | 21.5 | 0.47 | 0.56 |
| GTAC | 9 and 10 | 20 000 cycles | | |
| Pr | 2 and 5 | 57.25 | | |
| Pr+GTAC | 7 and 8 | 28.5 | 0.50 | 0.51 |
| | | $N_3$ (50%)[2] | | |
| Pr | 5 | 100.7 | | |
| Pr+GTAC | 8 | 37.1 | 0.37 | 0.43 |
| GTAC | 9 and 10 | 26 000 cycles | | |

[1] and [2], see footnotes at table 3.
[3] Prediction is based on the fatigue lives in column 3 of this table, employing the linear cumulative damage rule. There are 336 GTAC in one test period.

TABLE 5

The frequency of occurrence of the cracks for different load sequences

| *Type of crack* | *Code[1] number* | *Possible number of cracks in one tension skin* | *Number of cracks detected[2]* | | | | | | | |
|---|---|---|---|---|---|---|---|---|---|---|
| | | | *Variable-amplitude testing* | | | | *Constant amplitude testing* | | | |
| | | | *Spec. 1 and 4 R* | *Spec. 2 and 5 Pr* | *Spec. 3 and 6 R+GTAC* | *Spec. 7 and 8 Pr+GTAC* | *Spec. 9 and 10 GTAC* | *Spec. 13 High $P_a$* | *Spec. 11 Medium $P_a$* | *Spec. 12 Low $P_a$* |
| At end of bonded doubler | a1 | 80 | 5—11 | 9—27 | 8—18 | 5—50 | 15—18 | 11 | 30 | 19 |
| | a1′ | 80 | — | — | — | 0—5 | 0—4 | — | — | 1 |
| | a2 | 4 | 0—1 | — | 0—2 | — | — | — | — | 3 |
| | a3 | 12 | 0—6 | 0—2 | 0—1 | 3—5 | 0—2 | — | — | — |
| | a4 | 12 | — | — | 0—1 | — | — | — | — | — |
| At rivet or bolt holes | b1 | 4 | 0—1 | 1—3 | 0—4 | 0—2 | 3—4 | 3 | 4 | 1 |
| | b2 | 4 | — | — | (4)[3] | 0—1 | 1—3 | 3 | 4 | 4 |
| | b3 | 4 | — | — | (4)[3] | 1—2 | 1—2 | 4 | 3 | 4 |
| | b5 | 4 | — | 0—2 | — | — | — | — | — | — |
| | b6 | 4 | — | — | — | 0—1 | — | — | — | — |
| | b9/b9′ | 176 | — | — | — | — | 13—19 | 26 | 10 | 6 |
| | b10 | > 1000 | — | — | — | 1—6 | 14—19 | 83 | 58 | 21 |
| | b11 | 4 | — | — | — | — | 1—3 | 1 | — | 3 |
| | b12 | 8 | — | — | — | — | 0—1 | 1 | — | 2 |
| At open holes or sheet edges | c1 | 4 | 4 | 3—3 | 2—3 | 3—4 | 4 | 4 | 3 | 2 |
| | c2 | 16 | — | 0—2 | 1—3 | 0—1 | 5—7 | 8 | 6 | 4 |
| | c3 | 1 | 0—1 | 0—1 | 1—1 | 0—1 | 1—1 | 1 | 1 | 1 |
| | c4 | 2 | 2—2 | 1—2 | 0—2 | 2—2 | 1—2 | 2 | 2 | 2 |
| | c5 | 2 | 1—2 | — | 1—2 | 0—1 | 1—2 | 2 | 2 | 2 |
| | c6 | 2 | 0—2 | — | — | 0—1 | 2—2 | 2 | 1 | 2 |
| | c7 | 4 | 2—4 | 2—2 | 2—4 | 3—3 | 3—4 | 4 | 4 | 4 |
| | c8 | 4 | 1—2 | 1—2 | 0—2 | 1—2 | 1—2 | 2 | 3 | 2 |
| | c9 | 2 | 1—1 | 0—1 | 0—1 | 0—1 | 2—2 | 2 | 2 | 2 |
| | c10 | 2 | — | — | — | — | 0—1 | 1 | — | 2 |
| | c11 | 2 | — | — | — | — | 0—2 | 1 | 1 | 1 |
| | c12 | 2 | — | — | — | — | 0—1 | 1 | — | — |
| | c13 | 8 | — | — | — | — | 1—4 | 3 | 1 | 2 |
| | c14 | 4 | — | — | — | — | — | 1 | 2 | — |
| | c15 | 4 | — | — | — | — | 0—1 | — | — | — |
| | c19 | 12 | — | — | — | — | 1—3 | 2 | 1 | — |

[1] For the locations of the cracks see fig. 3, for additional comments see Appendix A.
[2] For two similarly tested specimens the smallest number has been given first for convenience.
[3] Small crack nuclei were indicated in specimen 3 by destructive testing after the test was completed.

TABLE 6

Damage calculations for fatigue lives

| *Type of crack* | $\Sigma\, n/N$ | | | |
|---|---|---|---|---|
| | *R* | *Pr* | *R+GTAC* | *Pr+GTAC* |
| b1 | 1.8 | 1.8 | 1.5 | 1.9 |
| c1 | 5.0 | 3.8 | 2.3 | 2.9 |
| c3 | 1.7 | 2.7 | 1.7 | — |
| c4 | 1.3 | 1.5 | 2.1 | 1.3 |
| c7 | 1.7 | 1.3 | 1.6 | 1.4 |
| c8 | 2.2 | 3.8 | 3.2 | 3.9 |
| c9 | 4.4 | 8.0 | 2.7 | 5.4 |
| Average | 2.6 | 3.3 | 2.2 | 2.8 |
| a1 | 1.5 | 1.8 | 1.0 | 1.4 |

TABLE 7

Damage calculations for crack propagation

| *Loading* | $\Sigma\, n_{3-20}/N_{3-20}$ |
|---|---|
| Pr | 1.0 |
| R+GTAC | 1.4 |
| Pr+GTAC | 1.5 |

$n_{3-20}$ is the number of cycles at a certain load amplitude during the crack propagation from 3 to 20 mm.

$N_{3-20}$ is the corresponding crack propagation life.

TABLE 8

Results of random load tests of Naumann (ref. 39)

See text page 15.

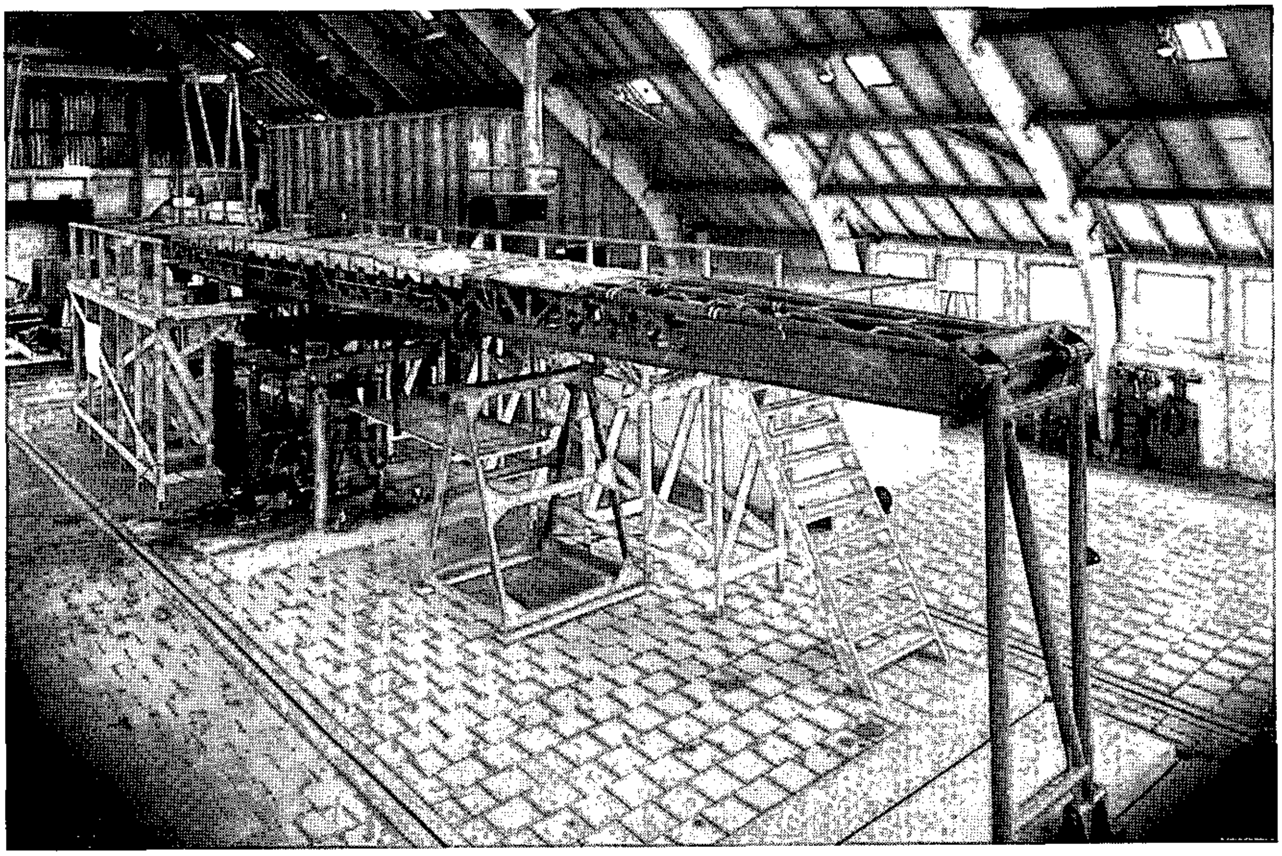

Fig. 1 General view of test set up.


Fig. 2 Inside view of specimen, SB, showing ribs 1040 (right) to 3050 (left). Specimen has failed.

The numbers in circles indicate the reference number of the type of crack. Number of rib shows distance to centerline (rib 0) in mm

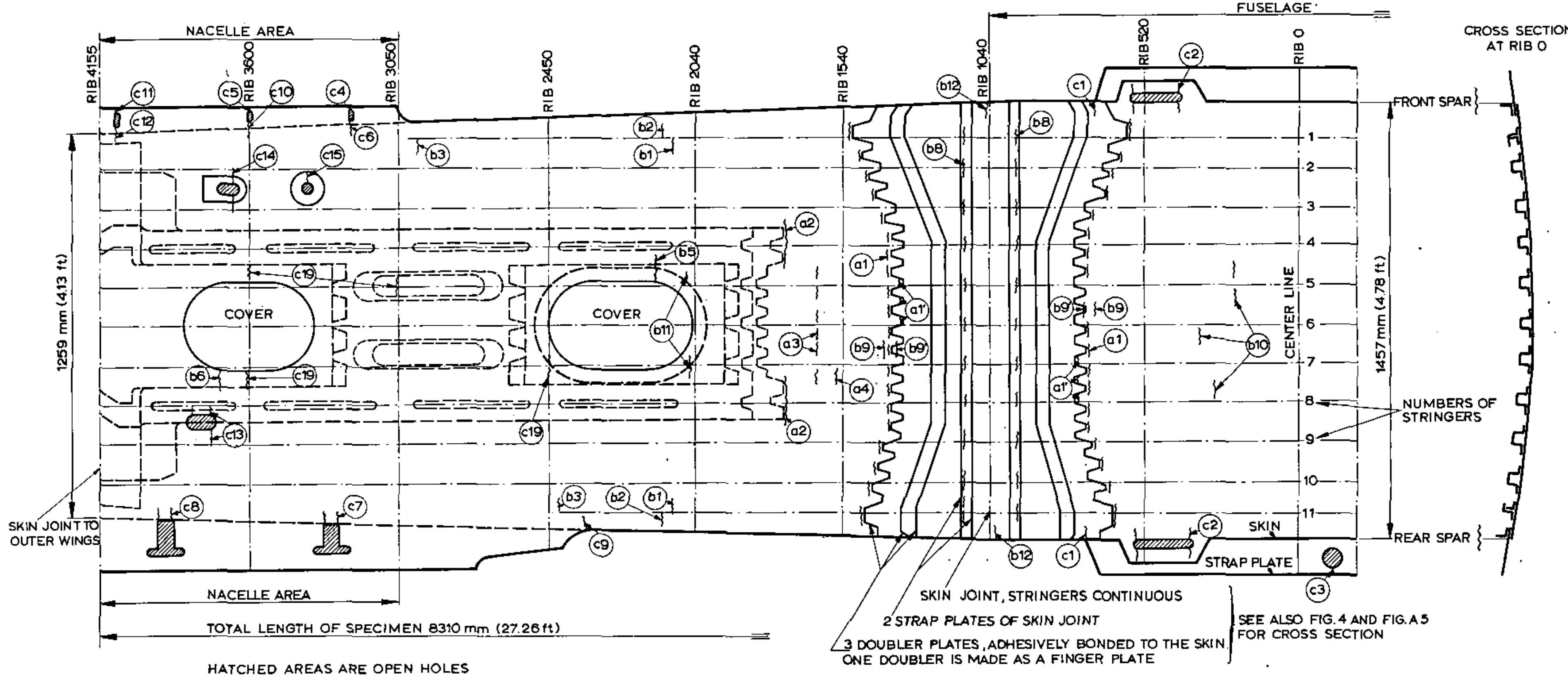


Fig. 3 Bottom plan view of specimen, SB half shown only.

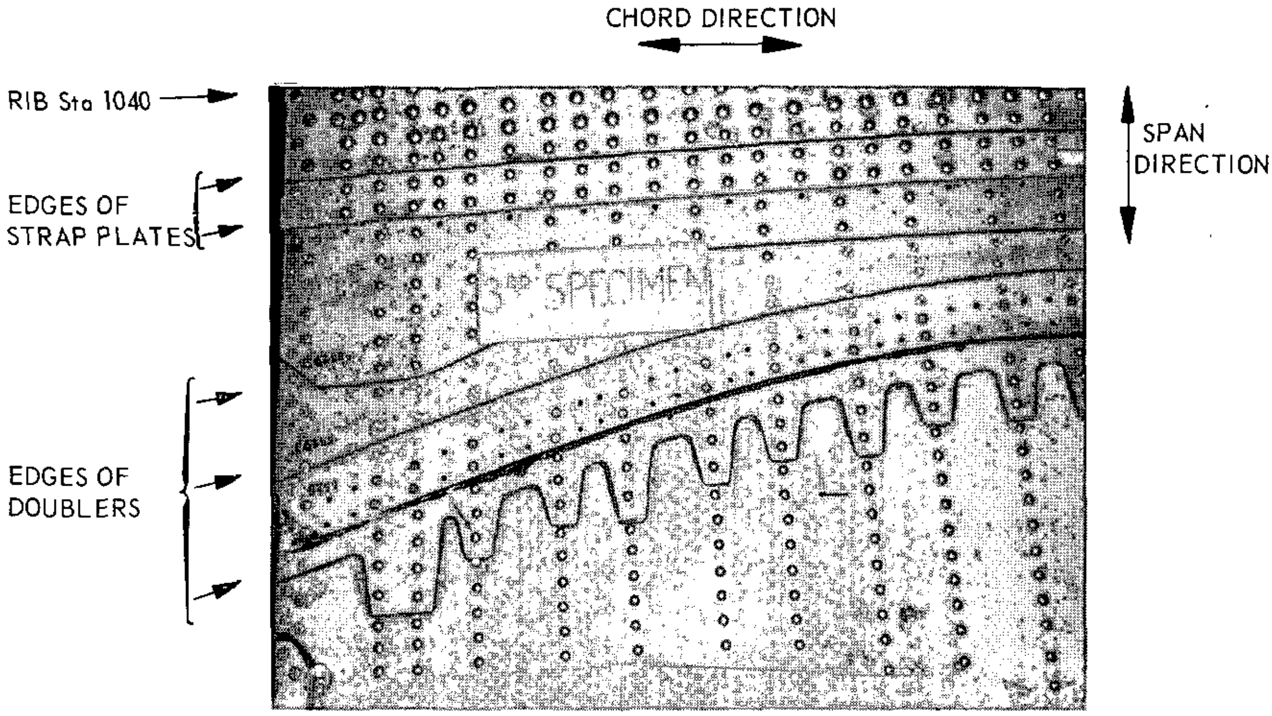


The thick black line is a remainder of a rubber sealing of the fuselage.

Fig. 4 Detail of the finger plate doubler with a crack (a1) in the skin.

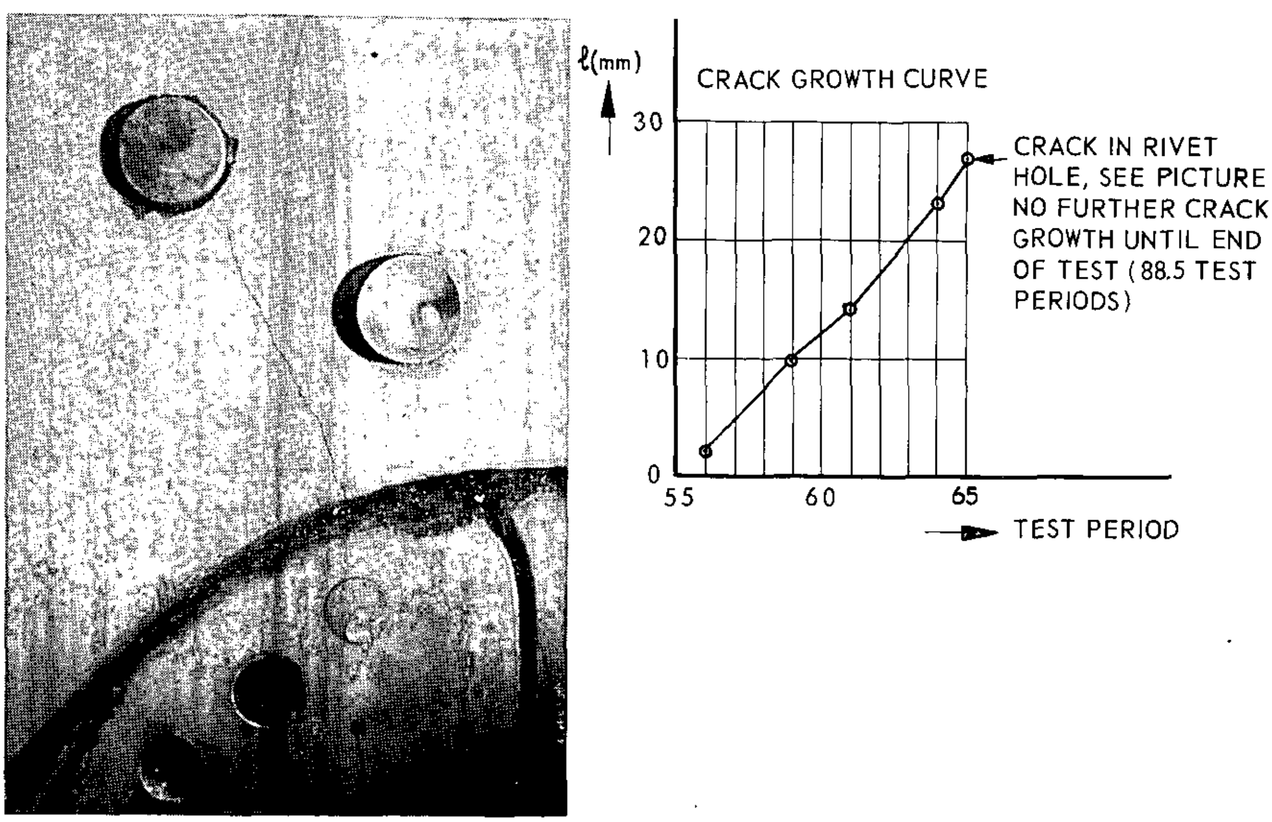


Magnification 1.5 ×

Fig. 5 Crack c9 in specimen 5 (SB).

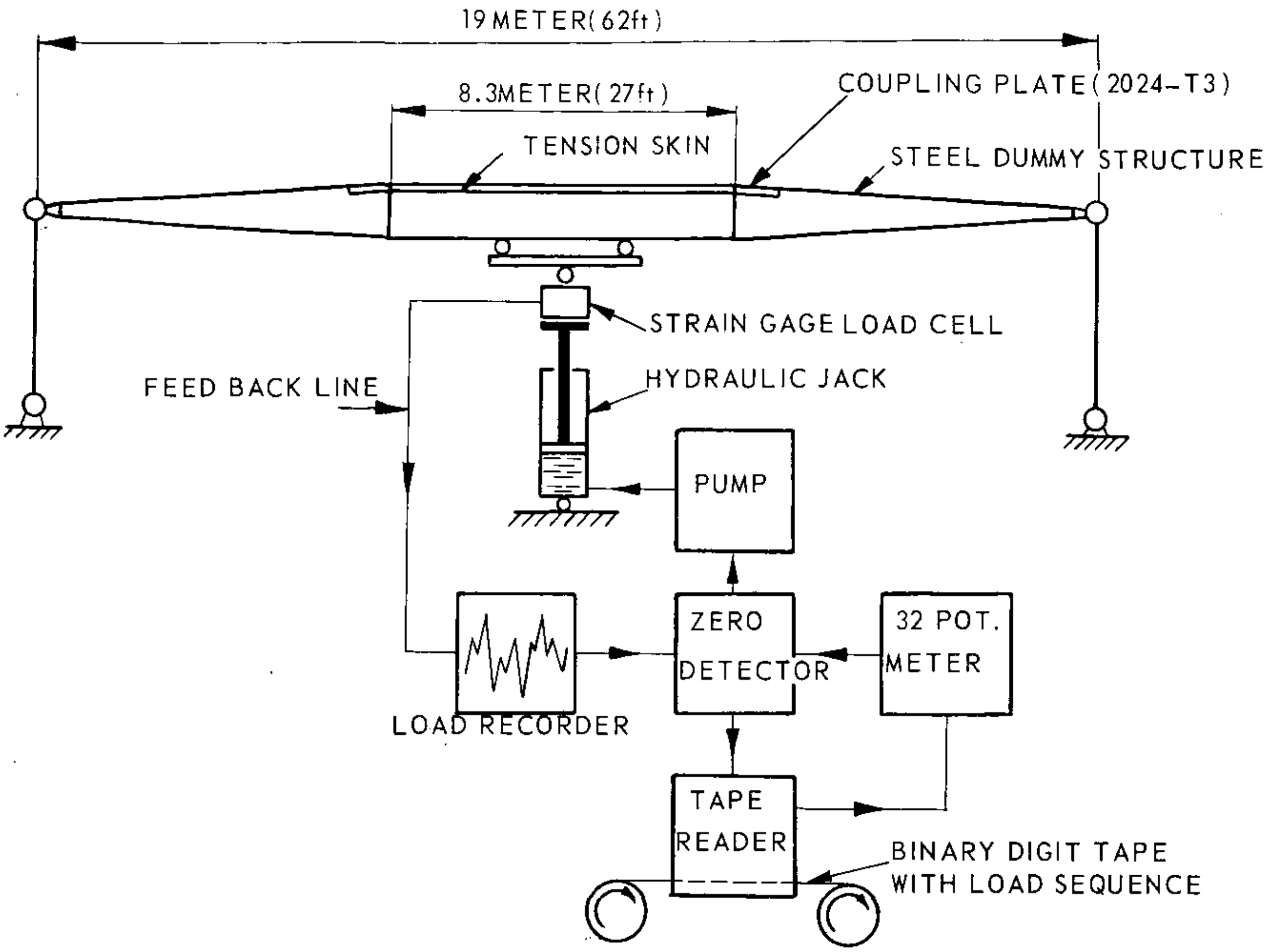


Fig. 6 Schematic view of test set-up.

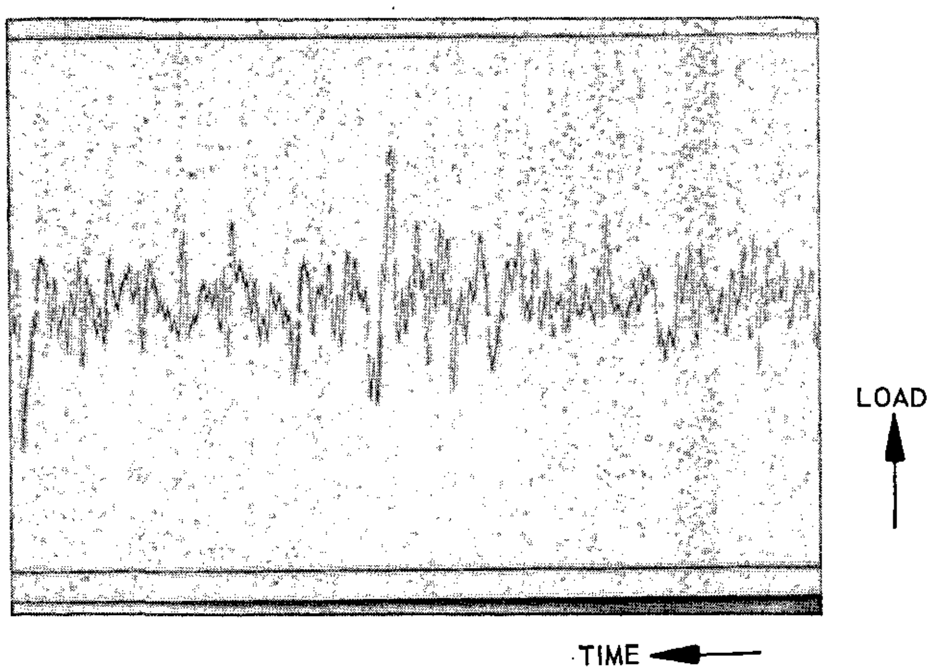


Fig. 7 Sample of the strain gage record, the aircraft flying in turbulent air.

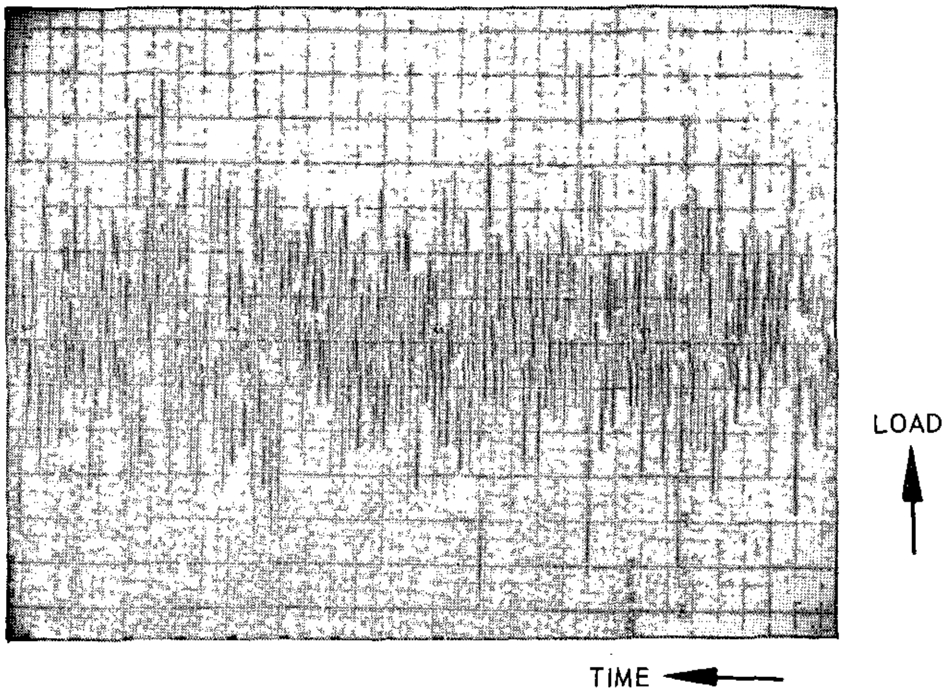


Fig. 8 Sample of a load recording during a random load test.

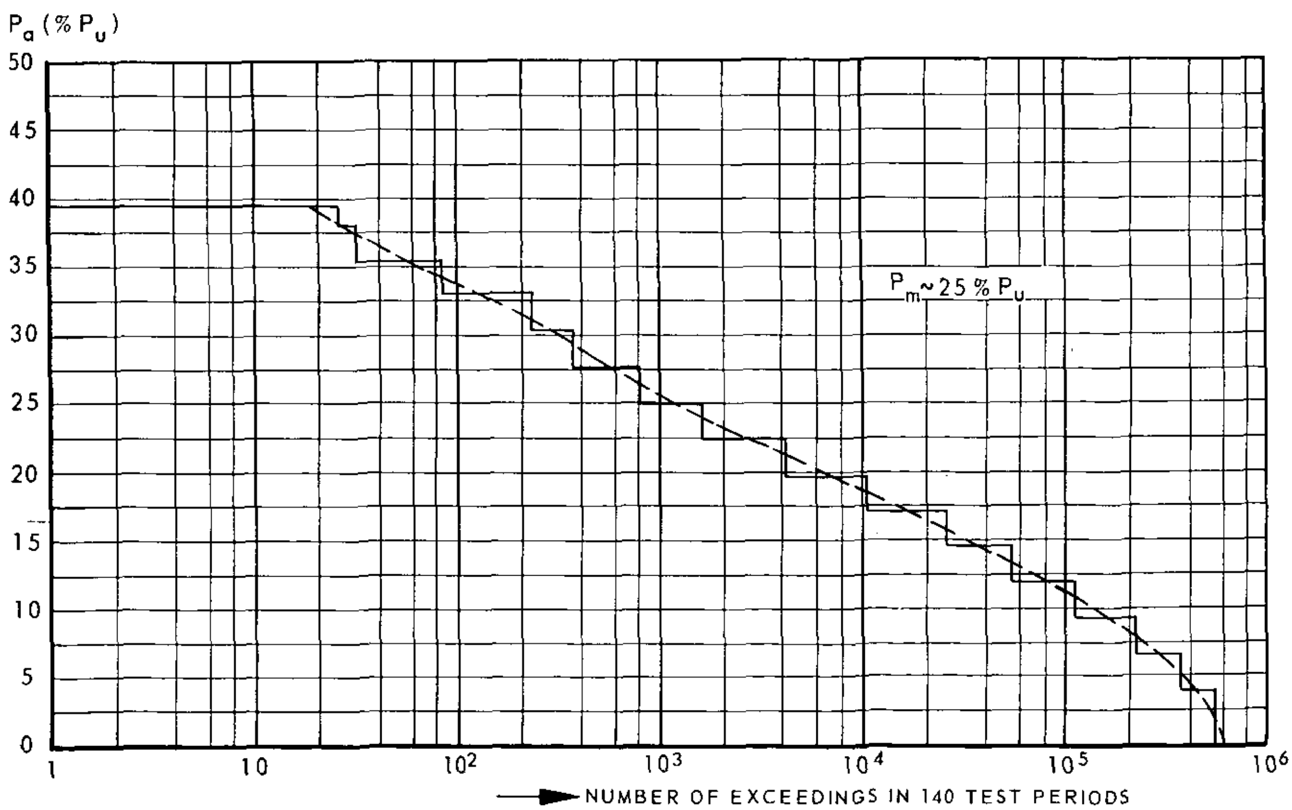


Fig. 9 Load spectrum ($P_a$) according to the mean-crossing peak count method.

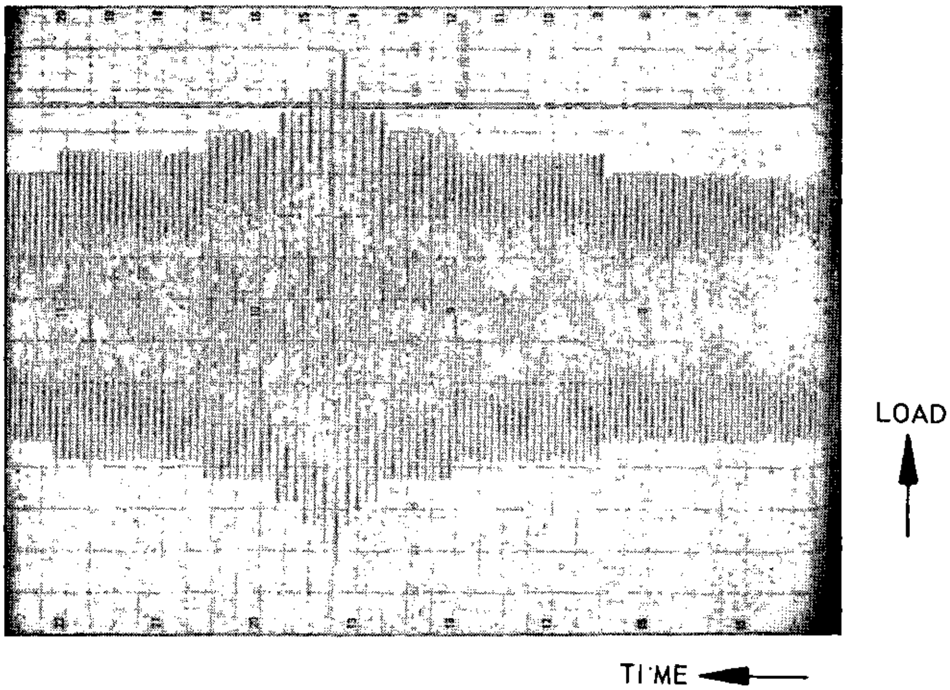


Fig. 10 Sample of a load recording during a program test.

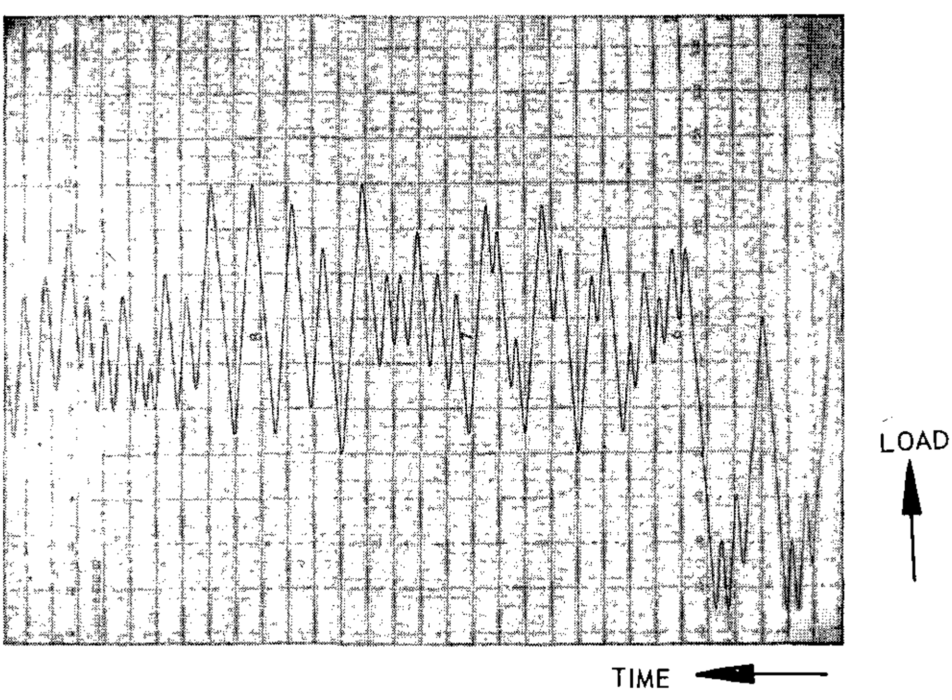


Fig. 11 Sample of a load recording during a random load test with ground-to-air cycles.

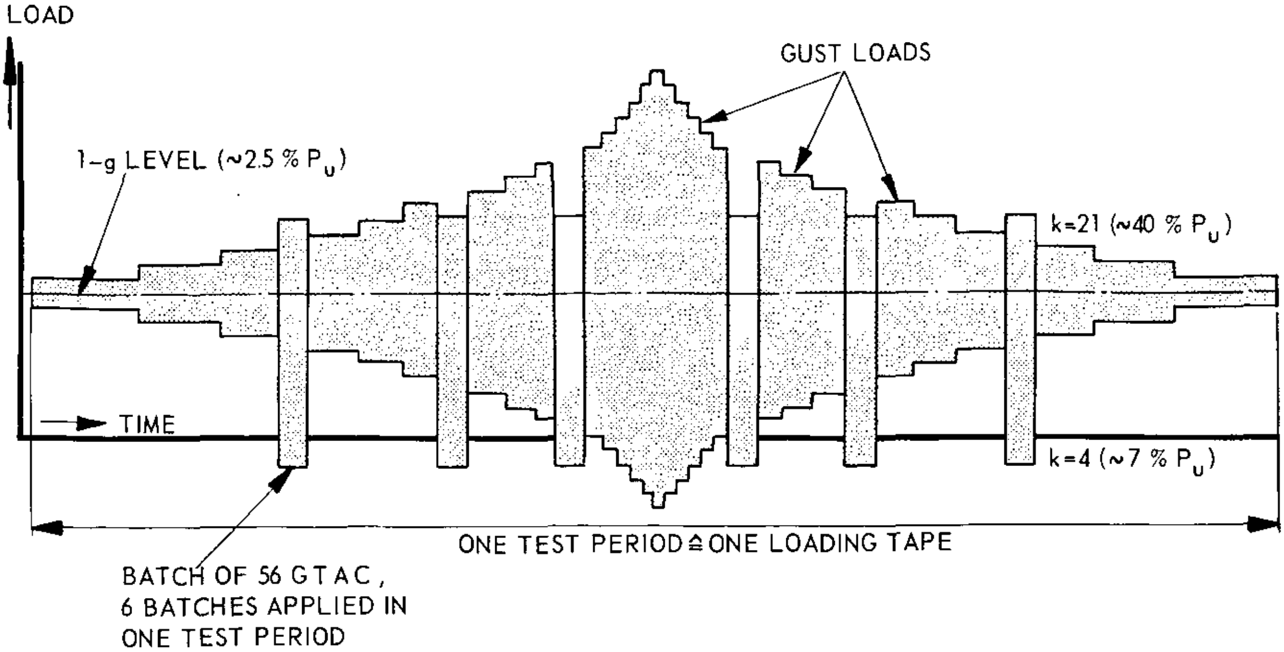


Fig. 12 Schematic picture of load sequence in one test period of a program test with ground-to-air cycles.

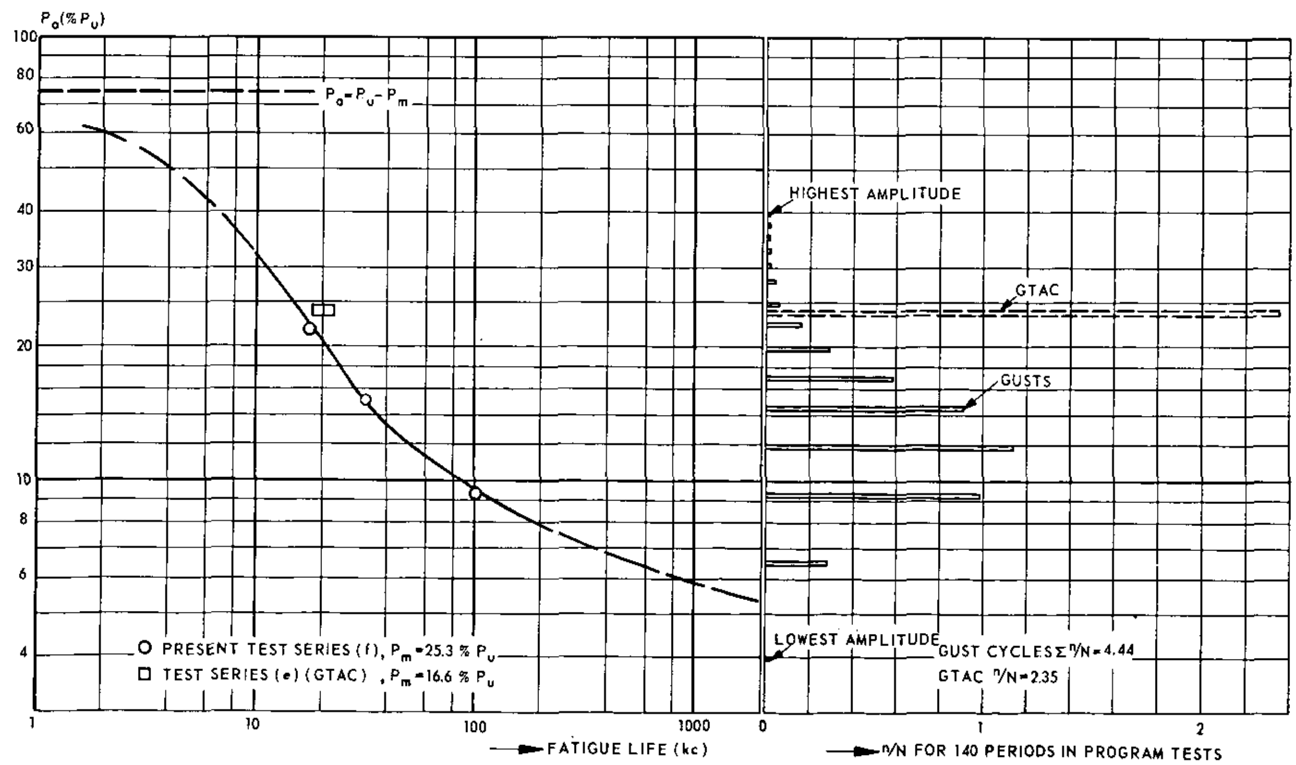


Fig. 13 Fatigue curve for failure at the finger tips and damage distribution.

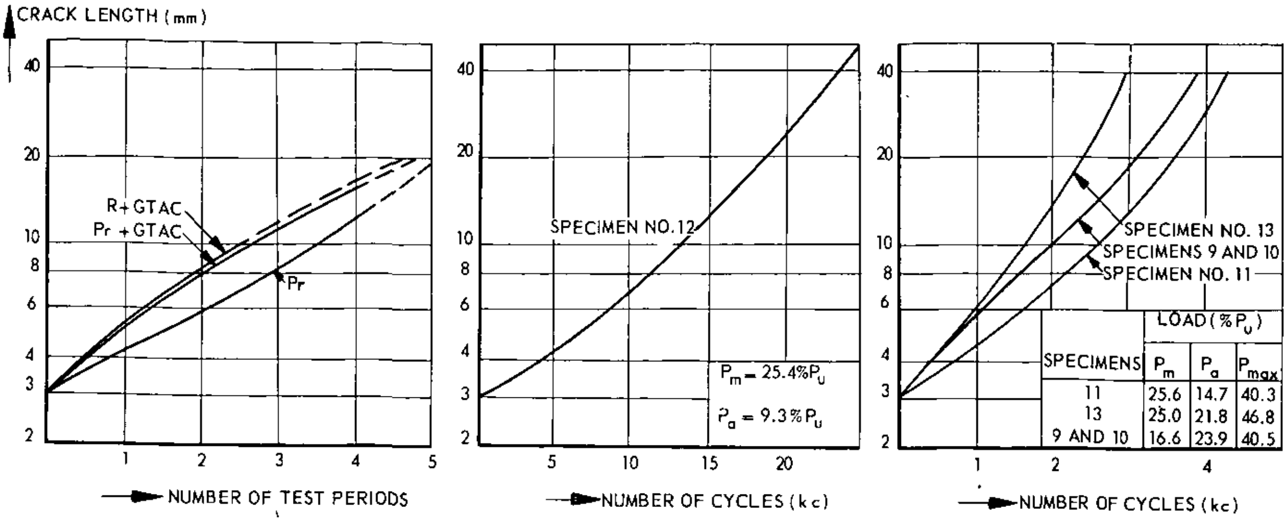


Fig. 14 Average crack propagation curves for the cracks at the finger tips.

Magnification 3 ×

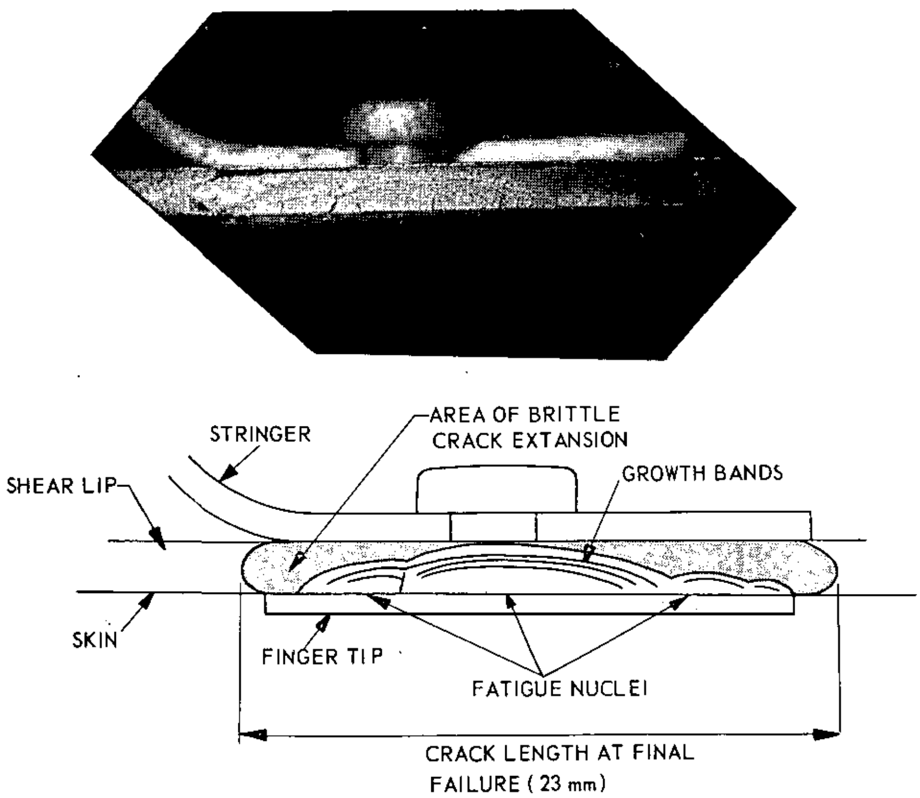


Fig. 15 Macroscopic features of fracture surface.

Magnification 220 times

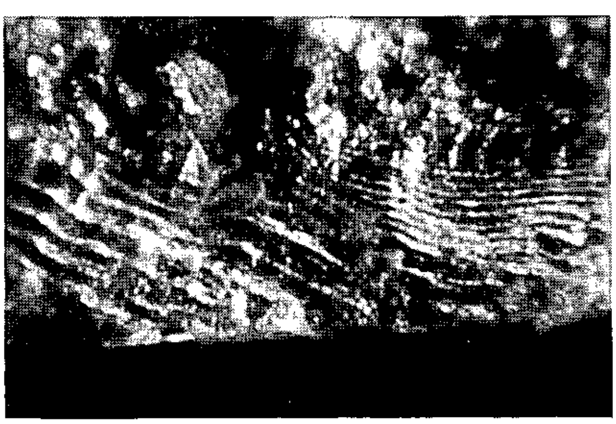

Fig. 16 Growth lines on the fracture surface shown in fig. 15.

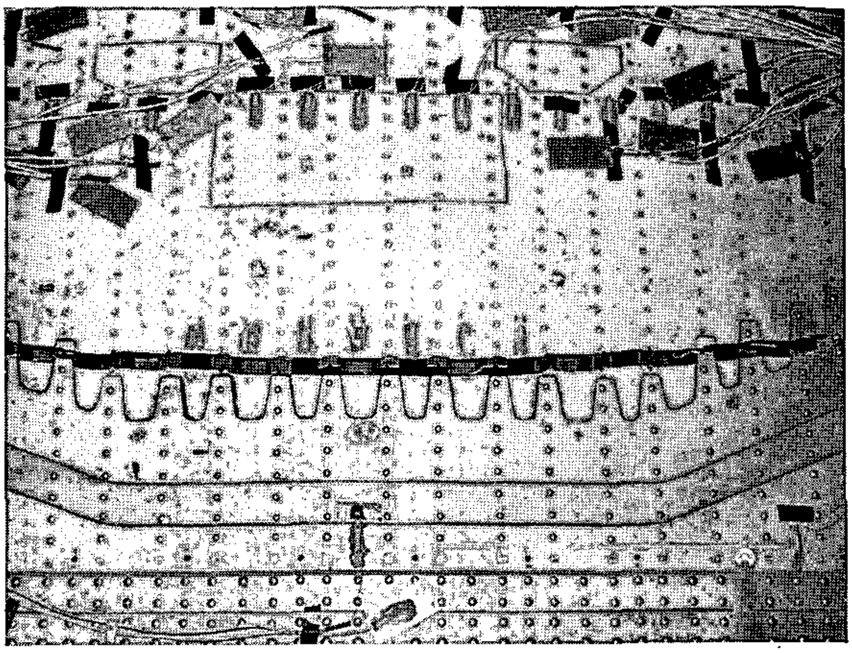

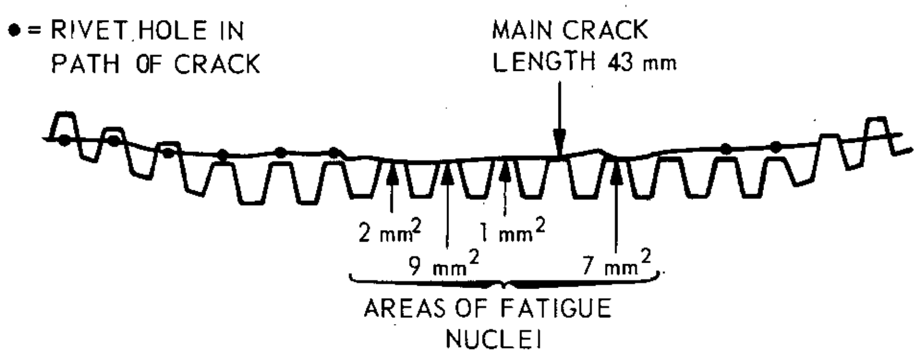


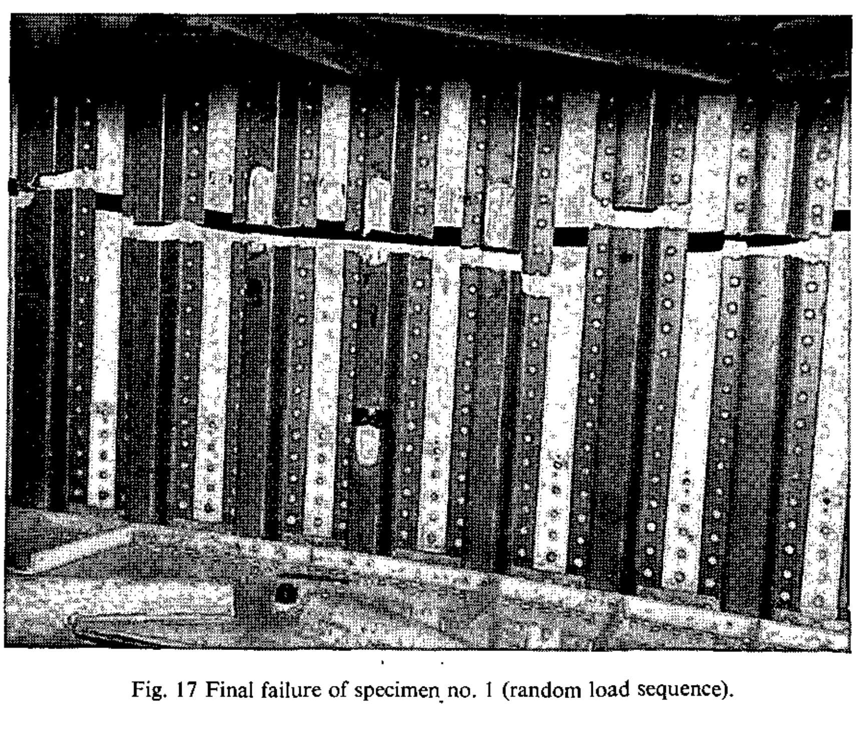

Fig. 17 Final failure of specimen no. 1 (random load sequence).

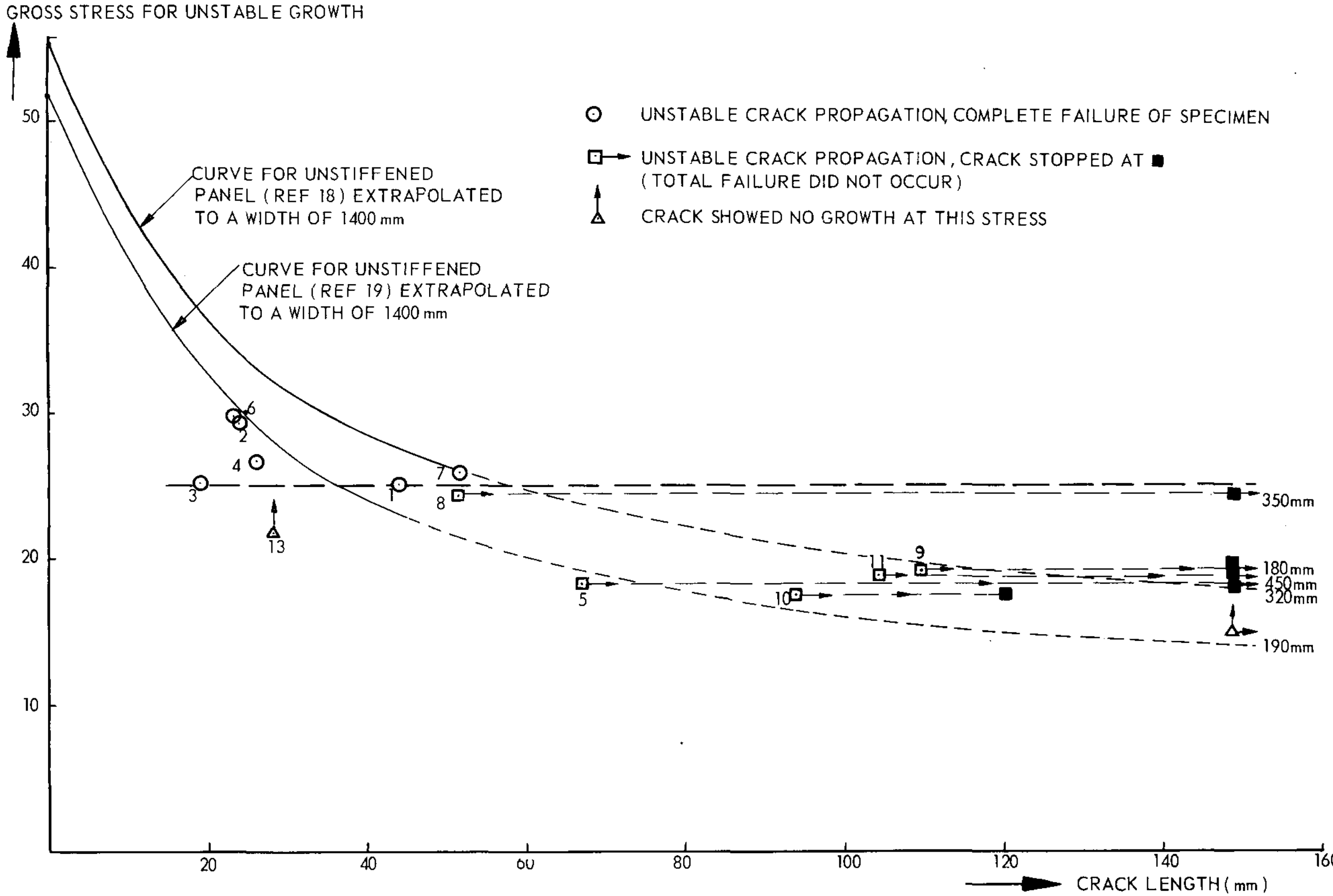


Fig. 18 Residual strength characteristics of the specimens.

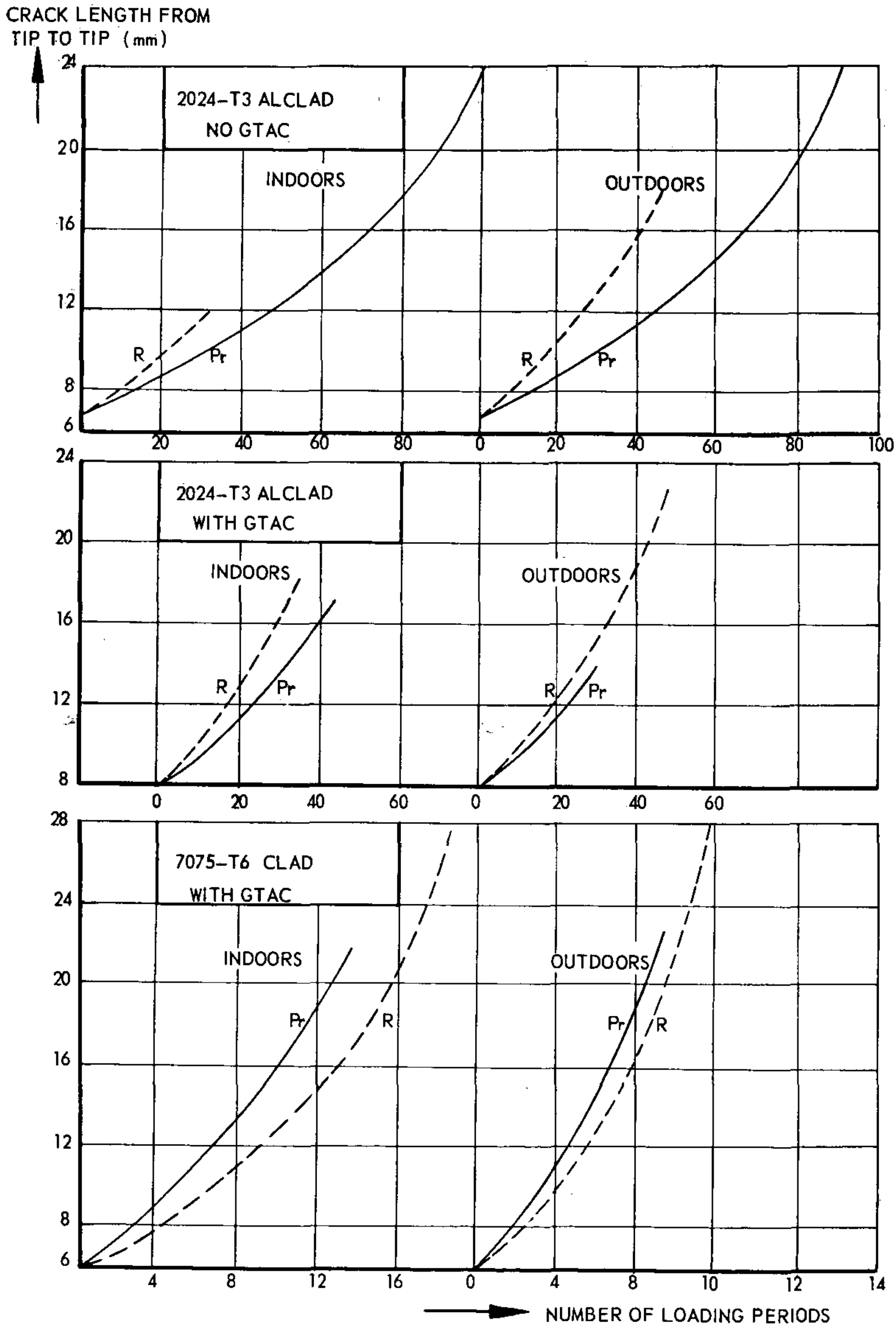


Average crack propagation curves of five central cracks in sheet specimens, loaded simultaneously with the tension skins of the present investigation. For all tests $S_m = 12.1$ kg/mm$^2$ and $S_{a,\max} = 11.6$ kg/mm$^2$.

Fig. 19 Comparison of the crack propagation under random loading and programmed loading. NLR investigation (ref. 27).

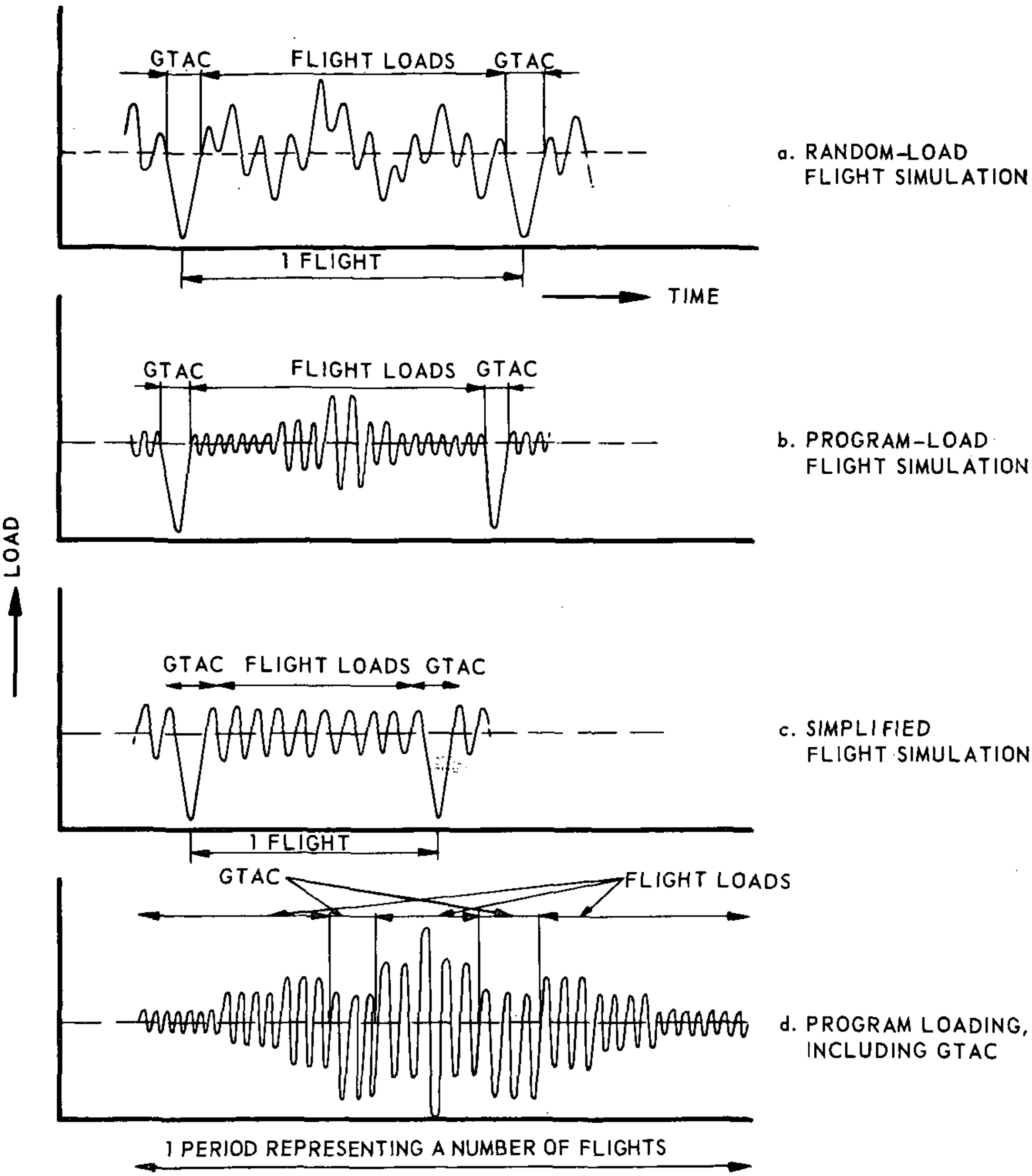


Fig. 20 Schematic pictures of combinations of flight loads and GTAC.

## APPENDIX A

### Survey of the cracks

In this Appendix brief comments are presented on the structural configuration at the locations of the cracks. The three categories of cracks mentioned in section 3.2 are successively discussed. Cracks b4, b7, c16, c17 and c18 were omitted from the survey. The first three of these cracks occurred in the covers and since the same covers were used in more than one test the fatigue lives could not be interpreted for the present purpose. Crack c17 was a consequence of a repair and crack c18 was incidentally found in the last specimens, whereas it could not be ascertained whether it had occurred in previous specimens.

*Cracks at the ends of adhesive bonded doublers*

*Crack a1.* The skin joint at rib 1040 is symmetric at both sides of rib 1040. The three reinforcing doublers are indicated in fig. 3 (see also fig. 4). The edge of the doubler on the skin was cut as a finger plate. Crack a1 originated in the skin from the edge of the fingertips, see fig. A1 (also fig. 4). Fingertips are present from front spar to rear spar, two at all hat stringers 2 to 10 and a single wider finger at stringers 1 and 11. In one specimen four fingerplates have a total of 80 fingers.

*Crack a1′.* This crack was of the same character as crack a1. Instead of growing from the fingertip it originated in the skin at the feet of the fingers, see fig. A1.

*Crack a2.* The crack in the skin (Sta. 1750) started from the edge of the first doubler plate (thickness 1.5 mm) that reinforced the cut out, see fig. 3. The doubler plate was bonded to the skin and the stringers (nos 4 and 8) were joggled over the edge of the doubler plate. There are four such joggles in one specimen.

*Cracks a3 and a4.* The flanges of stringers 5, 6 and 7, which terminate near the cover at rib 2040, are reinforced by staggered strips, partly bonded as indicated in fig. A2. Cracks of types a3 and a4 were found in the strips or in the stringer flange at the ends of bonded strips, as shown in the figure.

*Cracks at rivet holes and bolt holes*

*Crack b1.* The stringers 1 and 11 are built up from an angle section and a Z-stringer, joined by a single row of rivets, see fig. A3. Due to the tapering of the wing the stringers terminate near front and rear spar see figs. 2 and 3. At rib station 2024 the Z-section is tapered down and terminates, the angle section extending further. Cracks originated in the angle section at the last rivet connecting the two sections, see fig. A3. Four such end rivets are present in each specimen.

*Cracks b2 and b3.* Before terminating, both the Z-section and the angle section of stringers 1 and 11 are tapered down. The last rivets connecting the sections with the skin are again end rivets. Cracks in the skin originating from these end rivets are indicated in fig. 3 as b2 and b3, respectively, see also fig. A3. Each of these end rivets is found four times in a specimen.

*Cracks b5 and b6.* The covers are connected to the rabbets of the cut-outs by bolts. Crack b5 was initiated at a bolt hole in the rabbet, built up of bonded doubler plates, see fig. A4. Afterwards it also grew into the skin. The bolt in this hole is not an end bolt, but the hole is near the transition from the straight part to the semicircular part of the edge of the opening and is therefore in a region of stress concentration. A similar crack (type b6, see fig. 3) originated at the cover in the nacelle area.

*Crack b8.* At the skin joint at rib 1040 the stringers are continuous. At the outside of the structure two strap plates are joining the skin, which is locally reinforced by three bonded doublers, see fig. A5 (also fig. 3). Cracks were initiated at the holes from the end rivets of the joint, see fig. A5. The cracks first grew in the doublers and at a later stage penetrated into the skin.

*Cracks b9 and b9′.* These cracks started from rivet holes near the fingertip, viz. the first hole ahead of the fingertip and the first hole on the fingertip, see fig. A1. The latter crack occurred in the skin and in general not in the fingerplate.

*Crack b10.* Cracks in the skin starting from apparently arbitrary rivet holes were found between rib 1040 SB and rib 1040 P (fig. 3). The cracks had the same character as cracks b9 and b9′.

*Crack b11.* The hat sections of stringers 5, 6 and 7 terminate at the cut out between ribs 2040 and 2540 (figs. 2 and 3). Stringers 5 and 7 extend further as L-sections. The hat section, cut down to its top hat (U-section), is riveted to the L-section. Cracks started in the L-section from the hole of the end rivet, see fig. A6.

*Crack b12.* The crack occurred in the outer strap plate of the skin joint at rib Sta 1040 (see fig. A5) near the front or rear spar (see fig. 3). It started from a rivet hole nearest to Sta 1040, which is an end rivet for the strap plate.

*Cracks starting from open holes and sheet edges*

*Crack c1.* Cracks of this type were initiated at rounded corners (radius 18 mm) of the edge of a strap plate near rib 520 at the front spar and the rear spar, see fig. 3. The cracks grew in the strap plate between the skin and the spar cap.

*Crack c2.* At rib 520 there are open holes in the skin and the strap plate (fig. 3). Forgings for the connection of the wing to the fuselage passed through these holes. The forgings were not present on the specimens. Cracks c2 started from the corners (radius 6 mm) of the holes, see fig. 3.

*Crack c3.* In the strap plate at the rear spar near rib 0 there is another open hole with a diameter of 53 mm. A crack was initiated at this hole and grew to the free edge of the strap plate, see fig. 3, crack type c3. There is only one such hole in a specimen.

*Cracks c4–c8 and c10–c12.* Cracks were initiated from open holes in the nacelle region, see fig. A7. The skin is protruding ahead of the front spar and behind the rear spar. The holes are present for connection purposes of the nacelle and for auxiliary equipment.

*Crack c9.* This crack started from the edge of the skin at the rear spar near rib 2540, see fig. A7. A picture of a crack of this type is shown in fig. 5.

*Cracks c13–c15.* In the nacelle area there are open holes between stringers 2 and 3 and between stringers 8 and 9, see fig. 3. Equipment and control lines are passing through these holes. Cracks c13–c15 started in the skin from the edges of the reinforced holes (radii 20, 20 and 25 mm, respectively).

*Crack c19.* Cracks of this type occurred in the L-section of stringers 5 and 7 (see description of crack b11). Cutaways in the top of the L-sections permitted the passing of the flanges of three ribs, see fig. A6. Cracks started from the edges of the cutaways (radii from 30–60 mm).

It should be pointed out that several cracks cannot be considered as typical for the pre-modification F-27 design in view of the difference between the specimen and the actual aircraft, such as the connection to the fuselage, the nacelles and the leading and the trailing edges.

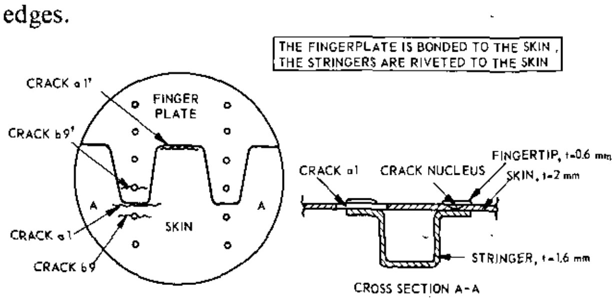


Fig. A1 The locations of the cracks near the finger tips.

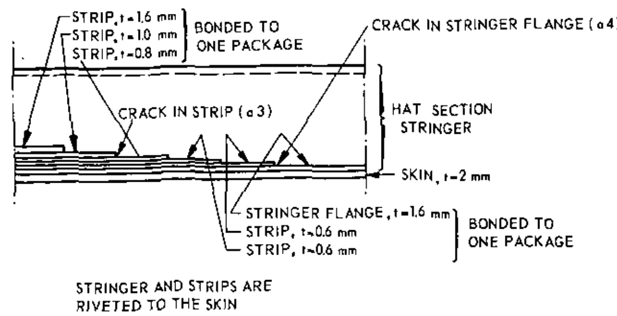


Fig. A2 Location of cracks in stringer flange and strip at the reinforcing strips (crack type a3 and a4).

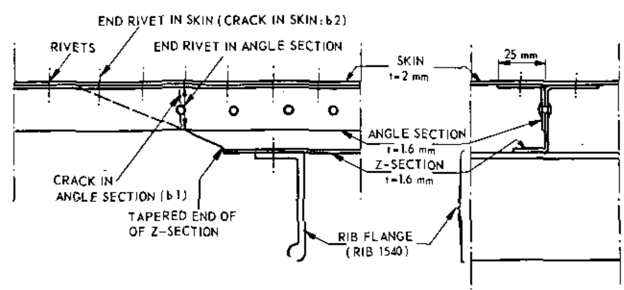


Fig. A3 *Cracks at end rivet in the angle of section of stringers I and II (crack type b1).*

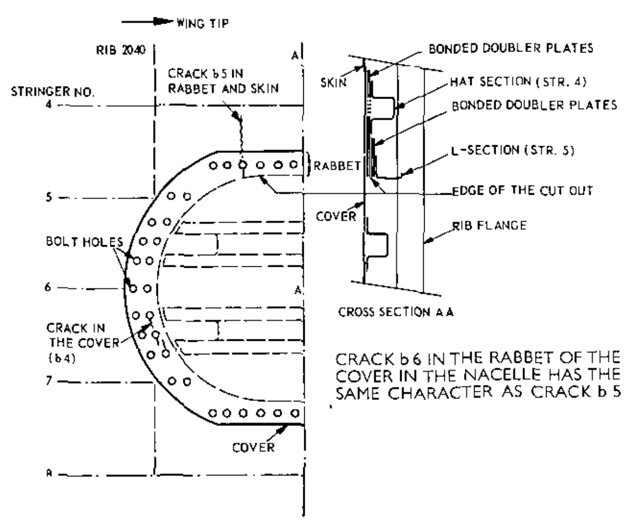


Fig. A4 Crack b5 starting from a bolt hole in the rabbet of the cover between ribs 2040 and 2540 (see fig. 3).

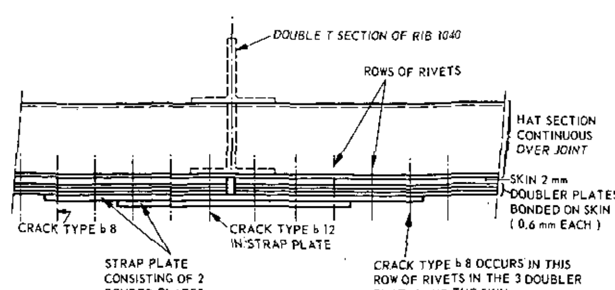


Fig. A5 Cross section of skin joint at rib 1040.

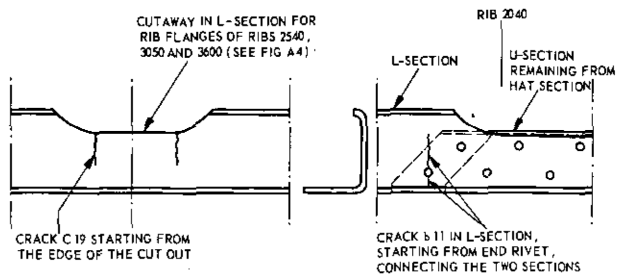


Fig. A6 Cracks b11 and c19 in the L-section of stringers 5 and 7.

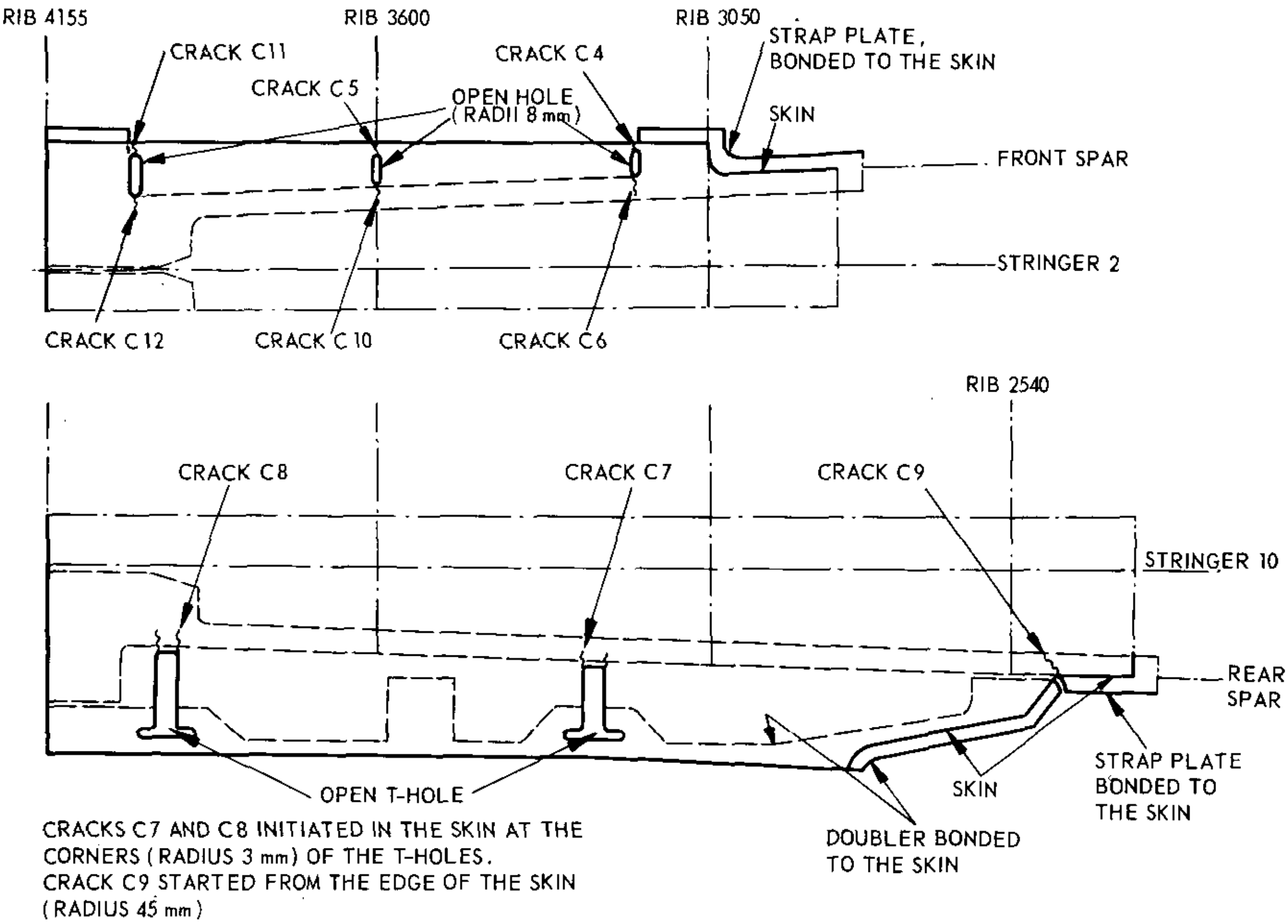


Fig. A7 Cracks in the skin starting from open holes (c4–c8, c10–c12) and from the edge of the skin (c9) near the spars in the nacelle region.

## APPENDIX B

### Measurements of the loads

The load on the strain gage dynamometer was continuously recorded on a strip-chart recorder during all tests. The dynamometer with the recorder were calibrated 10 times during the investigation. The standard deviation of the calibration factor was 0.4% of the mean value of this factor, which is considered to be an excellent result. It was further ascertained by employing a second dynamometer and a U.V.-recorder that the static calibration of the strip-chart recorder was also valid for the fatigue loading.

The loads were measured from the load records. The average values of the load amplitudes in the eight variable-amplitude tests are given in table B1. For each amplitude the standard deviation of the eight values was calculated. There appeared to be a low scatter, the average standard deviation being 0.2% $P_u$, which is 0.25% of the difference between the maximum and the minimum loads applied in the tests. This is a very favorable result for a fatigue test. The scatter of the load within a single test was of the same order of magnitude or lower.

The loads obtained from the records of the constant-amplitude tests have been compiled in table B2. For the GTAC the results for the program and the random tests with GTAC were included for comparison. The differences between the GTAC in these tests and in the constant-amplitude tests are negligible.

TABLE B1

The fatigue loads applied in the eight variable-amplitude tests

| *Load levels*[1] *($k_{max}$–$k_{min}$)* | $P_a$ (% $P_u$) for specimen no. 1 | 2 | 3 | 4 | 5 | 6 | 7 | 8 | *Mean* $P_a$(% $P_u$) | $\sigma$ (% $P_u$) |
|---|---|---|---|---|---|---|---|---|---|---|
| 17—15 | 4.0 | 4.2 | 4.1 | 3.8 | 3.8 | 3.9 | 3.9 | 3.8 | 3.94 | 0.15 |
| 18—14 | 6.6 | 6.9 | 6.6 | 6.3 | 6.6 | 6.6 | 6.6 | 6.4 | 6.58 | 0.16 |
| 19—13 | 9.0 | 9.6 | 9.3 | 9.0 | 9.4 | 9.1 | 9.3 | 9.1 | 9.23 | 0.21 |
| 20—12 | 11.7 | 12.0 | 11.9 | 11.7 | 12.0 | 11.9 | 12.0 | 11.9 | 11.89 | 0.12 |
| 21—11 | 14.4 | 14.6 | 14.4 | 14.3 | 14.4 | 14.5 | 14.6 | 14.5 | 14.46 | 0.12 |
| 22—10 | 16.8 | 17.3 | 17.1 | 16.8 | 17.0 | 17.2 | 17.3 | 17.1 | 17.08 | 0.20 |
| 23— 9 | 19.5 | 19.8 | 19.76 | 19.5 | 19.5 | 19.8 | 19.9 | 19.7 | 19.68 | 0.16 |
| 24— 8 | 22.0 | 22.5 | 22.4 | 22.1 | 22.3 | 22.4 | 22.4 | 22.3 | 22.30 | 0.17 |
| 25— 7 | 24.7 | 25.1 | 25.1 | 24.3 | 24.9 | 25.1 | 25.0 | 24.9 | 24.89 | 0.27 |
| 26— 6 | 27.4 | 27.9 | 27.9 | 26.9 | 27.6 | 27.8 | 27.6 | 27.5 | 27.58 | 0.33 |
| 27— 5 | 30.0 | 30.6 | 30.6 | 30.1 | 30.3 | 30.3 | 30.2 | 30.1 | 30.28 | 0.23 |
| 28— 4 | 32.4 | 33.2 | 33.0 | 32.6 | 32.8 | 33.0 | 32.9 | 32.6 | 32.81 | 0.26 |
| 29— 3 | 35.1 | 35.6 | 35.4 | 35.1 | 35.3 | 35.6 | 35.6 | 35.3 | 35.38 | 0.21 |
| 30— 2 | 37.8 | 38.2 | 37.7 | 37.5 | 37.7 | 38.0 | 38.1 | 37.9 | 37.86 | 0.23 |
| 31— 1 | 39.9 | 40.2 | 39.3 | 39.0 | 39.3 | 39.6 | 39.5 | 39.5 | 39.54 | 0.37 |
| *Mean value* | 22.1 | 22.5 | 22.3 | 21.9 | 22.2 | 22.3 | 22.3 | 22.2 | | 0.2 |

[1] The mean load in the fatigue test is load level no. 16; load levels nos 17 to 31 are above the mean load and load levels 1 to 15 are below the mean load.

TABLE B2

The loads applied in the constant-amplitude tests

| *Test series* | *Loads* | *Specimen no.* | *Magnitude of loads (%$P_u$)* $P_{max}$ | $P_{min}$ | $P_a$ | $P_m$ |
|---|---|---|---|---|---|---|
| e | GTAC | 9 and 10 | 40.5 | —7.2 | 23.85 | 16.65 |
| c and d | | 3, 6, 7 and 8 | 40.2 | —7.0 | 23.6 | 16.6 |
| | | 11 | 40.3 | 10.9 | 14.7 | 25.6 |
| f | Gusts | 12 | 34.7 | 16.0 | 9.35 | 25.35 |
| | | 13 | 46.8 | 3.2 | 21.8 | 25.0 |

## APPENDIX C

### X-ray inspections

Cracks in the skin emanating from the ends of adhesive bonded doublers (cracks of category a, see Appendix A) were hard to observe visually since they were hidden by the excess of adhesive at the edge of the doubler. This especially applies to crack type al since after penetration through the skin the crack was hidden there under stringer flanges. For this type of crack, which occurred quite frequently, the X-ray method was extensively used.

All X-ray pictures were made by the Röntgen Technische Dienst (Dutch firm specialized on non-destructive testing) with a 60 kV X-ray unit. X-ray inspections were made in 10 of the 13 tests starting at approximately 50% of the anticipated fatigue life. Pictures were made at the end of each test period. The specimen was loaded slightly above the mean load (25% $P_u$) to increase the sensitivity. The effect of loading the structure is clearly shown in the table below (results of specimen no. 3)

| *Crack no.* | *Crack length (mm) on the X-ray film at four different loads* 25% $P_u$ | 12.5% $P_u$ | 5% $P_u$ | 0% $P_u$ |
|---|---|---|---|---|
| 13 | 4 | — | — | — |
| 14 | 3.7 | 3 | — | — |
| 17 | 8.5 | 3 | — | — |
| 12 | 3 | | — | |
| 13 | 16.5 | | 16 | |
| 14 | 21 | | 21 | |
| 15 | 8 | | — | |
| 16 | 4 | | — | |
| 17 | 23 | | 23 | |

In the table a horizontal dash means that the crack was invisible. The stress in the skin at $P_u$ was in the order of 40 kg/mm$^2$ (56 ksi). The three longest cracks were through cracks whereas the other cracks were part-through cracks. The latter ones could not be detected on the X-ray films at $P = 5\%\ P_u$.

Destructive testing of coupons cut from the skin of specimen no. 3, including a single finger tip each, indicated that the length of a through crack indicated on the X-ray film was equal or slightly smaller than the actual length. For the part-through cracks, however, the length on the film was some 30 to 50% less, depending on the penetration. Cracks with an average depth of penetration below 0.4 mm (20% of skin thickness) were not indicated at all on the X-ray films. A through crack was clearly visible on the X-ray film as a sharp black line. The part-through cracks produced faint lines on the film only. Apparently the opening of the crack is of great importance for the sensitivity of the X-ray inspection.

Crack type a2 did not occur frequently. In a few cases X-ray inspections were unsuccessful for this type of crack although some through cracks were present. Probably the X-ray tube was not correctly positioned in line with the plane of the crack.

Crack b8 was initiated from rivet holes under the strap plates at the skin joint at Sta 1040. This crack was also inaccessible for visual inspection. The X-ray method was successful in this case. Inspections were made on the last three specimens only, since the crack had not been detected in the first 10 specimens.

It should be noted that the conditions for taking X-ray pictures were very favorable as compared with taking pictures of a complete wing structure in service. First a tensile load could be applied and, secondly, the pictures had not to be taken through the compression skin, which was absent in the present test series.

## APPENDIX D

### Summary of the strain measurements

This Appendix has been based on refs. 3 and 7. The strain gages were bonded to the outside and the inside of the tension skins and the coupling plates. Measurements were made on each tension skin before fatigue testing started by loading the skin to approximately $30\% P_u$ and continuously recording the strain gage output as a function of the load on the structure. The records were linearly extrapolated to $100\% P_u$ and from these results the stresses $S_u$ (at $100\% P_u$) were calculated, adopting an E-value of 7240 kg/mm² (10300 ksi).

The number of gages bonded to specimens nos. 1, 2 and 8 were 120, 82 and 74, respectively; the number for the specimens nos. 3–7 and 9–13 was 24. The stress level (at $P_u$) in the skin near the finger tips was in the order of 40 kg/mm² (57 ksi). At other locations at which cracks were found the stress level varied from 25 to 35 kg/mm² (35 ksi to 50 ksi). As an example of the results the chordwise stress distribution near the finger tips is shown in fig. D1.

Since 24 gage locations were adopted in all 13 tests, the scatter of the stresses at these locations could be determined. For the stress at a certain location the standard deviation of the 13 test results was calculated. The average of the 24 calculated standard deviations was 1.09 kg/mm² (1.55 ksi), corresponding to approximately 3% of the indicated stress levels. After the 24 stress values of each specimen were averaged, the standard deviation of these average stress levels was 0.56 kg/mm² (0.80 ksi) or 1.5% of the average stress level $S_u = 36.9$ kg/mm² $\triangleq$ 52.5 ksi. The latter values are small enough to conclude that the specimens as mounted on the dummy structure were loaded in the same way in all tests.

A further confirmation of this conclusion is offered by the strain measurements on the two coupling plates (see fig. 6). Ten gages were bonded to each coupling plate and apart from a few gages that were damaged during the investigation, the gages remained on the plates during all tests. The average of the standard deviations of the stresses (at $P_u$) was 0.28 kg/mm² (0.40 ksi) or 1.7% of the indicated stress. The standard deviation of the average stresses in the coupling plates was 0.19 kg/mm² (0.27 ksi) or 1.1% of the indicated average stress ($\bar{S}_u = 16.7$ kg/mm² $\triangleq$ 23.8 ksi).

In the course of some fatigue tests, testing was interrupted for carrying out additional static and dynamic strain measurements. In all cases these static measurements were in good agreement with the measurements made before the fatigue test on the specimen started. The dynamic strain-measurements indicated approximately 3% higher stresses than the values calculated from the applied fatigue loads on the basis of the static strain measurements. This was due to a small overshoot induced by the massive test rig.

As a general remark it may be said that the low scatter of the strain measurements have fully confirmed the reliability of the strain gage technique.

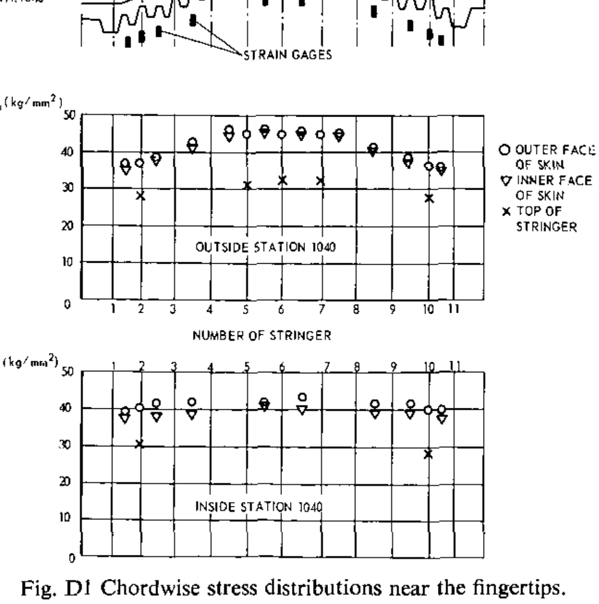


Fig. D1 Chordwise stress distributions near the fingertips.

## APPENDIX E

**Statistical properties of the random load**

A random load sequence can be analysed according to various counting methods or by the power spectral method. These methods are extensively discussed in ref. 15. The counting methods are based on three types of occurrences, viz. peaks (maxima and minima), ranges (differences between maxima and minima) and level-crossings. The following counting methods, illustrated in fig. E1, will be considered:

*Peak count method (fig. E1a)* All maximum values and all minimum values of the load-time history are counted. The restriction can be made that only maximum values above the mean load and minimum values below the mean load are counted.

*Mean-crossing peak count method (fig. E1b)* Between two successive mean-crossings only one count is made, viz. the highest maximum or the lowest minimum. The number of counts is necessarily smaller than for the peak count method, compare figs. E1a and E1b.

*Level-crossing count method (fig. E1c)* Each time the load exceeds a certain load level above the mean load a count is made. This is done for a number of load levels. (A similar procedure is applied to load levels below the mean load.) The number of level crossings of a load level need not be equal to the number of maxima above that level, as is frequently assumed; it is equal to the difference between the number of maxima and the number of minima above that level. Nevertheless, the assumption is accepted hereafter.

*Range count method (fig. E1d)* A load range is defined as the difference between two successive peak values and can thus be either positive or negative. All ranges are counted. The mean value of the ranges, i.e. the mean load between two successive peak loads, will vary from range to range, but this fact is ignored.

*Range-pair count method (fig. E1e)* Ranges are counted in pairs of equal magnitude and opposite sign, disregarding intermediate smaller ranges. An alternative interpretation of this method is discussed in ref. 15.

The load levels indicated by the rank numbers $k = 1, 2, 3, \ldots 30, 31$ were approximately equally spaced between the minimum ($k = 1$) and the maximum ($k = 31$) applied in the tests. The mean load (1g load) is represented by $k = 16$. The statistical analysis of the random load was made on the basis of the rank numbers by an electronic digital computer. The statistical symmetry of the loads around the mean load appeared to be good (ref. 2). In view of this symmetry the results of the countings will be given as averages of the numbers of maxima and minima and of the numbers of positive and negative ranges. Numerical data were given in detail in ref. 2. The results are summarized in figs. E2 and E3.

Fig. E2 shows the number of exceedings for the peak count method, the mean-crossing peak count method and the level-crossing count method. The differences between the counting results are small and restricted to the lower amplitude.

Fig. E3 shows the differences between the range count method, the range-pair count method and the mean-crossing peak count method. There is a marked difference between the former two methods, whereas the range-pair count method gives approximately 20% lower numbers of counts than the mean-crossing peak count method except for the lower amplitudes. It is thought that the range count method is not realistic since it overemphasizes the significance of small ranges at the expense of large ranges. In fig. E1d, for example, the consequence of the occurrence of range $r_2$ is that the range from A to B is not counted. Some comments on the differences between the counting methods are given in ref. 2 and a more elaborate discussion is presented in ref. 15. A similar comparison of statistical properties of random load-time histories was made by Leybold and Naumann (refs. 16 and 17) who arrived at similar results.

The VGH-recorder may be associated with the mean-crossing peak count method, whereas the Fatiguemeter (counting accelerometer) gives results between those obtained by the mean-crossing peak count method and the peak count method. In the present case (see fig. E2) the two instruments would have yielded approximately the same results. The Vickers Strain Range Counter is operating in accordance with the range-pair count method and would have given slightly smaller numbers of exceedings, as noted above.

In chapter 7 is was explained that the random tapes (load records) B1-E1 were derived from tape A1 by a non-linear amplification affecting the higher loads only and that tapes A2-E2 were derived from tapes A1-E1 by a linear reduction of the load amplitudes to 75%. The numbers of occurrences of the load levels in the 10 tapes and the sequence of the tapes in the tests are given in table E1. Within each tape the random gust load sequence of the original flight record was preserved.

The numbers of occurrence of the load amplitudes applied in the three tapes used in the program tests are given in table E2. The tapes are different for the highest amplitudes only. The sequence of application of the tapes is also indicated in the table.

TABLE E1

Loads applied in the random tests

| *Load level* | *Numbers of occurrences of load levels on tapes*[1] | | | | | | | | | |
|---|---|---|---|---|---|---|---|---|---|---|
| | *A1* | *B1* | *C1* | *D1* | *E1* | *A2* | *B2* | *C2* | *D2* | *E2* |
| 1 | — | 1 | 1 | 3 | 3 | — | — | — | — | — |
| 2 | — | — | 2 | 1 | 1 | — | — | — | — | — |
| 3 | 1 | 2 | 1 | — | — | — | — | — | 1 | 1 |
| 4 | 3 | 1 | 1 | 1 | 1 | — | — | 1 | 1 | 1 |
| 5 | 2 | 2 | 2 | 2 | 2 | — | 1 | 1 | 2 | 2 |
| 6 | 3 | 3 | 2 | 2 | 2 | 1 | 1 | 2 | — | — |
| 7 | 8 | | | | | 3 | 2 | 1 | 1 | 1 |
| 8 | 37 | | | | | 3 | 3 | 2 | 2 | 2 |
| 9 | 73 | | | | | 7 | | | | |
| 10 | 181 | | | | | 49 | | | | |
| 11 | 369 | | | | | 129 | | | | |
| 12 | 700 | | | | | 395 | | | | |
| 13 | 969 | Same as | | | | 886 | Same as | | | |
| 14 | 1312 | tape A1 | | | | 1331 | tape A2 | | | |
| 15 | 1480 | | | | | 1677 | | | | |
| 16 | 1589 | | | | | 1657 | | | | |
| 17 | 1499 | | | | | 1631 | | | | |
| 18 | 1304 | | | | | 1370 | | | | |
| 19 | 982 | | | | | 777 | | | | |
| 20 | 585 | | | | | 409 | | | | |
| 21 | 395 | | | | | 144 | | | | |
| 22 | 178 | | | | | 155 | | | | |
| 23 | 86 | | | | | 14 | | | | |
| 24 | 34 | | | | | 3 | 3 | 2 | 2 | 2 |
| 25 | 10 | | | | | 3 | 1 | 2 | 1 | 1 |
| 26 | 9 | 9 | 9 | 8 | 8 | — | 1 | — | 1 | 1 |
| 27 | 2 | 1 | — | 1 | 1 | — | 1 | 1 | 1 | — |
| 28 | 2 | 1 | 1 | 1 | 1 | — | — | 1 | — | 1 |
| 29 | — | 1 | 1 | 1 | 1 | — | — | — | 1 | — |
| 30 | — | — | 1 | — | — | — | — | — | — | 1 |
| 31 | — | 1 | 1 | 2 | 2 | — | — | — | — | — |

[1] The sequence of the tapes is indicated in the table below.

| *Tape series* | *Sequence of tapes in the tape series* |
|---|---|
| T1 | A1, A2, A1, A2, C1 A2, A1, A2, A1, C2 |
| T2 | A1, A2, A1, A2, D1, A2, A1, A2, A1, D2 |
| T3 | A1, A2, A1, A2, E1, A2, A1, A2, A1, E2 |
| T4 | A1, A2, A1, B2, B1, A1, A2, A2, B1, B2 |

Sequence of tape series in the tests: T4, T1, T4, T4, T2, T1, T1, T4, T2, T4, T4, T4, T1, T3

TABLE E2

Load cycles applied in the program tests

| *Load cycle* $k_{max}$–$k_{min}$ | $P_a$ ($\%P_u$) | *Number of cycles on tapes* | | | *Number of cycles in 140 tapes*[1] |
|---|---|---|---|---|---|
| | | *P1* | *P2* | *P3* | |
| 31–1 | 39.5 | — | 1 | — | 26 |
| 30–2 | 37.9 | — | — | 1 | 8 |
| 29–3 | 35.4 | — | 2 | — | 52 |
| 28–4 | 32.8 | 1 | 1 | 1 | 140 |
| 27–5 | 30.3 | 1 | 1 | 2 | 148 |
| 26–6 | 27.6 | 3 | 4 | 2 | 438 |
| 25–7 | 24.9 | 6 | 4 | 4 | 772 |
| 24–8 | 22.3 | 18 | 20 | 24 | 2620 |
| 23–9 | 19.7 | 42 | 44 | 44 | 5948 |
| 22–10 | 17.1 | 108 | 104 | 102 | 14968 |
| 21–11 | 14.5 | 226 | 226 | 226 | 31640 |
| 20–12 | 11.9 | 422 | 422 | 422 | 59080 |
| 19–13 | 9.2 | 702 | 702 | 702 | 98280 |
| 18–14 | 6.6 | 1092 | 1092 | 1092 | 152880 |
| 17–15 | 3.9 | 1244 | 1244 | 1244 | 174160 |
| Total number | | 3865 | 3867 | 3866 | 541160 |

[1] The sequence of the tapes is indicated in the table below.

| *Tape series* | *Sequence of tapes in tape series* |
|---|---|
| A | P1, P1, P2, P1 |
| B | P1, P1, P3, P1 |
| C | P1, P1 |

Sequence of tape series in the tests: A, A, A, B, A, A, A, B, A, A, A, B, A, C and then repeated

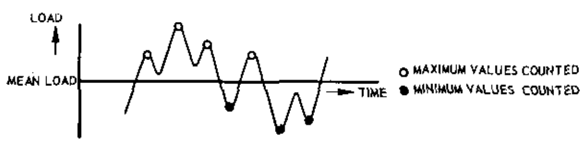


Fig. E1a Peak count method.

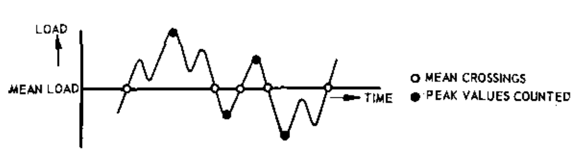


Fig. E1b Mean-crossing peak count method.

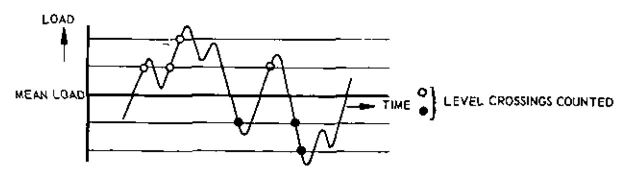


Fig. E1c Level-crossing count method.

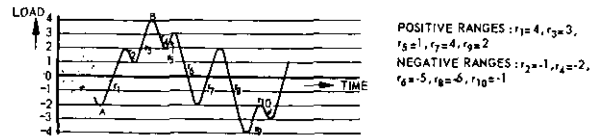


Fig. E1d Range count method.

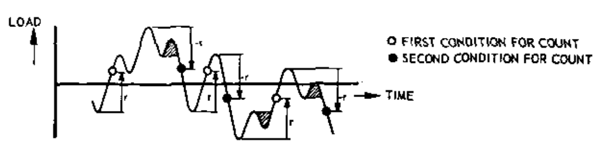


Fig. E1e Range-pair count method.

Fig. E1 Counting methods for statistical analysis of a loading record.

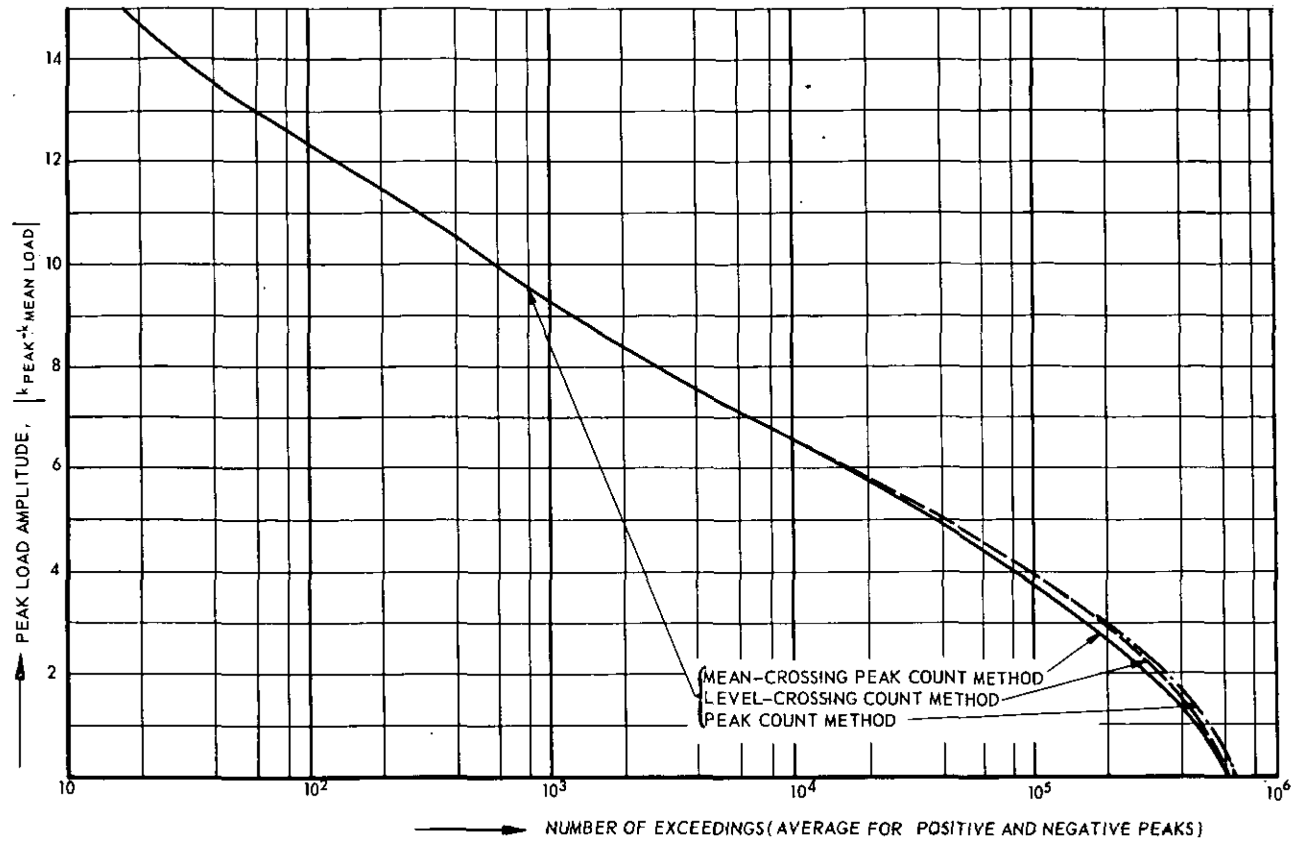


Fig. E2 Comparison of the number of exceedings of peak values as counted by three methods. The results apply to 140 test periods (tapes).

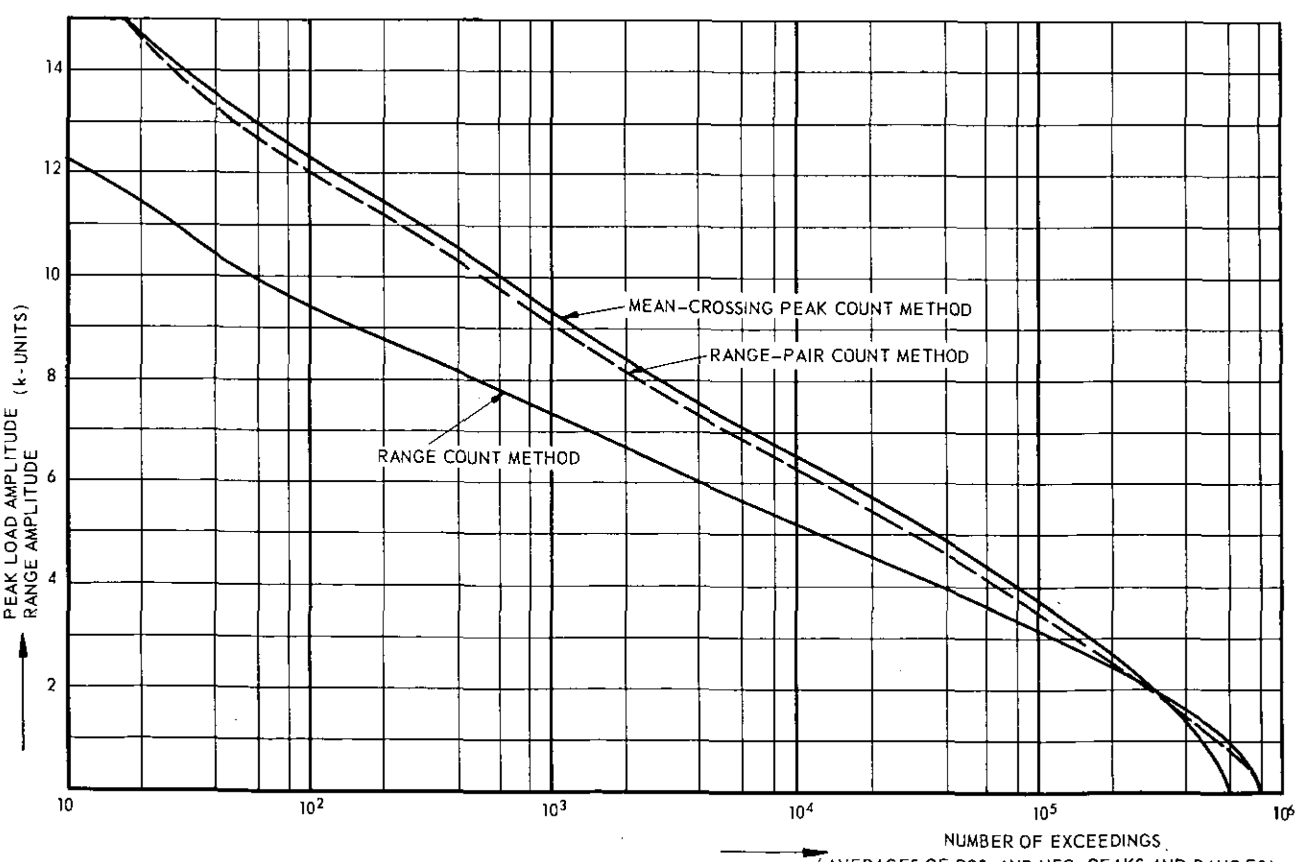


Fig. E3 Comparison of the number of exceedings of peak values and ranges as counted by three methods. The results apply to 140 test periods (tapes).

## APPENDIX F

### Evaluation of the scatter of the fatigue life at the finger tips (crack a1)

The fatigue life $N_3$ was defined as the life at which the crack length was 3 mm, according to the X-ray data. A small value was selected in order to obtain a number of $N_3$-data as large as possible. On the other hand the value was large enough for assessing $N_3$ with a reasonable accuracy.

The number of finger tips in one specimen is 80, but they are not all at the same stress level. A number of 52 finger tips was selected for which $S_u$ is approximately 40 kg/mm$^2$. This included finger tips at stringers 2–10 inside rib 1040 and at stringers 3, 4, 8 and 9 outside rib 1040. The corresponding $N_3$-values were given in refs. 4, 6 and 7.

For the statistical analysis the $N_3$-values were arranged to an increasing order of magnitude and allotted rank numbers i. The corresponding probability of failure is then defined as:

$$\text{Probability of failure} = \frac{i}{m+1} \quad \text{with} \quad m = 52$$

This quantity has been plotted against log $N_3$ on normal probability paper in fig. F1. The standard deviation of log $N_3$, denoted by $\sigma_{\log N_3}$, can be derived from the slope of the graphs. The values of $\sigma_{\log N_3}$ are indicated in fig. F1. A recapitulation of the scatter data of all tension skins is given in table F1.

During testing of specimens nos. 1, 2 and 4 no X-ray inspections were made. An $N_3$-distribution graph for the random tests (specimens 1 and 4) could therefore not be plotted. Specimen no. 2 was X-rayed after it had failed with no indications of cracks being obtained. On the fracture surface some fatigue nuclei were present from which two nuclei would probably have been detected if X-raying had been done. For specimens 6 and 7 the numbers of available data were too small for statistical handling.

Although the graphs suggest that the distribution function of $N_3$ could be approximately normal (Gaussian) there are also indications that deviations from this distribution function for low values of the probability of failure are possible.

In view of the number of data points in the graphs of figure F1 it will be clear that the accuracy of the $\sigma_{\log N_3}$ values cannot be large. Nevertheless it seems justified to say that there will be a small standard deviation for this type of crack. The average value was 0.085.

It is somewhat disquieting to notice that two specimens tested with the same loading probably yield different distribution functions. This is suggested by figs. F1a, F1c and F1d. The differences between the fatigue lives of two similarly tested specimens (at the same probability of failure) are not alarming since they still have quite usual values for fatigue. Nevertheless, it has to be admitted that the finger tips in one specimen need not belong to the same population as the finger tips in another specimen. In other words: apart from the scatter within a single structure there is another source of scatter giving differences between structures.

TABLE F1

Survey of scatter data concerning fatigue life at the finger tips

| *Specimen no* | *Type of loading* | *Number of available data* | *$N_3$ at 50% prob. of failure* [1] *test periods* | *cycles* | $\sigma_{\log N_3}$ | *coefficient of of variation for log $N_3$*[2] |
|---|---|---|---|---|---|---|
| 3 | R+GTAC | 9 | 33.9 | 142000 | 0.090 | 1.7% |
| 5 | Pr | 15 | 100.7 | 390000 | 0.067 | 1.2% |
| 8 | Pr+GTAC | 34 | 37.1 | 156000 | 0.125 | 2.4% |
| 9 | GTAC [3] | 9 | | 24300 | 0.086 | 2.0% |
| 10 | | 7 | | 27600 | 0.061 | 1.4% |
| 11 | | 15 | | 40500 | 0.062 | 1.3% |
| 12 | Constant $P_a$ | 14 | | 232000 | 0.131 | 2.4% |
| 13 | | 6 | | 24000 | 0.060 | 1.4% |
| Mean | | | | | 0.085 | 1.7% |

[1] $N_3$ was read from the probability graphs

[2] For specimens nos 3, 5 and 8 $N_3$ was taken as the number of cycles

[3] The values of $\sigma_{\log N_3}$ for specimens nos 9 and 10 deviate from those in ref. 5. The latter ones were erroneous.

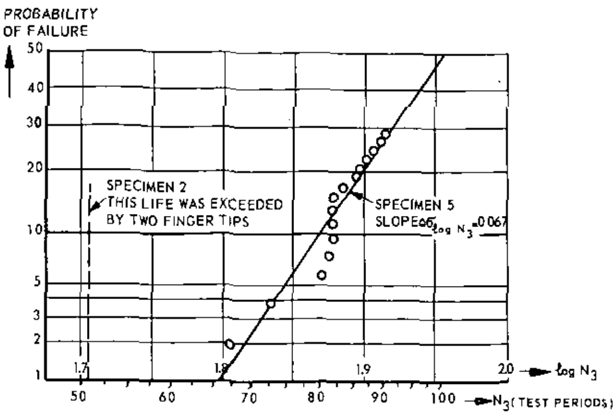


Fig. F1a Program tests.

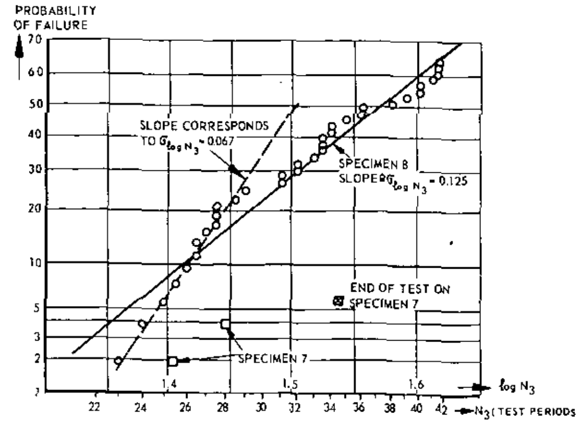


Fig. F1c Program tests with GTAC.

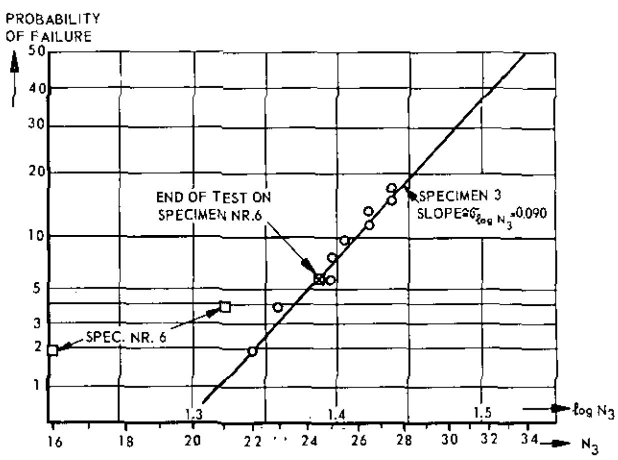


Fig. F1b Random tests with GTAC.

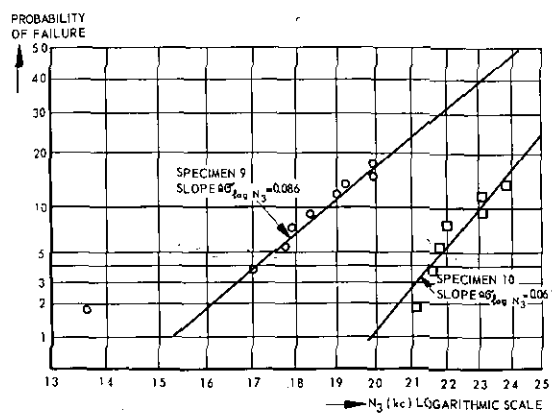


Fig. F1d Constant-amplitude tests (GTAC).

Fig. F1 The fatigue life at the finger tips ($N_3$) plotted on normal-probability paper.

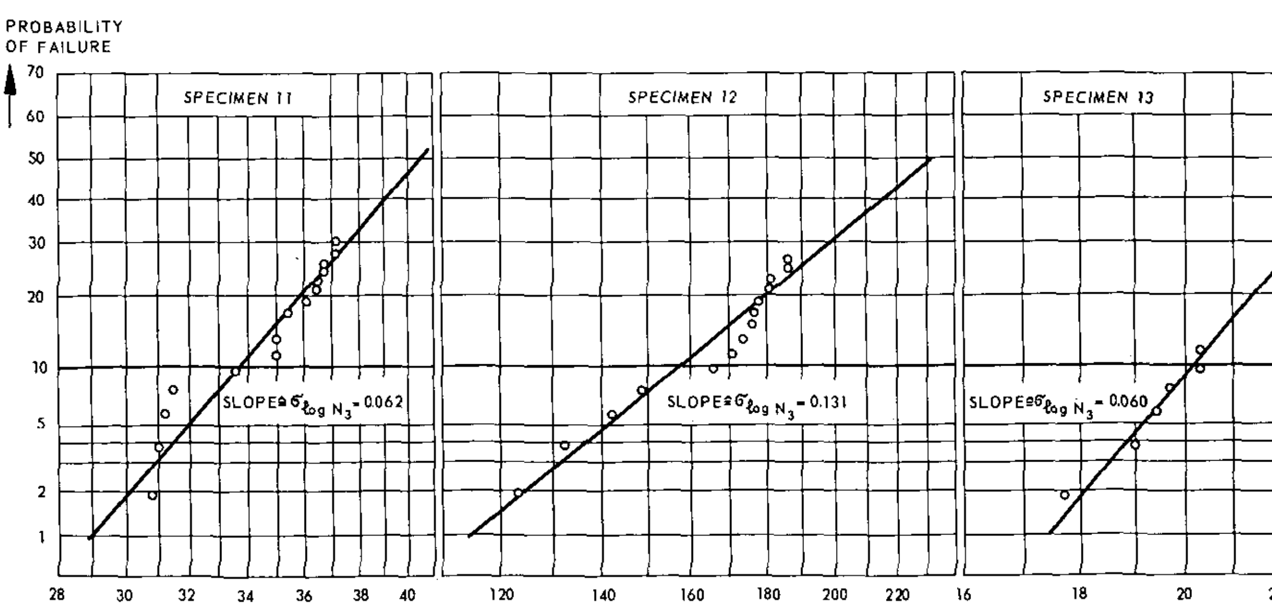


Fig. F1e Constant-amplitude tests (Gust amplitudes).

## APPENDIX G

### The effect of the ground-to-air cycle (GTAC) on the fatigue life

For wing structures there are two special features about the GTAC as compared with other fatigue loads, namely:

1) It is a periodically recurring load.
2) It is a downward load relative to the 1-g load in flight. An exception to the latter can be a fighter aircraft with an undercarriage located far outboard (ref. 32).

The GTAC has the reputation of being highly damaging and this has led to the incorporation of GTAC into many full-scale prototype tests. The testing then has the character of flight simulation. Obviously the contribution of the GTAC to the fatigue damage will depend on its magnitude and frequency in relation to the severity of the other fatigue loads, such as gusts and maneuvers.

There appear to be two reasons why the GTAC could be extra damaging. Firstly, the GTAC, considered in combination with an upward load occurring in flight, implies an increase of stress ranges. Secondly, infrequent, high upward loads may introduce favorable residual stresses and these stresses may be obliterated by the downward GTAC, depending on its magnitude. The first reason means that the GTAC itself is damaging, the second one implies that it is also increasing the damage done by other load cycles. Before making recommendations for the application of GTAC in full-scale tests the empirical evidence on the effect of the GTAC on the fatigue life will be summarized.

The effect on the fatigue life was studied in several tests series by making comparisons between tests with GTAC and tests with the same flight loads but the GTAC being omitted. The most relevant information comes from tests for which the flight loads had a random character. The results of these tests and of simplified flight simulation tests (see fig. 20) have been summarized in table G1. The table gives data on the type of specimen or structure, the number of flight loads per flight and the severity of the GTAC as compared with the 1-g load level. By adding GTAC the fatigue life obtained in tests without GTAC is reduced with an amount indicated in column (6) of the table. The reduction is the damage contribution of the GTAC. The predicted damage contribution according to the Palmgren-Miner rule is obviously equal to the cycle ratio of the GTAC ($n_{GTAC}/N_{GTAC}$), which is presented in column (7). The ratio between the actual damage and the predicted damage is given in column (8).

The most interesting information of table G1 is in column (6), showing the fatigue life reduction due to the GTAC. Although there are considerable differences between the various investigations (severity and frequency of GTAC, severity of flight loads, type of specimen etc.) the conclusion is justified that the GTAC induced a most important reduction of the fatigue life. The smaller reductions (0–30%) apply to the NLR crack propagation tests. This can be understood since during crack propagation negative loads are prevented from being harmful by closing of the crack and secondly since cracks allow an easy restoration of favorable residual stresses (ref. 40).

A comparison of the predicted damage of the GTAC with the actual damage (column 8 of table G1) shows that the latter is always larger and in most cases much larger. The predicted damage depends on the definition of the magnitude of the GTAC, the definition being in fact unconservative for most tests (see footnote 3 of the table). Several definitions were studied by Melcon and McCulloch (refs. 11 and 25) and no satisfactory definition could be obtained to suit their own results. In view of the qualitative explanation of the effect of the GTAC as given before, it can hardly be expected that some definition can be given which could have a general applicability in such a way that the damage of the GTAC would be correctly predicted. For the tests of Barrois and those of the present investigation one might have expected that the definition was at least conservative. Nevertheless, the actual damage of the GTAC was considerably underestimated. It has to be concluded that the Palmgren-Miner rule is essentially unreliable for estimating the damage contribution of the GTAC.

Since the damage of the GTAC cannot be reasonably estimated by means of Palmgren-Miner rule (which moreover requires relevant S-N data) and since the GTAC can apparently reduce the fatigue life with some 70 to 90% of its value if no GTAC were applied, it will be clear that application of the GTAC in full-scale tests is indispensable.

The reduction of the fatigue life under program loading induced by adding GTAC was also the subject of several investigations that are summarized in table G2. The GTAC are now applied in batches and again a considerable effect on the fatigue life is noticed (see column 6 of the table). Also here the predicted damage (column 7) is generally smaller than the actual life reduction. An exception is the present test series, which shows a good agreement between prediction and test result. The definition of the GTAC in the program tests was of course no problem since the GTAC were applied as separate cycles. The table may then be considered as a confirmation of the unreliability of the Palmgren-Miner rule for judging the damaging effect of the GTAC.

An interesting observation comes from tests of Gassner and Horstmann (ref. 41). Table G2 shows that application of 10 batches of 75 GTAC in each period reduced the fatigue life to 25%. Some unpublished check tests with only one GTAC in each batch gave approximately the same life reduction (private communication of professor Gassner). This clearly confirms that the damaging effect of the GTAC mainly occurred by its detrimental effect on the residual stress, rather than by its contribution to microcrack extension per se. This is one other reason to apply GTAC in a full-scale test with the periodicity as it occurs in service relative to other fatigue loads. In other words full-

TABLE G1

The reduction of the fatigue life in flight simulation tests as caused by the GTAC

| *(1)* *Type of test* | *(2)* *Investigation of* | *(3)* *Type of specimen*[1] | *(4)* *Number of flight load cycles per flight* | *(5)* $\frac{(S_{min})_{GTAC}}{(S_m)_{in\ flight}}$ | *(6)* *Reduction*[2] *of fatigue life due to GTAC(%)* | *(7)* $\frac{n_{GTAC}}{N_{GTAC}}$[3] *(%)* | *(8)* *Ratio (6)/(7)* | *(9)* *Remarks* |
|---|---|---|---|---|---|---|---|---|
| Simplified flight simulation | Barrois (ref. 34) | Riveted lap joint (2024) | 5 | +0.16 | 92 | 48 | 1.9 | |
| | | | 10 | | 87 | 36 | 2.4 | |
| | | | 49 | | 74 | 15 | 5 | |
| | | | 99 | | 72 | 8 | 9 | |
| | | | 999 | | 49 | 1.4 | 35 | |
| | Winkworth (ref. 35) | Dakota wings (2024) | 5 | < 0 | 65 | 10 | 6 | Location A |
| | | | 15 | | 29 | 7 | 4 | Location A |
| | | | 5 | | 78 | 14 | 5 | Location B |
| | | | 15 | | 35 | 7 | 5 | Location B |
| | NLR (ref. 36) | Crack propagation (2024) | 10 | +0.06 | 34 | 22 | 1.5 | Propagation from 6 to 80 mm |
| | | | 50 | | 12 | 5.7 | 2 | sheet width 160 mm |
| Random load flight simulation | Mann and Patching (ref. 37) | Mustang wings (2024) | 23 | −1.2 | 77 | 14 | 5 | Final failure tank bay area |
| | | | | | 64 | 6[4] | 10 | Initial failure gun bay area |
| | | | | | 78 | | | Initial failure tank bay area |
| | Finney, Mann and Patching (refs. 37 and 38) | Specimen with circum-ferential V-notch $K_t = 7$ | 23 | −0.97 | 46 | 25 | 1.8 | 2024-T3, Al-Cu alloy |
| | | | | −0.19 | 59 | 33 | 1.8 | DTD-363A, Al-Zn alloy |
| | | | | < 0 | 57 | | | DTD-364B, Al-Cu alloy |
| | | | | < 0 | 50 | | | 7178-T6, Al-Zn alloy |
| | Melcon and McCulloch (refs. 11 and 25) | Specimens with central notch (7075) | 13 | −0.25 | 89 | 5 | 18 | $K_t = 4$ severe gust spectrum |
| | | | 110 | −0.25 | 49 | 3 | 12 | $K_t = 4$ severe gust spectrum |
| | | | 13 | −0.25 | 83 | | | $K_t = 7$ severe gust spectrum |
| | | | 13 | −0.50 | 82 | ~ 2 | 40 | $K_t = 4$ mild gust-spectrum |
| | | | 13 | −0.50 | 87 | ~ 2 | 40 | $K_t = 7$ mild gust-spectrum |
| | | | 30 | −0.55 | 67 | ~0.01 | ~$10^4$ | $K_t = 4$ Maneuver-spectrum |
| | Naumann (ref. 39) | Edge notched specimens, $K_t = 4$ | 34 | −0.5 | 77 | 8 | 10 | 7075-T6, different types of randomness |
| | | | | 0 | 54 | 5 | 11 | 7075-T6, different types of randomness |
| | | | | −0.5 | 79 | 10 | 8 | 7075-T6, different types of randomness |
| | | | | −0.5 | 82 | 10 | 8 | 7075-T6, different types of randomness |
| | | | | −0.5 | 83 | 7 | 12 | 2024-T3 |
| | NLR present tests | Tension skins (7075) | 12 | −0.28 | 53 | 36 | 1.5 | |
| | NLR (ref. 27) | Crack propagation (2024) | 12 | +0.21 | 27 | | | Tested indoors |
| | | | | | 2 | | | Tested outdoors |

[1] The alloy is indicated in parentheses. If not indicated the alloy is mentioned in the last column.

[2] The reduction applies to the number of flight load cycles.

[3] For most test series $N_{GTAC}$ is related to tests with $P_{max}$ equal to the mean load in flight. Exceptions for the simplified flight simulation tests are those of Barrois and the NLR for which $P_{max}$ of the GTAC was equal to $P_{max}$ of the flight loads. For the random load flight simulation tests the only exception is the present NLR test series for which $P_{max}$ of the GTAC was equal to $P_{max}$ of that positive gust load which on the average occurred once per flight. In the tests of Melcon and McCulloch $P_{min}$ of the GTAC was the mean load of taxiing loads which were superimposed on the ground load.

[4] $N_{GTAC}$ was estimated from ref. 23 as being 100,000 cycles.

scale tests should have a flight simulation character rather than being program tests.

In service taxiing loads are superimposed on the ground load. When considering the damaging effect of the taxiing loads two aspects have to be considered: (1) Their amplitudes are usually small as compared with those of the flight loads and the GTAC itself. (2) The taxiing loads occur at a mean load that is low, viz. the ground load level. As a consequence the direct contribution to the fatigue damage will be small if not negligible. Indirectly the taxiing loads will certainly be damaging because they further decrease the load level attained during a GTAC and thus increase the load range of the GTAC.

There are hardly any experimental data available on the above subject. Relevant tests were carried out by Gassner and Jacoby (ref. 43) on notched sheet specimens ($K_t = 3.5$, 2024 material). They performed flight simulation tests with programmed gust loads. The GTAC contained none, 1 or 20 taxi load cycles. Stress levels in terms of the mean stress $S_m$ in flight were: $S_{min}$ for the GTAC and the taxiing loads was $-68\%\ S_m$ and $S_{max}$ of the taxiing loads was $-14\%\ S_m$, the range of the taxiing loads thus being $54\%\ S_m$. From the test results it turned out to be unimportant whether the taxiing loads were present or not. This is an encouraging result because it indicates that in flight simulation tests it might suffice to decrease the ground load in accordance with the maximum amplitude of the taxiing loads occurring once per flight. The taxiing load cycles itself could then be omitted.

Some further substantiation for the latter procedure is given by the observation of Naumann (ref. 17) that the fatigue life under random loading was not affected by omitting small load fluctuations (see chapter 9). More experimental evidence on this topic remains desirable.

TABLE G2

The reduction of fatigue life in program tests as caused by adding GTAC

| *(1) Investigation of* | *(2) Type of specimen* | *(3)* $\frac{n_{\text{flight loads}}^{1}}{N_{\text{GTAC}}}$ | *(4)* $n_{\text{GTAC}}^{2}$ *per period* | *(5)* $\frac{(S_{\min})_{\text{GTAC}}}{(S_m)_{\text{flight}}}$ | *(6) Reduction[3] of fatigue life due to GTAC (%)* | *(7)* $\frac{n_{\text{GTAC}}}{N_{\text{GTAC}}^{4}}$ *(%)* | *(8) Ratio (6)/(7)* | *(9) Remarks* |
|---|---|---|---|---|---|---|---|---|
| Gassner and Horstmann (ref. 41) | specimen with elliptical hole $K_t = 3.5$ (2024) | 666 | 10×75 | −0.38 | 75 | 6.5 | 12 | |
| McCulloch and Melcon (refs. 11 and 25) | specimens with central notch (7075) | 13 | 1×185 | −0.25 | 84 | 13 | 6 | $K_t = 4$ severe gust spectrum |
| | | 110 | 1×90 | −0.25 | 65 | 4 | 16 | $K_t = 4$ severe gust spectrum |
| | | 13 | 1×1170 | −0.5 | 84 | 13 | 6 | $K_t = 4$ non-severe gust spectrum |
| | | 13 | 1×113 | −0.5 | 73 | 7 | 10 | $K_t = 7$ non-severe gust spectrum |
| Crichlow et al. (ref. 42) | double butt splice joint (7075) | 12 | 1×3250 | −0.25 | 48[5] | | | gust spectrum |
| | | 30 | 1×665 | −0.88 | 66[5] | | | maneuver spectrum |
| Naumann (ref. 9) | edge-notched specimen, $K_t = 4$ (7075) | 12 | 1×125 | −0.5 | 64 | 23 | 3 | |
| NLR present tests | tension skins (7075) | 12 | 6×56 | −0.28 | 50 | 48 | 1 | |
| NLR (ref. 27) | crack propagation | 12 | 6×56 | +0.21 | 35 | | | Tested indoors, 2024 |
| | | | | | 55 | | | Tested outdoors, 2024 |
| | | | | | 68 | | | Tested indoors, 7075 |
| | | | | | 43 | | | Tested outdoors, 7075 |

1 This column gives the ratio between the number of flight loads and the number of GTAC. The ratio is the average number of flight loads per GTAC.

2 The first number gives the number of batches of GTAC per period and the second number indicates the number of GTAC in each batch.

3 The reduction applies to the number of flight load cycles.

4 For all test series $N_{GTAC}$ is related to the GTAC as applied in the program tests. For all test series except the NLR tests $P_{max}$ of the GTAC was equal to $P_m$ of the flight loads. In the NLR tests it was equal to $P_{max}$ of the positive gust load which on the average occurred once per flight.

5 Apart from the GTAC also taxiing loads were applied with a mean load equal to $P_{min}$ of the GTAC.

## APPENDIX H

### The significance of the Palmgren-Miner rule for full-scale fatigue testing

The rule $\Sigma\, n/N = 1$ was first proposed by Palmgren and it received wide attention by a paper of Miner. It is frequently referred to as the "linear cumulative damage theory" although it is not necessary to assume a linear accumulation of damage, as was done by Miner, to arrive at the rule. It is necessary, however, that the fatigue damage at a given moment is fully characterized by a single damage parameter (for instance crack length) and that this damage parameter in a test with constant $S_a$ and $S_m$ is a (monotonically) increasing function of the cycle ratio $n/N$, which is the same for all values of $S_a$ and $S_m$ (ref. 44). These requirements are already so restrictive that with the present state of knowledge about the fatigue phenomenon it is justified to say that the rule is physically incorrect and the same applies to other theories employing only one independent damage parameter. One could only hope that the Palmgren-Miner rule would give reasonable approximate results for those loading conditions that are of practical interest.

Considering the value of the Palmgren-Miner rule for the designer one could think of the following three applications:

1 Life estimations in the design stage.
2 Indication of fatigue loads that are important and other fatigue loads, which are not important, for instance for planning a full-scale test.
3 Correcting of fatigue lives obtained by testing to other load spectra.

In view of the first application many investigations were performed to check the validity of the Palmgren-Miner rule and several reviews of these investigations were published in the literature. Two such reviews regarding aluminum alloys were prepared at the NLR (refs. 45 and 20, see also ref. 46). In the first review it was shown that unconservative life estimates by the Palmgren-Miner rule (i.e. test results $\Sigma\, n/N < 1$) were almost exclusively coming from rotating beam specimens ($S_m = 0$) and mainly from unnotched specimens. It was also indicated that for notched specimens loaded at a positive mean stress conservative estimates (i.e. test results $\Sigma\, n/N > 1$) were generally obtained. In the second review (ref. 20) the latter trend was confirmed by reviewing the results of program fatigue tests available at that time (1960). It had to be admitted, however, that the rule was not very accurate since considerable deviations from $\Sigma\, n/N = 1$ could occur. Most deviations could be explained by considering the role played by residual stresses. Since then a number of investigations were published, which allowed a further checking of the Palmgren-Miner rule (for instance refs. 32, 37–43 and 47–53) and which further substantiated the above trends.

In spite of its inaccuracy it was still concluded (ref. 46) that the Palmgren-Miner rule was a useful tool for obtaining rough life estimates in the design stage of an aircraft. The major problem for application of the rule for this purpose was considered not to be the inaccuracy of the rule but rather the limited accuracy of relevant S–N data and load statistics required for the calculations.

Considering now the second and third applications of the Palmgren-Miner rule as mentioned above, it may be said first that the third one is included in the second one. Correcting for deviating load spectra implies accounting for some extra fatigue loads and the omission of some other fatigue loads. Decisions whether these loads are important for fatigue could be made on the basis of the Palmgren-Miner rule and this is the second application mentioned above.

It was stated in ref. 46 that the Palmgren-Miner rule is unreliable for judging whether a certain type of service load will contribute substantially to the damage induced by other types of loading. Two notorious examples are the GTAC and the loads with an amplitude below the fatigue limit. The first case is discussed in Appendix G. Loads below the fatigue limit are not damaging according to the Palmgren-Miner rule, whereas program tests have shown that they are. Although this result does not necessarily apply to random loading it is still another indication that the Palmgren-Miner rule is uncapable of accounting for interaction effects between different loads applied in the same test.

As an example of the unreliability of the Palmgren-Miner rule for the third application mentioned above, a modification of the load spectrum implying a reduction of the numbers of the higher loads will be considered. According to the rule such loads are almost non-damaging due to the relatively low number of occurrence. Consequently the modification of the load spectrum should have a negligible effect. However, experimental evidence regarding the highest load level in program tests (ref. 49) and program-load flight simulation tests (ref. 43) revealed significant effects.

It is now postulated that the invalidity of the Palmgren-Miner rule is not an urgent matter for full-scale testing. This is based on the following arguments: (1) If the rule was valid full-scale testing would still be necessary for establishing accurate S–N data. The problem is that more than one test and more than one specimen are required for this purpose. (2) With the presently available hydraulic equipment the more complicated load sequence in a flight simulation test can hardly be considered as a serious disadvantage.

The conclusion does not want to question the value of experimental investigations regarding the fatigue life under variable-amplitude loading. On the contrary, it was from such investigations that the importance of various kinds of fatigue loads for an aircraft structure has emerged and that the rule played by residual stresses became clearer. It is even thought that there is still ample room for more experimental investigations of this type. In fact, the present test series can also be regarded as such an investigation.

One remark with respect to $\Sigma\, n/N$ values has to be made here. In spite of the nonvalidity of the Palmgren-Miner rule, the damage value $\Sigma\, n/N$ as a test result of a variable-amplitude test is considered to be a useful yardstick for appreciating the test result. This is true because if there were no interactions between the damaging effects of load cycles of different amplitudes the deviations from the Palmgren-Miner rule would probably be small. Consequently, the deviation from $\Sigma\, n/N=1$ gives an indication about the question whether such interactions have been active and whether they can be regarded as favorable or unfavorable. Consequently, it is thought useful in research investigations on fatigue under variable-amplitude loading to carry out constant-amplitude tests also.

## APPENDIX J

### The influence of the loading history on the indication of fatigue-critical components

In section 10.2.4 it was explained that high loads will introduce local stress redistributions around notched and that the effect on the fatigue life may be different for different notches, depending on $K_t$, stress gradient and nominal stress level. The consequence is that the indication of the most fatigue-critical component in a structure may depend on the selected load spectrum. Fatigue tests on large structures reported in the literature give some information on this question. They are summarized in this Appendix.

*Tests on Mustang wings.* Results of an extensive test program on Mustang wings were reported in refs. 23, 37 and 55. The following types of tests were carried out:

(1) Constant-amplitude tests, various $P_a$ and $P_m$ values
(2) Program tests with 3 amplitudes, $P_{max} \cong 33\% \, P_u$
(3) Random load tests, gust spectrum, $P_{max} = 63\% \, P_u$
(4) Random load tests with GTAC, same gust spectrum, $P_{min}$ for GTAC $-24\% \, P_u$
(5) Random load tests, maneuver spectrum, including negative maneuver loads, $P_{max} = 75\% \, P_u$

The l-g load level for test series 2-5 was $20\% \, P_u$. The stresses at $P_u$ were in the order of 28 kg/mm$^2$.

Cracks were mainly found in two areas, indicated as the tank bay area and the gun bay area. For the two areas intersecting S–N curves were found in test series no. 1, both for initial cracking and final failure. This shows that a certain component, which under constant-amplitude loading is more fatigue critical than another component, can be less critical at another load level.

In test series 2–5 the initial failure was always first observed in the gun bay area. However, cracking in the tank bay area could be more serious. The final failure occured in both areas in test series 2 (lower $P_{max}$ value) and in the tank bay area only in test series 3, 4 and 5. In the random gust tests without GTAC the gun bay area was then in an advanced stage of cracking, whereas this failure was almost completely suppressed in the random gust tests with GTAC. The latter was partly true also for test series no. 5.

*Tests on Commando wings.* Results of tests on Commando wings were reported by Huston in ref. 56. Three types of tests were conducted, viz:

(1) Constant amplitude tests ($P_{max}$ values $\leqslant 59\% \, P_u$)
(2) Program tests with a gust spectrum ($P_{max} \sim 75\% \, P_u$)
(3) Program tests with a maneuver spectrum ($P_{max} \sim 78\% \, P_u$)

A limited amount of service experience was available. The program tests were randomized step tests. The stress at $P_u$ was low, viz. about 19 kg/mm$^2$.

Constant-amplitude tests revealed only 1 or 2 fatigue-critical locations, which were different for high and low amplitudes. In test series 2 and 3 cracks were found at 7 different locations. With respect to the first crack to turn up, the crack at location F (code of ref. 56) was the most frequent one in test series 2 and 3, whereas this location was not very important in the constant amplitude tests. The most critical crack with respect to final failure was found at location B in the constant-amplitude tests and at location III in the program tests.

A comparison between the cracks found in service (4 aircraft) and in the program tests (gust spectrum) yielded a reasonable agreement regarding the locations at which cracks were found.

*Tests on Dakota wings.* In ref. 35 Winkworth reported the results of testing 4 Dakota wings and a comparison with service experience.

The following four tests were carried out:

(1) Gust cycles only, constant amplitude, $P_a$ corresponding to 12 ft/sec gust
(2) Simplified flight simulation, 15 gust cycles (as applied in test no. 1) per flight
(3) Same as test no. 2, except 5 instead of 15 gust cycles per flight
(4) GTAC only, $P_{max}$ at 1-g level, $P_{min} < 0$.

Cracks occurred at three different locations A, B and C. The most critical crack in tests nos. 1 and 2 occurred at location A and in tests nos. 3 and 4 at location C. Cracks at location B were found in all tests. In service cracks were predominantly found at location B and cracks at location A did not occur. Cracks were also found in service at a location at which no cracks were found in the tests. It cannot be said that a fair agreement between service experience and testing was obtained. This may be partly due to the simplified flight-simulation load sequence adopted for the tests.

*Tests for a swept back wing.* Results of constant-amplitude tests and program tests on a wing of a fighter were reported by Rosenfeld (ref. 32). In the program tests two different maneuver spectra were used. In one test series GTAC were inserted (in batches), which in this case were upward loads rather than downward loads. Values for $P_{max}$ from 55 to 100% $P_L$ ($P_L$ is limit load) were used in the constant-amplitude tests and from 35 to 125% $P_L$ in the program tests. $P_{min}$ was 13.3% $P_L$ in all tests.

In each wing failure always occurred at a bolt hole. In the program tests (4 different programs) failures occurred at locations A (6 times), C (once), E (twice) and F (once). In the constant-amplitude tests failures occurred at locations A (7 times, especially at the higher load levels), B (twice), C (once) and D (twice, at the lowest load level only).

*Present test series.* The results were reported in chapter 8. The following comments may be made here. Contrary to Huston's findings the number of locations at which cracks were detected was larger in the constant-amplitude tests than in the random load and the program tests. Secondly if no repairs had been made the cracks at the finger tips would have been the most critical ones in all tests. This was due to the locally high nominal stress level.

Two trends have turned out from the available information: (1) The picture of fatigue-critical elements in an aircraft structure depends on the load-time history applied. (2) The same is true for the indication of the most fatigue-critical component in the structure. Some explanations are possible, viz:

(a) The trends are a consequence of differences between the load sequences
(b) The trends are due to differences in the highest load applied in the test causing different degrees of stress redistribution. With respect to the second trend the residual strength characteristics at different fatigue-critical locations in the structure may also be important.
(c) The trends have to be related to scatter.

On the basis of the test results it is very difficult to discriminate between the three causes. An application of exactly the same load spectrum, but having different load sequences was used in the present test series (random vs. program loading). The picture of fatigue-critical elements appeared to be independent of the load sequence. It is indeed thought that the second cause, differences between the highest loads applied, is the predominant one. Apart from the results summarized, further substantiation for this view is offered by various test series on structures and joints concerning variable-amplitude testing and constant-amplitude loading with and without high loads (refs. 20, 23, 32, 47, 57 and 58). They clearly confirm the influence of high loads on the fatigue life, especially if the high loads recurred periodically.

The third cause, scatter, is in principle a contributing factor. However, as a whole the results summarized are considered to allow the conclusion that scatter was not the main factor causing the trends observed.

## APPENDIX K

### Some comments on component testing

Testing of components can be adopted for two reasons, namely:

(1) Alternative method to full-scale testing.
(2) Design development.

It was pointed out in section 10.1 that full-scale testing should be preferred to component testing for proving any new aircraft design. If one still wants to stick to the latter method for assessing fatigue characteristics, then all recommendations on planning the load sequence made in the previous sections and recapitulated in the conclusions (chapter 11) remain valid. That means that flight-simulation has to be preferred to program loading. Flight simulation tests can be performed on fatigue machines that have been commercially available for some time.

With respect to comparative tests on components for design development purposes, it is curious to see how the idea that constant-amplitude testing is good enough to this end is still held by so many. Obviously it is better than nothing, but it is really a poor representation of the actual service load-time history. A component that is superior to another component at a certain constant-amplitude loading may be inferior to it at a different constant-amplitude loading (intersecting S–N curves, see Appendix J). Under a more realistic load sequence, the relative merits of the two components may again have changed. Constant-amplitude tests may thus give misleading information on the values of design modifications. Moreover, there is the risk of a large scatter if the fatigue life is long.

It has been advocated in the literature to perform constant-amplitude tests at "the most damaging level", a level to be estimated by employing the Palmgren-Miner rule and some S–N curve. Since the rule assumes the absence of any interaction effects between different load levels it is thought that the assessment of a meaningful "most damaging level" is fully illusory.

Program loading is certainly a better method for design development studies than constant-amplitude testing. Fatigue machines that allow an automatic application of infrequent high loads generally permit an automatic flight-simulation test also, which should then be preferred. However, the older fatigue machines and all resonant fatigue machines do not allow the application of small numbers of high loads, although program loading may be possible. For program tests on such machines the maximum load amplitude should be chosen as high as the program apparatus of the machine allows. Resonance machines with an additional "slow drive" make further improvements of the program possible. The minimum load amplitude should be selected as low as possible. The GTAC have to be included in batches now. For the maximum load of the GTAC one could adopt the maximum positive load that on the average occurs once per flight. This has led to satisfactory results in the present test series. Further recommendations for planning a program were given in refs. 20 and 46.